SHOCK STUDY WITH AN EXTENDED-MHD MODEL USING A POSITIVITY-PRESERVING SEMI-IMPLICIT DISCONTINUOUS GALERKIN SCHEME

A Dissertation

Presented to the Faculty of the Graduate School

of Cornell University

in Partial Fulfillment of the Requirements for the Degree of

Doctor of Philosophy

by

Xuan Zhao

January 2015

SHOCK STUDY WITH AN EXTENDED-MHD MODEL USING A POSITIVITY-PRESERVING SEMI-IMPLICIT DISCONTINUOUS GALERKIN SCHEME

Xuan Zhao, Ph.D.

Cornell University 2015

A positivity-preserving discontinuous Galerkin (DG) scheme (Zhang, X. & Shu, C.W., J. Comp. Phys., 229(23), 8918-8934.) is used to solve the Extended Magnetohydrodynamics (XMHD) model, which is a two-fluid model expressed with a center-of-mass formulation. We prove that the DG scheme with a positivity-preserving limiter is stable for the system governed by the XMHD model or the resistive MHD model. We use the relaxation system formulation (Seyler, C. E., & Martin, M. R. Physics of Plasmas, 18, 012703.) for describing the XMHD model, and solve the equations using a split level implicit-explicit time advance scheme, stepping over the time step constraint imposed by the stiff source terms. The magnetic field is represented in an exact locally divergence-free form of DG (Li, F., & Shu, C. W. 22(1-3), 413-442.), which greatly improves the accuracy and stability of MHD simulations. As presently constructed, the method is able to handle a wide range of density variation, solve the XMHD model on MHD time scales, and provide greatly improved accuracy over a Finite Volume implementation of the same model.

The extended-MHD code DG-PERSEUS, which is an implementation of this method on a 3D Cartesian coordinates, has been applied to the study of the magnetized shock in the context where a magnetized flow is interacting with a solid obstacle. Several physics issues are found to be associated with this problem,

such as bow shock, reconnection, plasmoids, which have been studied. The inflow parameters, such as the magnetosonic mach number M_f and the ratio of thermal pressure to magnetic pressure β can significantly affect the physical structures of the flow-obstacle interaction, which can be used as a diagnostic tool for the flow. The Hall effect can also significantly influence the results. Interplanetary physics - the solar wind interacting with Mars - is also studied. Simulations are carried out to show that the interplanetary features (bow shock, reconnection) can also be achieved with laboratory parameters.

BIOGRAPHICAL SKETCH

Xuan Zhao was born in Lianyungang, China. She grew up in a beautiful town on the seaside. She went to Donghai Senior High School where she developed her interest in science. She went to University of Science and Technology of China as an undergraduate. Her love for science prompted her to pursue physics as her major. She received her BS in Applied Physics in 2010. Then she came to the US for further studies. She began her Ph.D. program at Electrical and Computer Engineering department at Cornell University in 2010. She received her MS in Electrical and Computer Engineering in 2013.

To my parents, whose love towards me is the foundation of my life.

And

To Charles E. Seyler, an advisor I could never thank enough.

ACKNOWLEDGEMENTS

The Ph.D. program is an exciting and rewarding journey which cannot be completed alone by myself. May I pay tribute to those who has helped bring to this point in this special part of the dissertation.

I am very grateful to the useful guidance offered by my special committee: Professors Charles Seyler, David Hammer and Richard Lovelace. Especially, I would like to express my gratitude to Charles Seyler, a caring, understanding, kind and supportive advisor. He not only taught me how to become a better researcher, but more importantly, how to become a better person. I am also very appreciative to John Greenly, whose mentorship and insightful inputs made this dissertation as it is now. I would also like to extend my thanks to Yang Yang, who has taught me how to think as a Mathematician. Furthermore, I would like to thank my officemate, Nat Hamlin, for the support and all the insightful discussions. In addition, the support and encouragement of my colleagues in the Laboratory of Plasma Studies has been invaluable, thank you all.

Thank you Yuxiao, your support has provided me the power to move forward.

CONTENTS

Biographical Sketch . . . iii

Dedication . . . iv

Acknowledgements . . . v

List of Tables . . . ix

List of Figures . . . xi

1 Introduction **1**

2 Extended-MHD Model **8**

2.1 Full Two-fluid Model . . . 9

2.2 Two Fluid Model with a Center-of-mass Formulation . . . 11

2.3 Extended-MHD Model . . . 13

2.4 Resistive MHD model . . . 15

2.5 Relaxation Model . . . 17

3 Positivity-preserving Semi-implicit Discontinuous Galerkin Scheme **19**

3.1 Local divergence-free discontinuous Galerkin formulation . . . 19

3.2 Positivity-preserving Limiter . . . 23

3.2.1 Proof of positivity-preserving property of extended-MHD model . . . 23

3.2.2 Proof of positivity-preserving property of two-fluid model 28

3.2.3 Implementation of the Positivity-preserving Limiter . . . 32

3.2.4 Remark on Difference between Positivity-Preserving Limiter vs a TVD Limiter . . . 33

3.3 Structure Preserving Limiter . . . 35

3.4 Boundary Conditions . . . 40

3.5 Time Integration Scheme . . . 45

4 Numerical Tests **47**

4.1 Accuracy Test . . . 48

4.2 The Brio-Wu shock-tube problem . . . 52

4.3 Pressure Balance Test . . . 53

4.4 Moving Planar Foil . . . 54

4.5 Kelvin-Helmholtz Instability . . . 56

4.6 Some remarks on the comparison between DG and FV . . . 59

4.7 Two-dimensional tests and comparison of XMHD to MHD . . . 60

4.7.1 Collisional Bow-Shock Problem . . . 61

4.7.2 Magnetic Reconnection . . . 63

4.8 The Study of Radial Foils with 3D DG-PERSEUS . . . 66

4.9 Summary of Numerical Tests . . . 68

5 A Novel Configuration for Driving Magnetic Reconnection **71**

5.1 Introduction . . . 71

5.2 Inverse Skin Effect . . . 77

5.3 Background: Experimental Set Up and Selected Experimental Results . . . 81

5.4 Simulation Study . . . 86

5.4.1 Simulation Set-Up . . . 87

5.4.2 Analysis of Simulation Results . . . 87

6 Magnetized Shocks **99**

6.1 Hydrodynamic Bow Shock . . . 99

6.2 MHD waves . . . 105

6.3 MHD shocks . . . 108

6.3.1 Slow Shock Test . . . 111

6.3.2 Fast Shock Test 114

7 Magnetized Flow Interacting with Obstacle 118

7.1 Introduction 118

7.2 Problem Setup 120

7.3 Simulation with the MHD Model 121

7.3.1 Simulation Result 122

7.3.2 Bow Shock 122

7.3.3 Analytic Evaluation on why Bow Shock is a Fast Shock . . 125

7.3.4 Magnetic Reconnection in the Shock Tail 127

7.3.5 Magnetotail Reconnection Outflow is Bounded by Slow Shock 130

7.3.6 Plasmoids Generated in the Shock Tail 130

7.3.7 Reason for Different Magnetotail Structures 133

7.3.8 Cases with Same Upstream Mach Numbers 139

7.3.9 Results Change With the Variation of Upstream Mach Numbers 140

7.4 Simulation with XMHD Model 142

7.4.1 Simulation Result 142

7.4.2 Cases with same upstream Mach numbers 145

7.4.3 Results Change With the Variation of Upstream Mach Numbers 147

7.4.4 Results Change With the Variation of Upstream β 149

7.5 Comparison between the results of extended-MHD and MHD . . 151

7.5.1 XMHD results to approach MHD results 152

7.5.2 MHD results to approach XMHD results 156

7.6 Evaluation of Experimental Results 157

7.7 Hall Term Facilitates Reconnection 162
7.8 Biermann Battery Effect 165

8 Simulation on Interplanetary Physics of Mars 167
8.1 Solar wind Interaction of Planets 168
8.2 XMHD simulation of Mars 170
8.2.1 Problem Set Up 170
8.2.2 Simulation Results 171
8.3 Reproduction of Martian Phenomena with Lab Parameters 173

9 Conclusions 175
9.1 Summary 175
9.2 Future Work 178

A Energy Conservative Form with Extended-MHD Model 179

B Calculation of Freezing Speed 183

Bibliography 195

LIST OF TABLES

3.1 Comparison between TVD limiter and Positivity-Preserving Limiter 36

4.1 Characteristic Scales used to Non-dimensionalize Parameters . . 49
4.2 Accuracy Test Result 51

8.1 Characteristic Scales used to Non-dimensionalize Parameters . . 171

LIST OF FIGURES

3.1 Sketch showing the left boundary on x direction 44
3.2 When performing parallel computing, the information on the boundary has to be communicated between computational cores. Take two cores as an example, the area highlighted in red is the information to be communicated. 45

4.1 Diagram showing the density profile along the first quarter of the diagonal; 4 tests are presented, with a resolution of 50×50, 100×100, 200×200, 400×400, respectively. Analytical solution is also provided for comparison. It is clearly shown in this diagram that, when we increase the resolution, the numerical solution is approaching the analytical solution. 51
4.2 Brio Wu shock tube test. Density as a function of position, captured at $t = 2.1 \times 10^{-2}$ 53
4.3 DG vs FV result for Pressure Balance Test. FV with 200 cells is most diffusive shown in black, DG with 200 cells shown in green agrees with analytical results best; FV with 1600 cells shown in red is closer to analytical results but still not as good as DG results with 200 cells. 54
4.4 number density n as a function of position x captured at $t = 34$ ns; Initial foil position: $x = 5$mm. 56
4.5 Magnetic field B as a function of position x captured at $t = 34$ ns. 56
4.6 Comparison between DG and FV results for Kelvin-Helmholtz instability. The figures are color plots of vorticity $\nabla \times \mathbf{v}$. It is clear from the figures that the instability growth rate is severely suppressed by the numerical diffusion of FV method, one needs to refine the resolution to as high as 800×400 to get to a result closer to DG with a resolution of 200×100. The time taken for reaching these same results is: FV, 1365s, DG, 211s, which means that DG is 6 times faster than FV for achieving comparable results for this particular case. 57
4.7 Kelvin Helmholtz instability growth 59
4.8 Bow shock simulation, captured at $t = 140$ns 63
4.9 GEM challenge problem 65
4.10 Setup of Radial foil problem. Radius of the radial foil is 9mm, diameter of the central post is 1mm. 66

4.11 The development of radial foil physics. First the ablation of the foil starts to form a precursor jet, then the ablated foils form a bubble, the return current forms another central column jet inside the bubble. As the bubble grows larger and larger, the central column carrying the return current grows thicker and thicker. Kink instability gradually develops in the central jet column. When the bubble grows sufficiently large, the upper part will get detached from the lower region. 68

5.1 Measurement of Reconnection Rate. O denotes the center point of the X shape, In/out flow are shown in blue, the magnetic field lines are shown in black, the diffusion region shown by the grey box, the red dashed box shows the integration loop Γ 75
5.2 Sweet-Parker model of Reconnection. Diffusion region denoted by a rectangular box with thickness as 2δ and length as $2L$, u_{in} denotes the inflow speed, u_{out} denotes the outflow speed, B_{in} denotes the magnetic field in the inflow region. 76
5.3 Petschek model of Reconnection. Diffusion region denoted by a rectangular box, u_{in} denotes the inflow speed, u_{out} denotes the outflow speed, B_{in} denotes the magnetic field in the inflow region. The flow can get accelerated as it go through the slow shock denoted by the dashed blue line. 76
5.4 Plots showing the inverse skin effect: the decrease of magnetic field on the boundary, which is equivalent to the reversal of driving electric field, drives a reversed current on the surface of the wire, results in the reversal of magnetic force $\mathbf{J} \times \mathbf{B}$ at the edge of plasma, which pushes the plasma outwards; at the same time, the inner part of the plasma still carries current in the original direction, so the inner part is still compressing down. Continue on Figure 5.5. 79
5.5 Continued from Figure 5.4: Plots showing the inverse skin effect: the decrease of magnetic field on the boundary, which is equivalent to the reversal of driving electric field, drives a reversed current on the surface of the wire, results in the reversal of magnetic force $\mathbf{J} \times \mathbf{B}$ at the edge of plasma, which pushes the plasma outwards; at the same time, the inner part of the plasma still carries current in the original direction, so the inner part is still compressing down. 80
5.6 Typical COBRA pulse waveforms. 83
5.7 Crowbarred COBRA pulse 84

5.8 Sequence of XUV images, end-on view. Wires 16 mm apart, connected to the toothed anode edges at top and bottom of the images. Times (from left to right) are 130 ns, 160 ns, 240 ns, 260 ns and 360 ns respectively (refer to Figure 5.6 to see where these time slots are in the driving pulse waveform) 84
5.9 Side-on laser shadowgraph at 260 ns. The Upper Right picture is enlargement of central sheet. 85
5.10 (A) Upper figure. XUV images at 380 ns of normal pulse (The driving current pulse follows 5.6); (B) Lower figure. XUV images at 380 ns of a crowbarred pulse (The driving current pulse follows 5.7). The positions of the obstacles are as indicated by a white rectangle. 86
5.11 The setup of the simulation region. We have two circular wires with a diameter of 5.0mm, a number density of $6 \times 10^{19}/\text{cm}^3$; We drove the region with a circular magnetic field on the boundary, which is equivalent to apply a voltage/ a driving current on the direction into the plane. The shape of the driving current is as shown in Figure 5.12. For achieving the simulation results presented in this chapter, we used a resolution of 160×160. 88
5.12 The plot of driving current versus time. 89
5.13 t = 150ns, wires are still pinching down at this stage; And because of the attraction of the other wire, current starts to accumulate towards the point closest to the other wire. During the pinching-down process, magnetic energy is converted into internal energy, so that the thermal pressure inside the wire is building up. 91
5.14 t = 200ns, because of the decrease of the driving magnetic field, a reversed electric field is introduced, which drives a reversed current on the surface of the wires. This results in a $\mathbf{J} \times \mathbf{B}$ force pointing outwards, which causes the expansion of the wire. From the figure, it is clear that the current on the edges of plasma is negative, when the expanding plasmas meet with each other, the negative current on the edge will form an extended reversed current sheet. This current sheet supports the X configuration, and reconnection is able to happen. Because of the skin effect of plasma, the reversed electric field is not able to penetrate further into the wire, so the inner part of the wire still carries the original current, that is why the inner part of the wire is still pinching down at this stage. 92
5.15 t = 300ns, plasmas keep expanding, form an outflow, which is bounded by radiative shocks; The outflow is accelerated out by both pressure gradient force and $\mathbf{J} \times \mathbf{B}$ force. During this period, magnetic energy and internal energy are converted into kinetic energy. 93

5.16 t = 360ns, the outflow is bounded by slow shocks, and continues to be accelerated out. 94
5.17 t = 425ns, X point is still there, but is near to disappear. This is a good example that DG is better than FV. Since the numerical diffusion is small, the X-point is able to live until very late in time. If we did exactly the same simulation with FV, we will find that the X-point disappears around t = 350ns, and an O-point forms instead. 95
5.18 t = 500ns, driving current is zero, the plasma expansion continues, the X-point disappears, leaving an O-point there, and the open angle of the outflow becomes larger. 96
5.19 Force Analysis, Line plot over X-axis. Black Line: $(\mathbf{J} \times \mathbf{B}) \cdot \hat{\mathbf{v}}$, Green Line: $-\nabla P \cdot \hat{\mathbf{v}}$, Pink Line: $\mid v_A \mid$ (10^4m/s), Red Line: $\mid \mathbf{v} \mid$ (10^4m/s); Before 300ns, Pressure Gradient ∇P always plays a negative role in accelerating the outflow, and $\mathbf{J} \times \mathbf{B}$ is the main accelerating force. ∇P gradually comes into play, and accelerates the outflow. 97
5.20 Energy change as a function of time. 98

6.1 A stationary point source (fixed) which sends out small-amplitude perturbations is in a steady flow with velocity u. In the reference frame moving with flow, the perturbations propagate with velocity v_s spherically. In the frame of the source, we have to superimpose the reference velocity difference, which is just the flow velocity $\mathbf{u}$. So in the reference frame of the source, the perturbed region is not a sphere anymore. 103
6.2 Supersonic neutral gas interacting with an obstacle 104
6.3 Characteristic MHD shocks in the shock rest frame 111
6.4 Density, thermal pressure and transverse field in a slow switch-off shock with ideal-MHD model, 400 cells, initial shock position at $x = 0$, captured at $t = 0.5$ 112
6.5 Density, thermal pressure and transverse field in a slow switch-off shock with XMHD model, 400 cells, initial shock position at $x = 0$, captured at $t = 0.5$ 113
6.6 Brio Wu shock tube test re-presented. Density as a function of position, captured at $t = 2.1 \times 10^{-2}$; in the two figures, FR, SM, C, SS denote fast rarefaction wave, slow compound wave, contact discontinuity, and slow shock respectively. From the shapes of the slow shocks, we can observe that in the XMHD case, the slow shock structure is severely dissipated, or cannot be referred to as a shock any more. 113
6.7 Dispersion curves for oblique waves in low β plasma with $\mid \Omega_e \mid <$ ω_{pe} (After [6]) 115

6.8 Density, thermal pressure and transverse field in a fast switch-on shock with ideal-MHD model, 400 cells, initial shock position at $x = 0$, captured at $t = 0.5$ 116
6.9 Density, thermal pressure and transverse field in a fast switch-on shock with XMHD model, 400 cells, initial shock position at $x = 0$, captured at $t = 0.5$ 117

7.1 Set Up of the simulation for studying the magnetized flow interacting with an Obstacle, the flows are magnetized with a magnetic field that is perpendicular to the flow direction; The speed is **u**, the driving magnetic field is **B**. 121
7.2 Magnetic field lines with background color as the $\log\rho$. MHD simulation with estimated experimental parameters measured from reconnection outflow in the two-wire reconnection experiments depicted in chapter 5, captured at $t = 140ns$. 123
7.3 Picture elaborating that the bow shock is a fast shock. The left part is the result shown in Figure 7.3.1. The right part is the profile of variables along the white line segment across the bow shock shown in the left figure, including variables Temperature, tangential component of magnetic field B_t, log density $\log\rho$. Across the shock, the values of all three variables are increasing. The fact that B_t is increasing across the shock gives evidence that this bow shock is a fast shock. 124
7.4 Bow shock structures with same M_f, but M_a and M_s are different. 125
7.5 Perpendicular Shock Structure 127
7.6 The magnetic field lines can also pass through the obstacle through magnetic reconnection. Figure (a) schematic sketch showing how reconnection appears, and how the flows are directed through the X-point; Figure (b) shows a clear X-point behind the obstacle; Figure (c) shows an enlargement of X point area, which clearly shows that magnetic reconnection is happening at the X point. 129
7.7 The outflow from the tail reconnection is bounded by a slow shock, as evidenced by the fact that B_t is decreasing across the shock. 131
7.8 Growth Phase. Because of the presence of the obstacle, the magnetic field lines are bent, since there is not enough diffusion for the field lines to diffuse through, the magnetic flux has to get through by reconnecting. An X point denoted by 'X' forms behind the obstacle, through reconnection, some plasma flows are directed into the region A, so the energy inside the region A is piling up due to continuing flow into this region. 134

7.9 Expansion Phase. With the energy piling up in the closed flux in region A, A has to expand, because of the momentum pressure from the inflow, A region has to expand tail-wards. When region A is elongated to a certain level, it will break down into two parts to lower the potential energy, so as to stabilize the whole system. Some magnetic instabilities will also help the breaking out. That is the reason why another closed flux region B forms, B took some flux and energy away from A, so that the system can sustainably grow. The region denoted by B is often referred to as 'Plasmoid'. 135
7.10 Recovery Phase: Because of the momentum pressure from the inflow, the plasmoid denoted by B is pushed tail-wards. A current sheet forms between region A and B to support the X shape there. 136
7.11 Post-Recovery Phase. The plasmoid B propagates tail-wards into field lines in region C. When B collides with the field lines in C, magnetic field will reconnect again, and the flux energy inside B is dissipated in this process, then the closed flux lines break up, and merge into region C. In the same time, another plasmoid B' is generated from A, repeating the process extrapolated in 7.9(b) 137
7.12 By decreasing the inflow velocity, thus increasing the characteristic time scale of the problem, plasmoids can be developped on top of the magnetic reconnection event. 138
7.13 In these three tests, we vary B and ρ at the same time to keep the Mach numbers fixed (M_s = 16.9, M_A = 2.24, M_f = 2.22). Observation: the structures are almost identical with the same Mach numbers in MHD cases. 140
7.14 By changing the upstream Mach numbers through changing the inflow velocities, the phenomena including both the bow shock part and the magnetotail part change significantly. 141
7.15 Magnetic field lines with a background color plot $\log(n)$ with XMHD. Shock-obstacle simulation with XMHD model, captured at $t = 140ns$. 144
7.16 Analysis of XMHD simulation of shock-obstacle problem; (c) shows the profile of $\mathbf{J}$ along the black line in (b), it is obvious at the point denoted by $\mathbf{P}$, the current is negative, and we know that the inflow magnetic field is pointing up, which results in a $\mathbf{J} \times \mathbf{B}$ force that is perpendicular to the magnetic field line at that point directing towards the axis, and that is the main reason why the tail structure forms 145
7.17 In these three tests, we vary B and ρ at the same time to keep the Mach numbers fixed (M_s = 16.9, M_A = 2.24, M_f = 2.22). Observation: the structures change a lot. 147

7.18 By changing the upstream Mach numbers through changing the inflow velocities. Upstream $\beta = 0.012$ is kept a constant. The features, especially the bow shock region changes significantly. . 148
7.19 Color Plot of $\frac{\log P}{\log P_0}$, P_0 is the background pressure. By changing the upstream pressure ratio β through changing the inflow magnetic field and temperature, the phenomena, especially the tail region changes significantly. 150
7.20 Shock-obstacle simulation for MHD model and XMHD model, captured at $t = 140ns$ 152
7.21 Magnetic field lines with a background color plot $\log\rho$ with XMHD; $dx/\lambda_i = 1.9$; Captured at 100ns. 153
7.22 Simulation results with larger obstacle with a diameter of $d = 6.17\lambda_i$, captured at $t = 184ns$. From the pictures, the front portion of the XMHD and MHD results are close to each other. 155
7.23 Figure 7.23(b) shows the MHD simulation with the resistivity: $\eta = \eta_s + \eta_0\frac{\rho_{floor}}{\rho}$, η_0 is chosen to be consistent with Hall resistivity. We can see that by changing the resistivity model, the MHD results become much more similar to the XMHD results. 157
7.24 Experiments of two-wire reconnection with an obstacle in the outflow region, and the corresponding simulations. 158
7.25 Hydrodynamic simulation, bow shock feature is clear, but the bright tail feature is missing; thus does not agree with the experiment. 160
7.26 Simulation with magnetic field into the plane, bow shock feature is clear, but the bright tail feature is missing; thus does not agree with the experiment. The striations at the left boundary are due to an instability that we have not studied in detail. 161
7.27 The MHD simulation of Mars (a) reveals significant difference from the XMHD simulation (b), especially in the tail part. The main reason is due to the fact that Hall term can facilitate reconnection, making the reconnection rate faster; For that reason, we can observe the X-shape opens up more 163
7.28 Color Plot of B_z. Inflow from the left boundary into an obstacle. The presence of the obstacle caused a spatial variance of electron density and a spatial variance of P_e, this results in a non-zero $\nabla n_e \times \nabla P_e$, which means, the RHS of (7.7) is nonzero, that induces a magnetic field. Since the spatial variances of n_e and P_e are both in plane, $\nabla n_e \times \nabla P_e$, if nonzero, has to be out of plane, which means that B_z is induced. 166

8.1 Set Up of the simulation for studying the solar wind interacting with Mars, the flows are magnetized with a magnetic field that is perpendicular to the flow direction; The speed is **u**, the driving magnetic field is **B**. 170

8.2 Simulation of Solar Wind Interacting with Mars. A slip through the axis of symmetry of the 3D XMHD simulation result: Magnetic field lines with background color plot of x component velocity v_x. 172
8.3 Simulation with Lab Parameters to Reproduce Martian Phenomena. A slip through the axis of symmetry of the 3D XMHD simulation result: Magnetic field lines with background color plot of x component velocity v_x. 174

CHAPTER 1

INTRODUCTION

In High Energy Density (HED) plasma systems, we usually must deal with a wide dynamic range of current carrying densities. When the density is so low that the scale lengths are comparable to the ion inertial length, the single fluid model will break down. For these problems two-fluid physics is essential, but the applicability of existing numerical methods [54, 24, 38, 25, 9, 28] in this plasma regime is still limited. In this paper we develop a discontinuous Galerkin (DG) method to solve an extended Magnetohydrodynamics (XMHD) model based on a relaxation formulation, and will demonstrate that this numerical scheme has high accuracy, is computationally efficient, and can handle the large dynamic density range for HED plasmas.

DG schemes are widely used in the hyperbolic algorithms community, since the method can handle complex geometries, has an arbitrary order of accuracy, and is efficient in parallel calculations [12, 13, 14, 15, 50]. In addition, DG has further advantages for HED plasmas, since the density range is very wide, one often faces a problem where the initial density profile is nearly a δ-singularity (e.g. a fine wire). Such problems are difficult to approximate numerically, and most previous techniques are based on the modifications of the singularities with smooth kernels in some narrow region (e.g. [63, 60] and the references therein), and hence smear such singularities. However, DG methods depend on the weak form of the equations and can solve such problems without modification, leading to very accurate results [61]. The main challenge with DG implementations lies in preserving the stability of the system. Near discontinuities, strong oscillations often appear that might send the physically positive quantities negative.

When this occurs, the numerical simulation may break down. In our system, the quantities that should be preserved positive are: density ρ, pressure P, energy $\mathcal{E}$. To ensure these quantities satisfy a positivity-preserving property, one could use a Total Variation Diminishing (TVD) scheme; however, all TVD schemes will degenerate to lower order accuracy at smooth extrema [65]. In [64], a positivity-preserving high order DG scheme is developed for solving the compressible Euler equations, and in [62], the authors demonstrated the L^1-stability of such a scheme. This scheme has been applied on solving the ideal magnetohydrodynamic (MHD) equations [3, 8]. In this paper, we will demonstrate that the positivity-preserving DG scheme can establish a positivity-preserving property for a system described by an XMHD model or a resistive MHD model, thus preserving the stability of the system.

For solving the XMHD model, we use the relaxation algorithm proposed in [47] to solve the combination of generalized Ohm's law (GOL) and the Maxwell–Ampére law for the electric field. The relaxation method is essentially a semi-implicit time differencing proven to converge to the solution of the algebraic equations that have the stiff source terms set equal to zero. In the case of XMHD this means the solution converges to the GOL in which the electron inertial terms are neglected and to the Maxwell equation in which the displacement current term is neglected (Ampére's Law). Using this algorithm, one can avoid the constraint imposed by the under-resolved stiff source terms to step over electron plasma and cyclotron frequencies, which are often under-resolved in the characteristic regime, and thereby allow one to solve the the XMHD equations on MHD time scales. In this algorithm, the Hall term is locally implicit avoiding the substantial effort in solving a large linear system. Furthermore, with the XMHD model, in low-density regions, the current is suppressed by

both Hall and electron inertial terms, and one is able to use the unmodified Spitzer resistivity, which makes the plasma-vacuum transition automatic and physical. This algorithm has been implemented into an XMHD code called PERSEUS with a second-order finite volume (FV) scheme. Because of the extended stencil, FV is often too diffusive to characterize small-scale fluid instabilities and to resolve the local details of a shock structure without a large number of cells. On the other hand, the DG scheme is more compact in the sense that every cell is treated independently, and the solution is localized within a cell. This leads to reduced numerical diffusion. In this paper, we compare the performance of a DG formulation XMHD code to that of a FV formulation, and will demonstrate through numerical tests that DG has a significant advantage over the same order of FV in both memory and CPU time. Additionally we compare selected results with those found from the MHD model computed using the same algorithm. This comparison demonstrates the viability of the method for solving XMHD problems as well as to point out important deficiencies in MHD.

This Positivity-Preserving DG scheme has been implemented into an efficient high-resolution code called DG-PERSEUS on parallel supercomputers using a Message Passing Interface (MPI). Now DG-PERSEUS is available in 1D, 2D and 3D Cartesian coordinates. Because DG-PERSEUS has very small numerical diffusion, it can be applied on problems that need a high resolution to resolve important features, such as shock, instability and reconnection problems (especially the diffusion region).

First, we apply DG-PERSEUS to the study of the two wire magnetic reconnection problem [22]. Magnetic reconnection is the heart of many spectacular

events in the solar system, for example, solar flares and coronal mass ejections on the sun, etc.. Reconnection occurs in highly conductive plasmas and is featured by the conversion of magnetic energy into kinetic energy, thermal energy and particle acceleration. However, no favorable mechanism has been proposed to explain the fast energy conversion rate in solar coronal dynamics. Greenly et al. have carried out a two wire magnetic reconnection experiment, in which the reconnection is driven by an inverse skin effect. This reconnection is a typical quasi-two-dimensional separator reconnection where the four magnetic domains exchanging fluxes are separated by two lines. We perform simulations to better understand this problem and believe that the inverse skin effect could be a possible mechanism for driving reconnection in the solar corona.

In order to diagnose the outflow in the two wire magnetic reconnection experiment, we place a plastic obstacle in the stream of the obstacle. By observing the XUV image of the reconnection outflow interacting with the obstacle, we gain some insight into the nature of the reconnection outflow, such as whether it is supersonic, super-Alfvénic or both, the flow direction at a random point, etc.. We have set up a simulation to study the region where the flow interacts with the obstacle. By varying the inflow parameters, we found that the simulation results can change in a qualitatively significant manner and lead to identifiable features in the structure. These structures can be easily identified in an XUV image. We can find the parameter regime where certain phenomena occur, so that we can match the experimental results to these parameter regimes, and then we can acquire knowledge about the inflow properties.

This problem where a magnetized flow interacts with an obstacle involves some very important basic physics, primarily associated with shocks and recon-

nection phenomena. When the incoming flow is faster than the characteristic wave speed, then a shock will occur in front of the obstacle. If the shock front becomes detached from the obstacle, we call it a bow shock. The factors that determine the shape of this bow shock are to be discussed in this thesis. We also discuss some basic types of MHD shocks as a preparation for analyzing the realistic problems.

We also study the wake flow, which is the region of disturbed flow downstream of the obstacle. We found that if the incoming flow is magnetized, the wake flow structure can be very different from the hydrodynamic case. Some very interesting phenomena, such as magnetic reconnection and plasmoids can all appear in the wake. This is a very important subject, and we discuss it at length in this thesis.

We also found that the Hall term can play a very important role in these problems when the characteristic length scale L approaches the ion inertial length λ_i. To understand the role of Hall term, we will compare the XMHD and MHD results, where we can detect significant differences. This finding is a strong endorsement of the necessity of including Hall physics in plasma simulations of these problems.

The problem involving a magnetized flow interacting with an obstacle is analogous to numerous events in nature, for example, the solar wind interacting with planets. Thus we take the opportunity to explore the physics of this interaction by setting up a 3D simulation. We also scale this problem down to parameters that can be achieved in the lab, so we can study interplanetary physics with laboratory experiments.

The thesis is organized as follows. Most parts of Chapters 2-4 are the paper published in Journal of Computational Physics [66]. In Chapter 2, we introduce some typical models for studying two-fluid physics, and show how we finally arrive at the Extended-MHD model, and why we have chosen the Extended-MHD (XMHD) model as the physics model on which this thesis is based. We also introduce the relaxation algorithm, which allows us to solve XMHD problems on MHD time scales. In Chapter 3, we construct the DG scheme used in this thesis, and demonstrate that a positivity-preserving limiter can preserve the positivity property in a system governed by an XMHD model or a resistive MHD model. We will also give a brief introduction on the implementation of our algorithm. In Chapter 4, we present the results of numerical tests. In some of the tests, we do a comparison with FV, to show that DG is more accurate and more efficient. We also give examples of the method applied to fundamental plasma physics problems and provide a comparison with the MHD model for the same problems. In Chapter 5, we introduce a novel configuration for driving magnetic reconnection. Simulations are carried out for a better understanding of this problem. In Chapter 6, we study standard MHD shocks, including the slow, intermediate and fast shocks. We also consider some important situations in which these shocks appear. In Chapter 7, we study the problem where magnetized flow interacts with an obstacle. The basic physics involved in this process, such as a bow shock, magnetic reconnection, plasmoids, etc., are also studied. We also find through the comparison between MHD and XMHD results that the Hall term plays an important role in this problem. The electron pressure, which is another aspect of the XMHD model, has an important effect known as the Biermann battery effect. We use some basic simulation results to show that the electron pressure is properly included in the model. In Chapter

8, we carry out a computer simulation of the solar wind interacting with Mars, and scale the simulation down to laboratory parameters to provide guidance for experimentalists to study interplanetary physics in the lab. Concluding remarks are provided in Chapter 9.

CHAPTER 2

EXTENDED-MHD MODEL

In this chapter, we develop an appropriate model that is sufficient for describing plasmas that are in a High Energy Density regime. The fluid description of plasmas can be viewed as an extension of the kinetic theory of hydrodynamic fluids. However, because of the effects electric and magnetic field have on the motion of charged particles in plasmas, such a description is much more complicated than in charge-neutral fluids. Typically, there are two major approaches for doing plasma modeling. One solves the conservation laws in the form of fluid equations and the other solves the kinetic equation from which the fluid form of the conservation laws is derived. A kinetic description is achieved by solving THE Boltzmann equation or the Vlasov equation when the correct description of long-range Coulomb interaction is necessary, or by solving the Fokker-Planck equation. Codes developed following this description are called particle in cell (PIC) codes. On the other hand, by taking averages over the whole velocity space and using various approximations, one can develop macroscopic fluid moment descriptions for each species of charged particles contained in plasmas. In this thesis, we only discuss those plasmas with only two species, i.e., ions and electrons, which we refer to as a two-fluid plasma. The fluid model describes the plasma based on macroscopic quantities (velocity moments of the distribution such as density, mean velocity and mean energy). Compared to a kinetic description, this fluid description is much less computationally expensive. The model to describe this type of plasma is called a two-fluid model. In the regimes we are mostly interested in for this thesis, the particle/kinetic effects are not very important. Also because of limitation of our computation resources, we choose to focus on the fluid description.

2.1 Full Two-fluid Model

Here we start with a full two-fluid plasma model. It consists of a set of fluid equations for describing the density, mean velocity and mean energy of the electrons and ions respectively, plus the complete Maxwell's equations including displacement current.

Electron Fluid Moment Equations:

Density:

$$\partial_t n_e + \nabla \cdot (n_e \mathbf{u}_e) = 0 \tag{2.1}$$

Momentum:

$$m_e \partial_t (n_e \mathbf{u}_e) + \nabla \cdot [m_e n_e \mathbf{u_e} \mathbf{u_e} + \mathbf{I} P_e] = n_e q_e (\mathbf{E} + \mathbf{u}_e \times \mathbf{B}) - R_e \tag{2.2}$$

Energy:

$$\partial_t \mathcal{E}_e + \nabla \cdot [\mathbf{u}_e (\mathcal{E}_e + P_e)] = n_e q_e \mathbf{u}_e \cdot (\mathbf{E} + \frac{R_e}{n_e q_e}) \tag{2.3}$$

Alternatively, by electron entropy:

$$\partial_t S_e + \nabla \cdot (\mathbf{u}_e S_e) = (\gamma - 1) n_e^{1-\gamma} \eta \mathbf{J}^2 \tag{2.4}$$

Ion Fluid Moment Equations:

Density:

$$\partial_t n_i + \nabla \cdot (n_i \mathbf{u}_i) = 0 \tag{2.5}$$

Momentum:

$$m_i \partial_t (n_i \mathbf{u}_i) + \nabla \cdot [m_i n_i \mathbf{u_i} \mathbf{u_i} + \mathbf{I} P_i] = n_i q_i (\mathbf{E} + \mathbf{u}_i \times \mathbf{B}) - R_i \tag{2.6}$$

Energy:

$$\partial_t \mathcal{E}_i + \nabla \cdot [\mathbf{u}_i(\mathcal{E}_i + P_i)] = n_i q_i \mathbf{u}_i \cdot (\mathbf{E} + \frac{R_i}{n_i q_i}) \tag{2.7}$$

Maxwell Equations:

Faraday's Law:

$$\partial_t \mathbf{B} + \nabla \times \mathbf{E} = 0 \tag{2.8}$$

Ampére's Law:

$$\partial_t \mathbf{E} - c^2 \nabla \times \mathbf{B} = -\frac{1}{\epsilon_0}\mathbf{J} \tag{2.9}$$

Where, $R_e = -R_i = -\eta e n_e \mathbf{J}$, and n_s, P_s, $\mathbf{u}_s = (u_{xs}, u_{ys}, u_{zs})$, $\mathcal{E}_s$, $\mathbf{B} = (B_x, B_y, B_z)$, $\mathbf{E} = (E_x, E_y, E_z)$, $\mathbf{J} = (J_x, J_y, J_z)$ denote the density, pressure, velocity field, the sum of the kinetic and internal energies, magnetic field, electric field, current density for species s (s can be e or i) respectively. S_e denotes the electron entropy density. The resistivity is η. We also have $P_s = (\gamma - 1)(\mathcal{E}_s - \rho \mathbf{u}_s^2/2)$ and $P_e = S_e n_e^{\gamma - 1}$.

To solve the full two-fluid model, we need to respect both ion and electron plasma frequencies, meaning, we should have: $\Delta t < 1/\omega_{pe}$ and $\Delta t < 1/\omega_{pi}$. However, since those regimes where time scale is comparable to the electron plasma frequency are not of primary interest to us, it will be a waste of computational time and will also add in more numerical diffusion if we have to resolve the electron plasma frequency even when the time scale $t_0 \gg 1/\omega_{pe}$. Thus, for most of the HED plasma problems where the phenomena on the electron plasma time scale are not very important, we would like to step over the electron plasma frequency and electron cyclotron frequency. Thus, we need to explore some other models that can achieve this goal. In the following sections, we first introduce a center-of-mass formulation of the two-fluid model, and then we simplify this formulation by employing some assumptions to arrive at the extended-MHD

model.

2.2 Two Fluid Model with a Center-of-mass Formulation

In often times, we are more interested in the center-of-mass quantities than the quantities for each species. In this two-fluid plasma system, our center of mass quantities follow the following definitions:

$$\text{Density:} \qquad \rho = m_i n_i + m_e n_e \tag{2.10}$$

$$\text{Velocity:} \qquad \mathbf{u} = (m_i n_i \mathbf{u_i} + m_e n_e \mathbf{u_e})/(m_i n_i + m_e n_e) \tag{2.11}$$

$$\text{Current:} \qquad \mathbf{J} = e(Z n_i \mathbf{u_i} - n_e \mathbf{u_e}) \tag{2.12}$$

$$\text{Charge Density:} \qquad \rho_c = Z e n_i - e n_e \tag{2.13}$$

$$\text{Pressure:} \qquad P = P_e + P_i \tag{2.14}$$

$$\text{Energy:} \qquad \mathcal{E}_n = \mathcal{E}_e + \mathcal{E}_i \tag{2.15}$$

And we define:

$$\begin{aligned} \mu &= \frac{m_e n_e}{m_i n_i} \\ n &= (1+\mu) n_i \\ \mathcal{M} &= \frac{\mu}{1+\mu} + \frac{1}{1+\mu}\frac{n_e}{Z n_i} \end{aligned} \tag{2.16}$$

Together with (2.11), we arrive at:

$$\mathbf{u_e} = (\mathbf{u} - \frac{J}{Zen})/\mathcal{M}$$

$$\mathbf{u_i} = (\frac{n_e}{Z n_i}\mathbf{u} - \frac{\mu J}{Zen})/\mathcal{M}$$

Substitute $\mathbf{u_e}$ and $\mathbf{u_i}$ into (2.1) and (2.5), add the two equations together following $m_e\times$ (2.1)+$m_i\times$ (2.5), also make use of equation (2.16), we arrive at:

$$\partial_t\rho + \nabla\cdot(\rho\mathbf{u}) = 0 \tag{2.17}$$

By subtracting the two equations by $-e\times$ (2.1)+$Ze\times$ (2.5) , we achieve:

$$\partial_t\rho_c + \nabla\cdot\mathbf{J} = 0 \tag{2.18}$$

Then the addition of (2.2) and (2.6) gives:

$$\begin{aligned}&\partial_t(\rho\mathbf{u})+\\ &\nabla\cdot\Big[\frac{1}{\mathcal{M}^2}\left\{m_e n_e(1+\frac{m_i n_e}{Z^2 m_e n_i})\mathbf{uu}+\frac{m_e n_e(1+Z^2 m_e n_i/(m_i n_e))}{Z^2e^2n^2}\mathbf{JJ}\right.\\ &\left.+\frac{n_e(m_i\mu - Zm_e)}{Z^2 en}(\mathbf{Ju}+\mathbf{uJ})\right\}+\mathbf{I}(P_e+P_i)\Big] = \mathbf{J}\times\mathbf{B}+(Zn_ie-n_ee)\mathbf{E}\end{aligned} \tag{2.19}$$

$-\frac{e}{m_e}\times$ (2.2) + $\frac{Ze}{m_i}\times$ (2.6) gives us the Generalized Ohm's Law (GOL):

$$\begin{aligned}&\partial_t\mathbf{J}+\nabla\cdot\left[\frac{1}{\mathcal{M}^2}\left\{\frac{n_e(1+\mu)}{Zn}(\mathbf{Ju}+\mathbf{uJ})-\left(\frac{n_e-Z\mu^2 n_i}{Z^2en^2}\right)\mathbf{JJ}-en_e(1-\frac{n_e}{Zn_i})\mathbf{uu}\right\}\right.\\ &\left.+Ze\frac{\mathbf{I}P_i}{m_i}-e\frac{\mathbf{I}P_e}{m_e}\right] = \frac{e^2n_e}{m_e}\left(1+Z^2\frac{n_im_e}{n_em_i}\right)\mathbf{E}+\frac{n_ee^2}{m_e\mathcal{M}}(1+Z\frac{m_e}{m_i})\mathbf{u}\times\mathbf{B}\\ &-\frac{n_ee}{\mathcal{M}Znm_e}\left(1-Z^2\frac{m_e^2}{m_i^2}\right)\mathbf{J}\times\mathbf{B}-\frac{\eta en_e\mathbf{J}}{m_e}\left(1+Z\frac{m_e}{m_i}\right)\end{aligned} \tag{2.20}$$

The addition of the two energy equations (2.7) and (2.3) gives us:

$$\partial_t\mathcal{E}_n+\nabla\cdot[\mathbf{u}(\mathcal{E}_n+P)] = \mathbf{u}\cdot(\mathbf{J}\times\mathbf{B})+\eta\mathbf{J}^2 \tag{2.21}$$

The central momentum equation (2.19), the GOL equation (2.20), the continuity equation (2.17), charge density equation (2.18) together with the energy

equation (2.21), give us the following model, which is a two-fluid model expressed with a center-of-mass formulation:

$$\partial_t \rho + \nabla \cdot (\rho \mathbf{u}) = 0 \tag{2.22}$$

$$\partial_t \rho_c + \nabla \cdot \mathbf{J} = 0 \tag{2.23}$$

$$\begin{aligned} &\partial_t(\rho \mathbf{u}) + \\ &\nabla \cdot \Big[\frac{1}{\mathcal{M}^2} \Big\{ m_e n_e (1 + \frac{m_i n_e}{Z^2 m_e n_i}) \mathbf{u}\mathbf{u} + \frac{m_e n_e (1 + Z^2 m_e n_i/(m_i n_e))}{Z^2 e^2 n^2} \mathbf{J}\mathbf{J} \\ &+ \frac{n_e (m_i \mu - Z m_e)}{Z^2 e n} (\mathbf{J}\mathbf{u} + \mathbf{u}\mathbf{J}) \Big\} + \mathbf{I}(P_e + P_i) \Big] = \mathbf{J} \times \mathbf{B} + (Z n_i e - n_e e)\mathbf{E} \end{aligned} \tag{2.24}$$

$$\partial_t \mathcal{E}_n + \nabla \cdot [\mathbf{u}(\mathcal{E}_n + P)] = \mathbf{u} \cdot (\mathbf{J} \times \mathbf{B}) + \eta \mathbf{J}^2 \tag{2.25}$$

$$\partial_t S_e + \nabla \cdot (\mathbf{u}_e S_e) = (\gamma - 1) n_e^{1-\gamma} \eta \mathbf{J}^2 \tag{2.26}$$

$$\partial_t \mathbf{B} + \nabla \times \mathbf{E} = 0 \tag{2.27}$$

$$\partial_t \mathbf{E} - c^2 \nabla \times \mathbf{B} = -\frac{1}{\epsilon_0} \mathbf{J} \tag{2.28}$$

$$\begin{aligned} &\partial_t \mathbf{J} + \nabla \cdot \left[\frac{1}{\mathcal{M}^2} \left\{ \frac{n_e(1+\mu)}{Zn} (\mathbf{J}\mathbf{u} + \mathbf{u}\mathbf{J}) - \left(\frac{n_e - Z\mu^2 n_i}{Z^2 e n^2} \right) \mathbf{J}\mathbf{J} - e n_e (1 - \frac{n_e}{Z n_i}) \mathbf{u}\mathbf{u} \right\} \right. \\ &\left. + Ze \frac{\mathbf{I} P_i}{m_i} - e \frac{\mathbf{I} P_e}{m_e} \right] = \frac{e^2 n_e}{m_e} \left(1 + Z^2 \frac{n_i m_e}{n_e m_i} \right) \mathbf{E} + \frac{n_e e^2}{m_e \mathcal{M}} (1 + Z \frac{m_e}{m_i}) \mathbf{u} \times \mathbf{B} \\ &- \frac{n_e e}{\mathcal{M} Z n m_e} \left(1 - Z^2 \frac{m_e^2}{m_i^2} \right) \mathbf{J} \times \mathbf{B} - \frac{\eta e n_e \mathbf{J}}{m_e} \left(1 + Z \frac{m_e}{m_i} \right) \end{aligned} \tag{2.29}$$

Notice that, we used the electron entropy density equation instead of the electron energy equation here to close the system, we will explain why we made this choice in chapter 3.

2.3 Extended-MHD Model

When we are evaluating a regime where the characteristic length scale is much larger than Debye length, ie, $L \gg \lambda_D$, the space charge effects can be neglected,

we can employ the assumption of quasineutrality, i.e., $n_e = Zn_i$, also, if we take the leading order in m_e/m_i, the equation system (2.22) – (2.29) can be tremendously simplified, especially the equations (2.24) and (2.29). The model is as follows, we call this system an Extended-MHD (XMHD) model.

$$\partial_t \rho + \nabla \cdot (\rho \mathbf{u}) = 0 \tag{2.30}$$

$$\partial_t (\rho \mathbf{u}) + \nabla \cdot [\rho \mathbf{u}\mathbf{u} + \mathbf{I}P] = \mathbf{J} \times \mathbf{B} \tag{2.31}$$

$$\partial_t \mathcal{E}_n + \nabla \cdot [\mathbf{u}(\mathcal{E}_n + P)] = \mathbf{u} \cdot (\mathbf{J} \times \mathbf{B}) + \eta \mathbf{J}^2 \tag{2.32}$$

$$\partial_t S_e + \nabla \cdot (\mathbf{u}_e S_e) = (\gamma - 1) n_e^{1-\gamma} \eta \mathbf{J}^2 \tag{2.33}$$

$$\partial_t \mathbf{B} + \nabla \times \mathbf{E} = 0 \tag{2.34}$$

$$\partial_t \mathbf{E} - c^2 \nabla \times \mathbf{B} = -\frac{1}{\epsilon_0} \mathbf{J} \tag{2.35}$$

$$\begin{aligned} \partial_t \mathbf{J} + \nabla \cdot \left[\mathbf{J}\mathbf{u} + \mathbf{u}\mathbf{J} - \frac{1}{Zen} \mathbf{J}\mathbf{J} - \frac{e}{m_e} \mathbf{I} P_e \right] \\ = \frac{n_e e^2}{m_e} \left(\mathbf{E} + \mathbf{u} \times \mathbf{B} - \eta \mathbf{J} - \frac{1}{n_e e} \mathbf{J} \times \mathbf{B} \right) \end{aligned} \tag{2.36}$$

There is also a constraint implied in (2.27). Taking the divergence of (2.34) we get:

$$\nabla \cdot \partial_t \mathbf{B} = 0,$$

meaning that if $\nabla \cdot \mathbf{B}$ is initially 0, it is always 0. This gives us a constraint $\nabla \cdot \mathbf{B} = 0$. For local preservation of $\nabla \cdot \mathbf{B} = 0$, we use the locally divergence-free DG method [36], which eliminates the need for an expensive divergence cleaning scheme or the use of global divergence-free elements or a global divergence free reconstruction. The implementation of this method will also be introduced in chapter 3.

For the class of problems of interest to us XMHD has several important advantages over the full two-fluid model. These are: 1. A direct comparison to

MHD can be made by simply switching off some terms in Generalized Ohm's Law (2.36); 2. The relaxation method (to be discussed in section 2.5) can be used to step over the plasma frequency and electron cyclotron frequency when they do not have to be resolved. This greatly reduces the computational cost for XMHD modeling. We have not been successful thus far in implementing a similar scheme for the full two-fluid model. The reason for this is due to finite charge separation, which is a topic beyond the scope of this paper. Thus there would appear to be no advantage to the two-fluid model for quasineutral problems and many advantages for the XMHD model.

For the reasons above, we choose the XMHD model (2.30) - (2.36) to conduct the study in this thesis.

2.4 Resistive MHD model

By switching off the electron inertia term, electron pressure and the Hall term in equation (2.36), we get the resistive MHD model, which is the following

$$\partial_t \rho + \nabla \cdot (\rho \mathbf{u}) = 0 \tag{2.37}$$

$$\partial_t (\rho \mathbf{u}) + \nabla \cdot [\rho \mathbf{u}\mathbf{u} + \mathbf{I}P] = \mathbf{J} \times \mathbf{B} \tag{2.38}$$

$$\partial_t \mathcal{E}_n + \nabla \cdot [\mathbf{u}(\mathcal{E}_n + P)] = \mathbf{u} \cdot (\mathbf{J} \times \mathbf{B}) + \eta \mathbf{J}^2 \tag{2.39}$$

$$\partial_t \mathbf{B} + \nabla \times \mathbf{E} = 0 \tag{2.40}$$

$$\partial_t \mathbf{E} - c^2 \nabla \times \mathbf{B} = -\frac{1}{\epsilon_0} \mathbf{J} \tag{2.41}$$

$$\mathbf{E} + \mathbf{u} \times \mathbf{B} = \eta \mathbf{J}. \tag{2.42}$$

If not specified, for simplification, MHD model is used to refer to resistive MHD model throughout this paper.

The obvious differences between MHD model and XMHD model are the following:

1. MHD leaves out the Hall term $\mathbf{J} \times \mathbf{B}$, which is important when the length scale is on the order of ion inertial length λ_i; In the regime where Hall term is important, one can compare the results from XMHD model to those from MHD model, in order to study the importance of Hall term. This is the most significant difference between MHD and XMHD in the regimes we are interested in. For the study of the physics problems throughout this whole thesis, we want to explore the role that Hall term plays. Our XMHD model formulation makes this study very straightforward, since we only need to turn off the Hall term for a direct comparison to the MHD results. Also, we have an advanced algorithm (section 2.5)which allows us to execute an XMHD simulation on the same time scale as MHD simulations. To investigate the role that the Hall term plays in different physics problems is an important area of plasma study, and is a major topic in this thesis.

2. Electron pressure term $\frac{e}{m_e}\mathbf{I}P_e$ is left out in the MHD model. This term is important when $L \sim \lambda_i$. We found some interesting phenomena which are caused by the presence of this term, for example, the Biermann Battery effect. We will further discuss this in later chapters.

3. Electron inertia terms $\nabla \cdot [\mathbf{Ju} + \mathbf{uJ} - \frac{1}{Zen}\mathbf{JJ}]$ are left out in the MHD model. We will see the importance of these terms when we reach a scale $L \sim \lambda_e$, for example, in the electron inertial region of a collisionless reconnection problem.

2.5 Relaxation Model

Equations (2.35) and (2.36) are non-dimensionalized to exhibit the dimensionless parameters that characterize the relaxation. This gives the following [47]:

$$\partial_t \mathbf{E} = \frac{c^2}{v^2}(\nabla \times \mathbf{B} - \mathbf{J}) \tag{2.43}$$

$$\partial_t \mathbf{J} + \nabla \cdot \left(\mathbf{uJ} + \mathbf{Ju} - \frac{\lambda_i}{L_0 n}\mathbf{JJ} - \frac{m_i L_0}{m_e \lambda_i}\mathbf{I}P_e \right) = \frac{L_0^2 n}{\lambda_e^2}\left(\mathbf{E} + \mathbf{u} \times \mathbf{B} - \frac{\lambda_i}{L_0 n}\mathbf{J} \times \mathbf{B} - \eta \mathbf{J} \right), \tag{2.44}$$

where $v = L_0/t_0$ is the characteristic speed and L_0, t_0 are representative length and time respectively. The electron and ion inertial lengths are $\lambda_j^2 = m_j/n_0 e^2 \mu_0$. The relaxation parameters are c^2/v^2 and L_0^2/λ_e^2.

In High-Energy-Density (HED) plasmas the phenomena of interest often occur on time scales much slower than the characteristic electron plasma and electron cyclotron frequencies, which means, $v \ll c$ and $\lambda_e \ll L_0$, forcing that (2.43) and (2.44) relax to the following equilibrium:

$$\nabla \times \mathbf{B} = \mathbf{J} \tag{2.45}$$

$$\mathbf{E} + \mathbf{u} \times \mathbf{B} - \frac{\lambda_i}{L_0 n}\mathbf{J} \times \mathbf{B} + \frac{\lambda_i}{L_0 n}\nabla P_e = \eta \mathbf{J}. \tag{2.46}$$

This means that, when the electron inertial scale is under-resolved, the solution relaxes to the inertia-less GOL and $\mathbf{J}$ will be constrained by $\mathbf{J} = \nabla \times \mathbf{B}$. This model is implemented into an algorithm in which we use an implicit-explicit time advance, allowing time steps comparable to MHD. Thus we can solve problems in which the Hall effect is important without significant computational cost over that of standard MHD with the caveat that the CFL condition for the speed of light must be respected. Our experience has shown for most

problems we can use a much reduced speed of light without affecting the results significantly. Typically this reduction factor is in the range of 15 – 30 for HED problems. For more information on the relaxation method, please refer to [47].

The formulation of the XMHD model given by (2.30) - (2.36) is not standard [49, 46]. The differences are relevant for the implementation of the numerical algorithm. Note that the momentum and energy equations have source terms and as true source terms they depend only on the independent variables with no derivatives. In most formulations of XMHD the current is a dependent variable determined through Ampére's law and the electric field is determined by the generalized Ohm's law. In the present formulation in which displacement current is retained, the electric field and current density are independent variables having separate evolution equations. Hence the terms on the RHS of (2.31), (2.32), (2.36) and (2.33) are true source terms. There are issues that are potential cause for concern by not having a fully conservative form in which all terms are in divergence form. These are: 1. the $\mathbf{J} \times \mathbf{B}$ force term may affect shock capturing ability of the numerical discretization and 2. the non-positive form of the energy source term could affect the positivity of the pressure. We address the first concern by providing tests that show the DG scheme does well in capturing shocks and discontinuities and the second concern is addressed by proving that the positivity-preserving limiter preserves the stability of the system.

CHAPTER 3

POSITIVITY-PRESERVING SEMI-IMPLICIT DISCONTINUOUS GALERKIN SCHEME

In this chapter, we construct the DG methods that will be used for the XMHD model.

3.1 Local divergence-free discontinuous Galerkin formulation

In this section, we only consider problems which can be considered invariant in z direction. Therefore, we have $\partial_z = 0$, and $\nabla = (\partial_x, \partial_y, 0)$. Given this, we can summarize equations (2.30) - (2.36) with the following form:

$$\mathbf{U}_t + \mathbf{f}(\mathbf{U})_x + \mathbf{g}(\mathbf{U})_y = \mathbf{s}(\mathbf{U}), \tag{3.1}$$

where

$$\mathbf{U} = (\rho,\ m_x,\ m_y,\ m_z,\ \mathcal{E}_n,\ B_x,\ B_y,\ B_z,\ E_x,\ E_y,\ E_z,\ J_x,\ J_y,\ J_z,\ S_e)^T, \tag{3.2}$$

$$\mathbf{f}(\mathbf{U}) = (m_x,\ m_x u_x + P,\ m_y u_x,\ m_z u_x,\ (\mathcal{E}_n + P)u_x,\ 0,\ -E_z,\ E_y,\ 0,\ c^2 B_z,\ -c^2 B_y,$$

$$u_x J_x + J_x u_x - \frac{1}{Zne} J_x J_x - \frac{e}{m_e} P_e,\ u_x J_y + J_x u_y - \frac{1}{Zne} J_x J_y,\ u_x J_z + J_x u_z - \frac{1}{Zne} J_x J_z, S_e u_{ex})^T,$$

$$\mathbf{g}(\mathbf{U}) = (m_y,\ m_x u_y,\ m_y u_y + P,\ m_z u_y,\ (\mathcal{E}_n + P)u_y,\ E_z,\ 0,\ -E_x,\ -c^2 B_z,\ 0,\ c^2 B_x,$$

$$u_y J_x + J_y u_x - \frac{1}{Zne} J_y J_x,\ u_y J_y + J_y u_y - \frac{1}{Zne} J_y J_y - \frac{e}{m_e} P_e,\ u_y J_z + J_y u_z - \frac{1}{Zne} J_y J_z, S_e u_{ey})^T,$$

$$\mathbf{s}(\mathbf{U}) = (0,\ J_y B_z - J_z B_y,\ J_z B_x - J_x B_z,\ J_x B_y - J_y B_x,\ u_x(J_y B_z - J_z B_y) + u_y(J_z B_x - J_x B_z)$$

$$+u_z(J_x B_y - J_y B_x) + \eta(J_x^2 + J_y^2 + J_z^2),\ 0,\ 0,\ 0,\ -\frac{J_x}{\epsilon_0},\ -\frac{J_y}{\epsilon_0},\ -\frac{J_z}{\epsilon_0},$$

$$\frac{Zne^2}{m_e}(E_x + u_y B_z - \frac{1}{Zne} J_y B_z - \eta J_x),\ \frac{Zne^2}{m_e}(E_y + u_z B_x - \frac{1}{Zne} J_z B_x - \eta J_y)$$

$$\frac{Zne^2}{m_e}(E_z + u_x B_y - \frac{1}{Zne} J_x B_y - \eta J_z),\ (\gamma - 1) n_e^{1-\gamma} \eta (J_x^2 + J_y^2 + J_z^2))^T,$$

with

$$u_x = \frac{m_x}{\rho}, \quad u_y = \frac{m_y}{\rho}, \quad u_z = \frac{m_z}{\rho},$$

$$u_{xe} = u_x - J_x/(Zen), \quad u_{ye} = u_y - J_y/(Zen), \quad u_{ze} = u_z - J_z/(Zen).$$

We consider the computational domain $[0, L_x] \times [0, L_y]$, and use rectangular mesh defined as

$$0 = x_{\frac{1}{2}} < \cdots < x_{N_x + \frac{1}{2}} = L_x, \quad 0 = y_{\frac{1}{2}} < \cdots < y_{N_y + \frac{1}{2}} = L_y,$$

with $I_{ij} = [x_{i-\frac{1}{2}}, x_{i+\frac{1}{2}}] \times [y_{j-\frac{1}{2}}, y_{j+\frac{1}{2}}]$ representing the cells. For simplicity, we apply uniform meshes only, and denote Δx and Δy to be the mesh sizes in x and y directions, respectively.

Following [36], we define the finite element space as

$$V_h^k = \left\{ \mathbf{v} : \mathbf{v}|_{I_{ij}} \in \mathbf{P}^k(I_{ij}), (\frac{\partial v_6}{\partial x} + \frac{\partial v_7}{\partial y}) = 0 \right\},$$

where $\mathbf{P}^k(I_{ij}) = (\mathcal{P}(I_{ij}))^{15}$, with $\mathcal{P}(I_{ij})$ being the space of polynomials of degree at most k in cell I_{ij}. v_6 and v_7 are the sixth and seventh components of the basis functions used to expand B_x and B_y. By using such a finite element space,

$\nabla \cdot \mathbf{B} = 0$ is locally preserved automatically, we will explain this in detail at section 3.3. Although a local divergence free constraint does not guarantee global divergence free solutions, it has been shown that a local condition is very accurate [11], although [1] and [2] report some advantages in using a global divergence free reconstruction over a local constraint. We provide a numerical test of the global divergence of the magnetic field in section 5, which supports the conclusion of [11].

Then the DG scheme is the following: find $\mathbf{Q} \in V_h^k$, such that for any $\mathbf{v} \in V_h^k$

$$\begin{aligned}(\mathbf{Q}_t, \mathbf{v})_{ij} = & (\mathbf{f}(\mathbf{Q}), \mathbf{v}_x)_{i,j} + \int_{y_{j-\frac{1}{2}}}^{y_{j+\frac{1}{2}}} \widehat{\mathbf{f}}_{i-\frac{1}{2},j} \mathbf{v}^+_{i-\frac{1}{2},j} dy - \int_{y_{j-\frac{1}{2}}}^{y_{j+\frac{1}{2}}} \widehat{\mathbf{f}}_{i+\frac{1}{2},j} \mathbf{v}^-_{i+\frac{1}{2},j} dy \\ & + (\mathbf{g}(\mathbf{Q}), \mathbf{v}_y)_{i,j} + \int_{x_{i-\frac{1}{2}}}^{x_{i+\frac{1}{2}}} \widehat{\mathbf{g}}_{i,j-\frac{1}{2}} \mathbf{v}^+_{i,j-\frac{1}{2}} dx - \int_{x_{i-\frac{1}{2}}}^{x_{i+\frac{1}{2}}} \widehat{\mathbf{g}}_{i,j+\frac{1}{2}} \mathbf{v}^-_{i,j+\frac{1}{2}} dx \\ & + (\mathbf{s}(\mathbf{Q}), \mathbf{v})_{i,j}, \end{aligned} \tag{3.3}$$

where $(\mathbf{u}, \mathbf{v})_{ij} = \int_{I_{ij}} \sum_{\ell=1}^{15} u_\ell v_\ell dxdy$ and $\mathbf{v}^+_{i-\frac{1}{2},j}(y), \mathbf{v}^-_{i+\frac{1}{2},j}(y), \mathbf{v}^+_{i,j-\frac{1}{2}}(x), \mathbf{v}^-_{i,j+\frac{1}{2}}(x)$ are the traces of $\mathbf{v}$ on left, right, lower, upper edge of the cell I_{ij}, respectively. More details can be found in [64]. With the definition of the traces, the one-dimensional numerical fluxes are: $\widehat{\mathbf{f}}_{i-\frac{1}{2},j} = \widehat{\mathbf{f}}\left(\mathbf{Q}^-_{i-\frac{1}{2},j}(y), \mathbf{Q}^+_{i-\frac{1}{2},j}(y)\right)$ and $\widehat{\mathbf{g}}_{i,j-\frac{1}{2}} = \widehat{\mathbf{g}}\left(\mathbf{Q}^-_{i,j-\frac{1}{2}}(x), \mathbf{Q}^+_{i,j-\frac{1}{2}}(x)\right)$. The local Lax-Friedrichs (LLF) flux is used to evaluate $\widehat{\mathbf{f}}_{i-\frac{1}{2},j}, \widehat{\mathbf{g}}_{i,j-\frac{1}{2}}$:

$$\begin{aligned}\widehat{\mathbf{f}}_{i-\frac{1}{2},j} &= \frac{1}{2}\left[\mathbf{f}\left(\mathbf{Q}^-_{i-\frac{1}{2},j}(y)\right) + \mathbf{f}\left(\mathbf{Q}^+_{i-\frac{1}{2},j}(y)\right)\right] + \frac{1}{2} \mid \lambda \mid_{i-\frac{1}{2},j} \left[\mathbf{Q}^-_{i-\frac{1}{2},j}(y) - \mathbf{Q}^+_{i-\frac{1}{2},j}(y)\right] \\ \widehat{\mathbf{g}}_{i,j-\frac{1}{2}} &= \frac{1}{2}\left[\mathbf{g}\left(\mathbf{Q}^-_{i,j-\frac{1}{2}}(x)\right) + \mathbf{g}\left(\mathbf{Q}^+_{i,j-\frac{1}{2}}(x)\right)\right] + \frac{1}{2} \mid \lambda \mid_{i,j-\frac{1}{2}} \left[\mathbf{Q}^-_{i,j-\frac{1}{2}}(x) - \mathbf{Q}^+_{i,j-\frac{1}{2}}(x)\right], \end{aligned} \tag{3.4}$$

We do not presently have a solution for a full Riemann solver or even an approximate Riemann solver. Therefore we have used an ad-hoc form of a LLF flux based on an estimate of the maximum eigenvalues of the flux Jacobian computed respectively from the Euler ((2.30) - (2.32)), Maxwell ((2.34) - (2.35)), and GOL ((2.36) and 2.33) sub blocks. The calculation process of these maximum

eigenvalues is presented in the Appendix. For simplicity, the coupling terms of the GOL block are neglected. These maximum eigenvalues, which are sometimes called freezing speeds [56], are the local values of $|\mathbf{u}| + c_s$, c, $|\mathbf{u}_e| + c_{es}$ for the Euler, Maxwell, and GOL sub blocks respectively, where $c_{es}^2 = \frac{m_i}{m_e} c_s^2$ is the electron sound speed and $c_s^2 = \gamma P \rho^{-1}$ is the acoustic speed. We have found that the LLF flux based on these values to be entirely satisfactory and we note that the same values are used in the finite volume code and that with DG, far less diffusion is exhibited than FV, which will be shown in section.

$| \lambda |_{i,j}$ are the freezing speeds evaluated on cell $\{i,j\}$, and in equation (3.4) we set

$$| \lambda |_{i-\frac{1}{2},j} = \max\left(| \lambda |_{i-1,j} , | \lambda |_{i,j} \right)$$
$$| \lambda |_{i,j-\frac{1}{2}} = \max\left(| \lambda |_{i,j-1} , | \lambda |_{i,j} \right)$$

3.2 Positivity-preserving Limiter

3.2.1 Proof of positivity-preserving property of extended-MHD model

Physically, the density ρ and pressure P are positive. Therefore, the exact solution is in a convex set G [8], defined in the following:

$$G = \left\{ \mathbf{w} = \begin{pmatrix} \rho \\ m_x \\ m_y \\ m_z \\ \mathcal{E}_n \\ S_e \end{pmatrix} \middle| \rho > 0 \text{ and } P = (\gamma - 1)(\mathcal{E}_n - \frac{1}{2}(m_x^2 + m_y^2 + m_z^2)/\rho) > 0 \text{ and } S_e > 0 \right\}, \tag{3.5}$$

We want to construct the numerical solution which is also in the set (3.5). We use forward Euler for time integration and maintain the positivity of density, pressure and electron entropy density at time level $n+1$, provided that they are positive at time level n. It is clear that, $\mathcal{E}_n > 0$ is automatically established if we have $\rho > 0$ and $P > 0$. In this section, we prove that the positivity-preserving property can be guaranteed with a special limiter in our XMHD model.

We consider the first five equations and the last one in the system (3.3). Following [64], at time level n, we use a vector of polynomials of degree k, $\mathbf{w}_{ij}^n = (\rho_{ij}^n, m_{x_{ij}}^n, m_{y_{ij}}^n, m_{z_{ij}}^n, \mathcal{E}_{nij}^n, S_{e_{ij}}^n)$ to approximate the exact solution, and define the cell average $\overline{\mathbf{w}}_{ij}^n = (\overline{\rho}_{ij}^n, \overline{m}_{x_{ij}}^n, \overline{m}_{y_{ij}}^n, \overline{m}_{z_{ij}}^n, \overline{\mathcal{E}}_{nij}^n, \overline{S_e})$. In this section, we always use $\mathbf{u}_{ij}^n = (u_{x_{ij}}^n, u_{y_{ij}}^n, u_{z_{ij}}^n)^T$ for $\frac{\mathbf{m}_{ij}^n}{\rho_{ij}^n} = \left(\frac{m_{x_{ij}}^n}{\rho_{ij}^n}, \frac{m_{y_{ij}}^n}{\rho_{ij}^n}, \frac{m_{z_{ij}}^n}{\rho_{ij}^n}\right)^T$ as the numerical velocity in cell I_{ij} at

time level n. For simplicity, if we consider a generic numerical solution on the whole computational domain, then the subscript ij will be omitted. By taking the test function $\mathbf{v} = 1$ in (3.3) we have the scheme satisfied by the cell averages

$$\overline{\mathbf{w}}_{ij}^{n+1} = \frac{1}{2}\mathbf{H}_1 + \frac{1}{2}\mathbf{H}_2, \tag{3.6}$$

where

$$\begin{aligned}\mathbf{H}_1 = \overline{\mathbf{w}}_{ij}^{n} &+ \frac{2\Delta t}{\Delta x \Delta y}\int_{y_{j-\frac{1}{2}}}^{y_{j+\frac{1}{2}}} \hat{\mathbf{f}}\left(\mathbf{w}^{-}_{i-\frac{1}{2},j}(y), \mathbf{w}^{+}_{i-\frac{1}{2},j}(y)\right) - \hat{\mathbf{f}}\left(\mathbf{w}^{-}_{i+\frac{1}{2},j}(y), \mathbf{w}^{+}_{i+\frac{1}{2},j}(y)\right) dy \\ &+ \frac{2\Delta t}{\Delta x \Delta y}\int_{x_{i-\frac{1}{2}}}^{x_{i+\frac{1}{2}}} \hat{\mathbf{g}}\left(\mathbf{w}^{-}_{i,j-\frac{1}{2}}(x), \mathbf{w}^{+}_{i,j-\frac{1}{2}}(x)\right) - \hat{\mathbf{g}}\left(\mathbf{w}^{-}_{i,j+\frac{1}{2}}(x), \mathbf{w}^{+}_{i,j+\frac{1}{2}}(x)\right) dx \end{aligned} \tag{3.7}$$

$$\mathbf{H}_2 = \overline{\mathbf{w}}_{ij}^{n} + \frac{2\Delta t}{\Delta x \Delta y}\int_{I_{ij}} \mathbf{s}(x, y) dx dy, \tag{3.8}$$

with $\hat{\mathbf{f}}(\cdot,\cdot)$ and $\hat{\mathbf{g}}(\cdot,\cdot)$ being the one-dimensional numerical fluxes and

$$\mathbf{s} = (0,\, \mathbf{J}\times\mathbf{B},\, \mathbf{u}\cdot(\mathbf{J}\times\mathbf{B}) + \eta\mathbf{J}^2, (\gamma-1)n_e^{1-\gamma}\eta\mathbf{J}^2)^T.$$

For accuracy, we use L-point Gauss quadrature with $L \geq k+1$ to approximate the integral in (3.15). We refer the readers to [14] for more details of this requirement. The Gauss quadrature points on $\left[x_{i-\frac{1}{2}}, x_{i+\frac{1}{2}}\right]$ and $\left[y_{j-\frac{1}{2}}, y_{j+\frac{1}{2}}\right]$ are denoted by

$$p_i^x = \left\{x_i^\beta : \beta = 1, \cdots, L\right\} \text{ and } p_j^y = \left\{y_j^\beta : \beta = 1, \cdots, L\right\},$$

respectively. Also, we denote ω_β as the corresponding weights on the interval $[-1, 1]$. Then the Gauss quadrature formula on the interval $\left[x_{i-\frac{1}{2}}, x_{i+\frac{1}{2}}\right]$ can be written as

$$\int_{x_{i-\frac{1}{2}}}^{x_{i+\frac{1}{2}}} f(x)dx \approx \sum_{\beta=1}^{L} \omega_\beta f(x_i^\beta) h_i/2,$$

where $h_i = x_{i+\frac{1}{2}} - x_{i-\frac{1}{2}}$. Moreover, we use

$$\hat{p}_i^x = \{\hat{x}_i^\alpha : \alpha = 0, \cdots, M\} \text{ and } \hat{p}_j^y = \left\{\hat{y}_j^\alpha : \alpha = 0, \cdots, M\right\}$$

with $2M-1 \geq k$, as the Gauss-Lobatto points on $\left[x_{i-\frac{1}{2}}, x_{i+\frac{1}{2}}\right]$ and $\left[y_{j-\frac{1}{2}}, y_{j+\frac{1}{2}}\right]$, respectively. Also, we denote $\hat{\omega}_\alpha$ as the corresponding weights on the interval $[-1,1]$. Then the Gauss-Lobatto quadrature formula on the interval $\left[x_{i-\frac{1}{2}}, x_{i+\frac{1}{2}}\right]$ can be written as

$$\int_{x_{i-\frac{1}{2}}}^{x_{i+\frac{1}{2}}} f(x)dx \approx \sum_{\alpha=0}^{M} \hat{\omega}_\alpha f(\hat{x}_i^\alpha) h_i/2.$$

Let $\lambda_1 = \frac{\Delta t}{\Delta x}$ and $\lambda_2 = \frac{\Delta t}{\Delta y}$, then $\mathbf{H}_1$ becomes

$$\begin{aligned}\mathbf{H}_1 = \overline{\mathbf{w}}_{ij}^n &+ 2\lambda_1 \sum_{\beta=1}^{L} \omega_\beta \left[\hat{\mathbf{f}}\left(\mathbf{w}^-_{i-\frac{1}{2},\beta}, \mathbf{w}^+_{i-\frac{1}{2},\beta}\right) - \hat{\mathbf{f}}\left(\mathbf{w}^-_{i+\frac{1}{2},\beta}, \mathbf{w}^+_{i+\frac{1}{2},\beta}\right)\right] \\ &+ 2\lambda_2 \sum_{\beta=1}^{L} \omega_\beta \left[\hat{\mathbf{g}}\left(\mathbf{w}^-_{\beta,j-\frac{1}{2}}, \mathbf{w}^+_{\beta,j-\frac{1}{2}}\right) - \hat{\mathbf{g}}\left(\mathbf{w}^-_{\beta,j+\frac{1}{2}}, \mathbf{w}^+_{\beta,j+\frac{1}{2}}\right)\right], \end{aligned} \tag{3.9}$$

where $\mathbf{w}^-_{i-\frac{1}{2},\beta} = \mathbf{w}^-_{i-\frac{1}{2},j}(y_j^\beta)$ is a point value in the Gauss quadrature. Likewise for the other point values. Then we have the following lemma:

Lemma 3.1. *For the discontinuous Galerkin method with the LLF flux, if* $\mathbf{w^n} \in G$, *then* $\mathbf{H}_1 \in G$ *under the CFL condition*

$$\frac{\Delta t}{\Delta x} max\left(\|u_x + C_0\|_\infty, \|u_y\|_\infty, \|u_z\|_\infty\right) + \frac{\Delta t}{\Delta y} max\left(\|u_x\|_\infty, \|u_y + C_0\|_\infty, \|u_z\|_\infty\right) \leq \frac{\hat{\omega}_0}{2}, \tag{3.10}$$

and

$$\frac{\Delta t}{\Delta x} max\left(\|(u_e)_x\|_\infty\right) + \frac{\Delta t}{\Delta y} max\left(\|(u_e)_y\|_\infty\right) \leq \frac{\hat{\omega}_0}{2}, \tag{3.11}$$

where $C_0 = \sqrt{\frac{\gamma P}{\rho}}$, $\|v\|_\infty$ *is the standard* L^∞*-norm of* v *on the whole computational domain, and* $(u_e)_x$ *and* $(u_e)_y$ *are the* x *and* y *components of* $\mathbf{u_e}$.

Proof: The proof follows from [64] with some minor changes, so we omit it.

Now we consider the source term $\mathbf{s}$. We use a Gauss quadrature with L points to compute the integral of the source. Then $\mathbf{H}_2$ becomes

$$\mathbf{H}_2 = \sum_{\alpha=1}^{L} \sum_{\beta=1}^{L} \omega_\alpha \omega_\beta \mathbf{h}_{\alpha\beta},$$

where

$$\mathbf{h}_{\alpha\beta} = \mathbf{w}^n_{\alpha\beta} + 2\Delta t \mathbf{s}_{\alpha\beta}$$

and $\mathbf{w}^n_{\alpha\beta}$ denote the point value of $\mathbf{w}^n_{ij}$ at (x^α_i, y^β_j). Likewise for $\mathbf{s}_{\alpha\beta}$.

Lemma 3.2. *Suppose $\mathbf{w}^n \in G$, then we have $\mathbf{h}_{\alpha\beta} \in G$ under the condition*

$$\Delta t \leq \min_{i,j,\alpha,\beta} A_s(x^\alpha_i, y^\beta_j), \tag{3.12}$$

where

$$A_s = \frac{\eta \mathbf{J}^2 \rho + \sqrt{\eta^2 \mathbf{J}^4 \rho^2 + 2P(\mathbf{J}\times\mathbf{B})^2 \rho/(\gamma-1)}}{2(\mathbf{J}\times\mathbf{B})^2}$$

Proof: Suppose $\mathbf{h}_{\alpha\beta} = (\breve{\rho}, \rho\breve{\mathbf{u}}, \breve{\mathcal{E}}_n, \breve{S}_e)^T$, with $\breve{\mathbf{u}} = \frac{\breve{\mathbf{m}}}{\breve{\rho}}$. For simplicity, in this lemma, if we consider the point value at (x^α_i, y^β_j) at time level n, the corresponding index will be omitted. Then it is easy to show that $\breve{\rho} = \rho^n > 0$ and $\breve{S}_e > 0$. The second inequality is due to the positivity of the source term in (2.33). So we only need to show $\breve{P} = (\gamma-1)(\breve{\mathcal{E}}_n - \frac{1}{2}\breve{\rho}\breve{\mathbf{u}}^2) > 0$. Clearly, we have:

$$\breve{\mathbf{m}} = \mathbf{m} + 2\Delta t(\mathbf{J}\times\mathbf{B})$$

$$\breve{\mathcal{E}}_n = \mathcal{E}_n + 2\Delta t(\mathbf{u}\cdot(\mathbf{J}\times\mathbf{B}) + \eta\mathbf{J}^2)$$

which further yields

$$\begin{aligned}\frac{\breve{P}}{\gamma-1} &= \mathcal{E}_n + 2\Delta t(\mathbf{u}\cdot(\mathbf{J}\times\mathbf{B}) + \eta\mathbf{J}^2) - \frac{[\mathbf{m} + 2\Delta t(\mathbf{J}\times\mathbf{B})]^2}{2\rho} \\ &= \frac{P}{\gamma-1} + 2\Delta t\eta\mathbf{J}^2 - 2\Delta t^2\frac{(\mathbf{J}\times\mathbf{B})^2}{\rho}\end{aligned}$$

Therefore, $\breve{P} > 0$ provided

$$\Delta t \leq \frac{\eta \mathbf{J}^2 \rho + \sqrt{\eta^2 \mathbf{J}^4 \rho^2 + 2P(\mathbf{J}\times\mathbf{B})^2 \rho/(\gamma-1)}}{2(\mathbf{J}\times\mathbf{B})^2}.$$

This condition can be made physically transparent as follows:

$$\Delta t < \frac{1}{\sqrt{2(\gamma-1)}}\frac{v_{th}}{v_A v'_A} \quad \text{or} \quad \Delta \mathrm{t} < \frac{\eta}{\mu_0}\frac{1}{\mathrm{v}_\mathrm{A}^2}$$

is sufficient for $\check{P} > 0$, where v_{th} is the thermal speed, v_A is the Alfvén speed, $v'_A \equiv \frac{\nabla\times\mathbf{B}}{\sqrt{\mu_0 n m_i}}$.

Notice the fact that $\mathbf{w}^{n+1}$ is the convex combination of $\mathbf{H}_1$ and $\mathbf{h}_{\alpha\beta}$ we have the following result.

Theorem 3.1. *Consider the scheme satisfied by the cell averages of a DG formulation* (3.14) *with Lax-Friedrichs flux, if* $\mathbf{w}^n(\hat{x}_i^\alpha, y_j^\beta), \mathbf{w}^n(x_i^\alpha, \hat{y}_j^\beta), \mathbf{w}^n(x_i^\alpha, y_j^\beta) \in G$, *then* $\overline{\mathbf{w}}^{n+1} \in G$ *under the CFL condition* (3.18) *and* (3.19).

Remark 3.1 Since MHD model shares the first five equations with XMHD model in system (3.3), the proof that the positivity-preserving property can be guaranteed in MHD model follows exactly the same process, so we omit it here.

Remark 3.2 We have shown that the positivity-preserving property of pressure in the Euler equations extends to the XMHD model or MHD model. As indicated by (3.19), in extreme cases where the resistivity η is zero, and pressure P is very small, we may not be able to find a reasonable Δt to preserve the positivity of $\check{P}$. Apparently that is an exceptional situation, which we have not yet encountered.

Remark 3.3 We have chosen to model the electron equation of state using the electron entropy density given by $S_e = P_e/n_e^{\gamma-1}$ because we are unable to prove that the electron pressure will remain positive when the electron energy equation is used. The issue arising in the proof of electron pressure positivity is due to the non-positive nature of the electron energy equation source terms which directly involves the electric field; however, the electron entropy density source term is positive and we can easily prove electron pressure positivity. The proof

of positivity of the total pressure is also complicated by the non-positive nature of the total energy source term, but in that case the proof goes through if certain time-step restrictions are applied. The disadvantage of the use of the electron entropy density over the electron energy density is that the entropy density only allows for adiabatic changes in the thermodynamic variables and hence we cannot capture weak solutions in the form of electron shocks. Such circumstances could arise for instance in the form of Langmuir shocks. As we are primarily concerned with low-frequency phenomena, well below the electron plasma frequency, we do not consider the use of the electron entropy density to be a great restriction.

3.2.2 Proof of positivity-preserving property of two-fluid model

Now we also prove that the positivity-preserving limiter can also be applied to a full two-fluid model and also guarantee the stability of two-fluid model under certain conditions. We write this section for the convenience of other researchers who want to apply positivity-preserving limiter on a full two fluid model.

We first consider the first five equations in the full two-fluid system:

$$\begin{aligned}
&\partial_t \rho_s + \nabla \cdot (\rho_s \mathbf{u}_s) = 0 \\
&\partial_t (\rho_s \mathbf{u}_s) + \nabla \cdot [\rho_s \mathbf{u_s} \mathbf{u_s} + \mathbf{I} P] = n_s q_s (\mathbf{E} + \mathbf{u}_s \times \mathbf{B}) - \mathbf{R}_s \\
&\partial_t \mathcal{E}_s + \nabla \cdot [\mathbf{u}_s (\mathcal{E}_s + P_s)] = n_s q_s \mathbf{u}_s \cdot (\mathbf{E} + \frac{\mathbf{R}_s}{n_s q_s})
\end{aligned} \tag{3.13}$$

Here, $\rho_s = n_s m_s$. Writing (3.13) in the form of (3.1), we can use a similar manner as Equation (3.2) to get the corresponding $\mathbf{U}$, $\mathbf{f}(\mathbf{U})$, $\mathbf{g}(\mathbf{U})$, $\mathbf{s}(\mathbf{U})$ for this particular

system. And define a convex set G_s to which the exact solution of (3.13) should belong to:

$$G_s = \left\{ \mathbf{w_s} = \left(\begin{array}{c} \rho_s \\ m_{xs} \\ m_{ys} \\ m_{zs} \\ \mathcal{E}_s \end{array} \right) \middle| \rho_s > 0 \text{ and } P_s = (\gamma_s - 1)(\mathcal{E}_s - \frac{1}{2}(m_{xs}^2 + m_{ys}^2 + m_{zs}^2)/\rho_s) > 0 \right\}$$

Following [64], at time level n, we use a vector of polynomials of degree k, $\mathbf{w}_{sij}^n = (\rho_{sij}^n, m_{x}{}_{sij}^n, m_{y}{}_{sij}^n, m_{z}{}_{sij}^n, \mathcal{E}_{sij}^n)$ to approximate the exact solution, and define the cell average $\overline{\mathbf{w}}_{sij}^n = (\overline{\rho}_{sij}^n, \overline{m}_{x}{}_{sij}^n, \overline{m}_{y}{}_{sij}^n, \overline{m}_{z}{}_{sij}^n, \overline{\mathcal{E}}_{sij}^n)$. We want to prove here that if $\mathbf{w_s^n} \in G_s$, then $\overline{\mathbf{w}}_{\mathbf{s}}^{\mathbf{n+1}} \in G_s$. In this section, we always use $\mathbf{u}_{sij}^n = (u_{x}{}_{sij}^n, u_{y}{}_{sij}^n, u_{z}{}_{sij}^n)^T$ for $\frac{\mathbf{m}_{sij}^n}{\rho_{sij}^n} = \left(\frac{m_{x}{}_{sij}^n}{\rho_{sij}^n}, \frac{m_{y}{}_{sij}^n}{\rho_{sij}^n}, \frac{m_{z}{}_{sij}^n}{\rho_{sij}^n}\right)^T$ as the numerical velocity in cell I_{ij} at time level n. For simplicity, if we consider a generic numerical solution on the whole computational domain, then the subscript ij will be omitted. By taking the test function $\mathbf{v} = 1$ in (3.3) we have the scheme satisfied by the cell averages

$$\overline{\mathbf{w}}_{sij}^{n+1} = \frac{1}{2}\mathbf{H}_1 + \frac{1}{2}\mathbf{H}_2, \tag{3.14}$$

where

$$\begin{aligned} \mathbf{H}_1 = \overline{\mathbf{w}}_{sij}^n &+ \frac{2\Delta t}{\Delta x \Delta y} \int_{y_{j-\frac{1}{2}}}^{y_{j+\frac{1}{2}}} \hat{\mathbf{f}}\left(\mathbf{w}_{si-\frac{1}{2},j}^-(y), \mathbf{w}_{si-\frac{1}{2},j}^+(y)\right) - \hat{\mathbf{f}}\left(\mathbf{w}_{si+\frac{1}{2},j}^-(y), \mathbf{w}_{si+\frac{1}{2},j}^+(y)\right) dy \\ &+ \frac{2\Delta t}{\Delta x \Delta y} \int_{x_{i-\frac{1}{2}}}^{x_{i+\frac{1}{2}}} \hat{\mathbf{g}}\left(\mathbf{w}_{si,j-\frac{1}{2}}^-(x), \mathbf{w}_{si,j-\frac{1}{2}}^+(x)\right) - \hat{\mathbf{g}}\left(\mathbf{w}_{si,j+\frac{1}{2}}^-(x), \mathbf{w}_{si,j+\frac{1}{2}}^+(x)\right) dx \end{aligned} \tag{3.15}$$

$$\mathbf{H}_2 = \overline{\mathbf{w}}_{sij}^n + \frac{2\Delta t}{\Delta x \Delta y} \int_{I_{ij}} \mathbf{s}(x, y) dx dy, \tag{3.16}$$

with $\hat{\mathbf{f}}(\cdot,\cdot)$ and $\hat{\mathbf{g}}(\cdot,\cdot)$ being the one-dimensional numerical fluxes defined with (3.4) and

$$\mathbf{s} = (0,\ n_s q_s(\mathbf{E} + \mathbf{u}_s \times \mathbf{B}) - \mathbf{R}_s,\ n_s q_s \mathbf{u}_s \cdot (\mathbf{E} + \frac{\mathbf{R}_s}{n_s q_s}))^T.$$

For accuracy, we use L-point Gauss quadratures with $L \geq k+1$ to approximate the integral in (3.15). We refer the readers to [10] for more details of this requirement. The Gauss quadrature points on $\left[x_{i-\frac{1}{2}}, x_{i+\frac{1}{2}}\right]$ and $\left[y_{j-\frac{1}{2}}, y_{j+\frac{1}{2}}\right]$ are denoted by

$$p_i^x = \left\{x_i^\beta : \beta = 1, \cdots, L\right\} \text{ and } p_j^y = \left\{y_j^\beta : \beta = 1, \cdots, L\right\},$$

respectively. Also, we denote ω_β as the corresponding weights on the interval $\left[-\frac{1}{2}, \frac{1}{2}\right]$. Moreover, we use

$$\hat{p}_i^x = \{\hat{x}_i^\alpha : \alpha = 0, \cdots, M\} \text{ and } \hat{p}_j^y = \left\{\hat{y}_j^\alpha : \alpha = 0, \cdots, M\right\}$$

as the Gauss-Lobatto points on $\left[x_{i-\frac{1}{2}}, x_{i+\frac{1}{2}}\right]$ and $\left[y_{j-\frac{1}{2}}, y_{j+\frac{1}{2}}\right]$ respectively. Also, we denote $\hat{\omega}_\alpha$ as the corresponding weights on the interval $\left[-\frac{1}{2}, \frac{1}{2}\right]$.

Let $\lambda_1 = \frac{\Delta t}{\Delta x}$ and $\lambda_2 = \frac{\Delta t}{\Delta y}$, then $\mathbf{H}_1$ becomes

$$\begin{aligned}\mathbf{H}_1 = \overline{\mathbf{w}}_{sij}^n &+ 2\lambda_1 \sum_{\beta=1}^{L} \omega_\beta \left[\hat{\mathbf{f}}\left(\mathbf{w}^-_{si-\frac{1}{2},\beta}, \mathbf{w}^+_{si-\frac{1}{2},\beta}\right) - \hat{\mathbf{f}}\left(\mathbf{w}^-_{si+\frac{1}{2},\beta}, \mathbf{w}^+_{si+\frac{1}{2},\beta}\right)\right] \\ &+ 2\lambda_2 \sum_{\beta=1}^{L} \omega_\beta \left[\hat{\mathbf{g}}\left(\mathbf{w}^-_{s\beta,j-\frac{1}{2}}, \mathbf{w}^+_{s\beta,j-\frac{1}{2}}\right) - \hat{\mathbf{g}}\left(\mathbf{w}^-_{s\beta,j+\frac{1}{2}}, \mathbf{w}^+_{s\beta,j+\frac{1}{2}}\right)\right], \end{aligned} \tag{3.17}$$

where $\mathbf{w}^-_{si-\frac{1}{2},\beta} = \mathbf{w}^-_{si-\frac{1}{2},j}(y_j^\beta)$ is a point value in the Gauss quadrature. Likewise for the other point values. Then we have the following lemma

Lemma 3.3. *For the discontinuous Galerkin method with the local Lax-Friedrichs flux, if $\mathbf{w}_\mathbf{s}^\mathbf{n} \in G_s$, then $\mathbf{H}_1 \in G_s$ under the CFL condition*

$$\frac{\Delta t}{\Delta x} max\left(\|u_{xs} + C_{0s}\|_\infty, \|u_{ys}\|_\infty, \|u_{zs}\|_\infty\right) + \frac{\Delta t}{\Delta y} max\left(\|u_{xs}\|_\infty, \|u_{ys} + C_{0s}\|_\infty, \|u_{zs}\|_\infty\right) \leq \frac{\hat{\omega}_0}{2} \tag{3.18}$$

where $C_{0s} = \sqrt{\frac{\gamma P_s}{\rho_s}}$, $\|v\|_\infty$ is the standard L^∞-norm of v on the whole computational domain.

Proof: The proof follows from [64] with some minor changes, so we omit it.

Now we consider the source term $\mathbf{s}$. We use a Gauss quadrature with L points to compute the integral of the source. Then $\mathbf{H}_2$ becomes

$$\mathbf{H}_2 = \sum_{\alpha=0}^{L}\sum_{\beta=0}^{L} \omega_\alpha \omega_\beta \mathbf{h}_{\alpha\beta},$$

where

$$\mathbf{h}_{\alpha\beta} = \mathbf{w}^n_{s\alpha\beta} + 2\Delta t \mathbf{s}_{\alpha\beta}$$

and $\mathbf{w}^n_{s\alpha\beta}$ denote the point value of $\mathbf{w}^n_{sij}$ at (x_i^α, y_j^β). Likewise for $\mathbf{s}_{\alpha\beta}$.

Lemma 3.4. *Suppose* ${\mathbf{w}_\mathbf{s}}^n \in G$*, then we have* $\mathbf{h}_{\alpha\beta} \in G$ *under the condition*

$$\Delta t \le \min_{i,j,\alpha,\beta} A_s(x_i^\alpha, y_j^\beta), \tag{3.19}$$

where

$$A_s = \rho_s \frac{\mathbf{u_s}\cdot\mathbf{R}_s + \sqrt{2P_s[n_s q_s(\mathbf{E}+\mathbf{u_s}\times\mathbf{B}) - \mathbf{R}_s]^2/(\rho_s(\gamma-1)) + (\mathbf{u_s}\cdot R)^2}}{[n_s q_s(\mathbf{E}+\mathbf{u_s}\times\mathbf{B}) - \mathbf{R}_s]^2}$$

Proof: We omit the subscript s in this proof for simplicity. Suppose $\mathbf{h}_{\alpha\beta} = (\check{\rho}, \rho\check{\mathbf{u}}, \check{\mathcal{E}})^T$, with $\check{\mathbf{u}} = \frac{\check{\mathbf{m}}}{\check{\rho}}$. For simplicity, in this lemma, if we consider the point value at (x_i^α, y_j^β) at time level n, the corresponding index will be omitted. Then it is easy to show that $\check{\rho} = \rho^n > 0$. So we only need to show $\check{P} = (\gamma-1)(\check{\mathcal{E}} - \frac{1}{2}\check{\rho}\check{\mathbf{u}}^2) > 0$. Clearly, we have

$$\begin{aligned}
\check{\mathbf{m}} &= \mathbf{m} + 2\Delta t[nq(\mathbf{E}+\mathbf{u}\times\mathbf{B}) - \mathbf{R}] \\
\check{\mathcal{E}}_n &= \mathcal{E} + 2\Delta t nq\mathbf{u}\cdot(\mathbf{E} + \frac{\mathbf{R}}{nq})
\end{aligned}$$

which further yields

$$\begin{aligned}
\frac{\check{P}}{\gamma-1} &= \mathcal{E} + 2\Delta t nq\mathbf{u}\cdot(\mathbf{E}+\frac{\mathbf{R}}{nq}) - \frac{[\mathbf{m} + 2\Delta t[nq(\mathbf{E}+\mathbf{u}\times\mathbf{B}) - \mathbf{R}]]^2}{2\rho} \\
&= \frac{P}{\gamma-1} + 4\Delta t\mathbf{u}\cdot\mathbf{R} - \frac{2\Delta t^2[nq(\mathbf{E}+\mathbf{u}\times\mathbf{B}) - \mathbf{R}]^2}{\rho}
\end{aligned}$$

Therefore, $\check{P} > 0$ provided

$$\Delta t < \rho \frac{\mathbf{u}\cdot\mathbf{R} + \sqrt{2P[nq(\mathbf{E}+\mathbf{u}\times\mathbf{B})-\mathbf{R}]^2/(\rho(\gamma-1)) + (\mathbf{u}\cdot\mathbf{R})^2}}{[nq(\mathbf{E}+\mathbf{u}\times\mathbf{B})-\mathbf{R}]^2}$$

Notice the fact that $\mathbf{w}_s^{n+1}$ is the convex combination of $\mathbf{H}_1$ and $\mathbf{h}_{\alpha\beta}$ we have the following result.

Theorem 3.2. *Consider the scheme satisfied by the cell averages of a DG formulation* (3.14) *with Lax-Friedrichs flux, if* $\mathbf{w_s}^n(\hat{x}_i^\alpha, y_j^\beta), \mathbf{w_s}^n(x_i^\alpha, \hat{y}_j^\beta), \mathbf{w_s}^n(x_i^\alpha, y_j^\beta) \in G_s$*, then* $\overline{\mathbf{w_s}}^{n+1} \in G_s$ *under the CFL condition* (3.18) *and condition* (3.19)*.*

3.2.3 Implementation of the Positivity-preserving Limiter

Now, we summarize the implementation of the algorithm.

- Choose a small number consistent with the density that can be viewed as vacuum, which is typically $\varepsilon = 10^{-9}$.
- If $\overline{\rho}_{ij}^n > \varepsilon$, then proceed to the following steps. Otherwise, ρ_{ij}^n is identified as the approximation to vacuum, and we take $\mathbf{w}_{ij}^n = \overline{\mathbf{w}}_{ij}^n$ as the numerical solution and skip the following steps.
- In each cell, modify the density first. Evaluate

  $$\rho_{min} = \min_{\alpha\beta}\{\rho_{ij}^n(\hat{x}_i^\alpha, y_j^\beta), \rho_{ij}^n(x_i^\alpha, \hat{y}_j^\beta), \rho_{ij}^n(x_i^\alpha, y_j^\beta)\}.$$

  If $\rho_{min} < \varepsilon$, then take $\widetilde{\rho}_{ij}^n$ as

  $$\widetilde{\rho}_{ij}^n = \overline{\rho}_{ij}^n + \theta_{ij}^n(\rho_{ij}^n - \overline{\rho}_{ij}^n),$$

  with

  $$\theta_{ij}^n = \frac{\overline{\rho}_{ij}^n - \varepsilon}{\overline{\rho}_{ij}^n - \rho_{min}}.$$

  and use $\widetilde{\rho}_{ij}^n$ as the new numerical density by assigning: $\rho_{ij}^n = \widetilde{\rho}_{ij}^n$

- Modify the S_e. Evaluate

$$S_{emin} = \min_{\alpha\beta}\{S_{eij}^n(\widehat{x}_i^\alpha, y_j^\beta), S_{eij}^n(x_i^\alpha, \widehat{y}_j^\beta), S_{eij}^n(x_i^\alpha, y_j^\beta)\}.$$

  If $S_{emin} < \varepsilon$, then take $\widetilde{S}_{eij}^n$ as

$$\widetilde{S}_{eij}^n = \overline{S}_{eij}^n + \theta_{ij}^n(S_{eij}^n - \overline{S}_{eij}^n),$$

  with

$$\theta_{ij}^n = \frac{\overline{S}_{eij}^n - \varepsilon}{\overline{S}_{eij}^n - S_{emin}}.$$

  and use $\widetilde{S}_{eij}^n$ as the new electron entropy density by assigning: $S_{eij}^n = \widetilde{S}_{eij}^n$

- Modify the pressure: For each $\mathbf{q} \in \{\mathbf{w}(\widehat{x}_i^\alpha, y_j^\beta), \mathbf{w}(x_i^\alpha, \widehat{y}_j^\beta), \mathbf{w}(x_i^\alpha, y_j^\beta)\}$, compute $P(\mathbf{q})$. If $P(\mathbf{q}) \geq \varepsilon$, then we take $s_\mathbf{q} = 1$. Otherwise, we calculate $s_\mathbf{q}$ such that

$$P\left((1 - s_\mathbf{q})\overline{\mathbf{w}}_\mathbf{q} + s_\mathbf{q}\mathbf{q}\right) = \varepsilon.$$

  Modify $\widetilde{\mathbf{w}}_{ij}^n = \overline{\mathbf{w}}_{ij}^n + \theta\left(\mathbf{w}_{ij}^n - \overline{\mathbf{w}}_{ij}^n\right)$ with $\theta = \min_\mathbf{q}\{s_\mathbf{q}\}$.

- Use $\widetilde{\mathbf{w}}_{ij}^n$ as the DG approximation.

3.2.4 Remark on Difference between Positivity-Preserving Limiter vs a TVD Limiter

Numerical limiting is necessary in the high resolution schemes to prevent spurious oscillations near discontinuities, and also necessary to keep the stabilization of non-linear systems. For finite volume schemes, TVD limiters are often used, a TVD limiter is a limiter that can guarantee that the total variation of the numerical solution at this time step is less or equal to the previous time step, ie, if we use TV as the abbreviation of total variation, we should have:

$$TV(\mathbf{u}^{n+1}) \leq TV(\mathbf{u}^n).$$

With $TV(\mathbf{u})$ defined as:

$$TV(\mathbf{u}) = \sum_{j} \sum_{p=1}^{m} \mid (u_{j+1})^{(p)} - (u_j)^{(p)} \mid$$

Common TVD limiters include minmod limiter, Van Leer limiter, etc.. The TVD limiters can also be used in the discontinuous Galerkin method. The procedure is as described in [13, 38], we just briefly restate it here. Taking the limiting on the slope on x direction for example, a brief summary of the procedure is, we need to limit variable u in terms of characteristics, to do that, u has to be transformed to characteristic variables v where $v = Lu$, with L being the left eigenvector matrix of the flux Jacobian calculated from the mean variable value u_0. We apply L on the spatial differences of the mean values:

$$L(u_0^{i+1} - u_0^i) = \Delta^+ v_0,$$

$$L(u_0^i - u_0^{i-1}) = \Delta^- v_0.$$

We perform limiting on transformed variables v, $\Delta^+ v_0$, $\Delta^- v_0$, and then transform the limited solution back to determine the limited form of the slope on x direction, ie, u_x,

$$\tilde{u}_x = L^{-1} lm(u_x, \Delta^+ v_0, \Delta^- v_0),$$

we choose minmod limiter for example, then lm stands for a function defined by:

$$lm(a,b,c) = \begin{cases} max(a,b,c), \text{if sign(a) = sign(b) = sign(c) = -,} \\ min(a,b,c), \text{if sign(a) = sign(b) = sign(c) = +,} \\ 0, \text{otherwise.} \end{cases} \tag{3.20}$$

Notice that, the calculation of L can be very computationally expensive if we are dealing with a large system.

Another reason holding us back from using a TVD limiter is that, a TVD limiter will degrade the order of accuracy at smooth extrema. However, the purpose of developing this DG scheme is for a better accuracy and less diffusion, therefore it does not make sense for us to degrade the order of accuracy for any purpose.

With the scheme being a lower of accuracy near smooth extrema, and with some more numerical diffusion added in by using the TVD limiter, the TVD limiter does wipe out the oscillations near discontinuity. On the other hand, with the PP-limiter, some oscillations do appear. We will resolve this concern by performing various numerical tests to show that these oscillations do not harm the stability of the system, and do not impede our understanding of the physics.

The main comparison between using a TVD limiter and a PP-limiter is listed in table 3.1.

3.3 Structure Preserving Limiter

In this section, we will restate the way for locally preserving $\nabla \cdot \mathbf{B} = 0$ originally published in [36], in a format that is particular to our system. Also we provide the implementation of this method in DG-PERSEUS.

Since $\nabla \cdot \mathbf{B} = 0$ is implied by equation (2.34), we can simply consider equation (2.34) alone for constructing a basis function for a finite element space where

Table 3.1: Comparison between TVD limiter and Positivity-Preserving Limiter

TVD Limiter	Positivity-Preserving Limiter
Will degenerate the order accuracy at smooth extrema	Preserves a 2^{nd} order accuracy at smooth extrema
To guarantee TVD property, characteristic decomposition is needed, which is computationally expensive.	Only a simple rescaling operation is needed
Prevent oscillations from appearing near discontinuity	Some oscillations appear near discontinuity, slope limiter can be used to reduce the oscillations

$\nabla \cdot \mathbf{B} = 0$.

We first consider the 2-dimensional case.

Equation 2.34 can be written in the following form:

$$\frac{\partial Q}{\partial t} + \nabla \cdot F(Q) = \psi(Q), \tag{3.21}$$

where:

$$Q = (B_x, B_y, B_z)^T,$$

$$f(Q) = ((0, -E_z, E_y)^T, (E_z, 0, -E_x)^T),$$

$$S(Q) = 0.$$

For second order spatial accuracy, the basis set for each variable in this system on a unit square reference element is:

$$\{v_r\} = \{v_0, v_x, v_y\} = \{1, x, y\}. \tag{3.22}$$

Let

$$Q = \sum_r v_r Q_r \tag{3.23}$$

Multiply equation (3.21) with $\{v_r\}$, we can get the following three equations:

$$\frac{\partial Q_0}{\partial t} S + \sum_e \sum_l w_l (\mathbf{F} \cdot \mathbf{n} v_0) L_e = 0 S \tag{3.24}$$

$$\frac{\partial Q_x}{\partial t} S + 3 \sum_e \sum_l w_l (\mathbf{F} \cdot \mathbf{n} v_x) L_e - 3 \sum_m w_m (\mathbf{F} \cdot (\nabla v_x)) S = 3 \sum_m w_m \psi v_x S \tag{3.25}$$

$$\frac{\partial Q_y}{\partial t} S + 3 \sum_e \sum_l w_l (\mathbf{F} \cdot \mathbf{n} v_y) L_e - 3 \sum_m w_m (\mathbf{F} \cdot (\nabla v_y)) S = 3 \sum_m w_m \psi v_y S, \tag{3.26}$$

Where the integrals over the finite element volume S and finite element edges L_e are replaced by Gaussian quadrature. l denotes the quadrature points on a finite element edge with l denoting the associated weight. m refers to quadrature points in the finite element volume with w_m being the associated weight.

We write the three equations above as:

$$\frac{\partial Q_0}{\partial t} + G F_0 = 0 \tag{3.27}$$

$$\frac{\partial Q_x}{\partial t} + G F_x = 0 \tag{3.28}$$

$$\frac{\partial Q_y}{\partial t} + G F_y = 0 \tag{3.29}$$

Notice if we consider (B_x, B_y) together as a system, (B_x, B_y) can be described by the following basis:

$$\{(1,0)', (x,0)', (y,0)', (0,1)', (0,x)', (0,y)'\} \tag{3.30}$$

Following (3.23), B_x and B_y can be expanded as follows:

$$\begin{aligned} B_x &= Q_0(B_x) + Q_x(B_x)x + Q_y(B_x)y \\ B_y &= Q_0(B_y) + Q_x(B_y)x + Q_y(B_y)y \end{aligned} \tag{3.31}$$

Since in two dimensional Cartesian coordinate system, we have:

$$\nabla \cdot \mathbf{B} = \frac{\partial B_x}{\partial x} + \frac{\partial B_y}{\partial y} = 0 \tag{3.32}$$

Substitute equation (3.31) into equation (3.32), we can get:

$$Q_x(B_x) + Q_y(B_y) = 0 \tag{3.33}$$

Equation (3.33) defines the relationship between $Q_x(B_x)$ and $Q_y(B_y)$, thus two of the basis functions in (3.30), $(x,0)'$ and $(0,y)'$ can be combined into one $(x,-y)$. So (B_x, B_y) can be described by the following basis functions:

$$\tilde{\mathbf{v}} = \{(1,0)', (y,0)', (0,1)', (0,x)', (x,-y)'\} \tag{3.34}$$

$$\frac{\partial (B_x, B_y)}{\partial t} + \nabla \cdot (F(B_x), F(B_y)) = (0,0) \tag{3.35}$$

We multiply equation (3.35) with basis functions (3.34). We can get same results for $Q_0(B_x)$, $Q_0(B_y)$, $Q_x(B_y)$, $Q_y(B_x)$ as the results with basis functions (3.30), but different results for $Q_x(B_x)$ and $Q_y(B_y)$. When we multiply equation (3.35) with $\tilde{v}_5 = (x,-y)'$ and do integral over the finite element volume, by combining with Equations (3.28) and (3.29), we get:

$$\frac{\partial Q_x(B_x)}{\partial t} - \frac{\partial Q_y(B_y)}{\partial t} + GF_x(B_x) - GF_y(B_y) = 0 \tag{3.36}$$

Substitute Equation (3.33) into equation (3.36), we arrive at:

$$\frac{\partial Q_x(B_x)}{\partial t} + \frac{1}{2}(GF_x(B_x) - GF_y(B_y)) = 0 \tag{3.37}$$

With evolution equation (3.37) we can get values of $Q_x(B_x)$ at an advanced time step, then with

$$Q_y(B_y) = -Q_x(B_x),$$

we get the value of $Q_y(B_y)$. Thus we can get all the coefficients of polynomial (3.31) corresponding to the basis defined by (3.34), and we know that the solution satisfy $\nabla \cdot \mathbf{B} = 0$ automatically. With this method, we can locally preserve the divergence free of $\mathbf{B}$ to Machine accuracy.

We can extend this method to a 3D case following the same procedure.

In a 3D case, also for a second order accuracy, the basis set for each variable in this system on a unit cubic reference element is:

$$\{v_r\} = \{v_0, v_x, v_y, v_z\} = \{1, x, y, z\}.$$

Then the corresponding numerical solution on that element should be polynomial:

$$Q = Q_0 + Q_x x + Q_y y + Q_z z,$$

by replacing Q_r, with $r \in 0, x, y, z$ with Q'_r defined below, we can guarantee a locally divergence-free $\mathbf{B}$.

$$Q'_x(B_x) = \frac{2}{3}Q_x(B_x) - \frac{1}{3}(Q_y(B_y) + Q_z(B_z)) \tag{3.38}$$

$$Q'_y(B_y) = \frac{2}{3}Q_y(B_y) - \frac{1}{3}(Q_x(B_x) + Q_z(B_z)) \tag{3.39}$$

$$Q'_z(B_z) = \frac{2}{3}Q_z(B_z) - \frac{1}{3}(Q_x(B_x) + Q_y(B_y)) \tag{3.40}$$

3.4 Boundary Conditions

In a hyperbolic conservation equation system, we decide the boundary condition in the following manner:
Calculate the flux Jacobian (as defined in Appendix B) of the system, name it **M**. The eigenvalues of **M** are $\lambda_i, i = 1, 2, \ldots, n$. According to the sign of the eigenvalues, we have the following cases (we only consider the left boundary).

1. If for all i, we have $\lambda_i > 0$, then we use inflow boundary. In our case, we need to provide the values of edge points to the left of the boundary: $Q^+_{i=0}$
2. If for all i, we have $\lambda_i < 0$, then we use outflow boundary. In our case, we just use the values of edge points to the right of the left boundary, $Q^-_{i=1}$ as the boundary value. Mathematically written, this condition is implemented as follows:

$$Q^+_{i=0} = Q^-_{i=1} \tag{3.41}$$

3. Reflection boundary, people also call it solid boundary; the physics meaning of this kind of boundary is that, no density can penetrate through this boundary. The implementation of this boundary is that: the normal component of the velocity to the left of the boundary is set to the opposite of that to the right of the boundary; the values of other variables to the left of the boundary are set to be the same with the ones to the right of the boundary. They are written out mathematically below:

$$\begin{aligned} Q^+_{i=0} &= Q^-_{i=1} \\ Q(m_x)^+_{i=0} &= -Q(m_x)^-_{i=1} \end{aligned} \tag{3.42}$$

4. We have both positive and negative eigenvalues, ie, there $\exists i$ that $\lambda_i > 0$, also $\exists i$ that $\lambda_i < 0$, in this case, we cannot purely employ inflow boundary

or outflow boundary conditions. Actually, we need to do characteristic decomposition to decompose the values on the boundaries to be pure inflow values and pure outflow values. Here are the steps we need to follow to handle this case.

Say we have $\mathbf{u} = \{u_i\}$, $i = 1, 2, \ldots, n$,

$$\frac{\partial \mathbf{u}}{\partial t} + \mathbf{M}\frac{\partial \mathbf{u}}{\partial x} = 0 \tag{3.43}$$

We find matrix P satisfying: $P^{-1}\mathbf{M}P = diag\{\lambda_i\}, i = 1, 2, \ldots, n$, left multiply equation (3.43) with P^{-1}, we get:

$$P^{-1}\frac{\partial \mathbf{u}}{\partial t} + P^{-1}\mathbf{M}PP^{-1}\frac{\partial \mathbf{u}}{\partial x} = 0 \tag{3.44}$$

Let $\mathbf{v} = P^{-1}\mathbf{u}$, equation (3.44) becomes:

$$\frac{\partial \mathbf{v}}{\partial t} + diag\{\lambda_i\}\frac{\partial \mathbf{v}}{\partial x} = 0 \tag{3.45}$$

If v_i corresponds to $\lambda_i, \lambda_i < 0$, v_j corresponds to λ_j, and $\lambda_j = -\lambda_i$, then we have:

$$v_j = \alpha v_i + \beta \tag{3.46}$$

Since $\mathbf{v_{i,j}} = P^{-1}\mathbf{u_{i,j}}$, and u_i, u_j are linearly unrelated, α, β can be represented by a function of $u_{i,j}$. Here we use given value $\hat{u}_{i,j}$ to represent α, β. By given values, we mean the values that need to be provided. Knowing v_i, and with provided values $\hat{u}_{i,j}$, one can solve for v_j, which is the inflow value. For the values of v_i, according to the Item 2, should employ the numerical solution to the right of the left boundary at that particular time point. Then by $\mathbf{u_{i,j}} = P\mathbf{v_{i,j}}$, we know the values of $\mathbf{u_{i,j}}$ to the left of the left boundary, $Q^+_{i=0}$.

For clarity, we take Maxwell equations as an example:

$$\begin{aligned} \frac{\partial \mathbf{B}}{\partial t} + \nabla \times \mathbf{E} &= 0 \\ \frac{\partial \mathbf{E}}{\partial t} - c^2 \nabla \times \mathbf{B} &= -\frac{\mathbf{J}}{\epsilon_0} \end{aligned} \tag{3.47}$$

Just consider the flux part, and for the coupled variables B_z, E_y on the left x boundary, we have:

$$\begin{aligned} \frac{\partial B_z}{\partial t} + \frac{\partial E_y}{\partial x} - \frac{\partial E_x}{\partial y} &= 0 \\ \frac{\partial E_y}{\partial t} + c^2 \frac{\partial B_z}{\partial x} &= 0 \end{aligned} \tag{3.48}$$

The eigenvalue of the flux Jacobian of this problem is -c, c, so we need to apply the characteristic decomposition to achieve the pure inflow part and pure outflow part. For this system, we have:

$$\mathbf{u} = (B_z, E_y)'$$

$$\mathbf{M} = \begin{pmatrix} 0 & 1 \\ c^2 & 0 \end{pmatrix}$$

$$P = \begin{pmatrix} \frac{1}{\sqrt{2}} & -\frac{1}{\sqrt{2}} \\ \frac{1}{\sqrt{2}}c & \frac{1}{\sqrt{2}}c \end{pmatrix}$$

$$P^{-1} = \begin{pmatrix} \frac{1}{\sqrt{2}} & \frac{1}{\sqrt{2}c} \\ -\frac{1}{\sqrt{2}} & \frac{1}{\sqrt{2}c} \end{pmatrix}$$

$$P^{-1}\mathbf{M}P = diag\{\lambda_i\} = diag\{c, -c\}$$

Then:

$$\mathbf{v} = P^{-1}\mathbf{u} = \begin{pmatrix} \frac{1}{\sqrt{2}}B_z + \frac{1}{\sqrt{2}c}E_y \\ -\frac{1}{\sqrt{2}}B_z + \frac{1}{\sqrt{2}c}E_y \end{pmatrix}$$

The first component of $\mathbf{v}$ which is v_1 corresponds to the first eigenvalue, $c > 0$, which then corresponds to inflow, v_2 on the other hand corresponds to outflow. Then,

$$v_1 = \alpha v_2 + \beta,$$

by substituting in the expression for v_1 and v_2, we have:

$$\frac{1}{\sqrt{2}} B_z + \frac{1}{\sqrt{2}c} E_y = \alpha(-\frac{1}{\sqrt{2}} B_z + \frac{1}{\sqrt{2}c} E_y) + \beta.$$

Since in this problem, it is more convenient to provide the boundary condition on B_z, so we use:

$$\alpha = 1,$$

$$\beta = \sqrt{2}\hat{B}_z.$$

v_2 can be calculated with the numerical values $Q^-_{i=1}$, and we can calculate v_1 using:

$$v_1 = v_2 + \sqrt{2}\hat{B}_z.$$

With these, we can calculate $\mathbf{u}$ by:

$$\mathbf{u} = P\mathbf{v},$$

i.e.,

$$\begin{aligned} B_z &= v_1/\sqrt{2} - v_2/\sqrt{2} \\ E_y &= c(v_1/\sqrt{2} + v_2/\sqrt{2}) \end{aligned} \tag{3.49}$$

We apply these values to the left of the left boundary, $Q^+_{i=0}$.

One thing to emphasize here is, for applying the boundary conditions, we at most need the information to the right of the left boundary, ie, $Q^-_{i=1}$. We do not need information on any interior point. However, for implementing a second order finite volume scheme, one has to utilize the values of at least two cells

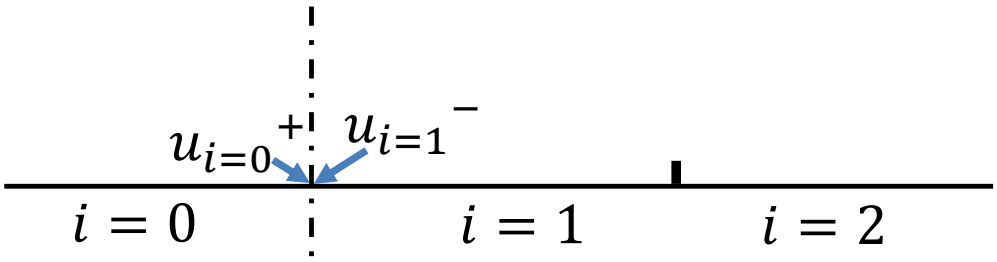

Figure 3.1: Sketch showing the left boundary on x direction

to the right of the left boundary. We call these two lines of cells guard cells. The guard cells do not participate in the time advancement; they exist just for the boundary conditions. This is a waste of computational effort. Especially if we use MPI or other parallelization methods, in every core, the two lines of cells on the boundary of the computational region of each core are wasted. That is a big portion of cells. Also, the boundary information needs to be communicated between computation cores when performing parallel computing. In finite volume, that would be the information of two lines of cells. On the other hand, in DG, only the edge information immediately to the inner side of the boundary has to be passed, for example, for the left x boundary, the information needed to be passed is $Q^{-}_{i=1}$. The information passing time is the biggest overhead time when performing parallel computing. The less information needed to be passed, the less overhead time is taken in the message passing, and the more efficient the algorithm is. For this reason, DG is more efficient in performing parallel computation. To illustrate this more clearly, we provide a diagram 3.2 showing which part of information needs to be communicated during a message passing process in parallel computing using a parallel computing

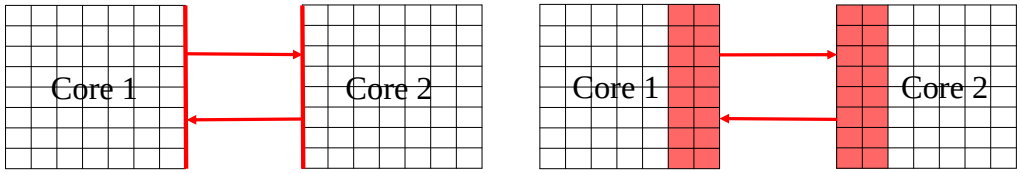

(a) DG. Only the red line, which denotes the edge values immediately to the inner part of the boundary, needs to be communicated between computational cores, i.e., core1 and core2.

(b) FV. The two lines of cells in red on the boundary need to be communicated between computational cores, i.e., core1 and core2.

Figure 3.2: When performing parallel computing, the information on the boundary has to be communicated between computational cores. Take two cores as an example, the area highlighted in red is the information to be communicated.

technique on distributed memories. Message-Passing-Interface (MPI) is incorporated into DG-PERSEUS, and enables the code to run on a 64-core cluster, gaining a speed-up of 40 comparing to the same code running on one core.

3.5 Time Integration Scheme

As described in [47, 42], we use a semi-implicit advance scheme for the stiff source terms in (2.44) and (2.43). The split level implicit-explicit time advance is performed as follows:

1. Use 2nd order Runge-Kutta (Heun) method to perform time advance for (2.30) - (2.34).
2. Use 2nd order Runge-Kutta method to perform time advance for flux part in (2.43) - (2.44):

$$\partial_t \mathbf{E} = \frac{c^2}{v^2}(\nabla \times \mathbf{B}) \tag{3.50}$$

$$\partial_t \mathbf{J} + \nabla \cdot (\mathbf{uJ} + \mathbf{Ju} - \frac{\lambda_i}{L_0 n}\mathbf{JJ} - \frac{m_i}{m_e}\frac{L_0}{\lambda_i}\mathbf{I}P_e) = 0 \tag{3.51}$$

3. Save the updated values obtained from step 1 and 2 as Q^*
4. Perform a semi-implicit time advance for the source terms in (2.43) - (2.44). This leads to the following spatially local linear algebraic equations for $\mathbf{E}^{n+1}$ and $\mathbf{J}^{n+1}$

$$\mathbf{E}^{n+1} = \mathbf{E}^* - \Delta t \frac{c^2}{v^2}\mathbf{J}^{n+1} \tag{3.52}$$

$$\mathbf{J}^{n+1} = \mathbf{J}^* + \Delta t \frac{L_0^2 n^*}{\lambda_e^2}\left(\mathbf{E}^{n+1} + \mathbf{u}^* \times \mathbf{B}^* - \frac{\lambda_i}{L_0 n^*}\mathbf{J}^{n+1} \times \mathbf{B}^* - \eta^* \mathbf{J}^{n+1}\right) \tag{3.53}$$

The semi-implicit step is performed after each step of the explicit Runge-Kutta time advance of (3.50) and (3.51). This time advance method forces a relaxation solution to (2.45) and (2.46) in the relaxation limit and accurately computes the current even if the relaxation limit is not approached, that is, when the electron inertial length scale is resolved [47]. The time advance could also be performed using a higher order strong-stability preserving integrator such as the third order Shu-Osher Runge-Kutta method [53].

CHAPTER 4

NUMERICAL TESTS

In the previous chapters, we have developed a positivity-preserving semi-implicit DG scheme, and we have developed this scheme into a code called DG-PERSEUS. DG-PERSEUS is now available in 2D Cartesian coordinates and 3D Cartesian coordinates. We have proved that this scheme is stable under suitable conditions defined by (3.19), and the scheme is consistent and convergent.

Since DG-PERSEUS is to be used for gaining insight into real physical problems, to guarantee that the simulation results can be trusted, we must verify and validate that the implementation of the scheme is consistent with the analytical properties of the algorithm, i.e., stable, convergent and consistent. We provide this verification through some numerical tests.

We consider five tests in this chapter. For the first test, we consider a smooth sine wave solution to verify that the scheme is 2nd order accurate. Secondly, we consider the shock capturing nature of the scheme, in order to show that, even with real source terms, the scheme is still shock capturing. We will also use this test to validate that the scheme can recover an MHD limit. Through tests 3-5, we want to demonstrate the advantages of a DG scheme over an FV scheme in dealing with problems containing a discontinuity or a δ function, or phenomena needing high resolution to resolve, e.g., instability problems. Especially in the moving foil test, we explicitly show that the scheme can handle a density range of 9 orders of magnitude. In the 6^{th} and 7^{th} tests, we show that the scheme developed in this thesis is able to handle a wide range of density variation and extreme cases. Through the 6^{th} test, we show that the scheme can cover the physics in the regime where the scale length is comparable to the ion inertial

length $\lambda_i \sim L$. Through the 7^{th} test, we demonstrate that in regimes where scale length is comparable to electron inertial length, the scheme can also cover most of the physics, since the results agree with published two-fluid and Particle In Cell results. Finally, we do a test with DG-PERSEUS on 3D Cartesian coordinates, to show that the scheme captures instability, ablation, jet formation and foil explosions physics very well.

For all the examples, if not otherwise stated, we use a 2^{nd} order DG scheme.

For the tests done in section 4.2 - 4.3, we non-dimensionalize (2.30) - (2.36) as follows: $\mathbf{U} = U_0\tilde{\mathbf{U}}$, where $\tilde{\mathbf{U}}$ is the set of dimensionless variables and U_0 is the set of dimensional normalization factors. For U_0 we used $n_0 = 6 \times 10^{28}\text{m}^{-3}$, $t_0 = 100$ ns, $L_0 = 1\text{mm}$, $v_0 = 10^4\text{ms}^{-1}$, $B_0 = 580\text{T}$, $E_0 = 5.8 \times 10^6\text{V/m}$, $J_0 = 4.6 \times 10^{11}\text{A/m}^2$, $T_0 = 28\text{eV}$, $\eta_0 = 1.3 \times 10^{-5}\Omega \cdot \text{m}$, and the ion mass number is taken to be 27 for Aluminum. Table 4.1 listed all the reference dimensional numbers. These numbers are chosen consistent to typical Z-pinch plasma regimes.

4.1 Accuracy Test

In this numerical accuracy analysis, we test with L^2 error with the following definition:

$$||\mathbf{x}||_2 = \sqrt{x_1^2 + x_2^2 + x_3^2 + \cdots + x_n^2} \tag{4.1}$$

We know that if a scheme is n^{th} order accurate, the numerical error of this scheme should be related with spatial discretization size Δx through:

$$\epsilon(\Delta x) = C\Delta x^n.$$

Table 4.1: Characteristic Scales used to Non-dimensionalize Parameters

Variable Name	Notation	U_0
Number Density	n_0	$6.0 \times 10^{22}\text{cm}^{-3}$
Time	t_0	100ns
Length	L_0	1.0mm
Velocity	v_0	$1.0 \times 10^{4}\text{m/s}$
Magnetic field	B_0	580T
Electric field	E_0	$5.8 \times 10^{6}\text{V/m}$
Current Density	J_0	$4.6 \times 10^{11}\text{A/m}^2$
Temperature	T_0	14eV
Resistivity	η_0	$1.3 \times 10^{-5}\Omega \cdot \text{m}$

Thus the numerical error with half the cell size should be:

$$\epsilon\left(\frac{\Delta x}{2}\right) = C\left(\frac{\Delta x}{2}\right)^n.$$

With this said, we can get the order of accuracy n through:

$$n = \log_2\left(\epsilon(\Delta x)/\epsilon\left(\frac{\Delta x}{2}\right)\right).$$

Here, we set up the test with the following initial conditions to test the order of accuracy of the numerical scheme on a 2 dimensional region:

$$\rho_0 = 1 + 0.5\sin(x + y),$$

$$v_{x0} = \cos(x + y),$$

$$v_{y0} = \cos(x + y),$$

$$\mathcal{E}_{n0} = 1/(\gamma - 1) + \frac{1}{2}\rho_0\left(v_{x0}^2 + v_{y0}^2\right).$$

To ensure that the equations have analytical solution, we have to add source terms to the equations, and the equations we are actually solving are:

$$\partial_t \rho + \nabla \cdot (\rho \mathbf{u}) = \cos(2x + 2y - 4t) - \cos(x + y - 2t) - 2\sin(x + y - 2t) \quad (4.2)$$

$$\begin{aligned} \partial_t(\rho \mathbf{u}) + \nabla \cdot [\rho \mathbf{u}\mathbf{u} + \mathbf{I}P] = {} & [\cos(2x + 2y - 4t)(\cos(2x + 2y - 4t) - 1.) \\ & - 0.5\sin(2x + 2y - 4t)\sin(x + y - 2t) \\ & + 2\sin(x + y - 2t) - 2\sin(2x + 2y - 4t)]\hat{\mathbf{u}} \end{aligned} \quad (4.3)$$

$$\begin{aligned} \partial_t(\mathcal{E}_n) + \nabla \cdot [\mathbf{u}(\mathcal{E}_n + P)] = {} & \cos^4(x + y - 2t) - 6\cos^2(x + y - 2t)\sin(x + y - 2t) \\ & - 3\cos^2(x + y - 2t)\sin^2(x + y - 2t) - 2\sin(x + y - 2t)\frac{\gamma}{\gamma - 1.} \\ & - \cos^3(x + y - 2t) + 4\cos(x + y - 2t)\sin(x + y - 2t)(1 + 0.5\sin(x + y - 2t)), \end{aligned} \quad (4.4)$$

and the analytical solutions are:

$$\rho = 1 + 0.5\sin(x + y - 2t),$$

$$v_x = \cos(x + y - 2t),$$

$$v_y = \cos(x + y - 2t),$$

$$\mathcal{E}_n = \frac{1}{\gamma - 1} + \frac{1}{2}\rho\left(v_x^2 + v_y^2\right).$$

We apply periodic boundary conditions. In this set up, the wave propagation is along the diagonal of the region. The density profile along a quarter of the diagonal is as shown in Figure 4.1, where we observe that, by increasing the resolution from 50×50 all the way to 400×400, the numerical result is closer and closer to the analytical result.

By calculating the error according to Equation (4.1) through all the cells in the computational region, we obtain the numerical error as shown in table 4.2. By observing the order of accuracy calculated according to these numerical

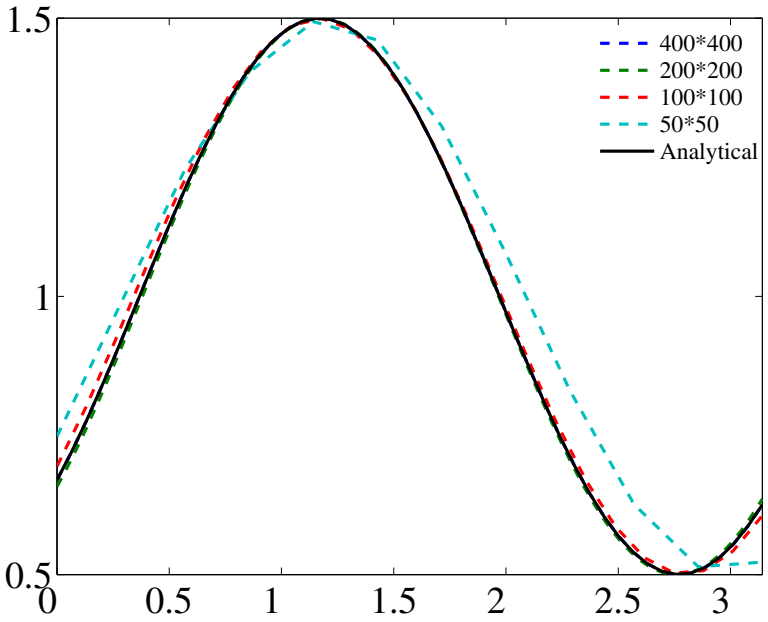

Figure 4.1: Diagram showing the density profile along the first quarter of the diagonal; 4 tests are presented, with a resolution of 50×50, 100×100, 200×200, 400×400, respectively. Analytical solution is also provided for comparison. It is clearly shown in this diagram that, when we increase the resolution, the numerical solution is approaching the analytical solution.

errors, we know that this scheme is 2^{nd} order accuracy for the variables tested, and ρ, m_x, E_n are listed out.

Table 4.2: Accuracy Test Result

N	Error(ρ)	Order n	Error(m_x)	Order n	Error(E_n)	Order n
50	1.90E-3	-	5.80E-3	-	1.03E-2	-
100	4.65E-4	2.03	1.40E-3	2.05	2.40E-3	2.10
200	1.16E-4	2.00	3.39E-4	2.04	5.73E-4	2.07
400	2.91E-5	2.00	8.36E-5	2.02	1.39E-4	2.04

4.2 The Brio-Wu shock-tube problem

We first test the code against the benchmark problem originally used by Brio and Wu [7]. We employ the initial condition:

$$(\rho, u_x, u_y, u_z, P, P_e, B_x, B_y, B_z) = \begin{cases} \text{for } x < 0 \\ (1.000\rho_0, 0, 0, 0, 1.0\rho_0, 0.50\rho_0, 0.75\sqrt{\rho_0}, +\sqrt{\rho_0}, 0) \\ \text{for } x > 0 \\ (0.125\rho_0, 0, 0, 0, 0.1\rho_0, 0.05\rho_0, 0.75\sqrt{\rho_0}, -\sqrt{\rho_0}, 0) \end{cases}$$

$$(E_x, E_y, E_z, J_x, J_y, J_z) = (0, 0, 0, 0, 0, 0)$$

When $\rho_0 = 10^{-2}$, with a resolution of 400, we have $\frac{\lambda_e}{\Delta x} = 4.34 \times 10^{-2}$ and $\frac{\lambda_i}{\Delta x} = 1.9$, so the ion inertial length λ_i is resolved by the spatial grid Δx, and the Hall term in (2.44) becomes important; The Hall term allows for decoupling of the ion motion from the electron flow into which the magnetic field is frozen. The Hall effect introduces dispersive whistler wave, which becomes the fastest wave in the system producing oscillations seen in Figure 4.2(a), which is distinctly different from MHD [7], but similar to the two-fluid results [38].

For comparison, the MHD result is presented in Figure 4.2(b), the model used is ideal-MHD model.

When the density is increased to $\rho_0 = 1$, with a resolution of 400, we have $\frac{\lambda_e}{\Delta x} = 4.34 \times 10^{-3}$ and $\frac{\lambda_i}{\Delta x} = 0.19$, consequently λ_i is not resolved by the spatial grid size, thus the result, as shown in Figure 4.2(c), becomes close to the MHD result in [7].

In this test, the flow is always outgoing on the boundaries, and we use an outflow boundary condition. However, when $\rho_0 = 10^{-2}$, oscillating waves are

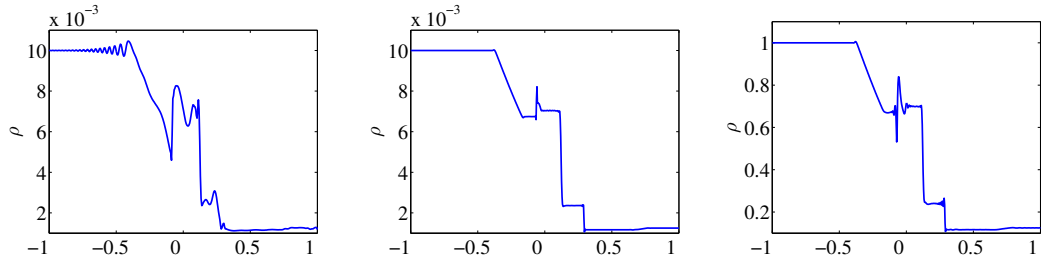

(a) XMHD, $\rho_0 = 10^{-2}$, 400 cells (b) MHD, $\rho_0 = 10^{-2}$, 400 cells (c) XMHD, $\rho_0 = 1$, 400 cells

Figure 4.2: Brio Wu shock tube test. Density as a function of position, captured at $t = 2.1 \times 10^{-2}$

introduced, causing the flow direction on the boundary to oscillate. We have to use inflow boundary condition when the flow becomes inward.

4.3 Pressure Balance Test

Here we provide a test [52] which more directly shows that DG is much less diffusive than FV and which shows the necessity of the PP-limiter. We set up the test with the following initial condition to guarantee the initial pressure balance:

$$(\rho, P, P_e, u_x, u_y, u_z, B_x, B_y, B_z) = \begin{cases} (1.0, 100., 50, 0, 0, 0, 0, 10.0000, 0) \text{ for } x < 0 \\ (0.1, 10.0, 5., 0, 0, 0, 0, 16.7332, 0) \text{ for } x > 0 \end{cases}$$

$$(E_x, E_y, E_z, J_x, J_y, J_z) = (0, 0, 0, 0, 0, 0)$$

We did this test with ideal-MHD model. The resistivity is set to zero leaving numerical diffusion as the only potential cause for plasma or magnetic flux to diffuse. In this way one can directly tell how diffusive a scheme is by observing the amount of diffusion. The result is as shown in Figure 4.3, from which we can see that, with the same resolution (200), FV result is far more diffusive than DG. We find that FV needs a 8 times the resolution (1600) to be comparable to DG

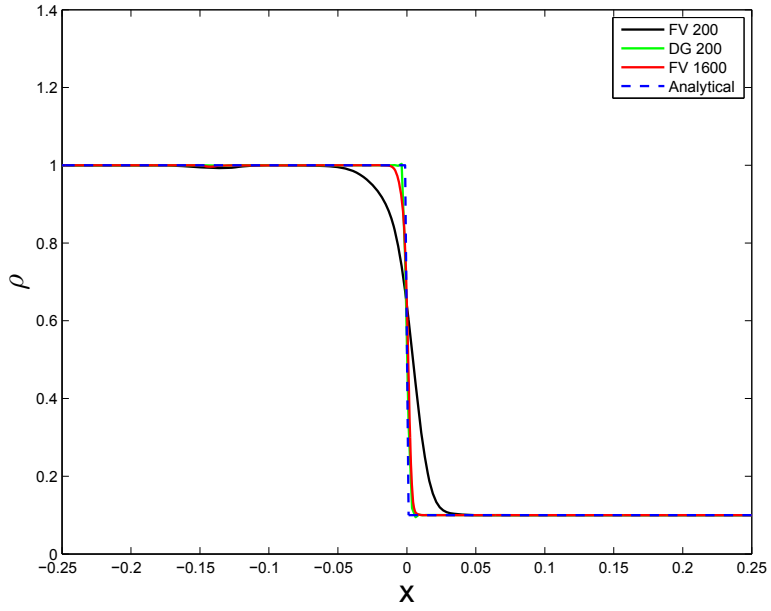

Figure 4.3: DG vs FV result for Pressure Balance Test. FV with 200 cells is most diffusive shown in black, DG with 200 cells shown in green agrees with analytical results best; FV with 1600 cells shown in red is closer to analytical results but still not as good as DG results with 200 cells.

with a resolution of 200, and FV takes 200 times longer than DG for producing comparable results.

4.4 Moving Planar Foil

For problems with solutions containing δ-singularities most numerical methods perform poorly, since many numerical techniques approach these problems by modifying them with smooth kernels, and the singularities are severely smeared as a result. However, DG methods are based on the weak formulation, hence can solve such problems without modifications, leading to very accurate results [61]. Here, we demonstrate this advantage by doing a moving planar alu-

minum foil problem with XMHD model. The planar foil, being sufficiently thin compared to our system, can be viewed as a δ-function. A magnetic field $\mathbf{B}$ is applied parallel to the foil, producing a current $\mathbf{J}$ flowing perpendicular to the direction of the applied magnetic field. As a result, a $\mathbf{J} \times \mathbf{B}$ force is produced perpendicular to the surface of the foil, accelerating it to the right. In the simulation, the foil is 6.25μm (one grid cell) thick, 10mm wide, magnitude of $\mathbf{B}$ is $116T$. Figure 4.4(a) - 4.4(c) are line plots captured at t = 34ns by viewing in the direction parallel to the foil. Figure 4.4(a) shows the DG result with 1600 mesh points. The δ structure is well preserved, the widest part spans only about 3 cells. Taking into account the thermal expansion, the widening because of numerical diffusion is small. However, for FV, also with 1600 mesh points, shown in Figure 4.4(b), the foil expands much more. When FV mesh is refined to 11200 cells, the result 4.4(c) is much closer to DG 4.4(a).

With exactly the same set up, we can test the magnetic diffusion respectively with DG scheme and FV scheme. Because of the presence of the planar foil, magnetic field in the left region should not be able to diffuse through to the right region. As elaborated in Figure 4.5, the magnetic field in the left part of FV result with a 1600 resolution diffuses to the right part a lot, while in DG result with 1600 resolution, the magnetic field retains in the left apart, with very few diffusion. This example clearly shows that finite volume will produce results that violate physics, due to strong numerical diffusion.

It is worth pointing out that this problem spans 9 orders of magnitude in density range, which covers near-vacuum($10^{19}\mathrm{m}^{-3}$) to solid density($10^{28}\mathrm{m}^{-3}$). That means, although a PP-limiter does not smooth oscillations near discontinuities as much as a TVD limiter does, it does preserve the stability of a system

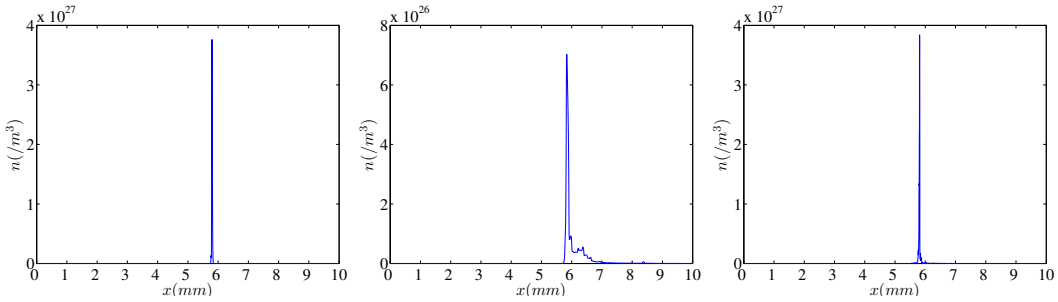

(a) DG with 1600 mesh points (b) FV with 1600 mesh points (c) FV with 11200 mesh points

Figure 4.4: number density n as a function of position x captured at t = 34 ns; Initial foil position: x = 5mm.

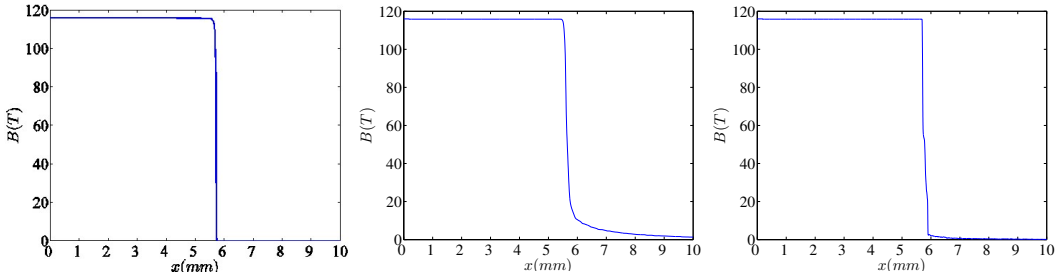

(a) DG with 1600 mesh points (b) FV with 1600 mesh points (c) FV with 11200 mesh points

Figure 4.5: Magnetic field B as a function of position x captured at t = 34 ns.

with a large dynamic range and steep density gradients. If the PP-limiter is turned off the results are very unstable and the test fails in a few time steps.

4.5 Kelvin-Helmholtz Instability

Since discontinuous Galerkin has a low numerical diffusion and a high resolution, it is also better than FV for problems where phenomena are strongly damped by numerical diffusivity. These problems include instability/turbulence problems. Here we provide Kelvin-Helmholtz instability test as

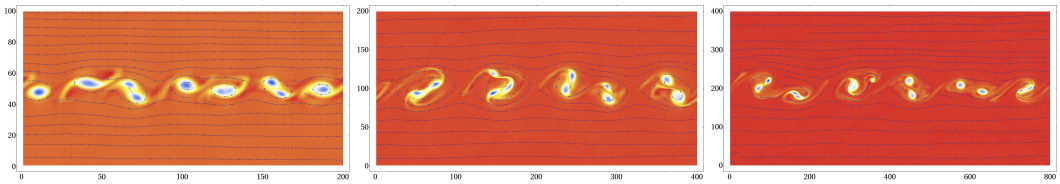

(a) DG, 200×100, T = 211s (b) DG, 400×200, T = 1124s (c) DG, 800×400, T = 6229s

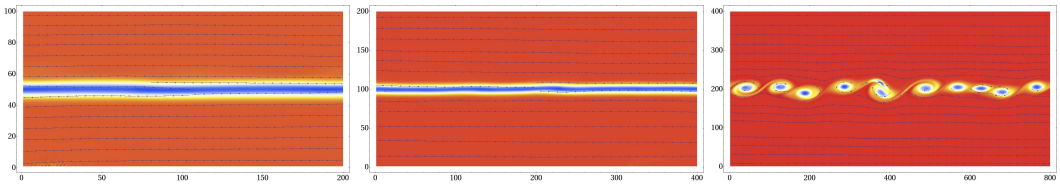

(d) FV, 200×100, T = 46.8s (e) FV, 400×200, T = 247s (f) FV, 800×400, T = 1365s

Figure 4.6: Comparison between DG and FV results for Kelvin-Helmholtz instability. The figures are color plots of vorticity $\nabla \times \mathbf{v}$. It is clear from the figures that the instability growth rate is severely suppressed by the numerical diffusion of FV method, one needs to refine the resolution to as high as 800×400 to get to a result closer to DG with a resolution of 200×100. The time taken for reaching these same results is: FV, 1365s, DG, 211s, which means that DG is 6 times faster than FV for achieving comparable results for this particular case.

an example to show that numerical diffusion can severely suppress the numerical instability growth rate. As shown in Figure 4.6, FV needs 4 times higher resolution in each dimension to approach the DG results. To achieve comparable results, FV takes 6 times longer than DG. With lower resolution, the instability hardly starts to develop until very late in time.

To provide a more analytical view on how fast the instability develops in the DG scheme, and how fast the solution converges, we set up a simulation for 2D Hydrodynamic KH instability following the theory derived in [26], a simplified version for our particular set up is presented as follows.

We assume the system is linear, and quantities have the linearized form:

$$Q = \tilde{Q} + \delta Q \exp(i(\mathbf{k} \cdot \mathbf{r} - \omega t)), \tag{4.5}$$

where $Q \in \{\rho, v_x, v_y, \mathcal{E}_n\}$. We pick $\delta\rho = 10^{-3}\tilde{\rho}$ and $k_\parallel = 6\pi$, here and in the following text, '$\parallel$' means in the direction of the unperturbed flows, '$\perp$' means perpendicular to the direction of unperturbed flow. Then we need to perturb the system following the perturbations governed by the values below:

$$
\begin{aligned}
\delta P &= c_s^2 \delta\rho \\
k_\perp &= \sqrt{\left(\frac{\omega - k_\parallel \tilde{v}_\parallel}{c_s}\right)^2 - k_\parallel^2} \\
\omega_i &= k_\parallel \tilde{v}_\parallel \sqrt{\frac{\sqrt{(M^2+1)^2 + M^2(2-M^2)} - M^2 - 1}{M^2}} \\
\omega &= i\omega_i \\
\delta \mathbf{v} &= \frac{\mathbf{k}\delta P}{\tilde{\rho}(\omega - k_\parallel \tilde{v}_\parallel)}
\end{aligned}
$$

Here, M is the Mach number $M \equiv \frac{\tilde{v}_\parallel}{c_s}$. ω_i is the growth rate of the KH instability. For the unperturbed values, we pick: $\tilde{\rho} = 1$, $\tilde{P} = 1$, $\tilde{v}_\parallel = 0.5\tanh(150y)$, $y \in [-0.25, 0.25]$, $c_s = \sqrt{\gamma P/\rho} = 1.18$. Plug these into (4.5) by setting $t = 0$, we have the initial conditions to set up the simulation. We use periodic boundary condition for left and right boundary, and an outflow boundary condition for upper and lower boundary.

By setting up runs following the description above, we can get the numerical linear instability growth curve $\ln(\frac{\|Q\|}{Q_0})$ as a function of t as shown in Figure 4.5. We can see from the figure that the results converge very well with the increase of resolution. The converged result has a slope smaller than the analytical result, this is because the analytical result is derived from a case with a step function as the initial parallel velocity profile, while we started with a hyperbolic tangent velocity profile, which will make the growth rate slightly lower. We did this to make the result less noisy.

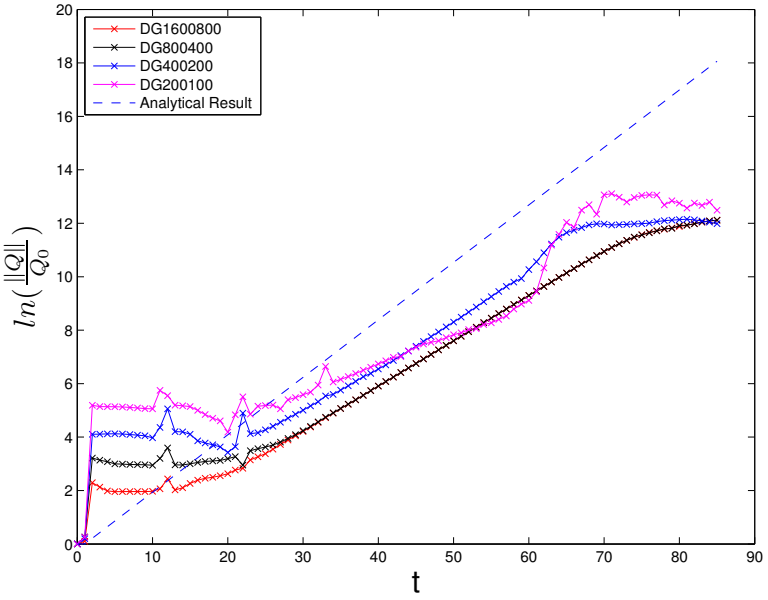

Figure 4.7: Kelvin Helmholtz instability growth

4.6 Some remarks on the comparison between DG and FV

From the tests done in section 4.3 & 4.4, and from some other tests we summarize our observations. The FV tests here are done with an implicit-explicit MUSCL scheme (Monotone Upwind Scheme for Conservation Laws) [20, 58, 34], using a TVD limiter (van Leer limiter). We did not use PP-limiter for the FV scheme because a PP-limiter restrict the Courant number to about 0.2, while with a TVD FV scheme we can use a Courant number up to 0.6, thus PP-limiter increases the CPU time by a factor of three. We decided that it was not worth implementing a PP-limiter for our FV test results, which we will further verify through future work. On the other hand, a TVD DG scheme also requires a Courant number around 0.2, thus there is no additional computational expense for DG to obtain the second order accuracy guaranteed by PP-limiter.

From all problems we have tested DG performs better than FV, as deter-

mined by less time and memory for producing comparable results. However, the quantitative comparison is problem-dependent. For certain kinds of problems, e.g., shock problem and problems with a density profile as a δ function or with a steep gradient, as shown in section 4.3 & 4.4, DG performs much better than FV by using a computation time orders of magnitude less. For other problems, FV usually takes 3–4 times larger resolution to achieve the same result as DG, and takes 2–6 times longer to run. The reason for the better performance is that DG scheme is more compact and stores more localized information, so that it resolves the boundary layers and detailed local structures better, while FV uses a more extended stencil, which makes it easier for local information to diffuse away.

4.7 Two-dimensional tests and comparison of XMHD to MHD

We provide two additional tests that demonstrate the two-dimensional capabilities of the method and further highlight the differences between XMHD and MHD. The first test is a two dimensional shock problem that requires demanding performance on the shock capturing ability of the algorithm and which illustrates how the Hall term can greatly affect the results when compared to MHD. It also shows that the implicit method allow computation of the Hall effect using a much reduced time step than would be required for an explicit computation. The second test is a collisionless reconnection test following the GEM challenge [5] tests. The purpose of this test is to display the method's capabilities in the parameter regime where electron inertia plays a fundamental physical role.

4.7.1 Collisional Bow-Shock Problem

The problem is set up as follows: The domain is $x \in (-20.0\text{mm}, 13.0\text{mm})$, $y \in (-20.0\text{mm}, 20.0\text{mm})$; 400 cells are used in y direction, while 330 cells for the x direction. The whole domain is initialized with uniform number density as $n = 10^{23}\text{m}^{-3}$, temperature as 14eV, magnetic field as $B_y = 16.4\text{T}$. We use Aluminum as the plasma material, and use Spitzer resistivity for η. Inflow from left boundary with velocity as $u_x = 200\text{km-s}^{-1}$, sonic Mach number as $M_s = 17$, Alfvénic Mach number as $M_a = 2.24$ and magnetosonic Mach number as $M_f = 2.22$. In the region, we put a block of size 0.6mm×0.6mm with its center 14mm from left boundary, 20mm from lower boundary. The block is constructed as a boundary condition on the block's 4 edges ensuring that the mass flux normal to every edge is zero.

The test is done with MHD model and XMHD models separately, and the results at $t = 140ns$ are shown in Figure 4.8(a) and 4.8(b). With the inflow being super-magnetosonic, a magnetosonic shock (fast shock in this case) will appear, as shown in both figures. However, the shapes are considerably different using these two models. The differences are due to the Hall term in XMHD in the region behind the block. In this low-density region the Hall term suppresses current flow thereby affecting the magnetic field. While in MHD, without a vacuum resistivity, there is no such suppression, allowing the current to grow unphysically large. The unphysical current forms a current sheet that is sufficient to support an X-point behind the block, then the plasma and magnetic flux piling up in front of the block gets through by reconnection. This mechanism for flux transport is mitigated by the Hall term in XMHD under the conditions we have chosen for this test, thereby producing very different results. If density

is increased so that the Hall term is rendered ineffective, we find that XMHD results approach MHD results.

We point out that the PP-limiter is essential for this test. When it is turned off a low pressure dip immediately forms behind the block and evolves to eventually become negative. We also point out that, we use same time step for XMHD simulation with a MHD simulation, which saves considerable computational cost as compared to a fully explicit algorithm.

We also point out that, by applying the relaxation scheme, we are able to use MHD simulation time step to do the XMHD simulations, which saves considerable computational cost as compared to a fully explicit algorithm.

It is important to note that the MHD results can be made to agree much better with XMHD by employing a suitable vacuum resistivity to suppress the current in low density region. However, one does not know *a priori* the spatial form or value needed for the vacuum resistivity to achieve physical results. One would first have to perform the more realistic XMHD simulation to which the MHD simulation could be adjusted to fit the results. This reveals one advantage of XMHD over MHD since one can use the realistic Spitzer resistivity model without any artificial modifications, which allows the self-consistent and physical transition from high density to low density regions. Moreover, one should not conclude that including a vacuum resistivity into the MHD equations is sufficient to recover all of the effects of the Hall term. Suppression of low-density currents is only one effect of the Hall term. The Hall modification of the electric field cannot be modeled by a vacuum resistivity and can generate anode-cathode asymmetries [21], enhanced magnetic reconnection [5], and can lead to instabilities not present in MHD [37] or instabilities modified by the Hall

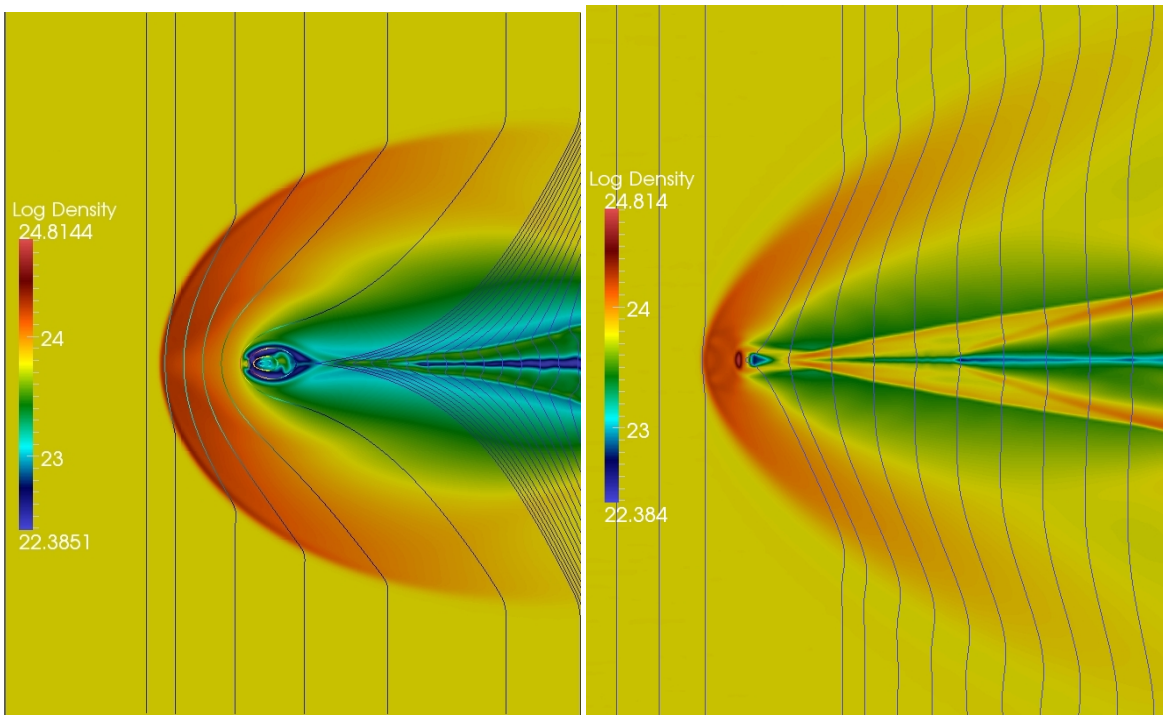

(a) Magnetic field lines with a background color plot log(n) with MHD

(b) Magnetic field lines with a background color plot log(n) with XMHD

Figure 4.8: Bow shock simulation, captured at t = 140ns

term [29, 30].

4.7.2 Magnetic Reconnection

For magnetic reconnection to occur, a mechanism is required to break the flux-frozen-in condition, which could be resistivity, electron inertia, or anisotropic electron pressure [5]. In this section, we demonstrate the XMHD algorithm developed in this paper can solve the equations on the scale where electron inertia is important and yield results that are consistent with the full two-fluid model.

We initialize the problem using the GEM reconnection challenge initial

conditions [5] modified appropriately for the XMHD model. The domain is $x \in (-12.8\lambda_i, 12.8\lambda_i)$, $y \in (-6.4\lambda_i, 6.4\lambda_i)$, speed of light is $c = 55v_A$, mass ratio is $m_i/m_e = 25$. The Harris sheet equilibrium is given by:

$$n(y) = \text{sech}^2\left(\frac{y - L_y/4}{w_0}\right) + \text{sech}^2\left(\frac{y + L_y/4}{w_0}\right) + 0.2$$
$$B_x(y) = \tanh\left(\frac{y + L_y/4}{w_0}\right) - \tanh\left(\frac{y - L_y/4}{w_0}\right) - 1$$

We perturb the equilibrium as follows:

$$\delta B_x = -0.1\frac{4\pi}{L_y}\cos\left(\frac{2\pi x}{L_x}\right)\sin\left(\frac{4\pi y}{L_y}\right)$$
$$\delta B_y = 0.1\frac{2\pi}{L_x}\sin\left(\frac{2\pi x}{L_x}\right)\left[1 - \cos\left(\frac{4\pi y}{L_y}\right)\right]$$

where $L_x = 25.6\lambda_i$, $L_y = 12.8\lambda_i$, and the initial current sheet thickness $w_0 = 0.5\lambda_i$. The simulation runs to $25\Omega_i^{-1}$ with a resolution of 800×400 cells. The legend values are based on the magnetospheric context for which we have chosen B=50nT, n=$1 \times 10^6 \text{m}^{-3}$, L_0=6×10^5m, $v_A = 1.1 \times 10^6 \text{ms}^{-1}$. The time step and cell size are $\omega_{pe}\Delta t = 0.2$ and $\lambda_e/\Delta x = 6.1$.

The results with XMHD model is as shown in Figure 4.9. In figure 4.9 we have added in some numerical diffusion in the form of a slope limiter [27] to smooth the oscillations and limit the thinness of the current sheet. Although we are able to obtain stable results by doing this, the scheme with the slope limiter is no longer second order accurate. Even with slope limiting there is remarkable detail visible in the flows inside and the shocks outside the separatrix. This result compares very favorably with those of [24], who used a finite volume two-fluid code with a Riemann solver. The time history of the reconnection rate shown in 5.1 is consistent with [24] and with the results of [48] who used a particle-in-cell method.

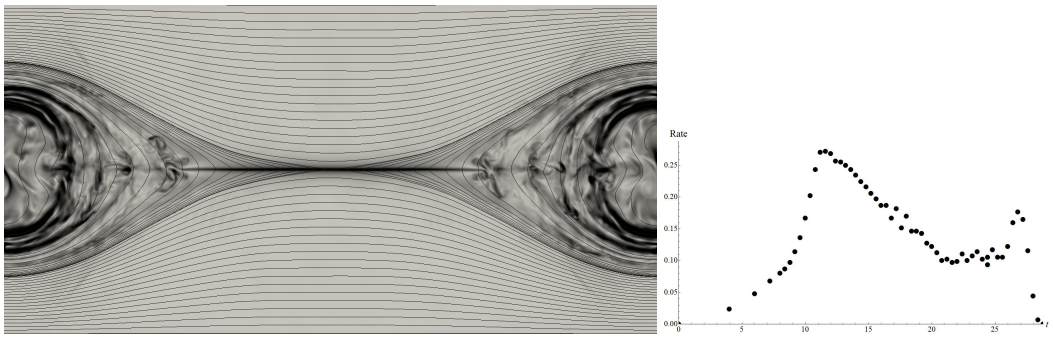

(a) Plot of | **J** | and B-field lines with a resolution of 1000×500 at t=25 Ω_i^{-1}

(b) Plot of the reconnection rate E_z(x − point)/$v_A B_0$ versus time in units of Ω_i^{-1}

Figure 4.9: GEM challenge problem

We tested the global divergence of the magnetic field for this problem as computed from the second order finite difference of adjacent cell mean values normalized to the average magnitude of the magnetic field divided by the cell length. This measure of the global divergence is $\Gamma = \frac{1}{2}[B_{x0}(i+1,j) - B_{x0}(i-1,j) + B_{y0}(i,j+1) - B_{y0}(i,j-1)]/|B|$. We compared the results with the local structure preserving constraint applied to the same simulation without structure preserving. We find the range of values of Γ without structure preserving is $-0.033 < \Gamma < 0.033$ and with structure preserving is $-0.002 < \Gamma < 0.002$. Furthermore we observe that the run without structure preserving began to diverge significantly from the run with structure preserving around $t = 10\Omega_i^{-1}$ and was completely different at $t = 25\Omega_i^{-1}$ and therefore in complete disagreement with the results of [24] who used a divergence cleaning method to preserve $\nabla \cdot \mathbf{B} = 0$.

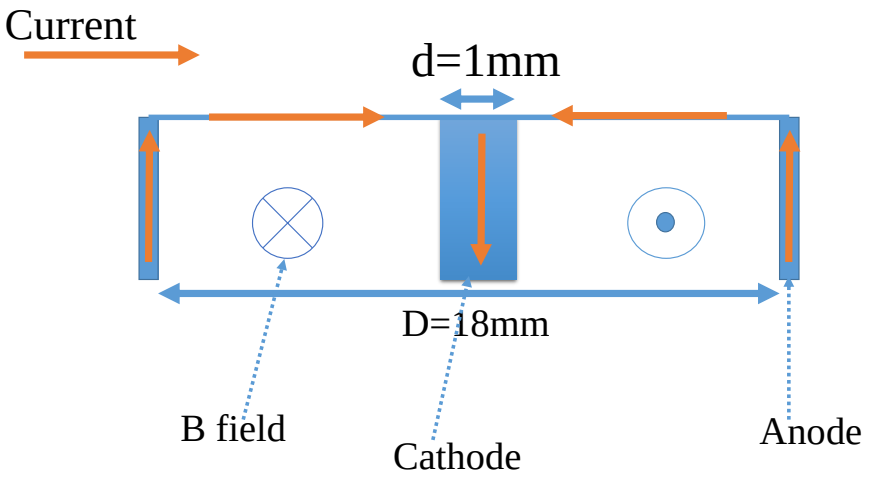

Figure 4.10: Setup of Radial foil problem. Radius of the radial foil is 9mm, diameter of the central post is 1mm.

4.8 The Study of Radial Foils with 3D DG-PERSEUS

For the testing of DG-PERSEUS code in 3D Cartesian coordinates, we choose the radial foil problem, since for this problem, the 2D result can significantly differ from a 3D result because of the configuration. The setup of the problem is as depicted in figure 4.10. So we have Cathode as a post, and a radial foil connecting Anode and cathode. Current flows radially towards the center. The scale of the setup is also as shown in the picture. The resolution used here is 80^3.

The physical processes occurring in the problem are as follows:

1. First, a pre-cursor jet appears, the reason for this is, $\mathbf{J}$ is proportional to $\frac{1}{r}$, thus, strongest towards the center, then Ohm's heating $\eta\mathbf{J}^2$ is strongest near the center, as the result, more plasma is ablated near the center than

outsides. The ablation forms a bubble, changing the current flow path, resulting in a $\mathbf{J} \times \mathbf{B}$ force perpendicular to the bubble surface pointing upwards and center-wards. At the same time, the ∇P force is pushing the plasma towards the center too. Plasma gathering along the central line starts to form this precursor jet. This process is depicted in 4.11(a).

2. The bubble continues to grow up, and another central column jet which carries the return current back to the cathode starts to develop and thicken. Shown in 4.11(b).
3. The central jet continues to pinch down and thicken, and becomes denser and stronger. The bubble continues to grow, and the upper part of the bubble starts to burst and disconnect from the lower part. Shown in 4.11(c).
4. A kink instability starts to emerge in the central jet column, which is difficult to detect in 4.11(d).
5. The kink instability in the central jet column starts to grow and develop, and becomes pronounced after a certain amount of time. Shown in 4.11(e).
6. The bubbles expand rapidly, leaving only the very lower part attached to the foil and the large-amplitude kink mode, as shown in 4.11(f).

This simulation result shows that the algorithm developed in this thesis can be used for a 3D modeling on Cartesian coordinates. With these simulations, we can also see that the method very well handles ablation physics, jet formation, foil explosions, kink instabilities, etc., with a modest number of cells.

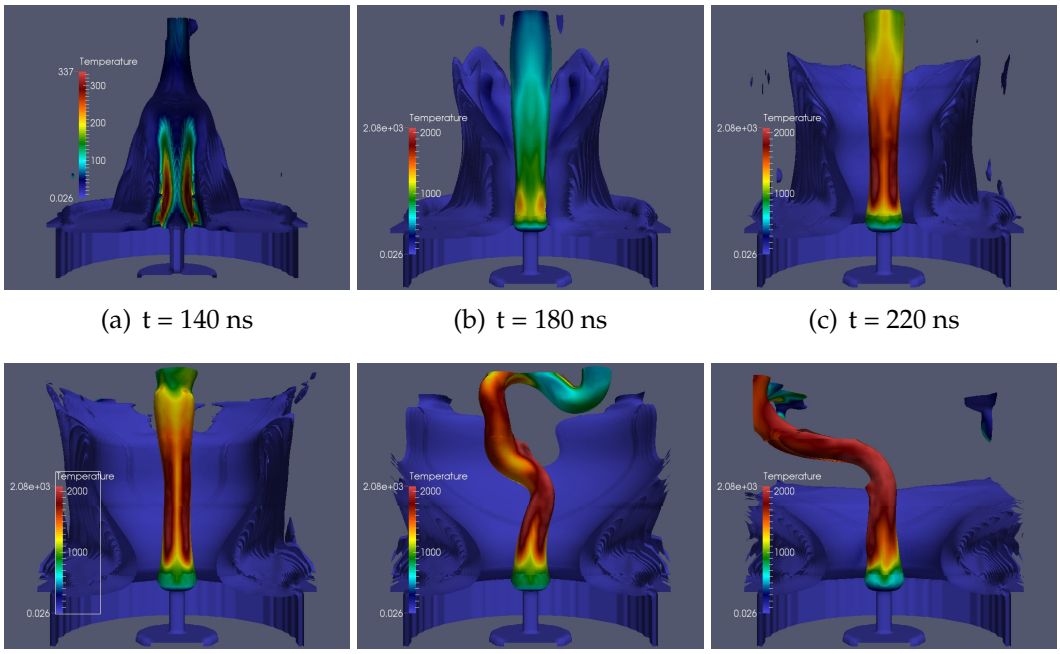

(a) t = 140 ns (b) t = 180 ns (c) t = 220 ns

(d) t = 260 ns (e) t = 300 ns (f) t = 340 ns

Figure 4.11: The development of radial foil physics. First the ablation of the foil starts to form a precursor jet, then the ablated foils form a bubble, the return current forms another central column jet inside the bubble. As the bubble grows larger and larger, the central column carrying the return current grows thicker and thicker. Kink instability gradually develops in the central jet column. When the bubble grows sufficiently large, the upper part will get detached from the lower region.

4.9 Summary of Numerical Tests

In this chapter, we have shown that the positivity-preserving semi-implicit DG scheme developed in this thesis has the following improvements over the previous XMHD or two-fluid model solvers:

1. This scheme maintains a 2^{nd} order accuracy at smooth extrema, while a scheme with a TVD limiter will degrade to 1^{st} order accuracy.

2. This scheme handles a large density span, and sharp transitions from a

dense plasma state to near vacuum.

3. Solves the XMHD equations on MHD time scales, by using the relaxation system formulation for describing the XMHD model. Thus, one can avoid the time step constraint imposed by the under-resolved stiff source terms to step over electron plasma and cyclotron frequencies, which are often under-resolved in the characteristic regime.

4. The DG scheme is much less diffusive than a finite volume scheme, so that DG can achieve comparable accuracy with FV with much less computational cost. In particular, we demonstrated here that DG is exceptionally good at solving problems with δ-function discontinuities, step-type contact discontinuities and instabilities, and takes orders of magnitude less computational time than FV for achieving comparable results.

5. We also demonstrate through the numerical tests that this scheme is able to stably simulate a wide range of density variation and extreme cases in many plasma regimes:

   (a) where the scale length is much larger than ion inertial length. In this regime, the XMHD results converge to the MHD results.

   (b) where the scale length is comparable to the ion inertial length. In this regime, the Hall effect introduces wave modes that are properly captured by our scheme.

   (c) where the scale length is comparable to electron inertial length. In this regime we obtain results that are consistent with previous PIC and two-fluid computations.

6. Magnetic field is represented in an exactly locally divergence-free form of DG, which improves the accuracy and stability of MHD simulations,

and eliminates the need for an expensive divergence cleaning scheme. Although the magnetic field is only constrained to be locally divergence free, we demonstrated through the magnetic reconnection test that the global divergence of the magnetic field is greatly reduced. The fact that the results agree with previous published two-fluid and PIC results show that this divergence-free scheme is totally satisfactory for the purpose of gaining physics insights.

CHAPTER 5

A NOVEL CONFIGURATION FOR DRIVING MAGNETIC RECONNECTION

5.1 Introduction

Magnetic reconnection is believed to be responsible for many spectacular events in the solar system. For example, solar flares, coronal mass ejections in the solar system are believed to be powered by magnetic reconnection. Also, in the Earth's magnetosphere, magnetic reconnection also occurs both on the dayside magnetopause and in the magnetotail. Reconnection occurs in highly conducting plasmas and is responsible for the conversion of magnetic energy into kinetic energy, thermal energy and particle acceleration.

Here we explain the basic idea behind magnetic reconnection. When two magnetic domains with opposite magnetic field directions are spliced into one another, an X-shape field line forms. At the very thin boundary layer of these two regions, the ideal MHD frozen-in assumption fails, and the field lines will tend to "break" and "reconnect" at the center point O of the X shape, as shown in figure 5.1, thus changing their connectivity with respect to the sources, in order to achieve an energetically favorable state.

In two dimensions, the most common model used to discuss reconnection is the separator reconnection, where the four magnetic domains separated by two lines exchange magnetic fluxes. In this chapter, we also use this model to discuss the basic theory behind magnetic reconnection. The experiment is also in a configuration that resembles this model.

The magnetic reconnection rate in steady-state, where there are equal incoming and outgoing mass, momentum and energy fluxes through the diffusion region, is normally used to characterize reconnection. Now we provide a method to numerically measure magnetic reconnection rate. Referring to Figure 5.1, we define the magnetic flux through the integration loop Γ as ϕ_B, from Faraday's law, we know:

$$\frac{d\phi_B}{dt} = -c \oint_\Gamma \mathbf{E} \cdot \mathbf{dl}, \tag{5.1}$$

$d\phi_B/dt$ denotes the rate of magnetic flux flowing away from the X-point, which can exactly represent the magnetic reconnection rate. We evaluate the RHS of equation (5.1). We know that the integral along the upper and lower edge of Γ adds to be zero with the assumption that no variation appears on the z-direction, and we can make the right edge to be at infinity, leaving the integral over the left edge to be the only contributing term. Assume the length of that edge is h, and again, there's no variation on the z-direction, equation (5.1) becomes:

$$\frac{1}{h}\frac{d\phi_B}{dt} = \frac{\partial}{\partial t}\int B_y dx = -cE_z, \tag{5.2}$$

thus, the out-of-plane electric field E_z at the center point O can be used to indicate the magnetic reconnection rate. From (2.44), we have:

$$\mathbf{E} = -\mathbf{u}\times\mathbf{B} + \eta\mathbf{J} + \frac{\lambda_i}{L_0 n}\mathbf{J}\times\mathbf{B} - \frac{\lambda_i}{L_0 n}\nabla P_e + \frac{\lambda_e^2}{L_0^2 n}\left(\partial_t\mathbf{J} + \nabla\cdot\left(\mathbf{uJ} + \mathbf{Ju} - \frac{\lambda_i}{L_0 n}\mathbf{JJ}\right)\right) \tag{5.3}$$

The right hand side of equation (5.3) includes (from left to right) the ideal electric field, the resistive term, the Hall term, the electron pressure term, and the electron inertia. In the ideal MHD limit, all the terms except $-\mathbf{u}\times\mathbf{B}$ become zero. Since the flows are stagnated at magnetic null denoted by point O as in figure 5.1, which renders $\mathbf{u} = 0$, the term $-\mathbf{u}\times\mathbf{B}$ also vanishes. As a result, in the ideal MHD limit, E_z is essentially zero at point O, so that reconnection rate is zero and no reconnection is happening. Another way to look at this is the magnetic

field lines are frozen into infinitely conducting (ideal) plasmas. Since charged plasma particles are confined to circular orbits around magnetic field lines, the infinitely conducting plasmas cannot diffuse across field lines and mix. As a result, two distinct field lines have to remain separate, since they cannot penetrate into the other side. However, if we include the resistive term, the perfect frozen-in condition is violated, and then the magnetic field line can slip relative to the plasmas allowing the lines to reconnect. We call this type of reconnection collisional reconnection.

The concept of magnetic reconnection was first proposed by Giovanelli [19] in an effort to understand fast energy release in solar flares. Giovanelli's idea is further developed by Sweet [55] and analyzed by Parker [43] into a neutral line merging model, which is now a fundamental model of magnetic reconnection, called "Sweet-Parker" model. Since the mechanism and treatment of collisional reconnection was introduced by Sweet and Parker, collisional reconnection is often referred to as "Sweet-Parker" reconnection. The configuration of Sweet-Parker model is as shown in Figure 5.2. Following the Sweet-Parker analysis [55, 43], the reconnection rate can be obtained by taking into account the mass conservation and energy conservation during the diffusion process. The reconnection rate is:

$$E_z \sim \left(\frac{v_{A,in}B_{in}}{c}\right)\frac{\delta}{L} \sim \sqrt{\frac{\eta}{v_{A,in}L}}\left(\frac{v_{A,in}B_{in}}{c}\right) \tag{5.4}$$

However, as pointed out later by Parker [44], the Sweet-Parker reconnection rate is on the order of square root of electrical resistivity, which is too slow to explain the short time scales of energy release during solar flares. The scaling of the reconnection region aspect ratio δ/L with the square root of the resistivity shows that it must be very small if Sweet-Parker scaling is correct. This

is because Sweet-Parker assumes that the plasma must go through the reconnection region. Upon observing this, Petschek [45] introduced the slow shock configuration into the reconnection, as shown in 5.3, so that plasma can gain energy and get accelerated by getting across the shock without going through the diffusion region. The flow, therefore, does not suffer from the bottle neck imposed by extremely small δ/L. Petschek's analysis [45] showed that a fast reconnection rate would scale with the log of the resistivity, which is much faster than the Sweet-Parker rate at high Lundquist numbers. However, it was found in high resolution simulations that the X-point geometry cannot be realized in high Lundquist number ($S > 10^4, S \sim 1/\eta$) regime, and in the low Lundquist number regime ($S < 10^3$), Petschek reconnection rate and Sweet-Parker reconnection rate are more or less on the same order. Also, the Petschek structure has never been seen in experiments. In this chapter, we introduce a novel configuration for experimentally generated magnetic reconnection whose outflow is bounded by slow shocks, which are very Petschek like. Interestingly, our results also reveal an extended current sheet that is very Sweet-Parker like.

To explain the high reconnection rate, many suggest that terms other than the resistive term in (5.3) need to be included to make E_z larger, thus facilitating reconnection. The Hall term can potentially be important in explaining the fast reconnection rate as discussed in [5]. We will evaluate the importance of Hall term in our magnetic reconnection configuration in this chapter.

In this chapter, a magnetic reconnection regime with compressible flow and shocks bounding the outflows is described. A parallel pair of fine wires much more massive than those used in imploding Z-pinches is driven by the COBRA 1 MA, 200 ns pulser. During the rise of current, magnetic and thermal

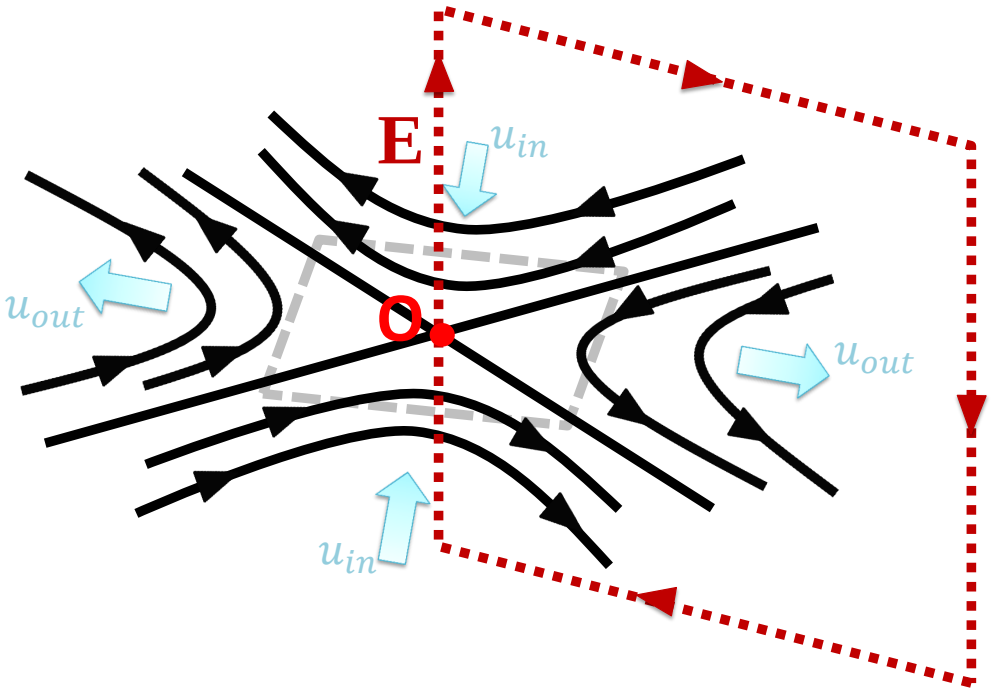

Figure 5.1: Measurement of Reconnection Rate. *O* denotes the center point of the X shape, In/out flow are shown in blue, the magnetic field lines are shown in black, the diffusion region shown by the grey box, the red dashed box shows the integration loop Γ

energy are stored in and around the two wire plasmas. When voltage reverses, the inverse skin effect results in reversed current in the outer layer of the two wires, resulting in a $\mathbf{J} \times \mathbf{B}$ force driving the outer layer away from the wire cores. These ablated plasmas carry reversed currents, and when the reversed currents from two wires meet each other, the X-point between the wires evolves into an extended reversed current sheet, so that a nearly 2D separator magnetic reconnection topology is formed. The expanded plasma diffuses from the inflow region to the outflow region, and forms the outflows which are bounded by slow

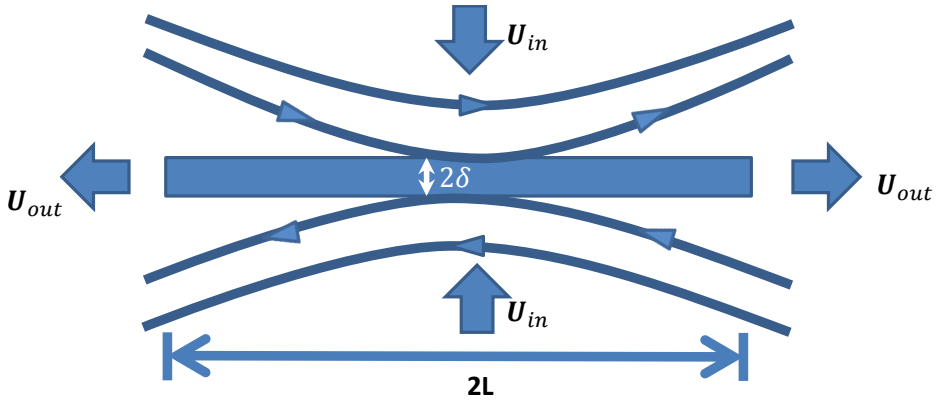

Figure 5.2: Sweet-Parker model of Reconnection. Diffusion region denoted by a rectangular box with thickness as 2δ and length as $2L$, u_{in} denotes the inflow speed, u_{out} denotes the outflow speed, B_{in} denotes the magnetic field in the inflow region.

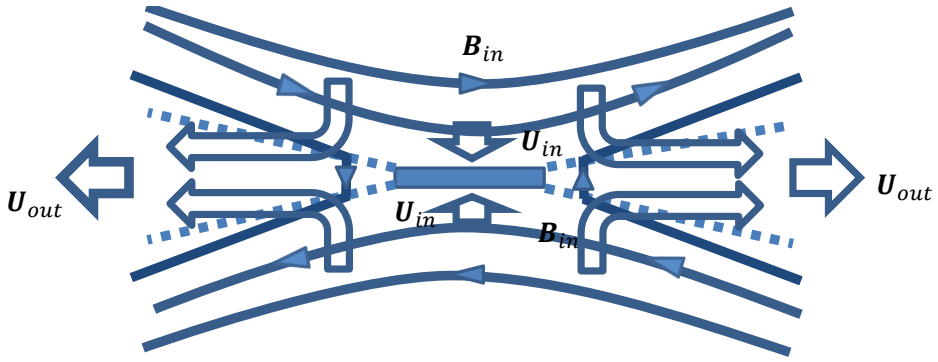

Figure 5.3: Petschek model of Reconnection. Diffusion region denoted by a rectangular box, u_{in} denotes the inflow speed, u_{out} denotes the outflow speed, B_{in} denotes the magnetic field in the inflow region. The flow can get accelerated as it go through the slow shock denoted by the dashed blue line.

shocks. The outflow is accelerated by both $\mathbf{J} \times \mathbf{B}$ force and the pressure gradient force $-\nabla P$, and can achieve a speed that is supersonic and super-Alfvénic, which will be verified later in this chapter. The magnetized shock structures produced around targets placed in the flows can help to quantify the flow speed. This use of electric field reversal to trigger and drive reconnection in the laboratory may have relevance to solar and astrophysical situations.

5.2 Inverse Skin Effect

When an applied pulsed power voltage is first applied on a plasma column, because of the skin effect, electric field has a finite penetration rate into the plasma column. In a time τ (on the order of $\mu\sigma a^2/15$ for a cylindrical conductor with a being the radius, μ and σ being the permeability and conductivity of the conductor respectively [23]), with the field penetrated into the plasma column, the current also diffuses into the wire.

When the driving voltage is suddenly reversed, the total current in the plasma column has to correspondingly decay. In this case, it is possible that the current on the surface of the plasma column reduces or even reverses with respect to its value deep inside the column. This effect is named *inverse skin effect* by Haines [23] who first studied it, and provided an analytical solution for a simplified problem. In [32], Jones and Silawatshananai investigated a stabilized Z-pinch carrying a falling current, and observed an expansion of the pinch.

We carry out a 1D slab simulation to understand the basic dynamics of this process. Here is a brief introduction of the setup of the simulation. We employ the dimensionless units as in table 4.1. A plasma column of density 10^{-4} with

width 16 is initialized in the middle of the simulation region. A magnetic field is applied on the left and right boundary, and the values are:

$$B_{left} = \begin{cases} 0.16 \quad \text{for } t < 2.0 \\ 0.3 - 0.07t \quad \text{for } t > 2.0 \end{cases}$$

and

$$B_{right} = -B_{left}.$$

The results are presented in Figures 5.4 and 5.5. Through these simulation results, we can summarize the physical process of the inverse skin effect as follows:

1. At the initial stage, before the decay of the driving magnetic field, the current column is compressing due to the $\mathbf{J} \times \mathbf{B}$ pinching force.
2. When the driving magnetic field starts to decrease, a reversed electric field is generated outside of the plasma column. This electric field cannot immediately penetrate into the column and can only drive a reversed current on the plasma surface with respect to its value deeper inside the plasma column.
3. This reversed current causes a $\mathbf{J} \times \mathbf{B}$ force on the surface of the plasma accelerating the outer layer plasma radially outwards with an increasing velocity.
4. Meanwhile, since the reversed electric field has not yet penetrated into the plasma column, the current in the inner part of the slab is still pinching down. This is especially clear from the v_x profile shown in figure 5.5(b), where we can see that direction of v_x has a reversal between the center of the slab and the edge of the slab. Figure 5.5(c) and 5.5(d) show the time

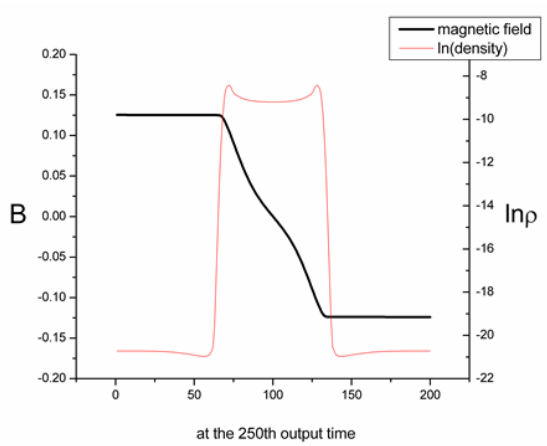

(a) t = 2.5, red line-ln(ρ), black line - magnetic field **B**

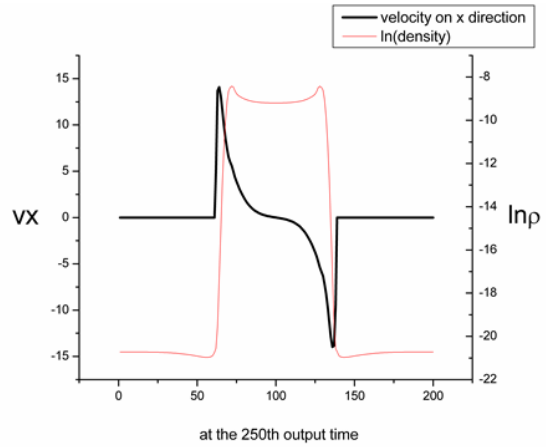

(b) t = 2.5, red line-ln(ρ), black line - v_x

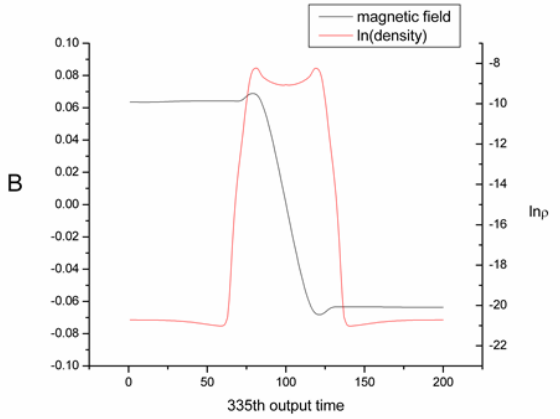

(c) t = 3.3, red line-ln(ρ), black line - magnetic field **B**

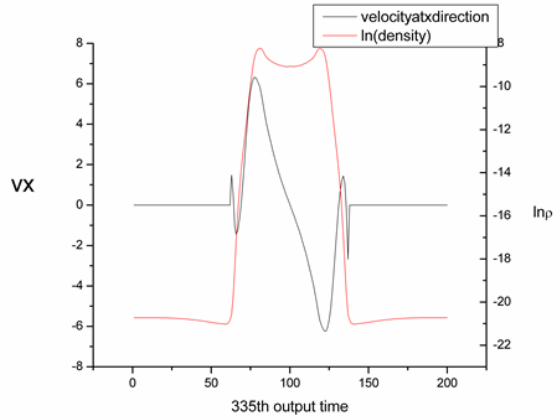

(d) t = 3.3, red line-ln(ρ), black line - v_x

Figure 5.4: Plots showing the inverse skin effect: the decrease of magnetic field on the boundary, which is equivalent to the reversal of driving electric field, drives a reversed current on the surface of the wire, results in the reversal of magnetic force $\mathbf{J} \times \mathbf{B}$ at the edge of plasma, which pushes the plasma outwards; at the same time, the inner part of the plasma still carries current in the original direction, so the inner part is still compressing down. Continue on Figure 5.5.

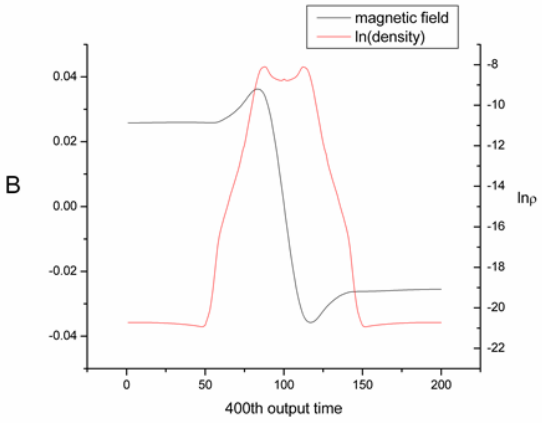

(a) t = 4.0, red line-ln(ρ), black line - magnetic field **B**

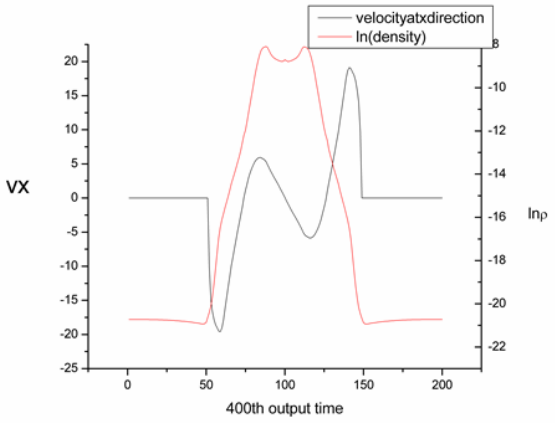

(b) t = 4.0, red line-ln(ρ), black line - v_x

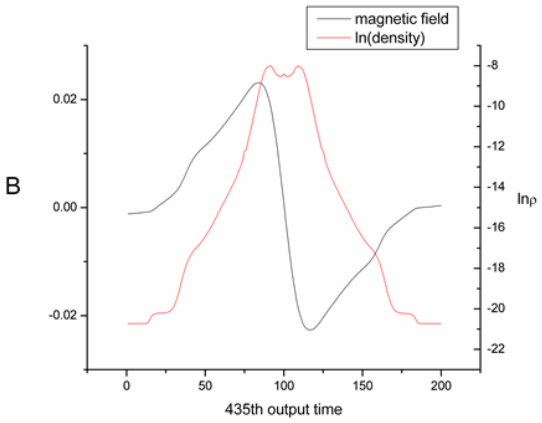

(c) t = 4.3, red line-ln(ρ), black line - magnetic field **B**

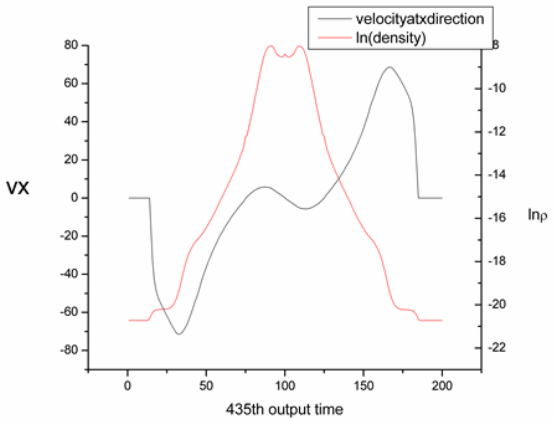

(d) t = 4.3, red line-ln(ρ), black line - v_x

Figure 5.5: Continued from Figure 5.4: Plots showing the inverse skin effect: the decrease of magnetic field on the boundary, which is equivalent to the reversal of driving electric field, drives a reversed current on the surface of the wire, results in the reversal of magnetic force $\mathbf{J} \times \mathbf{B}$ at the edge of plasma, which pushes the plasma outwards; at the same time, the inner part of the plasma still carries current in the original direction, so the inner part is still compressing down.

when magnetic field has been driven down to zero at the boundary. The edges of the plasma slab are moving outwards due to the reversed $\mathbf{J} \times \mathbf{B}$ force, while the inner slab is still compressing.

The rapid expansion caused by inverse skin effect happens only under the condition that the reversal of surface current density in accordance to the change of electric field or magnetic field acts on time scales shorter than the penetration time scale τ.

To summarize, when the driving voltage suddenly reverses, the current on the plasma surface can reverse due to the inverse skin effect. This can lead to a rapid expansion of the outer layers of the pinch, and if sustained, will work its way deeper into the plasma column.

5.3 Background: Experimental Set Up and Selected Experimental Results

Part of this section is borrowed from John, et al. [22] which has been submitted to Physics Review Letters.

In the experiment, on the COBRA 1MA, 200 ns pulser, we load two aluminum wires, 254μ m diameter, 20 mm long, in parallel to each other, 16 mm apart between the COBRA cathode and anode (ground). They connect at the edges of an opening in the anode allowing viewing with XUV imaging in the end-on direction along their axes. The orthogonal, side-on view is used for XUV imaging, laser shadowgraph and interferometry. Figure 5.8 shows a series of

five XUV images in the end-on view, oriented with the wires at top and bottom center of the images. The imaging is sensitive to photons above about 20 eV. In the first frame, at first current peak, no XUV is seen except from the expanded wire plasmas, centered about the original wire positions. In the second, before the final voltage reversal, the X-point magnetic separatrix between the wires is illuminated by plasma that has expanded out from the wires during the time between the two current peaks. The succeeding images show the rapid evolution of the X-point into an extended current sheet radiating strongly in the XUV immediately after voltage reversal. Magnetic probe measurements confirm the reconnection topology and field reversal across this null sheet. The plasma XUV emission brightens sharply at the separatrix surfaces bounding the outflows, indicating shock heating there. At 260 ns, the field is $12T$, 2mm from the sheet centerplane. Figure 5.9 shows a side-on view in 532 nm laser shadowgraph at 260 ns. The sheet is not straight, but the shape is static for > 100 ns, with no evolution indicative of instability. The shadowgraph shows the sheet is $\sim 400\mu$ m thick, with extremely sharp gradients at its edges indicative of a shock structure with supersonic inflow. Laser interferometry gives electron density of $1(+-0.3)\times 10^{17}/\mathrm{cm}^3$ just outside the sheet, with a jump of a factor of 3-6 inside the sheet. This increase is certainly partly due to an increase in the ionization state of the aluminum plasma, estimated at Z=3 outside the sheet from optical spectroscopy. The sheet is thinner than the ion inertial length $c/w_{pi} \sim 1$ mm, so Hall physics should be important in the dynamics of the reconnection layer [5]. If the stored flux around each wire were reconnected through the sheet in 100ns, an upper limit given that the current sheet persists for $> 200ns$, the reconnection electric field would be of order 10 kV/cm in the sheet. The GEM[5] reconnection results show the reconnection field in Hall mediated reconnection

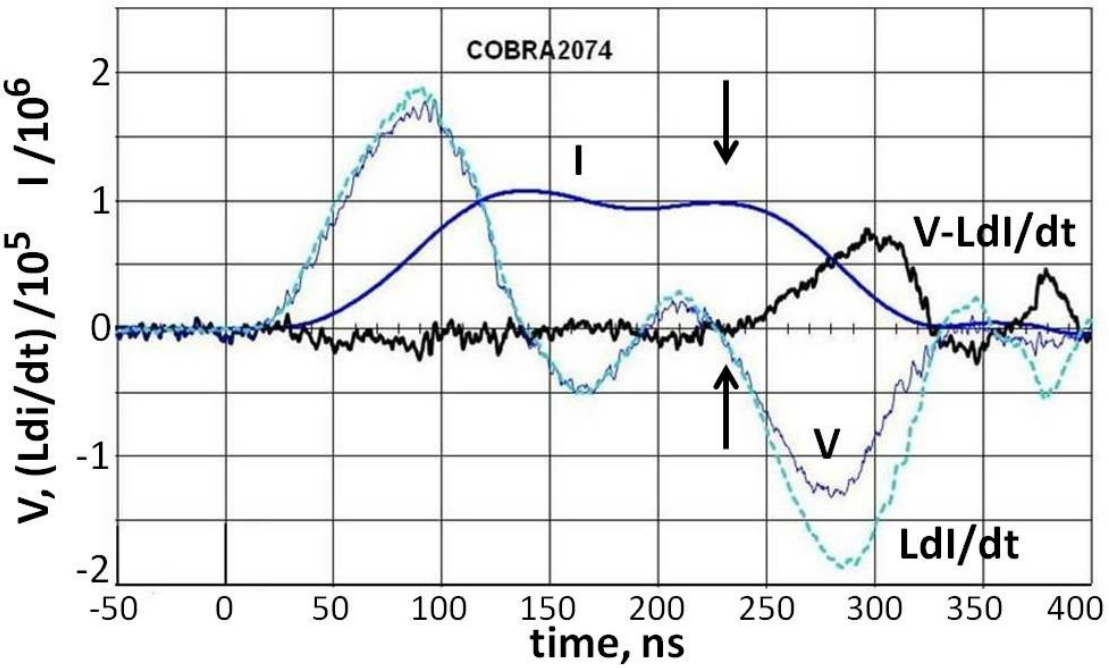

Figure 5.6: Typical COBRA pulse waveforms.

approaches $E \sim 0.24 B_0 V_A/c$. With $B_0 \sim 12$T and $V_A \sim 160$km/s, the field and estimated Alfvén speed respectively in the inflow, this gives $\mathbf{E} \sim 5$kV/cm. Thus this sheet structure appears to be consistent with fast driven reconnection. The plasma temperature in the inflow (from spectroscopy) is no higher than 50 eV, so the plasma beta, $8\pi nkT/B^2$, is much less than unity, of order 0.02. The Lundquist number, based on the current sheet length, is of order $10^2 - 10^3$.

Figure 5.10 shows two end-on XUV images with obstacles, 1mm wide copper strips standing parallel to the wire axes, placed in the outflow regions. The upper one of Figure 5.10 is at 260ns in a typical COBRA pulse (see Figure 5.6), and the lower one of Figure 5.10 is at the same time in a crowbarred pulse (see Figure 5.7). Figure 5.10[a] shows shock structures around the obstacle that radiate strongly in the XUV. The curved bow shock in front of the obstacle is

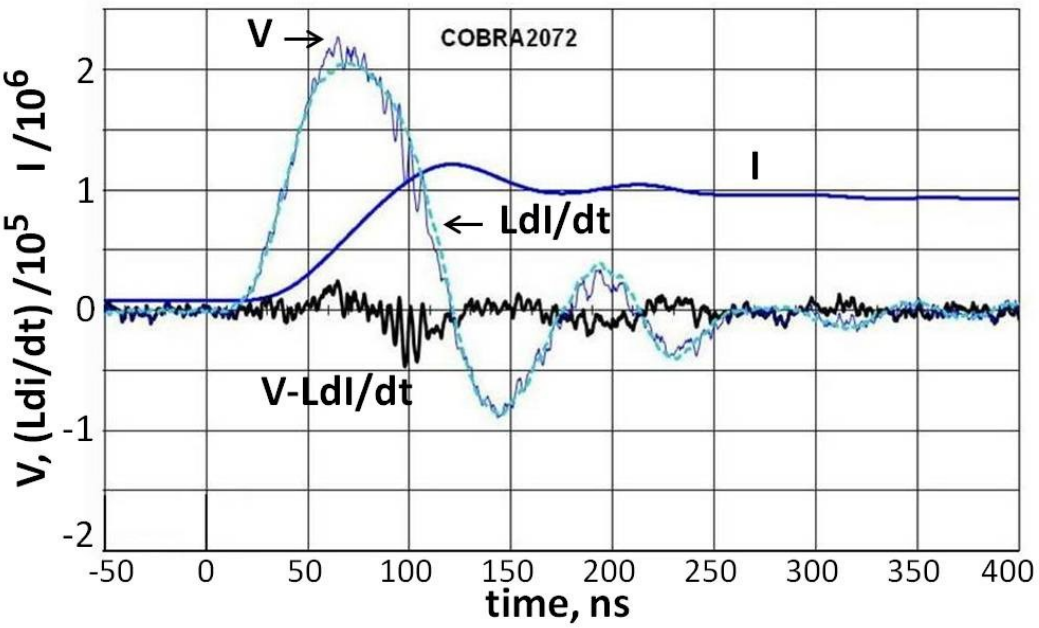

Figure 5.7: Crowbarred COBRA pulse

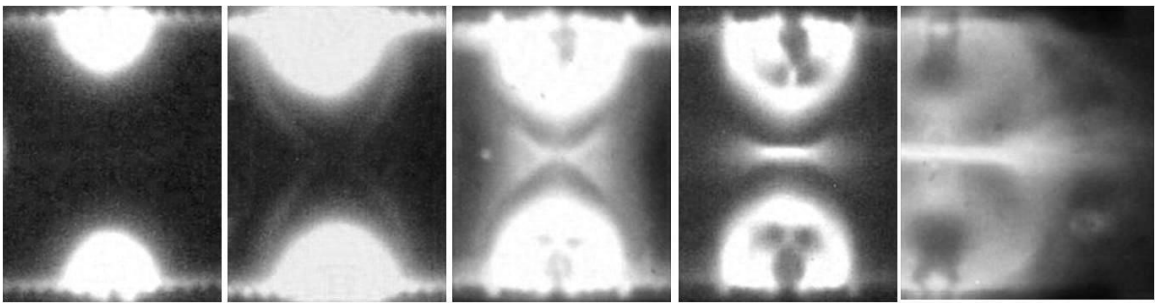

Figure 5.8: Sequence of XUV images, end-on view. Wires 16 mm apart, connected to the toothed anode edges at top and bottom of the images. Times (from left to right) are 130 ns, 160 ns, 240 ns, 260 ns and 360 ns respectively (refer to Figure 5.6 to see where these time slots are in the driving pulse waveform)

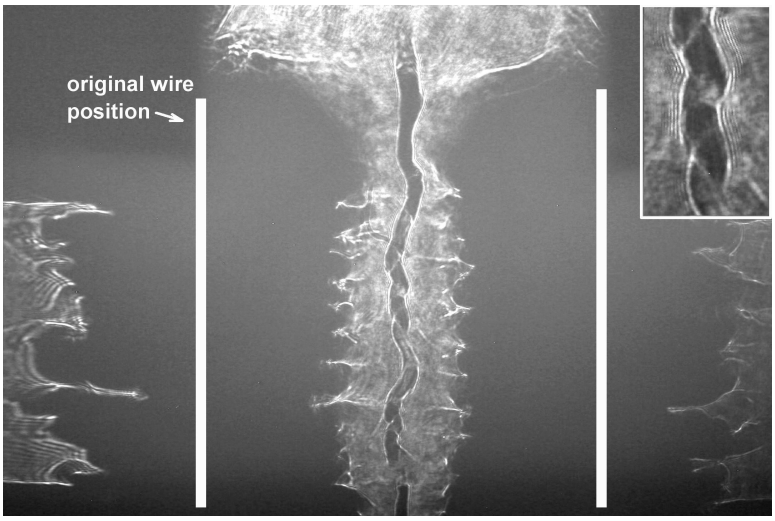

Figure 5.9: Side-on laser shadowgraph at 260 ns. The Upper Right picture is enlargement of central sheet.

evidence of supersonic flow, and the bright tail extending behind the obstacle is seen in simulations only with flows that are also super-Alfvénic, the tails being formed by plasma redirected by the perturbed magnetic field in the bow shock to converge to a line behind the obstacle. The detailed analysis of magnetized shocks with simulation will be delivered in later chapters in this thesis. An estimation of the outflow properties is: the field is $\sim$ 1T, n $\sim 10^{16}/\mathrm{cm}^3$, $V_A \sim$ 40km/s, while the flow velocity based on the elongation rate of the tail shock behind a target is 100 – 150km/s. The bow shock in this regime would be an MHD fast shock. In contrast, Figure 5.10[b] shows no bright shocks around the obstacle; a slightly darker, diverging wake behind the obstacle is noticeable. In this pulse without reversed driving voltage the current sheet still forms, probably driven mostly by thermal pressure of the expanding plasma columns, but the outflows are evidently not super-Alfvénic, nor are they strongly supersonic enough to cause significant heating and XUV brightening at stagnation by the obstacle. Again, in later chapters of this thesis, we will provide explanation of this.

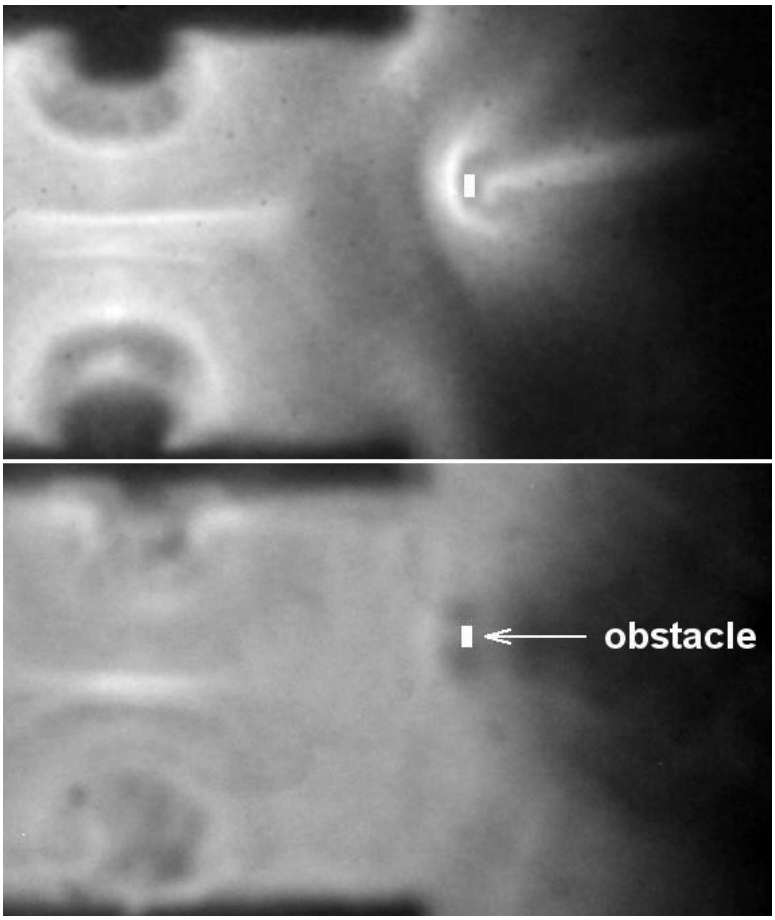

Figure 5.10: (A) Upper figure. XUV images at 380 ns of normal pulse (The driving current pulse follows 5.6); (B) Lower figure. XUV images at 380 ns of a crowbarred pulse (The driving current pulse follows 5.7). The positions of the obstacles are as indicated by a white rectangle.

5.4 Simulation Study

Numerical simulation of two-dimensional compressible magnetic reconnection is carried out in this section with DG-PERSEUS with extended-MHD models. From the simulation results, we will find that the magnetic reconnection presented in this chapter is primarily triggered by a rapid expansion of plasma with reversed current on the leading edge, which is a result of the inverse skin

effect.

5.4.1 Simulation Set-Up

As shown in Figure 5.11, the setup is as follows: We have two circular wires with a diameter of 5.0mm, a number density of $6\times10^{19}/\text{cm}^3$; We drove the region with a circular magnetic field on the boundary, which is equivalent to apply a voltage/ a driving current into the plane. The shape of the driving current is as shown in Figure 5.12. The reason we made the wires wider and less dense in the simulation than those used in the experiment is as follows: it is clear from the XUV image 5.8 that there is a cold core surrounding each wire. These cold cores are estimated to be caused by the radiative cooling. As the radiative cooling model in DG-PERSEUS is not realistic enough, we could not model the cold core accurately. Through trial and error, we found by making the wires wider while keeping their mass, the results are closer to the experiment. Also, since we are more interested in the region where reconnection happens (the diffusion region), and the outflow region, the physics immediately around the wires should not affect much.

5.4.2 Analysis of Simulation Results

Shown in the simulation results Figure 5.13 - 5.18 is the whole process of the two-dimensional compressible magnetic reconnection. Before $t = 150$ ns, the system has gone through a quiescent stage of magnetic energy and internal energy buildup (Figure 5.13). Magnetic energy is building up because the driv-

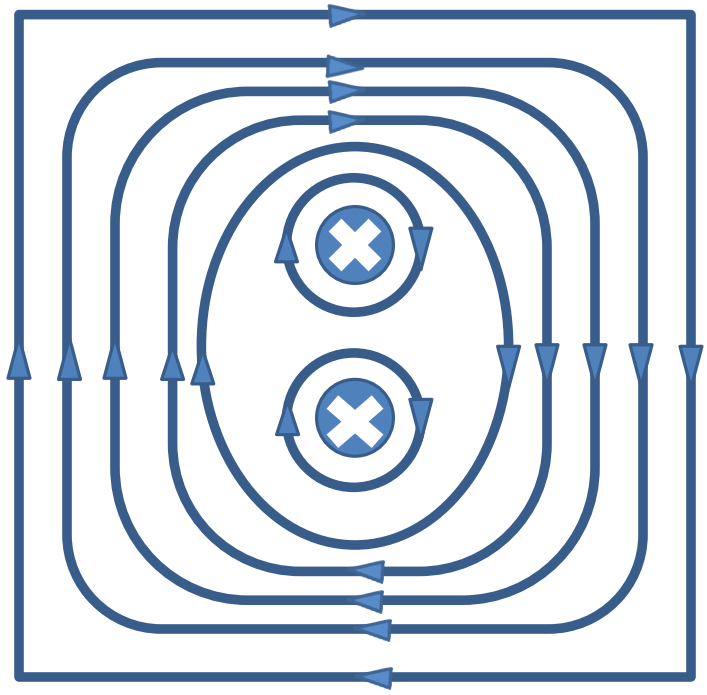

Figure 5.11: The setup of the simulation region. We have two circular wires with a diameter of 5.0mm, a number density of $6 \times 10^{19}/\text{cm}^3$; We drove the region with a circular magnetic field on the boundary, which is equivalent to apply a voltage/ a driving current on the direction into the plane. The shape of the driving current is as shown in Figure 5.12. For achieving the simulation results presented in this chapter, we used a resolution of 160×160.

ing current is increasing, and since the wires are compressing because of the magnetic pinching force, part of the magnetic energy is converted into internal energy. This process is followed by a rapid plasma expansion phase, as shown in Figure 5.14. The reason for the expansion is the inverse skin effect caused by the rapid decay of the driving current after 150ns. As discussed in Section 5.2, the inverse skin effect results in a reversed current on the surface of the

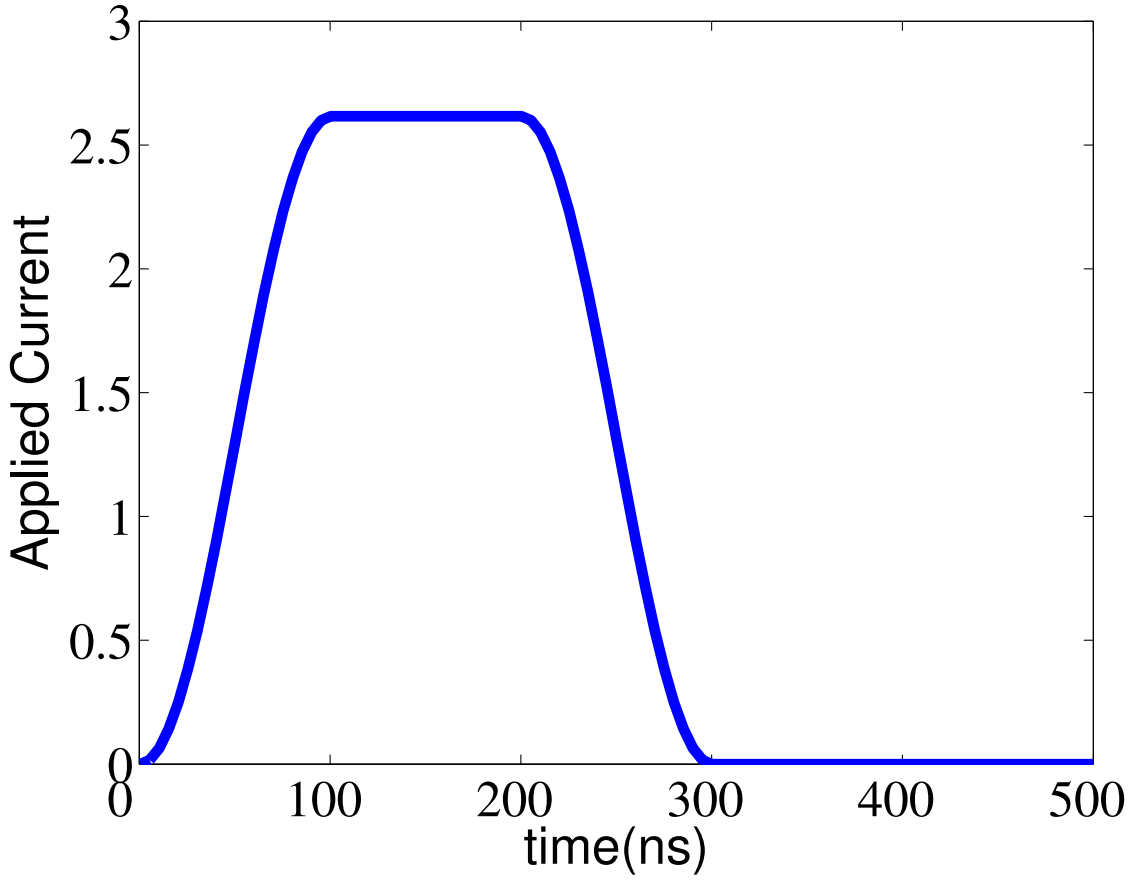

Figure 5.12: The plot of driving current versus time.

plasma column. This reversed current remains on the outer layer of the expanding plasma. It is also clear from Figures 5.13 and 5.14 that the current on the edges of plasma is negative. When the expanding plasmas meet each other, the negative current will form an extended reversed current sheet. This current sheet supports the X configuration, and reconnection is able to happen. Because of the skin effect of plasma, the reversed electric field is not able to penetrate further into the wire, so the inner part of the wire still carries current in the original direction and continues the pinching down phase. The expansion continues (Figure 5.15), converting magnetic and internal energy into kinetic energy. Being driven by both magnetic force $\mathbf{J} \times \mathbf{B}$ and pressure gradient force $-\nabla P$, the

outflow is formed and is accelerated to a speed higher than the local Alfvén speed, as evidenced by Figure 5.19(c). These outflows are bounded by slow shocks, which help accelerate the flows out. The X-point at the center remains until t = 425ns (Figure 5.17). Around this time, the closed flux on the boundary starts to decelerate the flow. When we did exactly the same simulation with FV method, the X-point can only last until t = 350ns when it is replaced by an O-point. This is because FV method is too diffusive, and X-point cannot be well supported, which provides another evidence that DG is better for simulating problems with phenomena needing a high resolution to resolve. At time 500ns, the X-point fully turns into an O-point, and the outflow is opening up.

Now we carry out a force analysis to evaluate between the pressure gradient force $-\nabla P$ and magnetic force $\mathbf{J} \times \mathbf{B}$, which one is more important for the acceleration of the outflow. As depicted in Figure 5.19 is the profiles of $(\mathbf{J} \times \mathbf{B}) \cdot \hat{\mathbf{v}}$ (black), $-\nabla P \cdot \hat{\mathbf{v}}$ (green), $\mid v_A \mid (10^4 \mathrm{m/s})$ (pink) and $\mid \mathbf{v} \mid (10^4 \mathrm{m/s})$ (red) along the X-axis, where $\hat{\mathbf{v}}$ is the unit vector on the direction of $\mathbf{v}$. Clearly, before 300ns, Pressure Gradient ∇P always plays a negative role in accelerating the outflow. This can be observed from Figure 5.15(b), where we see that the density maximum is achieved off center. This is because the X-shape magnetic field is directing the plasma away from heading towards the center. During this process, the $\mathbf{J} \times \mathbf{B}$ is the main force to accelerate the plasma outwards. ∇P gradually comes into play, and accelerates the outflow, but before time $360ns$, $\mathbf{J} \times \mathbf{B}$ has always been more important than ∇P. At 360ns, Alfvénic Mach number M_A reaches around 5, and ∇P is exceeding $\mathbf{J} \times \mathbf{B}$.

The change of energy as a function of time is as shown in Figure 5.20. This directs us to viewing the reconnection process via a global view. Before the

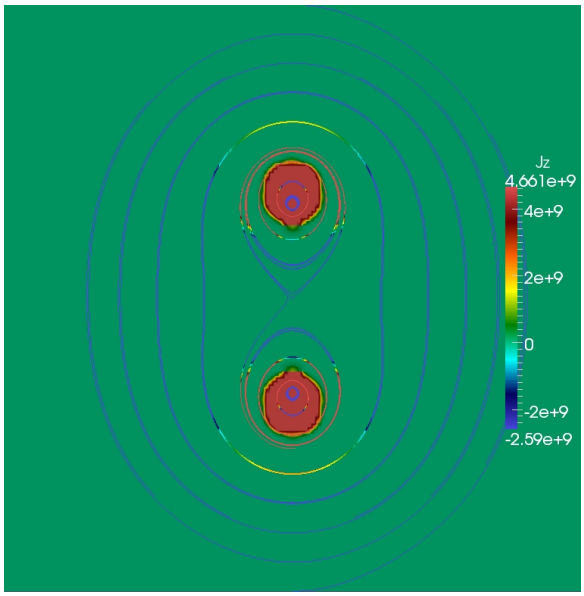

(a) Magnetic field lines with J_z as background contour color

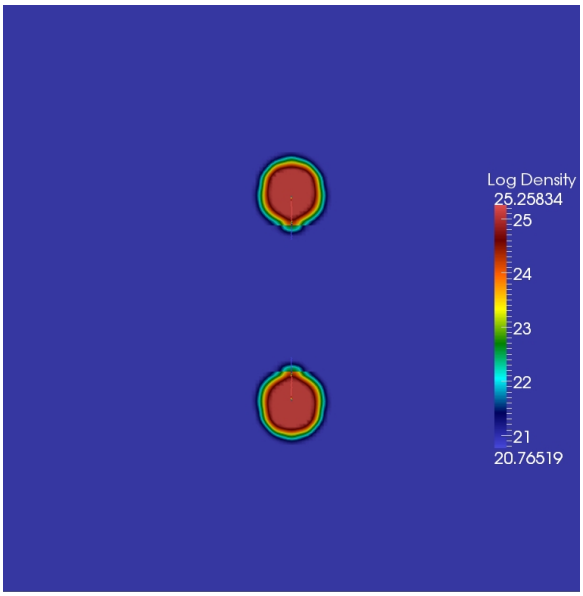

(b) Flow Lines with ρ as background contour color

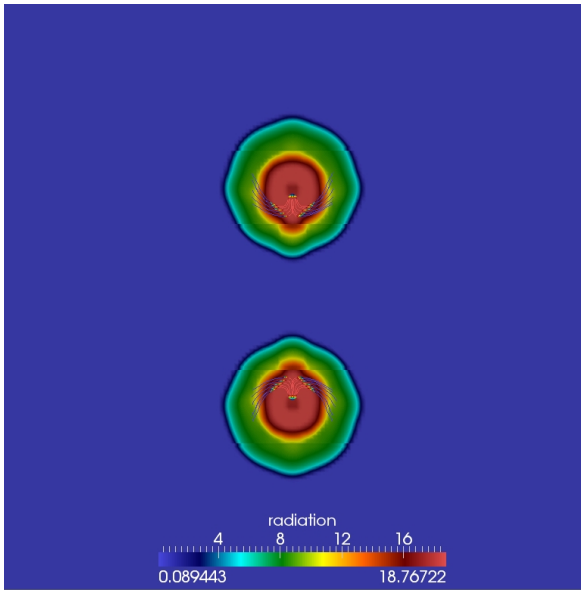

(c) Flow Lines with radiation $\sqrt{T}P^2$ as background contour color

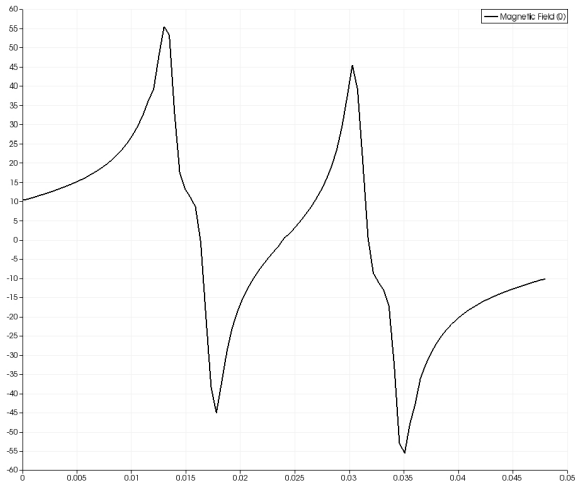

(d) B_x along the y axis

Figure 5.13: t = 150ns, wires are still pinching down at this stage; And because of the attraction of the other wire, current starts to accumulate towards the point closest to the other wire. During the pinching-down process, magnetic energy is converted into internal energy, so that the thermal pressure inside the wire is building up.

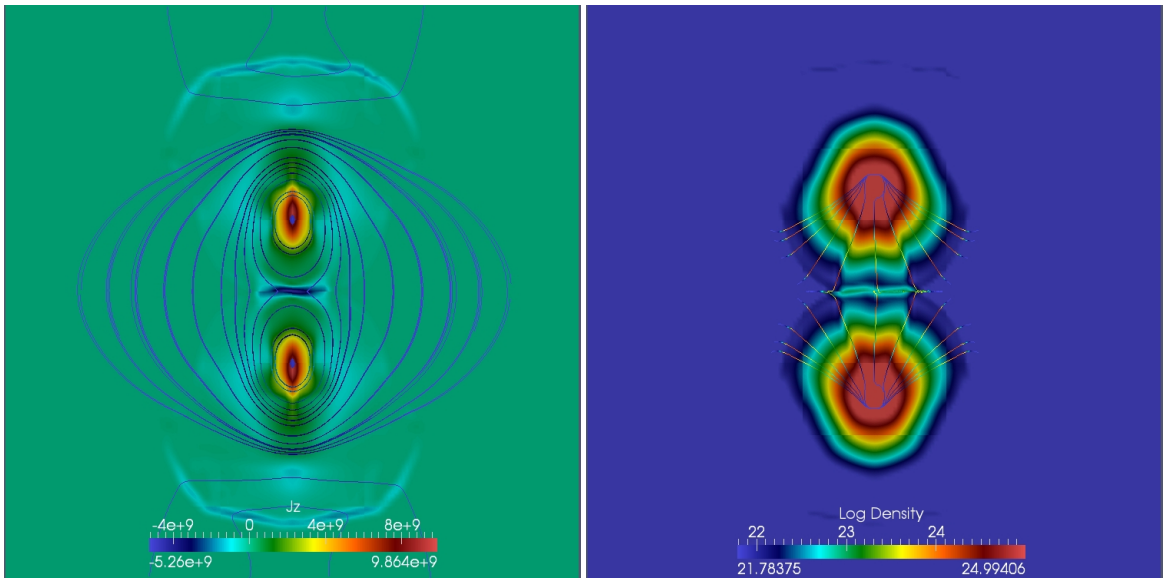

(a) Magnetic field lines with J_z as background contour color

(b) Flow Lines with ρ as background contour color

Figure 5.14: t = 200ns, because of the decrease of the driving magnetic field, a reversed electric field is introduced, which drives a reversed current on the surface of the wires. This results in a $\mathbf{J} \times \mathbf{B}$ force pointing outwards, which causes the expansion of the wire. From the figure, it is clear that the current on the edges of plasma is negative, when the expanding plasmas meet with each other, the negative current on the edge will form an extended reversed current sheet. This current sheet supports the X configuration, and reconnection is able to happen. Because of the skin effect of plasma, the reversed electric field is not able to penetrate further into the wire, so the inner part of the wire still carries the original current, that is why the inner part of the wire is still pinching down at this stage.

reversal of driving voltage at $t = 200ns$, the system goes through the initial accumulation of magnetic and thermal energy in plasma current channels. When the driving voltage reverses, because of inverse skin effect, the plasma column starts expanding, and both internal energy and magnetic energy start to decay. At the same time, kinetic energy starts to increase. In this process, the magnetic energy and internal energy are rapidly converted into kinetic energy.

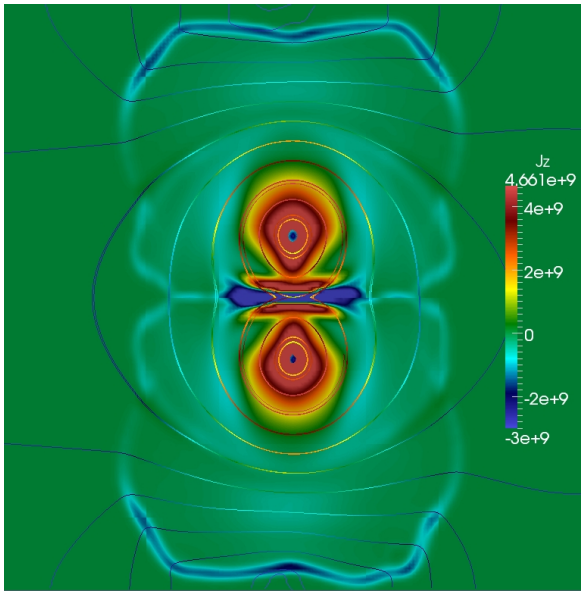

(a) Magnetic field lines with J_z as background contour color

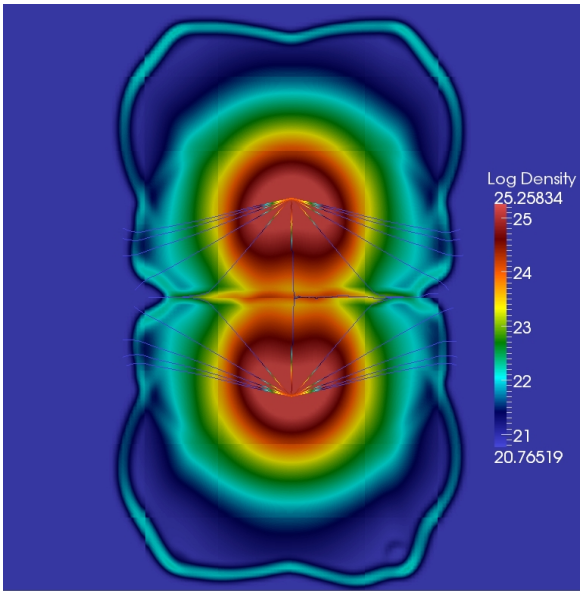

(b) Flow Lines with ρ as background contour color

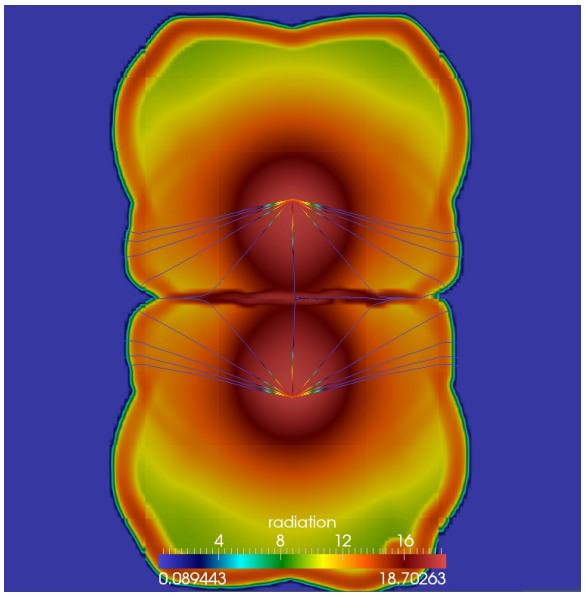

(c) Flow Lines with radiation $\sqrt{T}P^2$ as background contour color

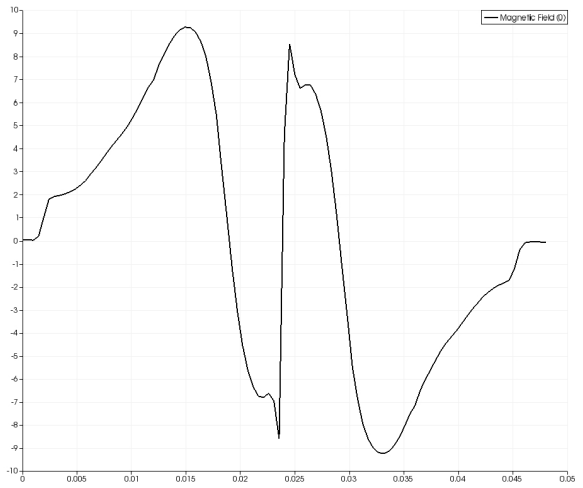

(d) B_x along the y axis

Figure 5.15: t = 300ns, plasmas keep expanding, form an outflow, which is bounded by radiative shocks; The outflow is accelerated out by both pressure gradient force and $\mathbf{J} \times \mathbf{B}$ force. During this period, magnetic energy and internal energy are converted into kinetic energy.

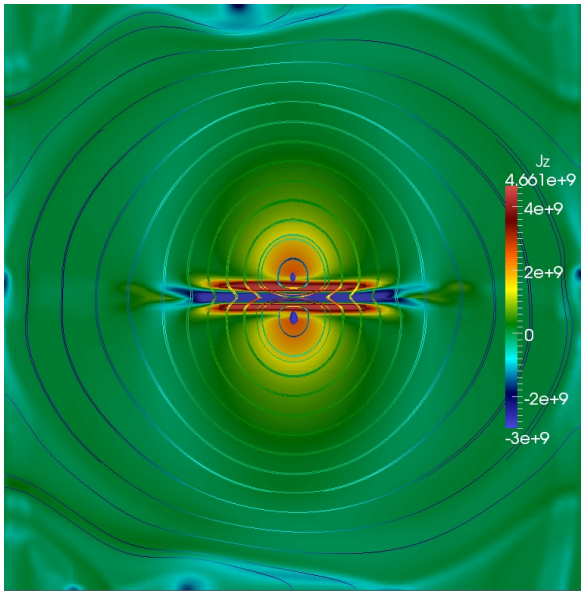

(a) Magnetic field lines with J_z as background contour color

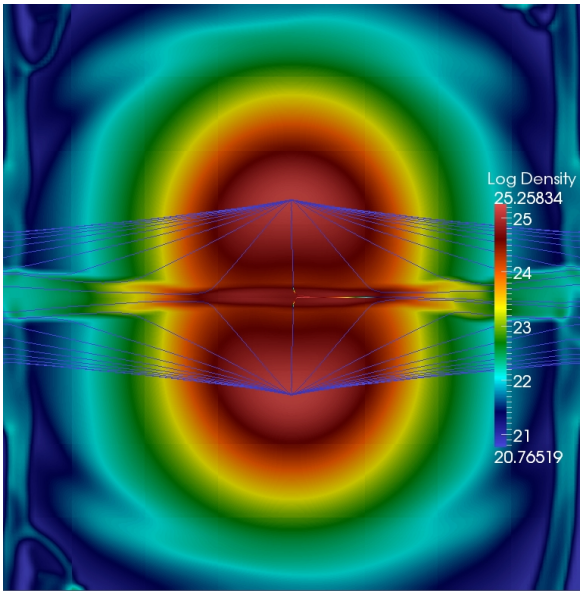

(b) Flow Lines with ρ as background contour color

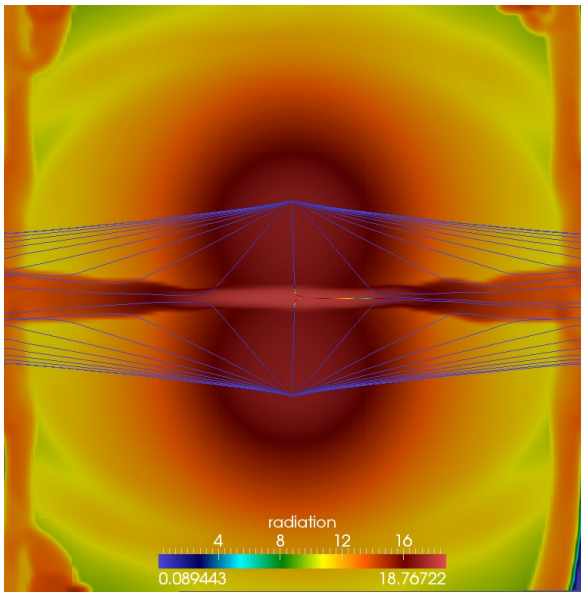

(c) Flow Lines with radiation $\sqrt{T}P^2$ as background contour color

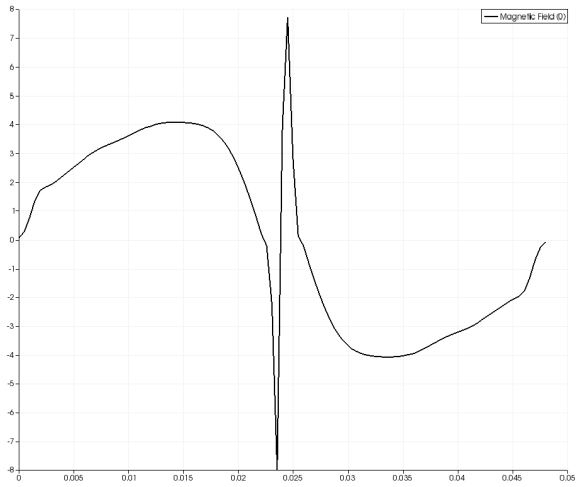

(d) B_x along the y axis

Figure 5.16: t = 360ns, the outflow is bounded by slow shocks, and continues to be accelerated out.

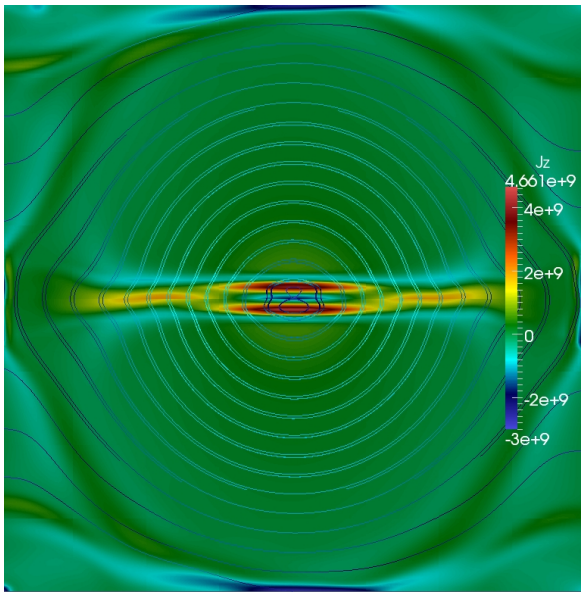

(a) Magnetic field lines with J_z as background contour color

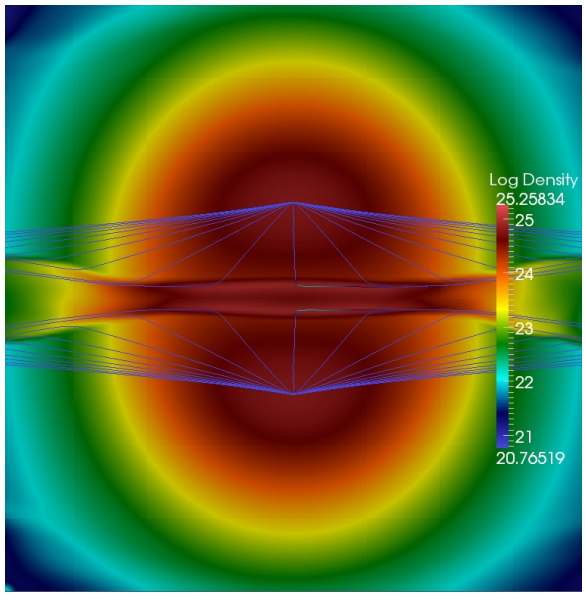

(b) Flow Lines with ρ as background contour color

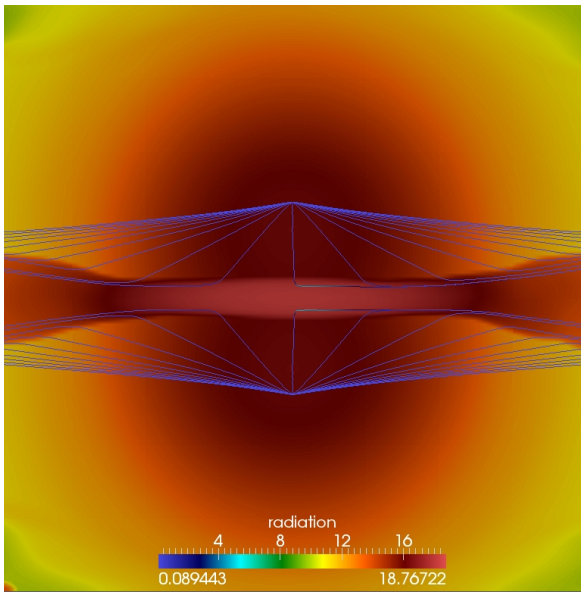

(c) Flow Lines with radiation $\sqrt{T}P^2$ as background contour color

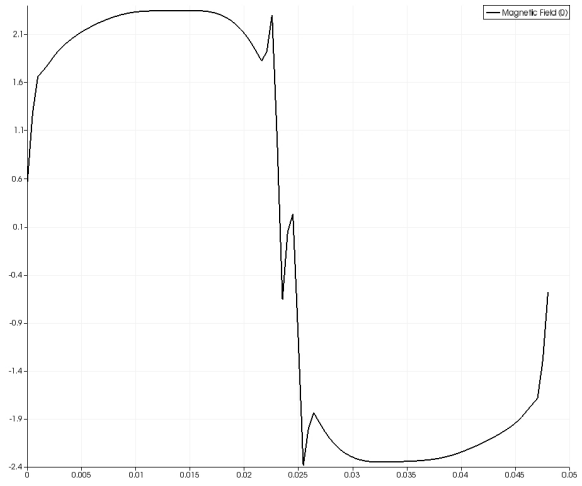

(d) B_x along the y axis

Figure 5.17: t = 425ns, X point is still there, but is near to disappear. This is a good example that DG is better than FV. Since the numerical diffusion is small, the X-point is able to live until very late in time. If we did exactly the same simulation with FV, we will find that the X-point disappears around t = 350ns, and an O-point forms instead.

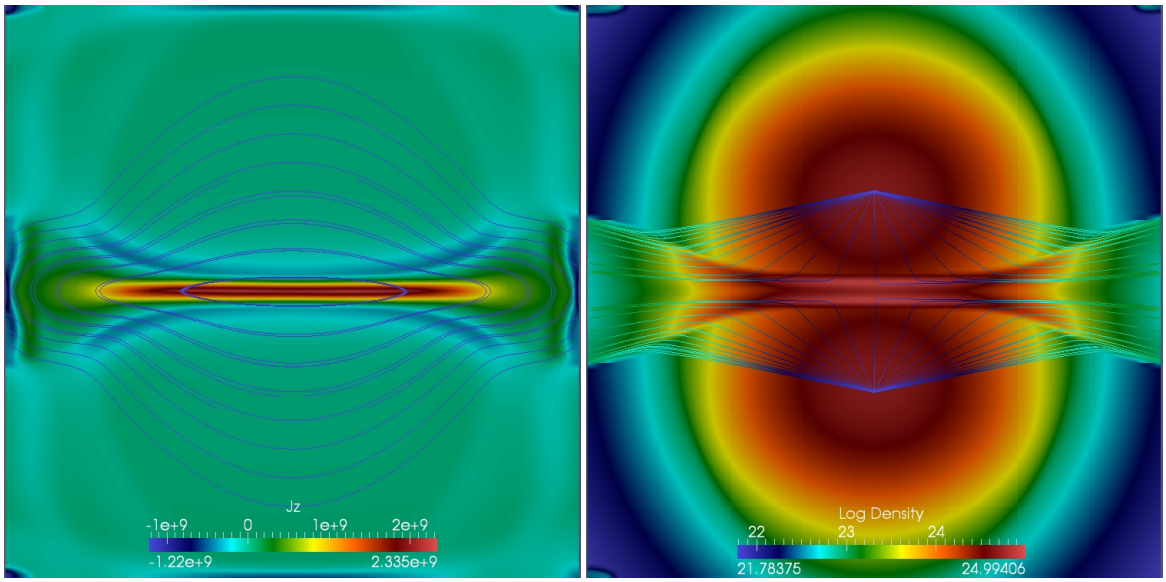

(a) Magnetic field lines with J_z as background contour color

(b) Flow Lines with ρ as background contour color

Figure 5.18: t = 500ns, driving current is zero, the plasma expansion continues, the X-point disappears, leaving an O-point there, and the open angle of the outflow becomes larger.

In this two-wire reconnection, the extended current sheet along the central line is like the diffusion region in the Sweet-Parker [55, 43] model, while the slow shocks bounding the outflow region are very Petschek like. So this configuration is a combination of both Petschek and Sweet-Parker. The inflows from the wire plasmas are supersonic but not super-Alfvénic, while the outflows exceed the local Alfvén speed. The diverging geometry of the inflows from the wire plasma columns may play a strong role in this combination of features, as compared with the planar inflows assumed in the classical models. This reconnection is driven by the inverse skin effect caused by a driving voltage reversal. A global understanding of the reconnection regime must take into account the fact that the initial accumulation of magnetic and thermal energy in plasma current channels and its final dissipation into kinetic energy of outflows by reconnection require opposite driving electric fields. To drive fast reconnection the

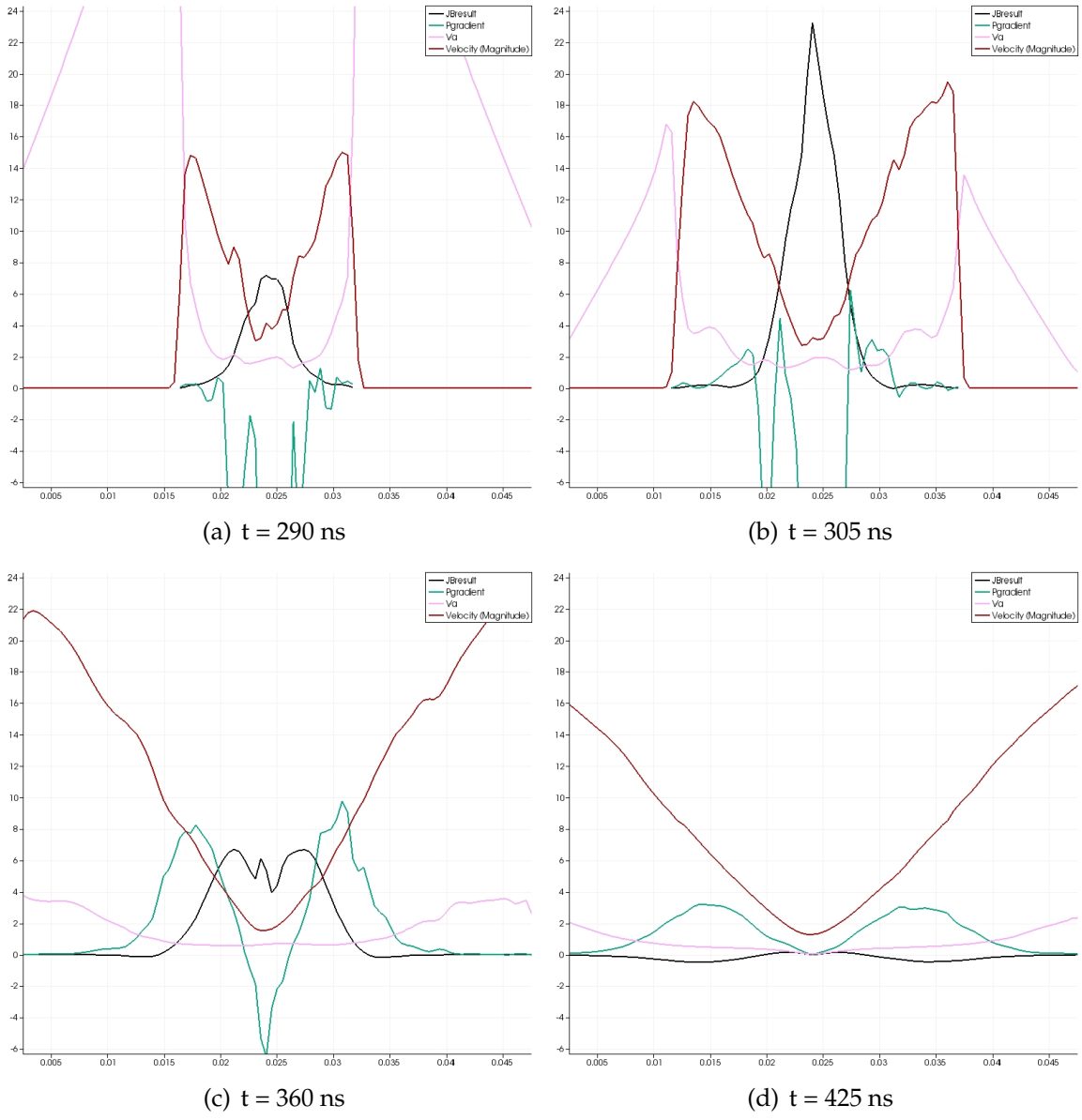

(a) t = 290 ns

(b) t = 305 ns

(c) t = 360 ns

(d) t = 425 ns

Figure 5.19: Force Analysis, Line plot over X-axis. Black Line: $(\mathbf{J} \times \mathbf{B}) \cdot \hat{\mathbf{v}}$, Green Line: $-\nabla P \cdot \hat{\mathbf{v}}$, Pink Line: $\mid v_A \mid (10^4 \mathrm{m/s})$, Red Line: $\mid \mathbf{v} \mid (10^4 \mathrm{m/s})$; Before 300ns, Pressure Gradient ∇P always plays a negative role in accelerating the outflow, and $\mathbf{J} \times \mathbf{B}$ is the main accelerating force. ∇P gradually comes into play, and accelerates the outflow.

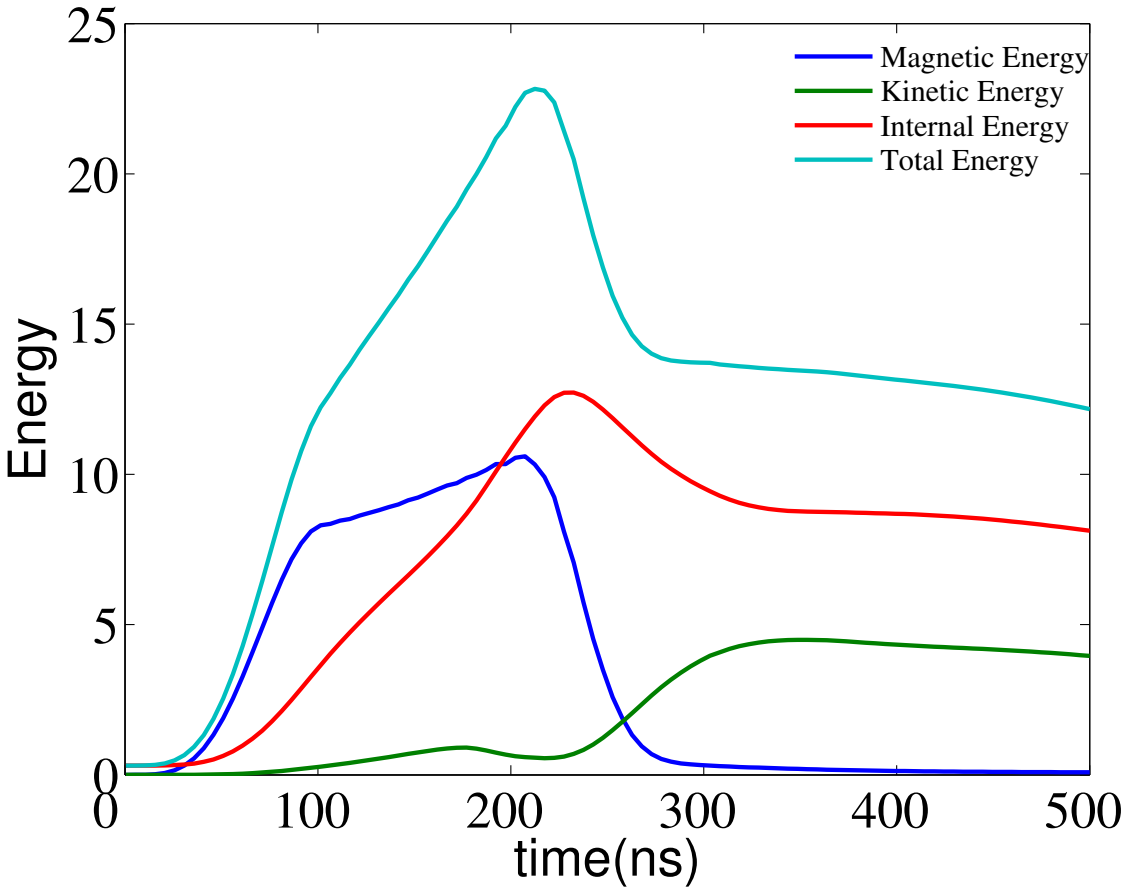

Figure 5.20: Energy change as a function of time.

reversal of current corresponding to the electric field changing must take place in a time shorter compared with resistive penetration time τ.

CHAPTER 6

MAGNETIZED SHOCKS

6.1 Hydrodynamic Bow Shock

Before talking about magnetized shocks, we want to first discuss the behavior of neutral gas, to give us some insight of what will happen in the shock phenomena in magnetized plasmas, and better prepare us for the understanding of magnetized shocks.

The hydrodynamic system can be described by the following equations,

$$\partial_t \rho + \nabla \cdot (\rho \mathbf{u}) = 0 \tag{6.1}$$

$$\frac{\partial}{\partial t}(\rho \mathbf{u}) + \nabla \cdot (\rho \mathbf{u}\mathbf{u} + \mathbf{I}P) = 0 \tag{6.2}$$

$$\frac{\partial \mathcal{E}_n}{\partial t} + \nabla \cdot [\mathbf{u}(\mathcal{E}_n + P)] = 0 \tag{6.3}$$

where we have macroscopic thermodynamic quantities pressure P, mass density ρ and specific total energy $\mathcal{E}$, and velocity vector $\mathbf{v}$. $\mathbf{I}$ is the unity matrix. Also, $\mathcal{E} = \frac{P}{\gamma - 1}$, $T = \frac{P}{\rho}$, where T is the temperature and γ is the adiabatic index. We are considering the ideal fluid here, so the non-idealized terms, such as viscosity, thermal conduction, etc., are not included in our model. Equations (6.1)-(6.3) are called the Euler equations. In our case, the effects dissipation causes do not affect our basic understanding of the fundamental physics of shock behavior, also the dissipation for most gases is so small that we can consider the ideal or dissipationless fluid a good approximation for the real gas, so we use Euler equation as the model for hydrodynamic modeling. So we just model these problems with the DG-PERSEUS code using the model (2.30)- (2.36), by

just letting **B**, **E**, **J** equal to zero, in which case, the model (2.30)- (2.36) is equivalent to the Euler equations. Now we analyze the system (6.1)- (6.3) to arrive at the characteristic speed in neutral gases - the sound speed, at which speed the sound waves propagate in the neutral gases. For this derivation, we write ∇ as $\partial/\partial\mathbf{x}$.

The combination of equation (6.1) and (6.2) gives us:

$$\frac{\partial \mathbf{u}}{\partial t} + \mathbf{u}\frac{\partial \mathbf{u}}{\partial \mathbf{x}} + \frac{\mathbf{1}}{\rho}\frac{\partial P}{\partial \mathbf{x}} = 0, \tag{6.4}$$

And equation (6.1) can be written as:

$$\partial_t \rho + \mathbf{u}\frac{\partial \rho}{\partial \mathbf{x}} + \rho\frac{\partial u}{\partial \mathbf{x}} = 0. \tag{6.5}$$

Assume **u** is small, and we can ignore all the higher order (≥ 2) terms of small numbers (eg. u), so equations (6.4), (6.5) become:

$$\frac{\partial \mathbf{u}}{\partial t} + \frac{1}{\rho}\frac{\partial P}{\partial \mathbf{x}} = 0, \tag{6.6}$$

$$\partial_t \rho + \rho\frac{\partial u}{\partial \mathbf{x}} = 0. \tag{6.7}$$

Also, since:

$$\frac{\partial P}{\partial \mathbf{x}} = \frac{dP}{d\rho}\frac{\partial \rho}{\partial \mathbf{x}}. \tag{6.8}$$

Substitute equation (6.8) into (6.6) and (6.7), we get:

$$\frac{\partial \mathbf{u}}{\partial t} + \frac{1}{\rho}\frac{dP}{d\rho}\frac{\partial \rho}{\partial \mathbf{x}} = 0, \tag{6.9}$$

$$\partial_t \rho + \rho\frac{\partial u}{\partial \mathbf{x}} = 0. \tag{6.10}$$

We perturb the system by applying $X = X_0 + X_1 \exp(ikx - i\omega t)$, where $X = \{\rho, \mathbf{u}, P\}$, then the system becomes:

$$-\omega u_1 + k\frac{1}{\rho_0}\left(\frac{dP}{d\rho}\right)_0 \rho_1 = 0, \tag{6.11}$$

$$-\omega \rho_1 + \rho_0 k u_1 = 0 \tag{6.12}$$

Doing some algebra gives us:

$$\frac{k^2}{\omega^2}\left(\frac{dP}{d\rho}\right)_0 = 1, \tag{6.13}$$

The small perturbations propagate with speed ω/k, which is:

$$v_s = \omega/k = \sqrt{\left(\frac{dP}{d\rho}\right)_0} \tag{6.14}$$

Assuming the process is adiabatic, we have:

$$P = K\rho^\gamma$$

Thus,

$$\frac{dP}{d\rho} = \gamma K\rho^{\gamma-1} = \gamma\frac{P}{\rho}$$

Finally, we arrive at the expression for sound speed v_s:

$$v_s = \sqrt{\frac{\gamma P}{\rho}} \tag{6.15}$$

As been said, v_s is the speed at which a disturbance in the neutral media propagates. If the source of the disturbance is stationary, set the flow velocity $u = 0$, and send out a signal at $t = 0$, then at time t the disturbance will propagate to a sphere with the source as center and with $v_s t$ as radius, as indicated by Figure 6.1(a). If the sound source is in a steady flow with velocity $u < a$, the disturbance still spreads out spherically at speed v_s with the origin moving at the flow speed. In a reference frame fixed in space, the area that the disturbance covers should be as shown in Figure 6.1(b). For these two cases, when $t \to \infty$, the disturbance can always reach the entire space. However, in a supersonic case, where $u > v_s$, as shown in Figure 6.1(c), the disturbance area is bounded by a cone shaped envelope. It is clear from this figure that the disturbance will not reach the entire space as $t \to \infty$, since the information can never propagate in the

upstream direction. This cone shaped envelope is often called the 'Mach Cone', where angle θ (Mach angle) in Fig. 6.1(c) is:

$$\sin\theta = \frac{v_s}{u} = \frac{1}{M_s},$$

where $M_s = u/v_s$ is the Mach number. It is an important dimensionless number to characterize the compressibility effects of fluid. $M_s < 1$, the flow is subsonic, referring to Figure 6.1(b), the sound waves propagate ahead of disturbance, and the response of the fluid could be smooth and adiabatic. When $M_s > 1$, the flow is supersonic. In this case, the sound wave propagates slower than the disturbance itself, and the fluid response is sharp and non-adiabatic. This is what we refer to as a shock.

Imagine a setup where we have a static obstacle in a supersonic steady flow. The flow has to go around the obstacle, thus causing a disturbance. When the body is thick (e.g., a large cylinder), from intuition, the disturbance will no longer be small, and the Mach cone becomes a shock front. Let's evaluate through simulation what will happen if we put a blunt obstacle in a supersonic flow. Shown in Figure 6.1 is a case with Mach number as 20. We see that there is an arc-like structure formed in front of the leading edge of the blunt obstacle. This arc-like structure is the bow shock. This arc-like structure is found to be distinctive when the flow is supersonic. One of the defining features of the bow shock is the existence of a deceleration region between the leading edge of the arc-like structure and the obstacle. Such a deceleration region with subsonic flow velocity must occur in order to keep the mass constant around the obstacle [51]. However, the flow farther upstream remains supersonic, so there has to be a shock surface to connect the supersonic region to the subsonic region. The region behind the bow shock has a higher thermal pressure to balance the dynamic pressure from the incoming flow.

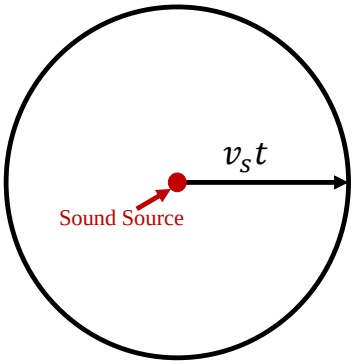

(a) Static, $u = 0$

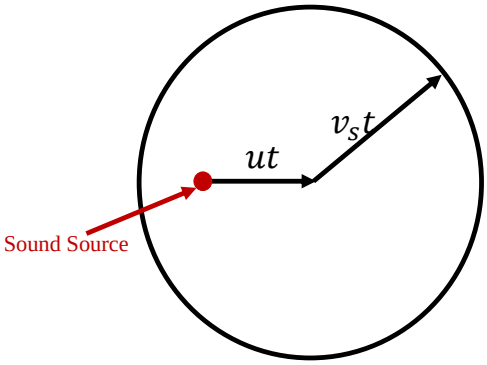

(b) Subsonic, $u < v_s$

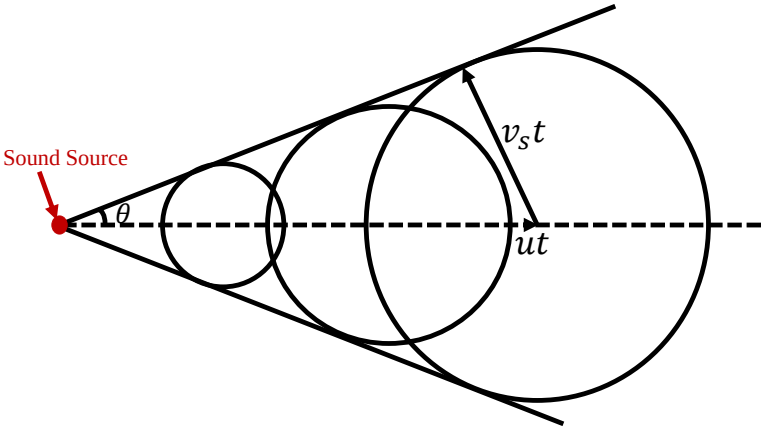

(c) Supersonic, $u > v_s$

Figure 6.1: A stationary point source (fixed) which sends out small-amplitude perturbations is in a steady flow with velocity u. In the reference frame moving with flow, the perturbations propagate with velocity v_s spherically. In the frame of the source, we have to superimpose the reference velocity difference, which is just the flow velocity **u**. So in the reference frame of the source, the perturbed region is not a sphere anymore.

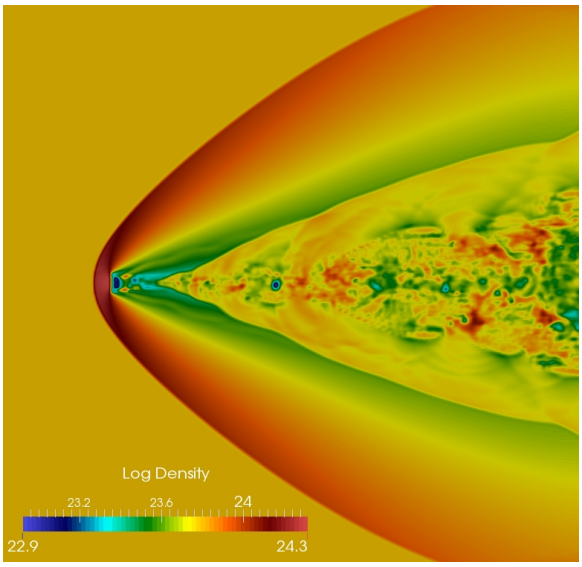

Figure 6.2: Supersonic neutral gas interacting with an obstacle

Since the flow is moving supersonically to the right, the disturbance cannot propagate to the left of the source point, as illustrated in (6.1(c)). However, the flow in front of the obstacle has to respond to the presence of the obstacle to behave accordingly, thus it requires that a subsonic region immediately in front of the obstacle. For this reason, the obstacle sends out waves which are capable of propagating to the left. However, the flow farther upstream remains supersonic, so there has to be a shock surface to connect the supersonic region to the subsonic region.

We also see a number of other structures in Figure 6.1, including boundary layer separation, turbulence wake, laminar separation, turbulent separation, etc.. Since our focus in this dissertation is not on neutral gases, but more on the behavior of ionized gases in the presence of magnetic field, we will leave the explanation of these complicated structures in the hydrodynamic shock tail part to others. Based on what we know, we can predict certain behavior for magne-

tized flows: 1. The perturbation in magnetized fluid does not propagate with v_s, but with another characteristic speed. However, since we expect the results to be analogous, the bow shock front can be explained in the same manner; 2. We know that magnetic field lines tend to stabilize the flow motion perpendicular to the fields, thus we expect the complicated structures to be stabilized. In this chapter, aside from discussing the bow shock, more emphasis will be put on the physics of the tail region.

6.2 MHD waves

Since characteristic wave speeds in typical MHD waves are very important in the explanation of the shocks in this chapter, here we derive the wave speeds following [68]. We start from ideal MHD equations:

$$\partial_t \rho = -\nabla \cdot (\rho \mathbf{u}) \tag{6.16}$$

$$\rho \left(\frac{\partial \mathbf{u}}{\partial t} + (\mathbf{u} \cdot \nabla)\mathbf{u} \right) = \frac{1}{\mu_0} (\nabla \times \mathbf{B}) \times \mathbf{B} - \nabla P \tag{6.17}$$

$$\frac{\partial \mathbf{B}}{\partial t} = \nabla \times (\mathbf{u} \times \mathbf{B}) \tag{6.18}$$

We perturb the system by applying $X = X_0 + X_1 = X_0 + X_1' \exp(ikx - i\omega t)$, where $X = \rho, \mathbf{u}, \mathbf{B}$, and linearize the three equations above by substituting the expression in, with the terms of order (≥ 2) ignored, we arrive at the following equations:

$$\frac{\partial \rho_1}{\partial t} = -\rho_0(\nabla \cdot \mathbf{u_1}) \tag{6.19}$$

$$\rho_0\left(\frac{\partial \mathbf{u_1}}{\partial t} + (\mathbf{u}\cdot\nabla)\mathbf{u}\right) = -\frac{1}{\mu_0}(\nabla \times \mathbf{B_0}) \times \mathbf{B_1} - v_s^2 \nabla \rho_1 \tag{6.20}$$

$$\frac{\partial \mathbf{B_1}}{\partial t} = \nabla \times (\mathbf{u_1} \times \mathbf{B_0}), \tag{6.21}$$

where we have incorporated the relationship: $\nabla P = v_s^2 \nabla \rho$.

By taking the time derivative of equation (6.20), and also substituting in (6.19) and (6.21), we arrive at:

$$\begin{aligned} \frac{\partial^2 u_1}{\partial t^2} &= -\frac{v_s^2}{\rho_0}\nabla\frac{\partial \rho_1}{\partial t} - \frac{\mathbf{B_0}}{\mu_0\rho_0} \times (\nabla \times \frac{\partial \mathbf{B_1}}{\partial t}) \\ &= v_s^2 \nabla(\nabla \cdot \mathbf{u_1}) - \frac{\mathbf{B_0}}{\mu_0\rho_0} \times (\nabla \times \nabla \times (\mathbf{u}_1 \times \mathbf{B}_0)) \end{aligned} \tag{6.22}$$

We introduce the definition of Alfvén speed here:

$$\mathbf{v}_A = \frac{\mathbf{B_0}}{\sqrt{\mu_0\rho_0}}, \tag{6.23}$$

then equation (6.22) becomes:

$$\frac{\partial^2 u_1}{\partial t^2} = v_s^2 \nabla(\nabla \cdot \mathbf{u}_1) - \mathbf{v}_A \times (\nabla \times (\nabla \times (\mathbf{u}_1 \times \mathbf{v}_A))) \tag{6.24}$$

Taking into account the wave form of X_1, and for simplicity, we write X_1' as X_1, then we get:

$$-\omega^2 \mathbf{u}_1 = -v_s^2(\mathbf{k}\cdot\mathbf{u_1})\mathbf{k} + \mathbf{v}_A \times (\mathbf{k} \times \mathbf{k} \times (\mathbf{u_1}\mathbf{v_A})) \tag{6.25}$$

Then:

$$-\omega^2 \mathbf{u}_1 + (v_A^2 + v_s^2)(\mathbf{k}\cdot\mathbf{u_1})\mathbf{k} = (\mathbf{k}\cdot\mathbf{v_A})[\mathbf{k}(\mathbf{v_A}\cdot\mathbf{u_1}) - \mathbf{u_1}(\mathbf{v_A}\cdot\mathbf{k}) + \mathbf{v_A}(\mathbf{k}\cdot\mathbf{u_1})] \tag{6.26}$$

A reformation of the above equations gives us:

$$[\omega^2 - (\mathbf{v_A}\cdot\mathbf{k})^2]\mathbf{u_1} = (\mathbf{k}\cdot\mathbf{u_1})\left[-(\mathbf{k}\cdot\mathbf{v_A})\mathbf{v_A} + (v_s^2 + \mathbf{v}_A^2)\mathbf{k}\right] - (\mathbf{k}\cdot\mathbf{v}_A)(\mathbf{u_1}\cdot\mathbf{v}_A)\mathbf{k} \tag{6.27}$$

We assume that $\mathbf{v_A}$ is directed along with z-axis, and that the wave-vector $\mathbf{k}$ is in the $x-z$ plane with an angle θ between $\mathbf{v_A}$ and $\mathbf{k}$. Then we can write (6.27) into an equation system:

$$\begin{pmatrix} \omega^2 - k^2 v_A^2 - k^2 v_s^2 \sin^2\theta & 0 & -k^2 v_s^2 \sin\theta\cos\theta \\ 0 & \omega^2 - k^2 v_A^2 \cos^2\theta & 0 \\ -k^2 v_s^2 \sin\theta\cos\theta & 0 & \omega^2 - k^2 v_s^2 \cos^2\theta \end{pmatrix} \begin{pmatrix} V_x \\ V_y \\ V_z \end{pmatrix} = 0 \tag{6.28}$$

The existence of non-trivial solution of $(V_x, V_y, V_z)^T$ implies the determinant of the square matrix in (6.28) is zero, which gives the following (dispersion relation):

$$(\omega^2 - k^2 v_A^2 \cos^2\theta)\left[\omega^4 - \omega^2 k^2 (v_A^2 + v_s^2) + k^4 v_A^2 v_s^2 \cos^2\theta\right] = 0 \tag{6.29}$$

The three independent roots of equation (6.29) correspond to three different types of MHD waves.

1.
$$\omega = k v_A \cos\theta \tag{6.30}$$
This mode is the shear Alfven wave, which propagates with a velocity of $v = v_A \cos\theta$.

2.
$$\begin{aligned} \omega &= k \frac{1}{2}\left[v_A^2 + v_s^2 + \sqrt{(v_A^2 + v_s^2)^2 - 4 v_A^2 v_s^2 \cos^2\theta}\right]^{\frac{1}{2}} \\ &= k v_+ \end{aligned} \tag{6.31}$$
This mode is fast magnetosonic wave, or simply fast wave. It propagates with a velocity of $v = v_+$.

3.
$$\begin{aligned} \omega &= k \frac{1}{2}\left[v_A^2 + v_s^2 - \sqrt{(v_A^2 + v_s^2)^2 - 4 v_A^2 v_s^2 \cos^2\theta}\right]^{\frac{1}{2}} \\ &= k v_- \end{aligned} \tag{6.32}$$

This mode is slow magnetosonic wave, or simply slow wave. It propagates with a velocity of $v = v_-$. In the low-β limit, where $v_A \gg v_s$ the dispersion relation of slow wave approximately becomes:

$$\omega \simeq k v_s \cos\theta, \tag{6.33}$$

which is just the sound wave in the presence of magnetic field.

The velocities v_A, v_- and v_+ are characteristic speeds at which the perturbations in MHD plasmas propagate. They are analogous to the sound speed in hydrodynamic case. It should hold that $v_+ \geq v_A \geq v_-$. Similar to the supersonic shocks in thehydrodynamic cases, we should have similar phenomena in magnetized fluids, when the propagation speed of disturbance exceeds any of these characteristic speeds. Given this, let us investigate the shock behavior in MHD fluids.

6.3 MHD shocks

When a shock occurs in magnetized fluids, the MHD equations should be integrated across the shock to provide the so called 'Jump Conditions', which relates the plasma properties on each side of the shock front. To achieve this, we first need to write the ideal-MHD model in conservation form:

$$
\begin{aligned}
\frac{\partial}{\partial t}\rho + \nabla\cdot(\rho\mathbf{u}) &= 0,\\
\frac{\partial}{\partial t}(\rho\mathbf{u}) + \nabla\cdot\left[\rho\mathbf{u}\mathbf{u} + \left(P + \frac{B^2}{2\mu_0}\right)\mathbf{I} - \frac{\mathbf{B}\mathbf{B}}{\mu_0}\right] &= 0,\\
\frac{\partial}{\partial t}\left(\frac{\rho u^2}{2} + \frac{P}{\gamma-1} + \frac{B^2}{2\mu_0}\right) + \nabla\cdot\left[\left(\frac{1}{2}\rho u^2 + \frac{\gamma}{\gamma-1}P\right)\mathbf{u} + \frac{\mathbf{B}\times(\mathbf{u}\times\mathbf{B})}{\mu_0}\right] &= 0,\\
\nabla\cdot\mathbf{B} &= 0,\\
\frac{\partial}{\partial t}\mathbf{B} - \nabla\times(\mathbf{u}\times\mathbf{B}) &= 0.
\end{aligned}
\tag{6.34}
$$

Here we employ the following assumptions: 1. the state is spatially uniform to the left of the shock front; 2. the state is spatially uniform to the right of the shock front; 3. it is a steady state (time independent). With the assumptions above, we have $\partial_t = 0$, $\partial_T = 0$ (T is the direction parallel to the shock front), and $\partial_N = 0$ (N is the direction normal to the shock front), except at the shock jump.

By integrating over the equations (6.34) in the direction normal to the shock front, $\mathbf{N}$, we get the jump condition, namely the Rankine-Hugoniot relations. The explicit Rankine-Hugoniot relations across the shock front are as follows:

$$
\begin{aligned}
&[\rho u_N] = 0,\\
&[\rho v_N^2 + P + \frac{B_T^2}{2\mu_0}] = 0,\\
&[\rho v_N \mathbf{v}_T - \frac{B_N}{\mu_0}\mathbf{B}_T] = 0,\\
&[\rho v_N \frac{v^2}{2} + \frac{\gamma}{\gamma-1}v_N P + v_N\frac{B_T^2}{\mu_0} - \frac{B_N}{\mu_0}(\mathbf{v}_T\cdot\mathbf{B}_T)] = 0,\\
&[B_N\mathbf{v}_T - v_N\mathbf{B}_T] = 0,\\
&[B_N] = 0,
\end{aligned}
\tag{6.35}
$$

where square brackets denote the change in the quantity across the shock front, The subscript N denotes the parameter component normal to the shock front, while the subscript T denotes the parameter component which is parallel to the

shock front. Using the conditions (6.35), we can determine the downstream parameters given the upstream parameters. Note that the model we used in this dissertation (2.30) - (2.36) is not in conservation form. One might be concerned that the real source terms, e.g., the $\mathbf{J} \times \mathbf{B}$ force term may affect the shock capturing ability of the numerical discretization. We address this concern in a later section through some shock tests to show that the DG-PERSEUS code does well in capturing shocks and discontinuities.

As discussed in section 6.2, there are three kinds of MHD waves, slow, intermediate or shear Alfvén wave and fast waves, they propagate with v_-, v_A and v_+ respectively with definitions found in Equations (6.31), (6.23), (6.32). Thinking of the MHD shocks as nonlinear versions of the associated MHD waves, there should be three kinds of shocks accordingly, and we name them slow shock, intermediate shock and fast shock respectively. The three different kinds of shocks are demonstrated in Figure 6.3. We denote the parameters to the left of the shock front (inflow region) with subscript 2, and the right with subscript 1. It follows that $B_{T2} > B_{T1}$ for a fast shock, whereas $B_{T2} < B_{T1}$ for a slow shock. A special case of the intermediate shock is referred to as a rotational discontinuity, where $B_{T2} \to -B_{T1}$. It is clear that fast shocks refract the magnetic field and plasma flow away from normal to the shock front towards the shock front, slow shocks refract towards the normal to the shock front. Also, the tangential magnetic field and plasma flows reverse across an intermediate shock front. The conditions for the existence of a slow, intermediate and fast shocks are respectively: $v_1 > v_-$, $v_1 > v_A \cos\theta$ and $v_1 > v_+$.

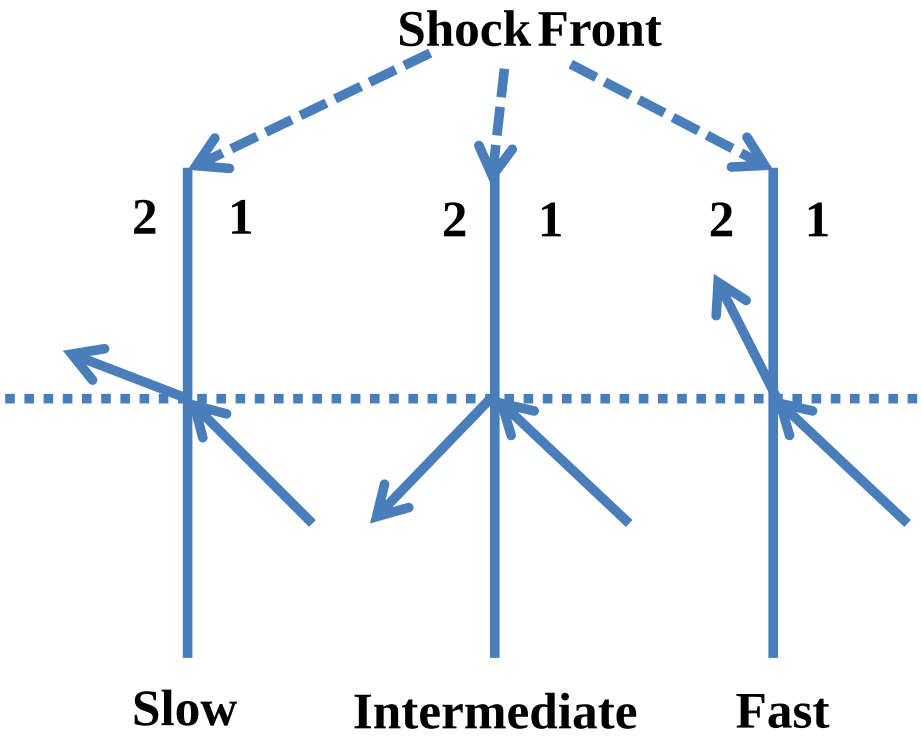

Figure 6.3: Characteristic MHD shocks in the shock rest frame

6.3.1 Slow Shock Test

The initial state is as follows:

$$(\rho, u_x, u_y, u_z, P, P_e, B_x, B_y, B_z)$$
$$= \begin{cases} (1.368\rho_0, 0.269, 1.0, 0, 1.769\rho_0, 0.8845\rho_0, \sqrt{\rho_0}, 0.0\sqrt{\rho_0}, 0) \text{ for } x < 0 \\ (1.000\rho_0, 0.000, 0.0, 0, 1.000\rho_0, 0.5000\rho_0, \sqrt{\rho_0}, 1.0\sqrt{\rho_0}, 0) \text{ for } x > 0 \end{cases}$$
$$(E_x, E_y, E_z, J_x, J_y, J_z) = (0, 0, 0, 0, 0, 0)$$

We set $\rho_0 = 10^{-4}$, with a resolution of $\lambda_e/\Delta x = 0.144$ and $\lambda_i/\Delta x = 6.3$. Figure 6.4 shows the ideal-MHD results, note that the shock structure is preserved very

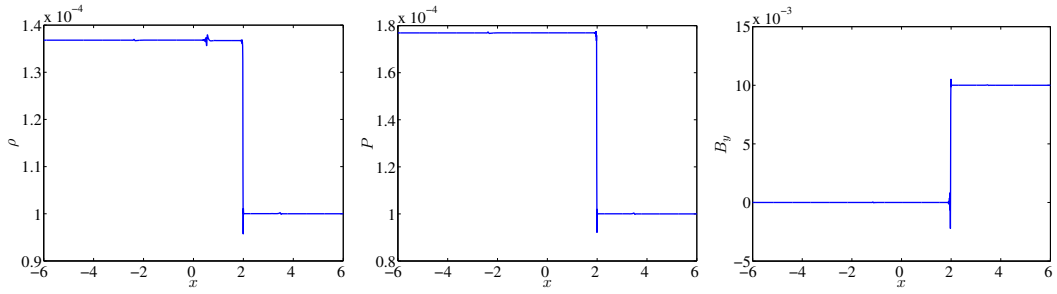

(a) density (ρ) (b) thermal pressure (P) (c) transverse field (B_y)

Figure 6.4: Density, thermal pressure and transverse field in a slow switch-off shock with ideal-MHD model, 400 cells, initial shock position at $x = 0$, captured at $t = 0.5$

well, with only 1-2 grid cell involved in the jump. There are small oscillations near the shock region, which are expected since positivity-preserving limiter (PP-limiter) is the only limiter used in this scheme, which does not smooth away oscillations as much as a TVD limiter does. The use of slope limiter [27] can remove all the oscillations. No noticeable difference is found using a finer mesh, which implies the scheme is converged with a resolution as low as 400.

With XMHD model, we obtain results shown in Figure 6.5. As there are no steady-state shock solutions in the XMHD model, the discontinuity emit waves that propagate outwards. The fact that there is a component of **B**, i.e., B_x, parallel to the wave vector **k** and no pressure or density perturbations suggests that whistler waves are emitted and cause the oscillations observed in the B_y plot 6.5(c).

From Figure 6.5, we can see the slow shock structure is seriously smeared. Actually, the shock structure is not there anymore. Same phenomena are observed from Figures 4.2(a) and 4.2(b). For reader's convenience, the two figures are re-presented here in 6.6(a) and 6.6(b) with the letters denoting the types of shocks/waves. The part denoted by 'SS' is slow shock. As observed,

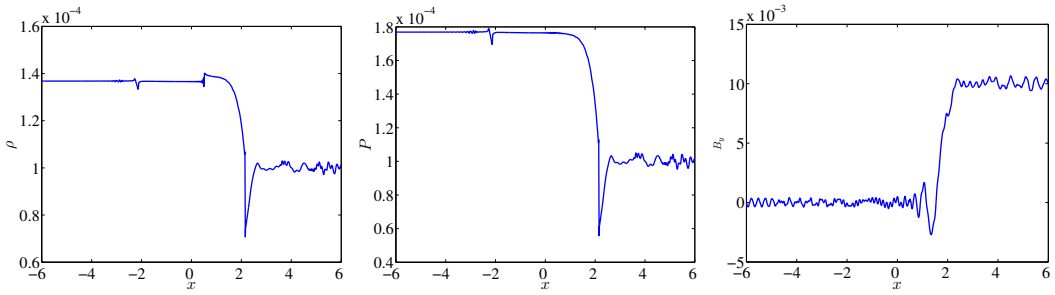

(a) density (ρ) (b) thermal pressure (P) (c) transverse field (B_y)

Figure 6.5: Density, thermal pressure and transverse field in a slow switch-off shock with XMHD model, 400 cells, initial shock position at $x = 0$, captured at $t = 0.5$

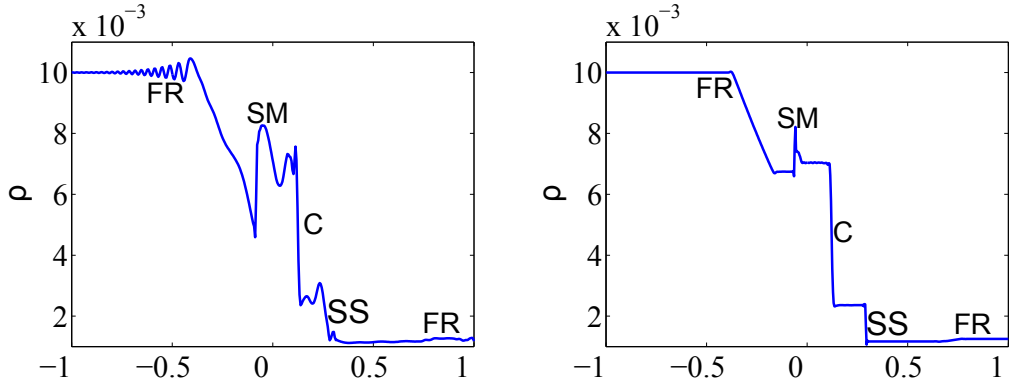

(a) XMHD, $\rho_0 = 10^{-2}$, 400 cells (b) MHD, $\rho_0 = 10^{-2}$, 400 cells

Figure 6.6: Brio Wu shock tube test re-presented. Density as a function of position, captured at $t = 2.1 \times 10^{-2}$; in the two figures, FR, SM, C, SS denote fast rarefaction wave, slow compound wave, contact discontinuity, and slow shock respectively. From the shapes of the slow shocks, we can observe that in the XMHD case, the slow shock structure is severely dissipated, or cannot be referred to as a shock any more.

the slow shock structure is severely dissipated in XMHD results. On the other hand, when we look at the fast shock structure presented in 7.1 and 6.9, the fast shock structure is still preserved even in the XMHD case. This means that slow shock can be severely smeared in a regime where the Hall term is important.

We can understand why slow shock tends to disappear by referring to the

dispersion curves for oblique waves 6.3.1. From the dispersion curves, we can observe that, when $\omega > \Omega_i$, ie, the system frequency is larger than the ion cyclotron frequency, the slow magnetosonic branch is cutoff, and the slow wave mode does not above the ion-cyclotron resonance; hence the dispersion will severely smear the jump. At the same time, the fast magnetosonic wave branch enters the Whistler mode, which is a signature of the Hall effects. Thus, in regimes where the Hall term is important, there is no slow wave, however, the fast wave remains. Naturally, the conclusion follows that the slow shock does not exist in the regime where the Hall term becomes important. That is why we do not see the slow shock in XMHD simulation results.

6.3.2 Fast Shock Test

The MHD fast shock is not captured by in the Brio-Wu initial conditions. Therefore we provide a test by following the fast shock initial conditions in [17], with minor modifications. This test shows that the scheme correctly captures the shock even though the magnetic force is represented by the $\mathbf{J} \times \mathbf{B}$ source term and is not in full conservation form.

The initial state is as follows:

$$
\begin{aligned}
&(\rho, u_x, u_y, u_z, P, P_e, B_x, B_y, B_z) \\
&= \begin{cases} (3\rho_0, 3.444, -1.333, 0, 16.33\rho_0, 8.16\rho_0, 3\sqrt{\rho_0}, 2.309\sqrt{\rho_0}, 0) \text{ for } x < 0 \\ (1\rho_0, 0.000, +0.000, 0, 1.000\rho_0, 0.50\rho_0, 3\sqrt{\rho_0}, 0.000\sqrt{\rho_0}, 0) \text{ for } x > 0 \end{cases} \\
&(E_x, E_y, E_z, J_x, J_y, J_z) = (0, 0, 0, 0, 0, 0)
\end{aligned}
$$

We set $\rho_0 = 10^{-4}$, with a resolution of $\lambda_e/\Delta x = 0.144$ and $\lambda_i/\Delta x = 6.3$. Figure 7.1 shows the ideal-MHD results, note that the shock structure is preserved very

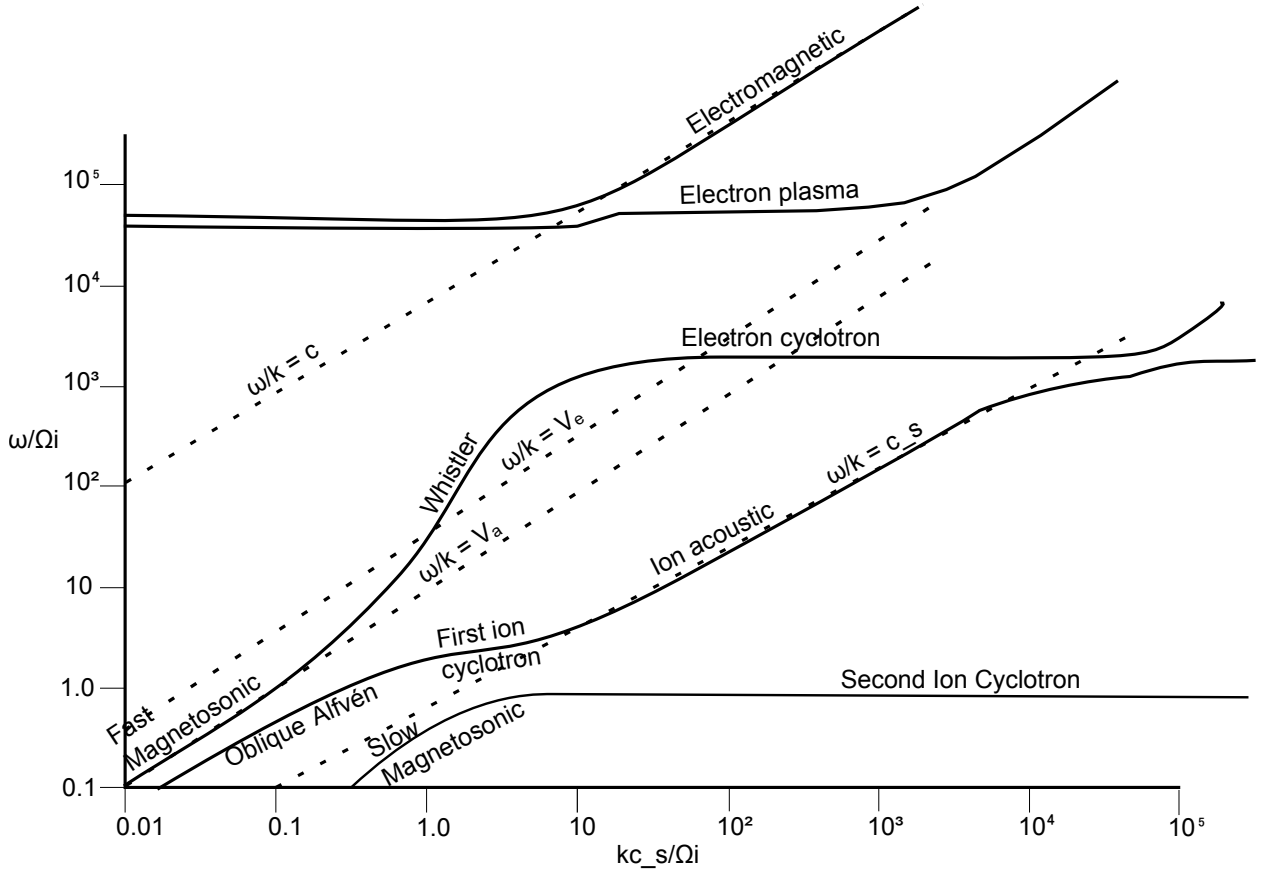

Figure 6.7: Dispersion curves for oblique waves in low β plasma with $|\Omega_e| < \omega_{pe}$ (After [6])

well, with only 1 grid cell in the shock. Same with the slow shock case, there appears some small oscillations near the shock region, which can be smoothed away by using the slope limiter. No noticeable difference is found using a finer mesh, which implies the scheme is converged with a resolution as low as 400. Numerical result gives an average shock speed as 5.14, while its analytical solution is 5.17, taken into consideration the measurement error, the results are very close.

With XMHD model, we obtain results shown in Figure 6.9. As there are no

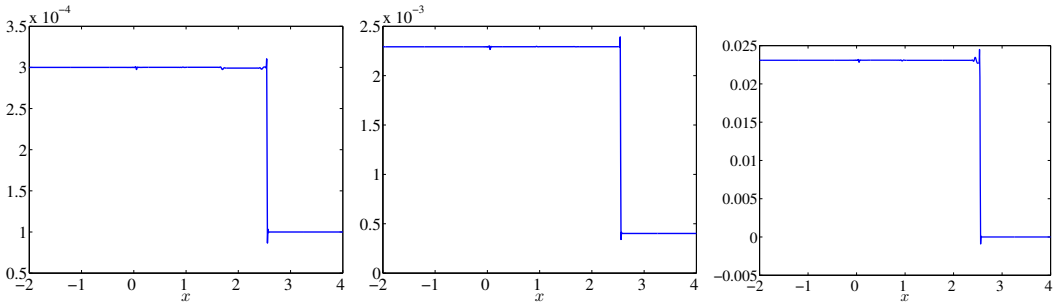

(a) density (ρ) (b) thermal pressure (P) (c) transverse field (B_y)

Figure 6.8: Density, thermal pressure and transverse field in a fast switch-on shock with ideal-MHD model, 400 cells, initial shock position at $x = 0$, captured at $t = 0.5$

steady-state shock solutions in the XMHD model, the discontinuity emit waves that propagate outwards. The fact that there is a component of **B**, i.e., B_x, parallel to the wave vector **k** and no pressure or density perturbations suggests that whistler waves are emitted and cause the oscillations observed in the B_y plot 6.9(c). Since whistler wave does not have an effect on density or temperature, we do not see observe the perturbation in the ρ and P plot. One thing to notice is that, in the XMHD regime with an XMHD model, the fast shock is well preserved, as seen in the ρ and P figures, being different from the slow shock which disappears in this regime.

For an example of fast-magnetosonic shock in a realistic situation, one can refer to section 7.3.2, where we explain the Bow Shock in a magnetized situation.

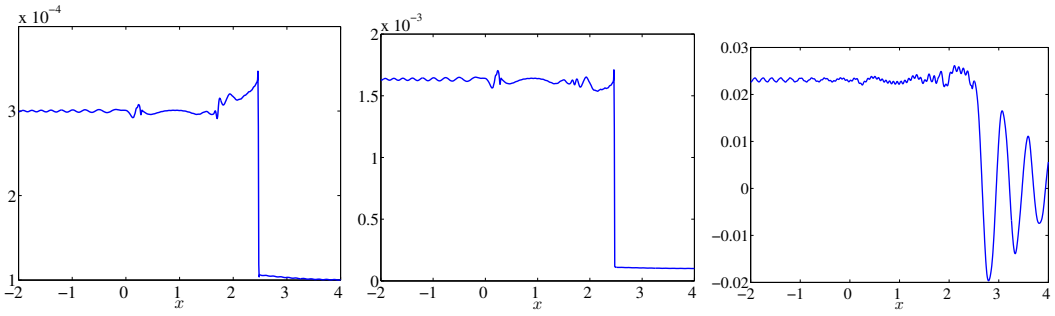

(a) density (ρ) (b) thermal pressure (P) (c) transverse field (B_y)

Figure 6.9: Density, thermal pressure and transverse field in a fast switch-on shock with XMHD model, 400 cells, initial shock position at $x = 0$, captured at $t = 0.5$

CHAPTER 7

MAGNETIZED FLOW INTERACTING WITH OBSTACLE

7.1 Introduction

The problem *magnetized flow interacting with obstacle* refers to a problem where a magnetized flow is disrupted by an obstacle, thus changing the profile of magnetic field lines and the flow lines. For simplicity, we use the term *shock-obstacle* to refer to these problems. The word *shock* appears in the term because these problems are often associated with the presence of shocks. We will start with a 2D simulation, so the obstacle is assumed to be a cylinder that is infinitely long in the direction perpendicular to the simulation plane. For the 2D simulation, we will place emphasis on the case where the initial magnetic field lines are in-plane. Then we will generalize the study to a 3D simulation, to find out what happens when a magnetized flow encounters a sphere.

The initial motivation for studying the shock-obstacle problem is that we want to use XUV images to diagnose the outflow in the two wire magnetic reconnection experiment explained in chapter 5. We seek deeper knowledge of the reconnection outflow, such as whether it is supersonic or not, super-Alfvénic or not, the flow direction at a random point, flow density, etc.. All of the above are inflow properties that we can vary as parameters in the simulations. By varying the parameters, we find the simulation results can change significantly. Each phenomenon is matched to a parameter regime. These changes can be easily recognized in the XUV images of the experiment. By identifying a certain phenomenon in the XUV images, we can match it to a parameter regime. Then we acquire some knowledge of the inflow properties. In the experiment, the ob-

stacle is a post of the same length as the wire and is placed parallel to the wires, since the length of the post is much longer than its width, thus simulation on 2D is approximately correct.

As the study proceeded, we found some very interesting physics associated with this problem. Using this set up, we have arrived at a deeper understanding of important physical processes like magnetic reconnection, substorm, fast and slow shocks. The two main structures we are considering are the bow shock and the wake flow. The bow shock is the shock structure located in front of the obstacle. We show that the bow shock shape, mechanism and features are similar to the hydrodynamic case with modification by some plasma parameters such as magnetosonic Mach number M_f, the ratio of thermal pressure to magnetic pressure β, etc.. The wake flow is the region of disturbed flow downstream of the obstacle. We found in magnetized flow, the wake flow structure can be significantly different from the non-magnetized flow for various reasons, and is a very interesting area to study. We will first discuss the bow shock, but will put more effort on understanding the wake flow structure.

We also found that the Hall term can play a very important role in this problem when $L \sim \lambda_i$. To understand the role of the Hall term, we will compare the XMHD results to the MHD results. This study provides us better intuition on why the Hall term is important, and in which way the term can affect the results.

If we generalize this simulation to 3D, we can study the solar wind's interaction with the unmagnetized planets, like Mars or Venus. We also scale this problem down to parameters that can be achieved in the lab, so that we can study the solar wind - rocky planet interaction in laboratory experiments.

7.2 Problem Setup

The 2D simulation is set up as depicted in Figure 7.1(a). This particular setup is for the study of perpendicular shocks with the angle θ between the magnetic field upstream of the shock and the shock normal being $\pi/2$. Under this setup, we drive a flow with velocity $\mathbf{u}$ from the left boundary, and the flow is magnetized with magnetic field $\mathbf{B}$. The magnetic field is perpendicular to the flow direction, i.e., we should have $\mathbf{B} \cdot \mathbf{u} = 0$ in the inflow. The most important parameters of the inflow are the non-dimensionalized quantities, e.g. the sonic Mach number $M_s = \mid \mathbf{u} \mid /v_s$, the Alfvénic Mach number $M_A = \mid \mathbf{u} \mid /v_A$, and fast magnetosonic Mach number $M_f = \frac{1}{\sqrt{1/M_a^2+1/M_s^2}}$, etc.. All these parameters are evaluated in the inflow region before encountering the solid obstacle. In a 2D simulation, the solid obstacle would mean an obstacle that is infinitely long and uniform along the direction perpendicular to the plane. Figure 7.1(b) illustrates what the set up looks like in 3D. If not specified, here are the parameters used in simulations in this chapter:

The domain is $x \in (-20\text{mm}, 20\text{mm})$, $y \in (-20\text{mm}, 20\text{mm})$; 400 cells are used on each direction. The whole domain is initialized with uniform number density as $n = 10^{23}\text{m}^{-3}$, temperature as 14eV, magnetic field as $B_y = 16.4\text{T}$, $dx/\lambda_i = 0.19$. We use Aluminum as the plasma material, and use spitzer resistivity for η. Inflow from left boundary has a velocity of $u_x = 200\text{km/s}$, sonic Mach number of $M_s = 16.9$, Alfvénic Mach number of $M_a = 2.24$ and magnetosonic Mach number of $M_f = 2.22$. In the region, we put a square obstacle of side length $d = 0.6\text{mm}$ with its center 14mm from left boundary, 20mm from lower boundary. $d/\lambda_i = 1.15$. The block is constructed as a boundary condition on the block's 4 edges ensuring that the mass flux normal to every edge is zero, following the

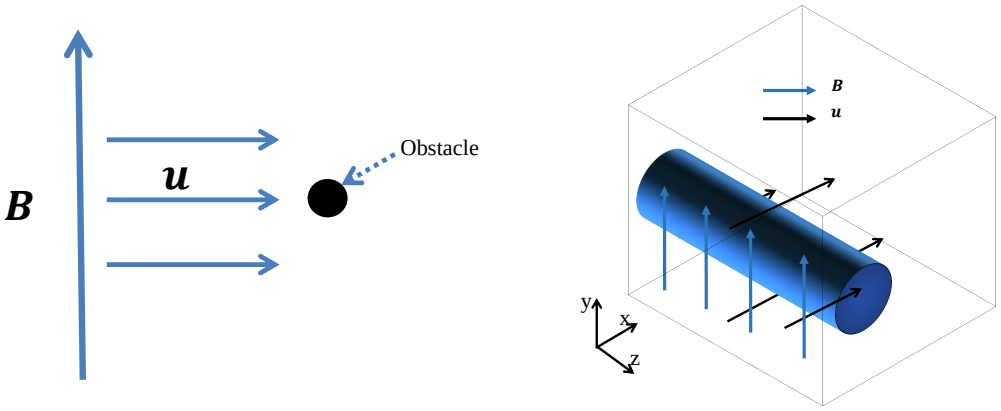

(a) 2D Simulation Set Up

(b) A 3D view of the 2D set-up in space

Figure 7.1: Set Up of the simulation for studying the magnetized flow interacting with an Obstacle, the flows are magnetized with a magnetic field that is perpendicular to the flow direction; The speed is **u**, the driving magnetic field is **B**.

implementation of solid boundary described in section 3.4.

The simulations in this chapter will be based on the parameters above. Changes of certain parameters are possible and will be specified. If not otherwise specified, the parameters will be the same as the ones stated in the last paragraph.

7.3 Simulation with the MHD Model

We first carry out a 2D simulation with the MHD model. Here we first try to model the experiment depicted in chapter 5, which is the interaction of reconnection outflow with an obstacle that is s squared-cross-sectional post. The parameters used in this simulation are the best estimation of the experimental results. Then we vary the parameters to see how the phenomena vary and what

the most important factors to impact the results are. With that, we hope for deeper insight into the physics involved in these series of problems.

7.3.1 Simulation Result

The results for MHD captured at time $t = 140ns$ are as shown in Figure 4.8(a). Here, we point out that the PP-limiter is essential for this test. When it is turned off a low pressure dip immediately forms behind the block and evolves to eventually become negative. The features appeared in this result, e.g., the bow shock structure, and tail structure behind the obstacle will be discussed in the following sections.

7.3.2 Bow Shock

The reason for the formation of bow shock is similar to the hydrodynamic case, which is the information carried by waves travels slower than the disturbance source itself. The momentum pressure in the upstream supersonic flow region is balanced by the thermal pressure and magnetic pressure in the deceleration region. These regions are connected by the bow shock. Figure 7.3.2 shows the simulation result as previously shown in Figure 7.3.1, and the profiles of $\log \rho$, tangential component of magnetic field B_t and temperature T along a line segment through the bow shock front are as shown in the right part of Figure 7.3.2. From the profiles, it is clear that B_t and $\log \rho$ are all increasing across the shock front. As discussed earlier, if the tangential component of magnetic field increased across the shock, this shock should be fast shock. Thus we conclude the

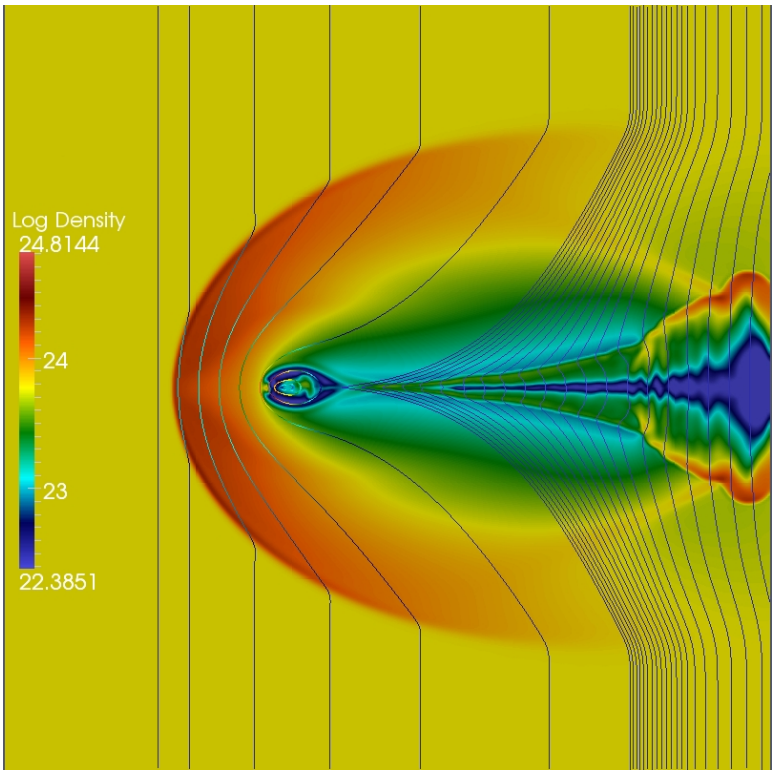

Figure 7.2: Magnetic field lines with background color as the $\log \rho$. MHD simulation with estimated experimental parameters measured from reconnection outflow in the two-wire reconnection experiments depicted in chapter 5, captured at $t = 140ns$.

bow shock is a fast shock, and is formed by the steepening of fast magnetosonic waves.

As depicted in figure 7.4, we vary M_A and M_s while keeping M_f the same. The extent by which we vary M_A and M_s is very large. In the cases shown in figure 7.4, difference in the bow shock shapes (angle, thickness, etc.) is not obvious. From this, we can tell that among the three important Mach numbers (M_A, M_s, M_f) which might have the most influence on this problem, M_f is more important than the other two mach numbers. We point out that these three tests have different β, since:

$$\beta = \frac{P}{P_{mag}} \propto \frac{T}{B^2} \propto \frac{M_A^2}{M_s^2},$$

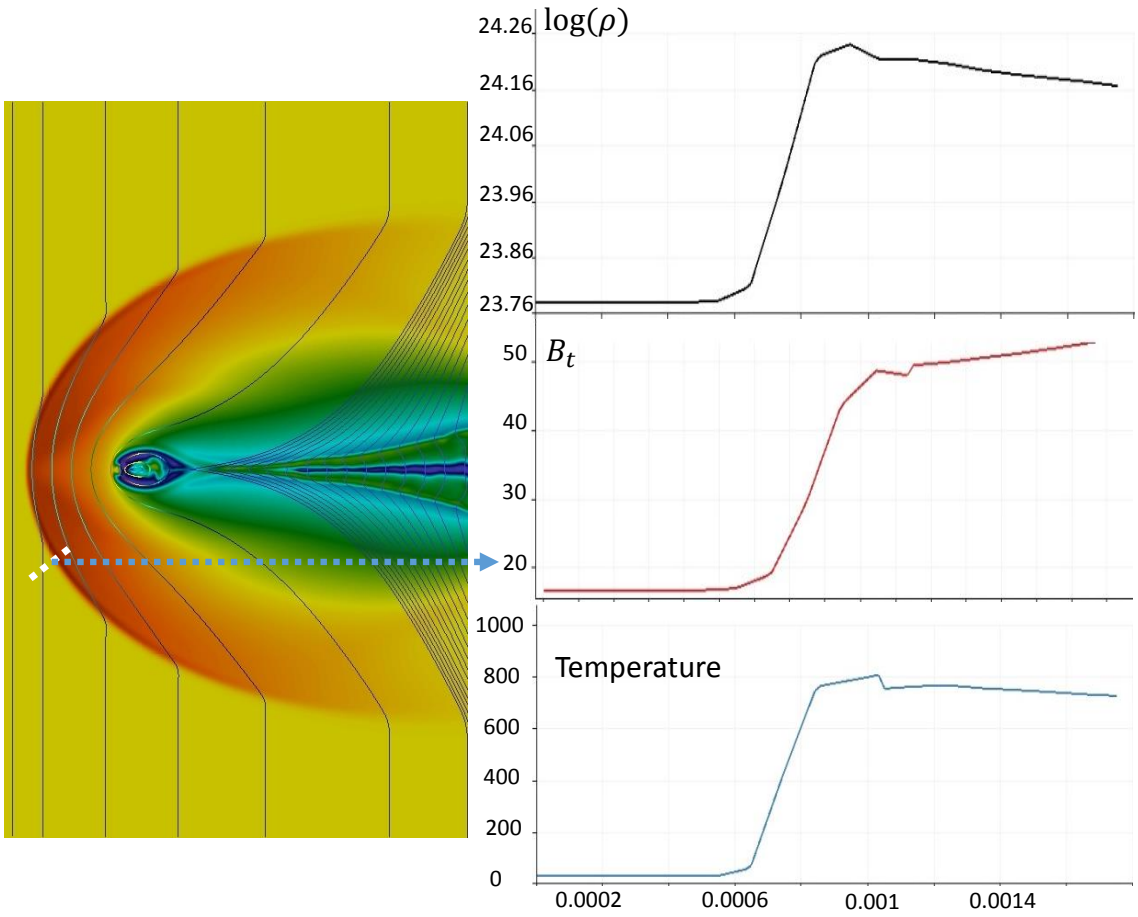

Figure 7.3: Picture elaborating that the bow shock is a fast shock. The left part is the result shown in Figure 7.3.1. The right part is the profile of variables along the white line segment across the bow shock shown in the left figure, including variables Temperature, tangential component of magnetic field B_t, log density $\log \rho$. Across the shock, the values of all three variables are increasing. The fact that B_t is increasing across the shock gives evidence that this bow shock is a fast shock.

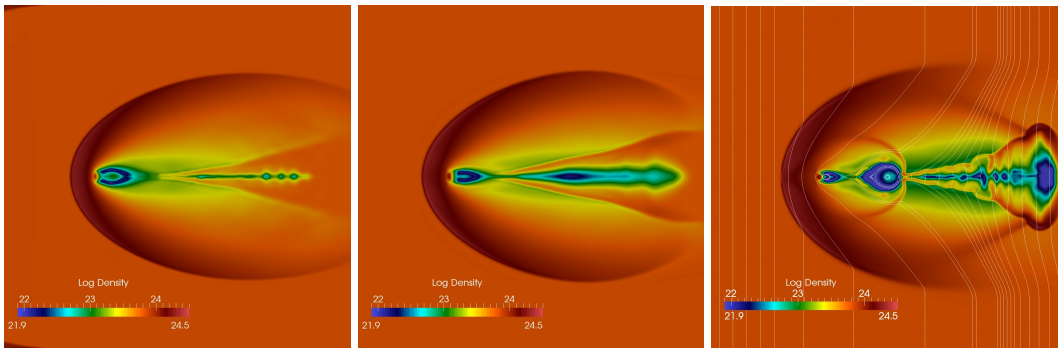

(a) $M_a = 4, M_s = 3$ (b) $M_a = 3, M_s = 4$ (c) $M_a = 2.42, M_s = 16.9$

Figure 7.4: Bow shock structures with same M_f, but M_a and M_s are different.

and M_A/M_s is different in these three cases. So this test also tells us that M_f also has a more pronounced impact than β. The fact that fast magnetosonic mach number is taking the control further confirms that the bow shock is a fast shock.

One thing to note is, the M_f defined by $1/\sqrt{M_s^2 + M_a^2}$ can fully control a perpendicular fast shock structure, but for an oblique shock, the controlling M_f has to be modified by the incidence angle. This can explain the slight difference among the three cases in figure 7.4.

7.3.3 Analytic Evaluation on why Bow Shock is a Fast Shock

In this section, we provide an analytical explanation on why the bow shock is a fast shock. We explain this from two points of view. 1. Fast magnetosonic wave is the only wave that can propagate strictly perpendicular to magnetic fields. 2. The fast magnetosonic wave in MHD plasmas is analogous to the sound wave in neutral fluids.

1. Fast magnetosonic wave is the only wave that can propagate perpendicular to magnetic fields. Here we evaluate the configuration of this problem. We have flow **u** perpendicular to the magnetic field **B**, as depicted in Figure 1, ie, $\mathbf{B} \perp \mathbf{u}$, and $\mathbf{u} \perp \mathbf{n}$. The flow propagation direction **k** is also perpendicular to **B**. In this case, the angle θ in equations (6.30), (6.31), (6.32), which is the angle between **B** and **k** is $\frac{\pi}{2}$, thus $\cos\theta = 0$, so that equation (6.30) reduces to $\omega = 0$, (6.31) reduces to $\omega = \sqrt{k(v_A^2 + v_s^2)}$, (6.32) also reduces to $\omega = 0$. That means, the propagation of both Alfvén wave and slow wave are cut off, leaving only the fast magnetosonic wave. Thus, the shock front immediately in front of the obstacle has to be the result of the steepening of fast magnetosonic wave, which is a fast shock.

2. The role the fast wave plays in magnetized fluids is analogous to the role sound wave plays in neutral fluids. The shock wave slows the flow and heats the plasma and deflects the flow, forms a planetary bow shock, which is analogous to the bow shock in the gas dynamics. The sound wave is an compressional wave and the corresponding compressional wave in MHD fluids is the fast magnetosonic wave. Also, we know that the sound wave is the zero magnetic field limit of fast magnetosonic wave by letting $\mathbf{B} = 0$ in Equation (6.31). As a compressional wave, the propagation of the slow wave will be cut off when $\mathbf{B} = 0$. Since the bow shock is caused by the steepening of sound wave in gas dynamics, in an analogous manner, the bow shock in magnetized fluids should be caused by the steepening of fast magnetosonic wave, which corresponds to a fast shock.

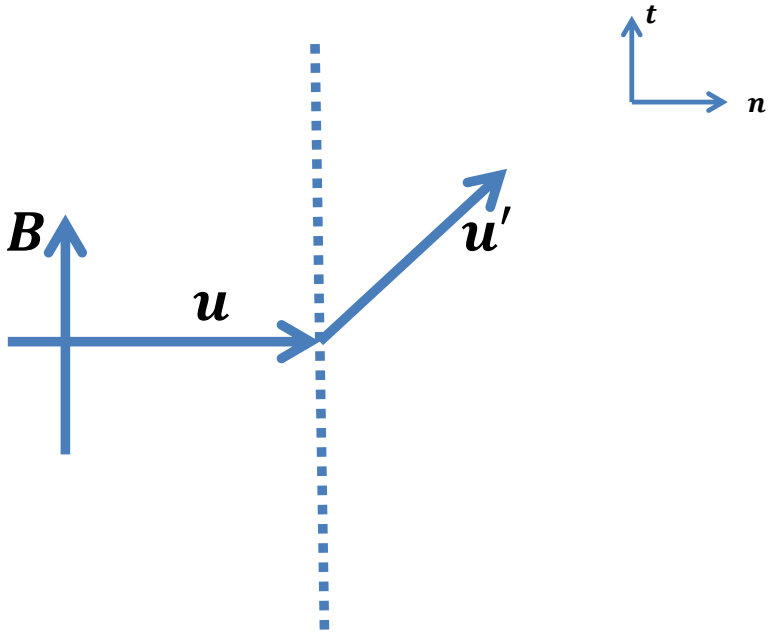

Figure 7.5: Perpendicular Shock Structure

7.3.4 Magnetic Reconnection in the Shock Tail

In the previous section, we discussed the bow shock region, in the following sections; we will move our emphasis to the tail structure that is formed behind the obstacle.

Remark 7.1 As we note here, the shock-obstacle problem has a configuration that is similar to the interplanetary problem, for example, the solar wind's interaction with Earth. Those problems have been studied in detail, and scientists have created terminology for better describing the phenomena. As readers

might be more familiar with that terminology, we will take advantage of the terminology in this thesis to describe corresponding phenomena in our simulation results. For example, the tail structure behind the obstacle will be named *magnetotail*. The magnetic bubbles produced in the magnetotail will be named *plasmoid*, and this will be discussed in the next section.

The study of the magnetotail is our focus in this chapter, as the various phenomena appearing there can deepen our understanding of some very important plasma physics concepts. We find in the MHD simulation results as already presented in Figure 7.3.1, there appears an X-shaped magnetic field profile right behind the obstacle. The region near the X-point is enlarged, as shown in figure 7.6(c). It is quite clear that the flow goess around the obstacle and comes in the X-point inflow region 1-2, and then through reconnection, the flow advects the magnetic field lines to the outflow region (3-4). An enlargement of the reconnection region is shown in Figure 7.6(c), where we see some flow streamlines going towards both regions 3-4, and we have opposite but nearly the same magnitude of velocities into these two regions. These are all clear signature of magnetic reconnection. Reconnection occurs due to several factors: first, the magnetic field lines are significantly bent by the obstacle. Except for a few field lines to diffuse through because of a finite resistivity, most field lines are frozen into plasmas which are stagnated in front of the obstacle; the field lines frozen in are stagnated as a result and get bent. Then from the point of view of any point along the center line behind the obstacle, the field lines in the upper region are opposite to the field lines in the lower region. The change of magnetic field direction has to be supported by a current sheet along the central line. This current sheet will be squeezed as the pressure increases in the lobe area, when the current sheet is thin enough, reconnection relaxes the configuration to a lower energy

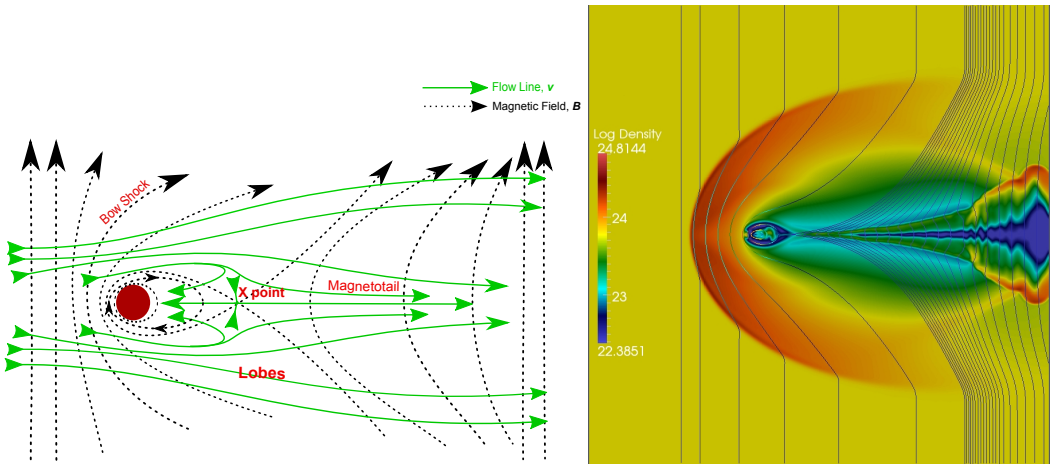

(a) Schematic sketch illustrating how magnetic reconnection appears in the magnetotail

(b) Magnetic Field Lines with log(ρ) as background color

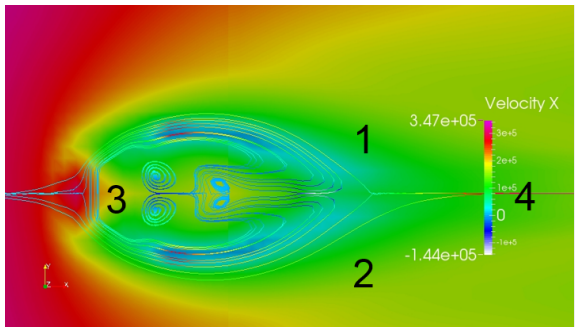

(c) enlargement of the reconnection region in subfigure (b), streamlines show the flow lines

Figure 7.6: The magnetic field lines can also pass through the obstacle through magnetic reconnection. Figure (a) schematic sketch showing how reconnection appears, and how the flows are directed through the X-point; Figure (b) shows a clear X-point behind the obstacle; Figure (c) shows an enlargement of X point area, which clearly shows that magnetic reconnection is happening at the X point.

state.

7.3.5 Magnetotail Reconnection Outflow is Bounded by Slow Shock

The outflow from the reconnection discussed in section 7.3.4 is bounded by a slow shock. Shown in Figure 7.7(a) are the profiles of density on a log scale ($\log \rho$), tangential component of magnetic field (B_T) along the white line in Figure 7.7(a). Clearly from the profiles that, across the shock front, we have a jump in both density and temperature, whereas the tangential component of magnetic field is decreasing. This provides direct evidence that the outflow from reconnection is bounded by a slow shock.

7.3.6 Plasmoids Generated in the Shock Tail

In sections 7.3.1 and 7.3.4, we consider a problem with an Alfvénic Mach number of approximately $M_A = 2.24$, and fast magnetosonic number as $M_f = 2.22$. In this section, we consider what happens when we lower the Mach number by half. The simulation results are as shown in Figures 7.8(b) - 7.11(b), the results are very different from what we found in section 7.3.4. Some magnetic flux bubbles are formed with trapped plasma. Because of the similarity of this phenomenon to the magnetic bubbles in Earth's magnetosphere, we also name it plasmoid. Now, we illustrate the process of the generation of these plasmoids in this section.

We categorize this process into three phases: the growth phase, expansion phase and the recovery phase. Together with the simulation results and diagrams, we explain what happens in each of these phases.

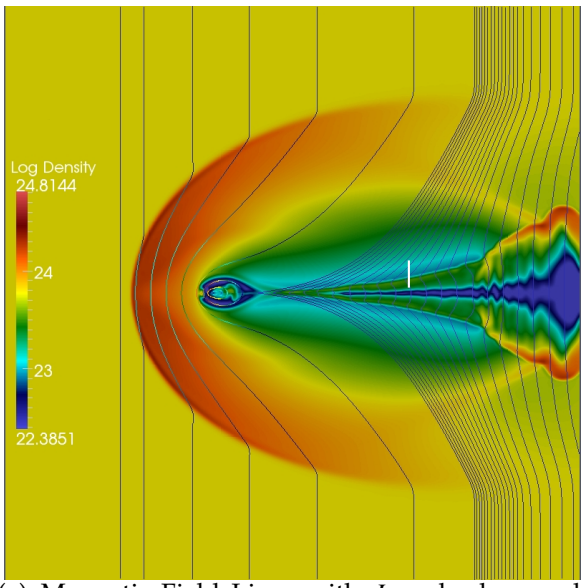

(a) Magnetic Field Lines with J_z as background color

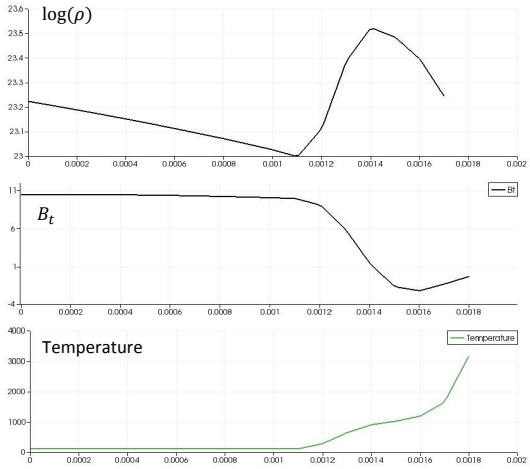

(b) Cross sectional distributions of log(ρ), B_t, *Temperature* on a cut along the white line in Figure 7.7(a).

Figure 7.7: The outflow from the tail reconnection is bounded by a slow shock, as evidenced by the fact that B_t is decreasing across the shock.

1. As in Figure 7.8(b), this is during the growth phase. Due to the presence of the obstacle, the magnetic field lines are bent, since there is not enough diffusion for the field lines to diffuse through, the magnetic flux has to get through by reconnecting. An *X* point denoted by *X* forms behind the obstacle, through reconnection, some plasma flows are directed into the closed flux region (or the trapping region) *A*, so the energy inside the region *A* is piling up due to continuing flow into. During this process, the tail lobes continue to expand with increasing stored magnetic energy. It is also widely believed that the energy stored in the tail lobes is the main reservoir of the energy that powers the events occurred in the magnetotail.

2. As in Figure 7.9(b), this process happens during the expansion phase. The energy stored in the closed flux in region *A* will be converted into kinetic energy and expand the region. The direction of the expansion of *A* has to be tailwards, due to the momentum pressure from the inflow region. When region *A* is stretched thin enough, reconnection happens again. To lower the energy state, the broken and reconnected halves of the magnetic field lines form two new magnetic field lines. The lines on the obstacle side, rebounds obstacle-wards, just like a released slingshot. Meanwhile, the magnetic field lines on the tail side lost its connection to the obstacle. The field lines on the tail side form another closed flux region *B*. *B* takes some flux and energy away from A, so that the system can sustainably grow; otherwise the energy inside A will grow towards infinity. The field lines in the bubble-shaped region *B*, together with the plasmas riding on it are often called plasmoid.

3. Figure 7.10(b) represents the recovery phase. The breakup of field lines provides plasma bubble *B* the initial momentum to move tailwards. The

inflow also provides a pressure to expel B tailwards. A current sheet forms connecting region A to B. The presence of the current sheet helps to support the X shape magnetic field configuration.

4. Figure 7.11(b) is a post-recovery phase, indicating that things are looping back to the growth phase and expansion phase. Since region B is expelled tailwards, region A returns to its initial state as described in the growth phase part. Then expansion phase happens again, and region A breaks into region A and B'. At the same time, the plasmoid B propagates tailwards into field lines in region C. When B collides with the field lines in C, magnetic field lines reconnect again, and the flux energy inside B is dissipated in this process, then the closed flux lines break up, and merge into region C.

7.3.7 Reason for Different Magnetotail Structures

The results in sections 7.3.4 and 7.3.6 are very different. In section 7.3.4, we found that a simple reconnection process had occurred when the inflow was sufficiently fast. We refer to this event as *reconnection*. In section 7.3.6, we found that for slower inflows a chain of reconnection events happen and plasmoids appear. We refer to this event as *plasmoid*. When inflow velocity is 200km/s, only reconnection appears, but if we lower the inflow velocity to 100km/s, plasmoids appear. The source of this difference is that, the characteristic time scale for these two cases are different. If we take the length scale of this particular problem as the length of the disturbed region, $\tilde{L} \sim 30$mm, then the time scale in the reconnection case is $\tilde{t}_{\text{reconnection}} \sim 150ns$, while the time scale in the plasmoid

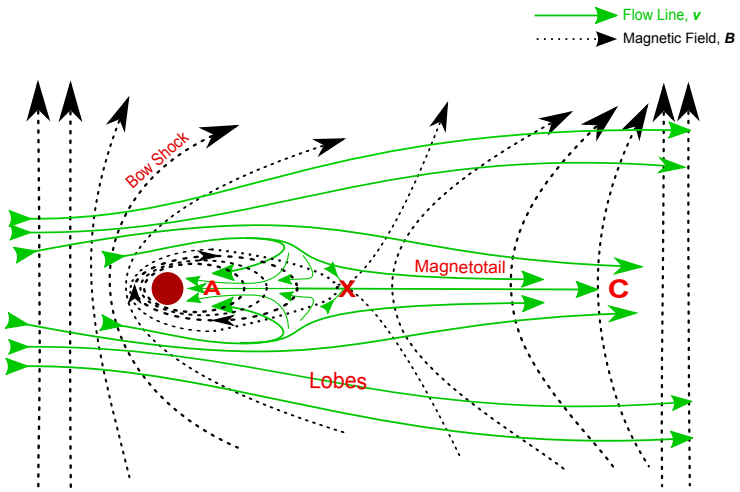

(a) Schematic sketch depicting the reconnecting process for forming the magnetotail.

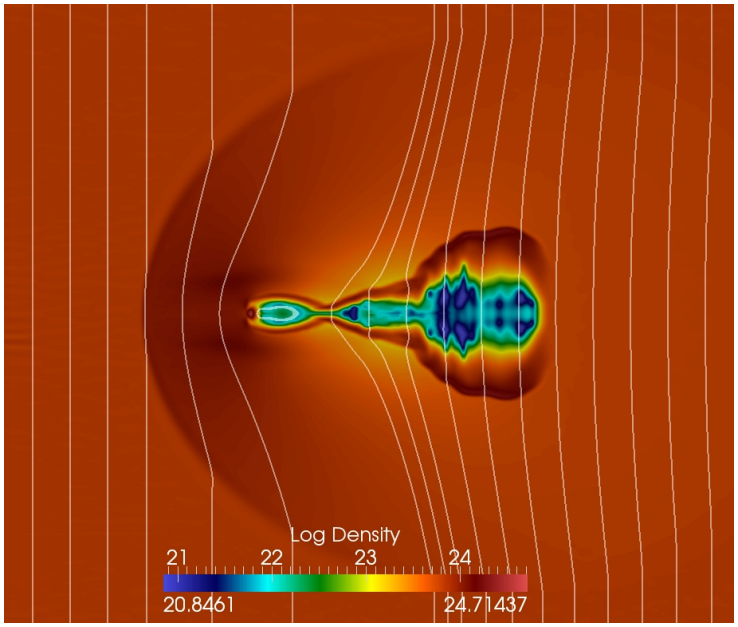

(b) Magnetic Field lines with background color plot of $\lg(\rho)$. Simulation figure taken at the time when reconnection is happening.

Figure 7.8: Growth Phase. Because of the presence of the obstacle, the magnetic field lines are bent, since there is not enough diffusion for the field lines to diffuse through, the magnetic flux has to get through by reconnecting. An X point denoted by 'X' forms behind the obstacle, through reconnection, some plasma flows are directed into the region A, so the energy inside the region A is piling up due to continuing flow into this region.

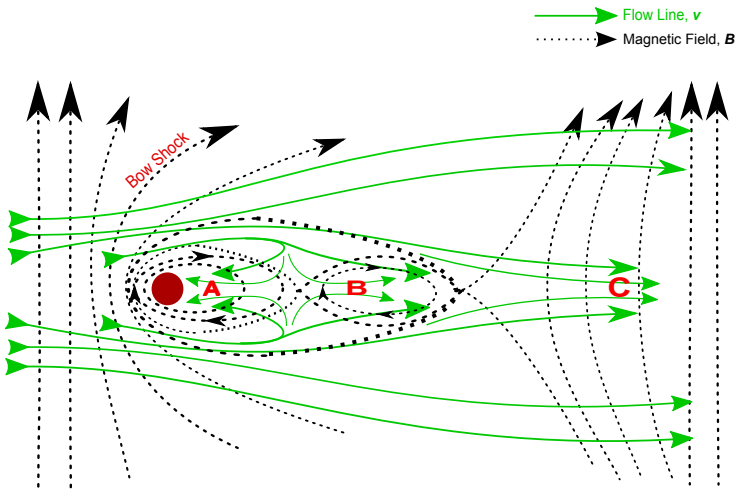

(a) Schematic sketch depicting the process for forming the plasmoid.

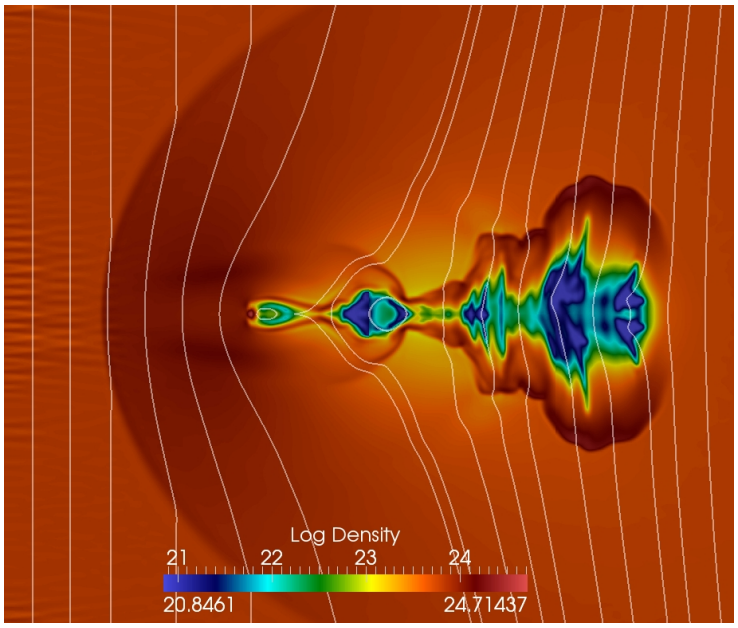

(b) Magnetic Field lines with background color plot of lg(ρ). Simulation figure shotted at the time when plasmoid forms.

Figure 7.9: Expansion Phase. With the energy piling up in the closed flux in region *A*, *A* has to expand, because of the momentum pressure from the inflow, *A* region has to expand tail-wards. When region *A* is elongated to a certain level, it will break down into two parts to lower the potential energy, so as to stabilize the whole system. Some magnetic instabilities will also help the breaking out. That is the reason why another closed flux region *B* forms, *B* took some flux and energy away from A, so that the system can sustainably grow. The region denoted by *B* is often referred to as 'Plasmoid'.

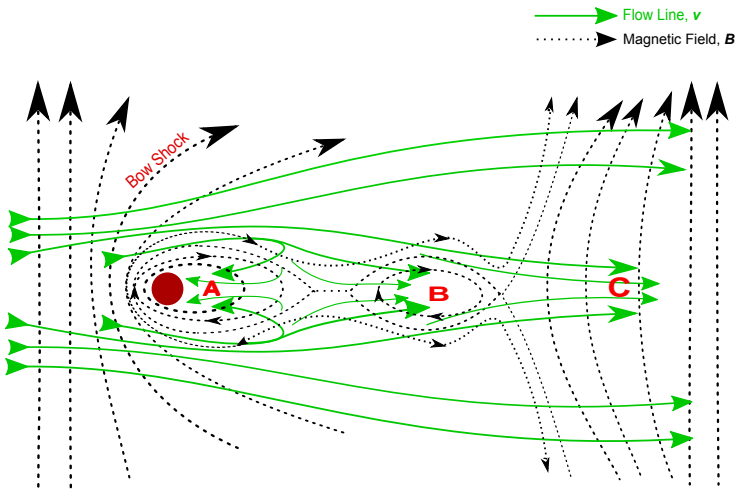

(a) Schematic sketch depicting the process where plasmoid is pushing tail-wards.

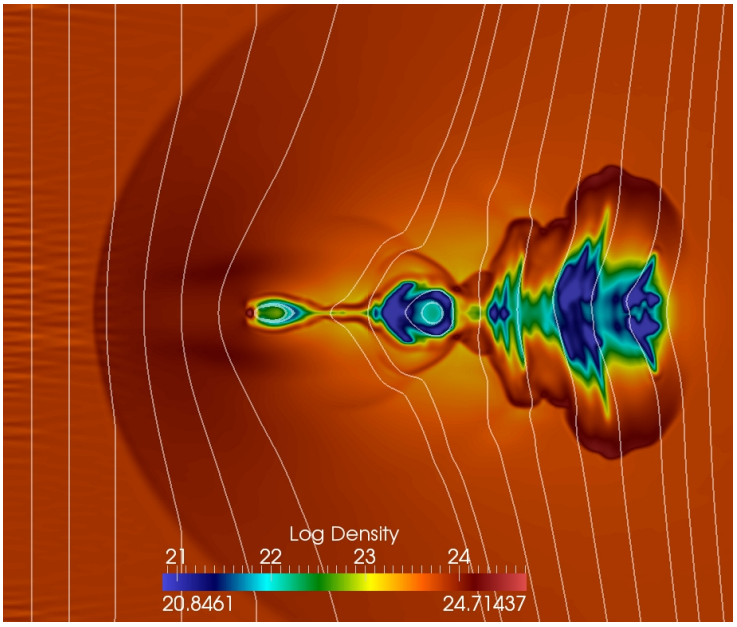

(b) Magnetic Field lines with background color plot of lg(ρ). Simulation figure shotted at the time when plasmoid is pushed tail-wards.

Figure 7.10: Recovery Phase: Because of the momentum pressure from the inflow, the plasmoid denoted by B is pushed tail-wards. A current sheet forms between region A and B to support the X shape there.

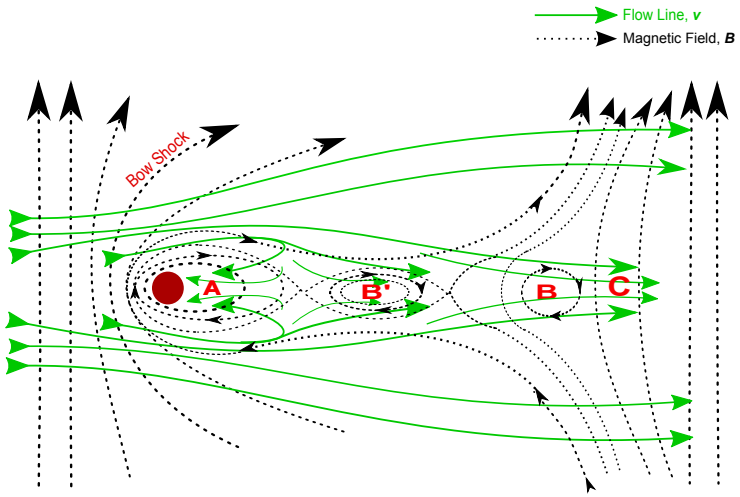

(a) Schematic sketch showing that plasmoids collide into downstream field lines

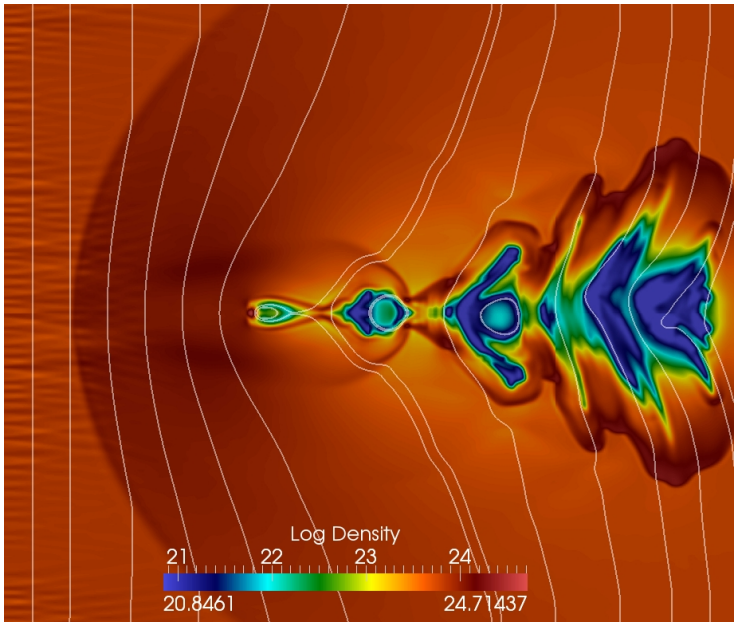

(b) Magnetic Field lines with background color plot of lg(ρ). Simulation figure shotted at the time when plasmoids collide into downstream field lines

Figure 7.11: Post-Recovery Phase. The plasmoid *B* propagates tail-wards into field lines in region *C*. When *B* collides with the field lines in *C*, magnetic field will reconnect again, and the flux energy inside *B* is dissipated in this process, then the closed flux lines break up, and merge into region *C*. In the same time, another plasmoid *B'* is generated from *A*, repeating the process extrapolated in 7.9(b)

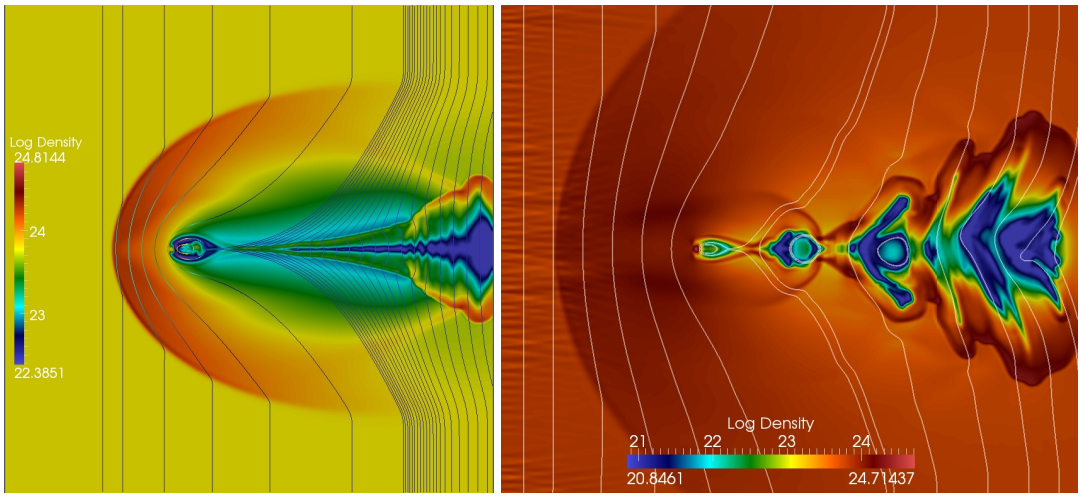

(a) $M_a = 2.2$, magnetic reconnection appears in the magnetotail.

(b) $M_a = 1.1$, plasmoids appear in the magnetotail part.

Figure 7.12: By decreasing the inflow velocity, thus increasing the characteristic time scale of the problem, plasmoids can be developped on top of the magnetic reconnection event.

case is $\tilde{t}_{\text{plasmoid}} \sim 300ns$. The reason why we only observe plasmoid features on a time scale $\tilde{t}_{\text{plasmoid}}$ is that these features all need a longer time than $\tilde{t}_{\text{reconnection}}$ to develop significantly. Those features include the storage of energy, the formation of bubbles and the bubbles being detached. Thus for this plasmoid process to occur, there has to be enough time for magnetic flux and energy to get stored in region A (refer to figure 7.8(a)) and also for region A to expand and break into two large plasma bubbles. If time is not long enough, region A gets stretched and smeared too quickly, without sufficient time for energy and flux to accumulate in the bubbles, as a result, the bubbles formed are small and hard to identify. There are also chances that the flow is too fast that the bubbles do not form at all. When the time scale $\tilde{t}$ is sufficiently short, no bubbles can form at all, resulting in a single X-point, and a single magnetic reconnection at the X point.

7.3.8 Cases with Same Upstream Mach Numbers

In previous sections, we found that bow shock structure is mainly determined by the upstream fast magnetosonic Mach number M_f. After our discussion on magnetotail structure, one could ask if M_f has a significant effect on magnetotail structure as well. To answer this question, let us go back to the three simulation results presented in Figure 7.4. It is not hard to find that, although the bow shock structure does not significantly change in these three cases, the magnetotail structure changes significantly. Thus we conclude that M_f alone cannot determine the magnetotail structure. Now we want to determine whether M_f together with M_s and M_A can determine the results. For this purpose, we carry out three tests, all with same upstream Mach numbers, but with different magnetic field magnitudes as well as different densities. The sonic Mach number, Alfvénic Mach number and magnetosonic Mach number for these three tests respectively are:

$$\begin{aligned} M_s &= \frac{v}{v_s} = 20 \\ M_A &= \frac{v}{v_A} = 2.4 \\ M_f &= \frac{v}{\sqrt{v_s^2 + v_A^2}} = 2.38, \end{aligned} \tag{7.1}$$

And for the three tests, the inflows are magnetized with magnetic fields respectively being $7.33T$, $16.4T$, $36.7T$, the corresponding flow densities are separately $1.2 \times 10^{17} cm^{-3}$, $6. \times 10^{17} cm^{-3}$ and $3. \times 10^{18} cm^{-3}$. Notice that, by doing this, we automatically hold constant the ratio of the plasma pressure to the magnetic pressure β. The results produced are as shown in figure 7.13. By observing the simulation results produced by these three cases, we can tell that they are almost identical to each other. Thus we can conclude that, in MHD simulations, results can almost be determined by the dimensionless numbers such as

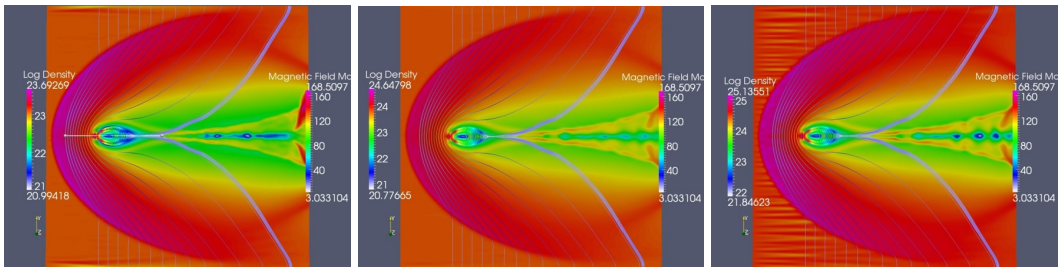

(a) $B = 7.33T$, $n = 1.2 \times 10^{17} cm^{-3}$ (b) $B = 16.4T$, $n = 6. \times 10^{17} cm^{-3}$ (c) $B = 36.7T, n = 3. \times 10^{18} cm^{-3}$

Figure 7.13: In these three tests, we vary B and ρ at the same time to keep the Mach numbers fixed ($M_s = 16.9$, $M_A = 2.24$, $M_f = 2.22$). Observation: the structures are almost identical with the same Mach numbers in MHD cases.

the Mach numbers and β. Other dimensionless numbers, like Lundquist numbers also matter, and we suppose that is the reason for the slight differences among these cases, but they do not seem to matter too much given the level of similarities among these three simulation results. We present this test also for comparison to an XMHD test with exactly the same set up and parameters. The XMHD tests will be presented later, and we will explain our findings from the comparisons at that time.

7.3.9 Results Change With the Variation of Upstream Mach Numbers

From the last section, we know that upstream/inflow dimensionless numbers, such as Mach numbers, determine the physical structure of the simulation results. In this section, we will support this argument from an opposite point of view, i.e., by merely changing the Mach numbers, the physical structures can significantly change. To reduce the dimension of complexity, we keep the mag-

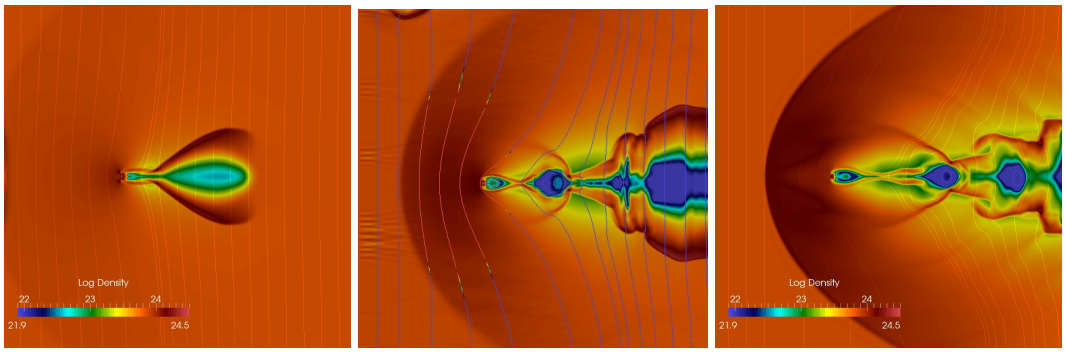

(a) $v = 50\text{km/s}$, $M_s = 4.2$, $M_A = 0.56$ (b) $v = 100\text{km/s}$, $M_s = 8.4$, $M_A = 1.12$ (c) $v = 150\text{km/s}$, $M_s = 12.6$, $M_A = 1.68$

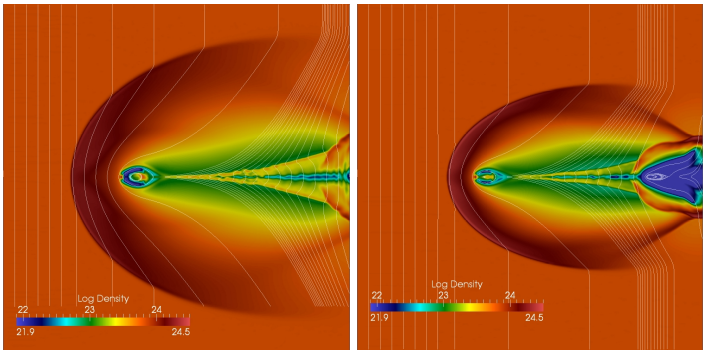

(d) $v = 200\text{km/s}$, $M_s = 16.8$, $M_A = 2.24$ (e) $v = 300\text{km/s}$, $M_s = 25.2$, $M_A = 3.36$

Figure 7.14: By changing the upstream Mach numbers through changing the inflow velocities, the phenomena including both the bow shock part and the magnetotail part change significantly.

netic field and inflow densities the same and only change the inflow velocities. Results are as shown in Figure 7.14. The velocities and corresponding Mach numbers are as stated in the caption of each figure. As velocities increase, we make the following observations:

1. **Bow shock:** When the flow is sub-Alfvénic, the bow shock does not exist at all as shown in figure 7.14(a), but starts to appear and gradually becomes more distinctive as the inflow velocities and Mach numbers increase. We also notice that the opening angle of the bow structure is decreasing at the

same time. The standard Mach theory can provide an intuition on this, which states that the opening angle θ of the Mach cone satisfies:

$$\sin\theta = \frac{v_w}{u} = \frac{1}{M}, \tag{7.2}$$

where v_w is the information transfer speed, in our case, this is roughly the propagation speed of fast magnetosonic wave v_+; M is the Mach number with the definition u/v_w. According to equation (7.2), it is obvious that θ is decreasing as the inflow velocity u increases.

2. **Magnetotail:** In the sub-magnetosonic case 7.14(a), nothing really happens except for a slight bending of the field lines. As the Mach number increases, plasmoids appear, then gradually the size of the plasmoid decreases to eventually disappears, leaving only a single X-point.

Through all these observations, one can conclude that the inflow Mach numbers can influence the physical phenomena significantly. The phenomena are so different that they can be easily identified in an XUV image. Thus, by identifying the features in a certain experimental result, one can infer the inflow properties. We will discuss this in more detail and provide examples in section 7.6.

7.4 Simulation with XMHD Model

7.4.1 Simulation Result

The problem is set up using exactly the same parameters as in the MHD simulation described in section 7.3. The result at $t = 140ns$ can be found in Figure 7.4.1. With the inflow being super-magnetosonic, a bow shock forms in front of

the obstacle, and the forming mechanism is same as explained in section 7.3.2. However, the magnetotail part is considerably different from the MHD results. The differences are due to the Hall term in the low-density region behind the obstacle. In this low-density region the Hall term suppresses current flow, preventing the current from becoming unphysically large. This can be interpreted as adding extra resistivity (i.e. Hall resistivity) in the low density region. This resistivity allows the field lines to diffuse through the low density region. While in MHD without vacuum resistivity, the current can grow unphysically high and the resistivity is very low in the low-density region, preventing the field lines from penetrating through. The unphysical current forms a current sheet that is sufficient to support an X-point behind the obstacle, then the plasma and magnetic flux piling up in front of the obstacle gets through by reconnection. This mechanism for flux transport is suppressed by the Hall term in XMHD under the conditions we have chosen for this test, thereby producing very different results. If we vary the parameters, so that the characteristic scale length is much larger than ion inertial length λ_i, then the Hall term should be rendered ineffective. Alternatively, if we do not resolve λ_i in the simulation, we will not observe the differences brought by the Hall term. Under these circumstances, XMHD results will approach the MHD results. We will do some tests to verify this in the next section.

Remark 7.2 *T*he resistivity model we are using here is isotropic resistivity, which is represented by a scalar. The term *Hall Resistivity* in this thesis refers to the resistive effect brought by the Hall term, which is different from the off diagonal term $\eta_\wedge$ in the anisotropic resistivity model.

Now let us evaluate the features in a specific XMHD simulation. We take the

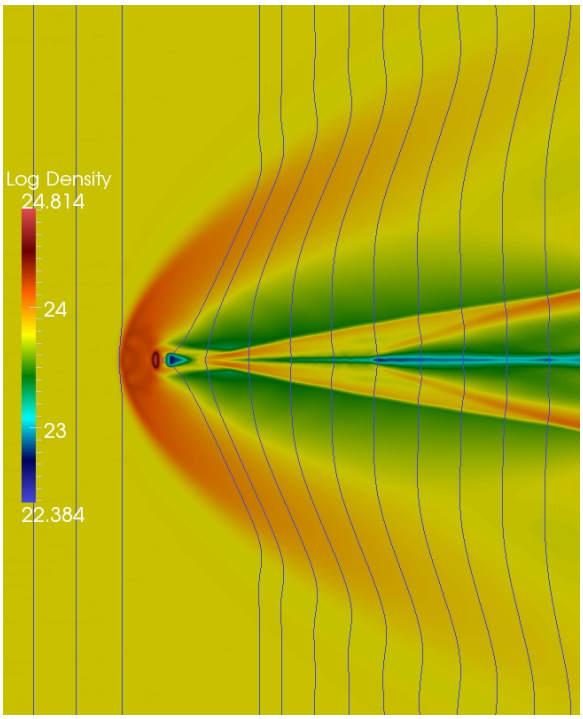

Figure 7.15: Magnetic field lines with a background color plot log(n) with XMHD. Shock-obstacle simulation with XMHD model, captured at $t = 140ns$.

simulation in Figure 7.16 as an example. As shown in Figure 7.16(a), we have a tail structure right behind the obstacle. From the magnetic field configuration in Figure 7.16(b), we can see that no X point is formed behind the obstacle, so no reconnection occurs. Thus the tail could not be an outflow from the reconnection. Now we explain how the tail forms. Through analysis done in Figures 7.16(b) and 7.16(c), we can summarize the process for forming the tail. When the incoming flow deviates around the obstacle and slows down due to the bow shock, the magnetic field lines are also draped and compressed. The variances of magnetic field introduce current with a profile shown in Figure 7.16(b) forms. Along the black line in Figure 7.16(b), the current profile is as shown in 7.16(c). Take the point **P** for example, the current at that point is negative as indicated by Figure 7.16(c), the magnetic field **B** at this point directs to the upper right,

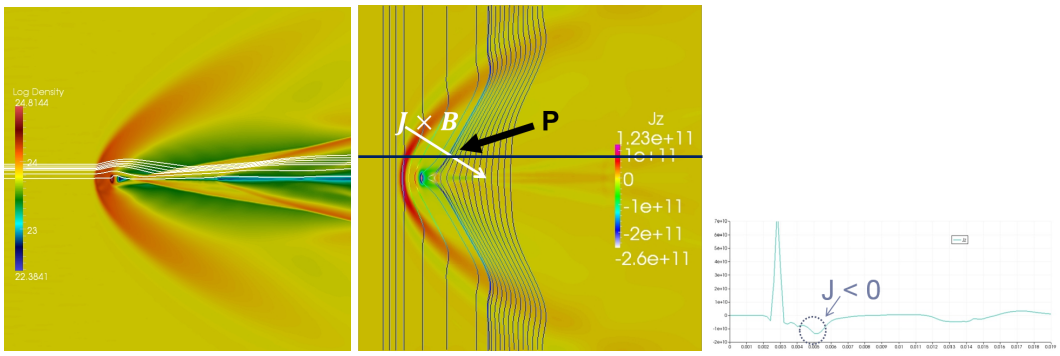

(a) Flow Lines with log(ρ) as background color

(b) Magnetic Field Lines with J_z as background color

(c) The J_z profile along the black line in subfigure (b)

Figure 7.16: Analysis of XMHD simulation of shock-obstacle problem; (c) shows the profile of **J** along the black line in (b), it is obvious at the point denoted by **P**, the current is negative, and we know that the inflow magnetic field is pointing up, which results in a $\mathbf{J} \times \mathbf{B}$ force that is perpendicular to the magnetic field line at that point directing towards the axis, and that is the main reason why the tail structure forms

resulting in a $\mathbf{J} \times \mathbf{B}$ normal to the magnetic field line pointing down and right towards the central axis. This $\mathbf{J} \times \mathbf{B}$ force accelerates and compresses the plasma onto the central axis. Since the geometry is symmetric about the central axis, we also have flow coming towards the central axis from the lower part, when these two flows collide together, the compression heats the plasma and a bright tail forms along the central axis.

7.4.2 Cases with same upstream Mach numbers

In a manner similar to section 7.3.8, we carry out three tests here with XMHD model all with same upstream Mach numbers, but with different magnetic field magnitudes as well as different densities. The sonic Mach number, Alfvénic Mach number and magnetosonic Mach number for these three tests respectively

are:

$$
\begin{aligned}
M_s &= \frac{v}{v_s} = 20 \\
M_A &= \frac{v}{v_A} = 2.4 \\
M_f &= \frac{v}{\sqrt{v_s^2 + v_A^2}} = 2.38,
\end{aligned}
\tag{7.3}
$$

And for the three tests, the inflows are magnetized with magnetic fields respectively being 7T, 15T, 32T, the corresponding flow densities are separately $1.2 \times 10^{17} cm^{-3}$, $6. \times 10^{17} cm^{-3}$ and $3. \times 10^{18} cm^{-3}$. The results produced are as shown in figure 7.17. The differences among these three cases are significant. However, when we did this test with MHD model as discussed in section 7.3.8, the differences are almost negligible. So the difference among the three results of XMHD model is must due to non-MHD terms. From these results, we have the following observations as we increase the density ρ and magnitude of B:

1. Shape of magnetic field changes, from almost no bending due to the obstacle, to being so significantly bent such that an X point forms behind the obstacle.

2. Density profile also changes, as we increase both ρ and B, the density is more concentrated towards the center line, that is because the field lines are bent more, so that the $\mathbf{J} \times \mathbf{B}$ force directs more flow towards the center, and forms a more concentrated tail.

3. XMHD approaches the MHD results as we increase ρ and B. Actually, we can make the XMHD results agree with MHD results when we increase the density to a regime where the non-MHD terms in XMHD are not effective. We will discuss this later in a section where we compare XMHD results with MHD results.

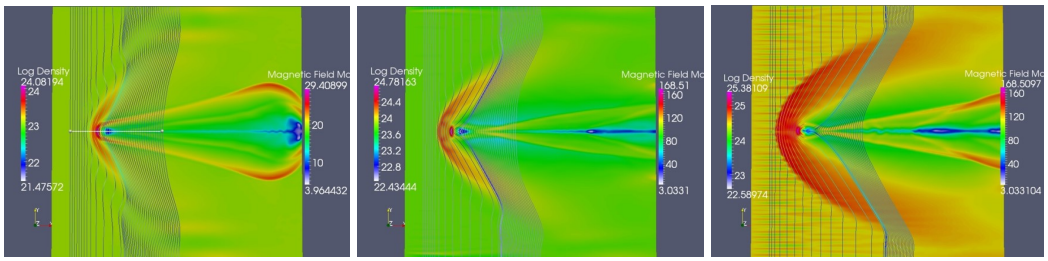

(a) $B = 7.33T$, $n = 1.2 \times 10^{17} cm^{-3}$ (b) $B = 16.4T$, $n = 6. \times 10^{17} cm^{-3}$ (c) $B = 36.7T$, $n = 3. \times 10^{18} cm^{-3}$

Figure 7.17: In these three tests, we vary B and ρ at the same time to keep the Mach numbers fixed ($M_s = 16.9$, $M_A = 2.24$, $M_f = 2.22$). Observation: the structures change a lot.

As discussed earlier, all these differences should be caused by non-MHD terms in XMHD model. We know that the most important non-MHD term on the scale $L \sim \lambda_i$ is the Hall term. We explained earlier that the Hall term plays an important role in the region behind the obstacle by suppressing the current in that region through Hall resistivity. The importance of the Hall term is largely dependent on the ratio of length scale to the ion inertial length λ_i. In these three test cases, we change the density, thus λ_i is changed, and consequently the impact of the Hall term is changed. The main effect of the Hall term in these cases is the change in the Hall resistivity affecting the rate of diffusion of the magnetic field and hence the different magnetic configurations in Figure 7.17.

7.4.3 Results Change With the Variation of Upstream Mach Numbers

In this section, we change the inflow Mach numbers to evaluate the changes due to different inflow Mach numbers. We keep the magnetic field and inflow densities the same and merely change the inflow velocities. Results are as shown in

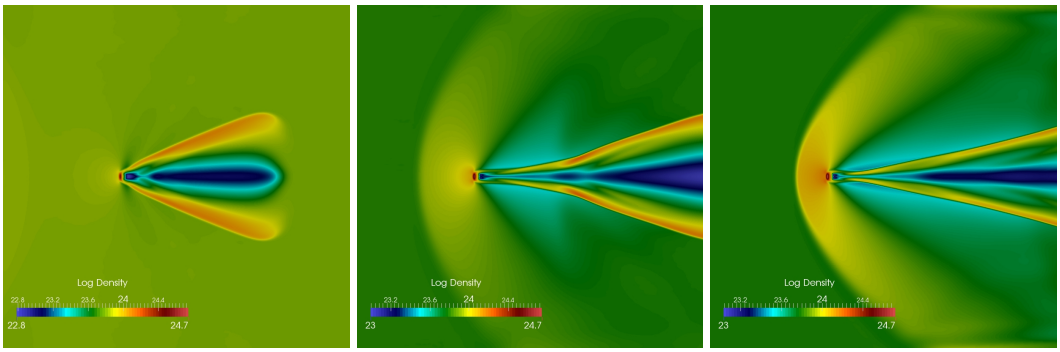

(a) $v = 50\text{km/s}$, $M_f = 0.55$ (b) $v = 100\text{km/s}$, $M_f = 1.1$ (c) $v = 150\text{km/s}$, $M_f = 1.65$

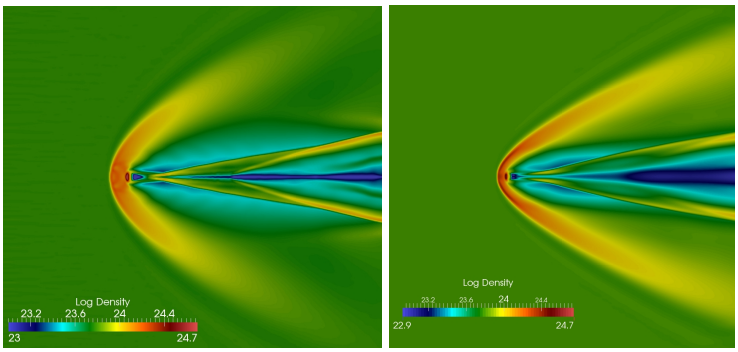

(d) $v = 200\text{km/s}$, $M_f = 2.2$ (e) $v = 300\text{km/s}$, $M_f = 3.3$

Figure 7.18: By changing the upstream Mach numbers through changing the inflow velocities. Upstream $\beta = 0.012$ is kept a constant. The features, especially the bow shock region changes significantly.

Figure 7.18. The velocities and corresponding Mach numbers are as stated in the caption of each figure.

Just as in the MHD case, with XMHD model, the bow shock structures also change significantly in these five cases. When the flow is sub-magnetosonic as in figure 7.18(a), we do not observe any bow shock structure. When the flow goes slightly super-magnetosonic, the bow shock starts to appear, but is very weak. The bow shock structure gradually becomes more distinctive as the inflow velocities and Mach numbers increase. Meanwhile, we notice that the opening angle of the bow structure is decreasing. The change of the physical

structures is so obvious that one can infer the inflow Mach number by observing the physical structures produced. Potentially, it could be used as a diagnostic of speed in the experiment. No bow shock or a dim bow shock implies that $M_f \leq 1$. A strong bow shock implies $M_f > 1$, considering $M_f = 1/\sqrt{\frac{1}{M_s^2} + \frac{1}{M_A^2}}$, we have $M_s > M_f > 1$ and $M_A > M_f > 1$, thus we can infer that the flow is both supersonic and super-Alfvénic.

7.4.4 Results Change With the Variation of Upstream β

In this section, we will show that the ratio of thermal pressure to magnetic pressure β of the inflow also has an influence on the downstream structures. We carry out a series of simulations, where we keep the upstream magnetosonic mach number $M_f = 2.4$ as a constant, but vary the upstream β. The sound speed and Alfvén speed are varied accordingly through the variations of temperature and magnetic field. Results are as shown in Figure 7.19, where the colorplot shows the $\frac{\log P}{\log P_0}$. P_0 is the initial pressure, also is the pressure value in the background area which is not perturbed by the presence of the obstacle. The reason we choose to plot pressure here is, we want to compare this result with the XUV image, which shows the XUV radiation. The XUV radiation is related to both temperature and density, but the form of the relationship is not known exactly. Thus we want to pick the most convenient variable that is related to both temperature and density, so we picked pressure as $P = \rho T$ in our model. The magnetic field magnitude and β are as stated in the caption of each figure. As β decreases, we make the following observations:

1. **Bow shock:** the shape and thickness of the bow shock does not change

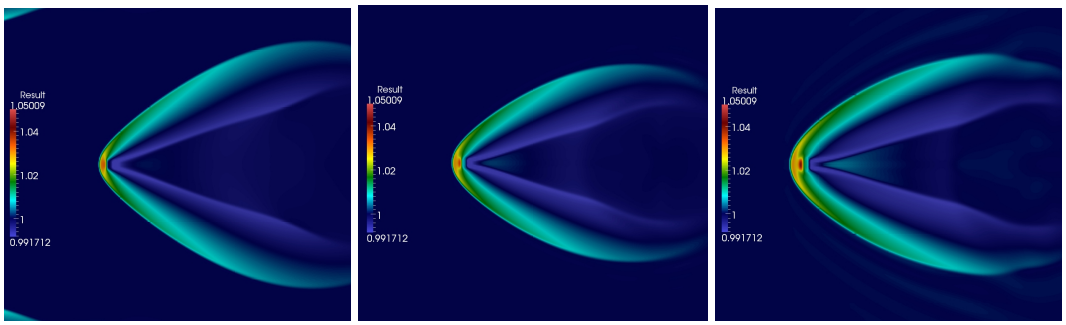

(a) $\beta = \infty$, $B = 0$T, $M_f = 2.4$ (b) $\beta = 3$, $B = 6.96$T, $M_f = 2.4$ (c) $\beta = 1.27$, $B = 8.7$T, $M_f = 2.4$

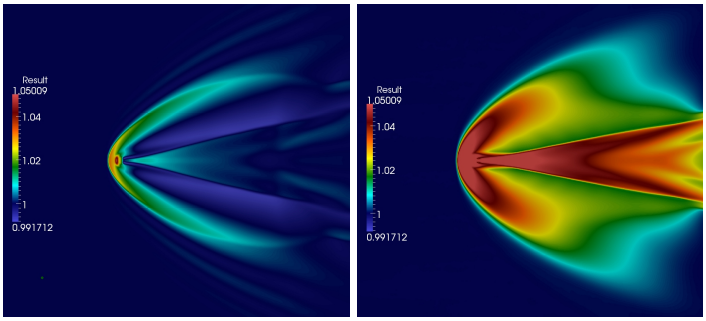

(d) $\beta = 0.4$, $B = 11.6$T, $M_f = 2.4$ (e) $\beta = 0.016$, $B = 15.08$T, $M_f = 2.4$

Figure 7.19: Color Plot of $\frac{\log P}{\log P_0}$, P_0 is the background pressure. By changing the upstream pressure ratio β through changing the inflow magnetic field and temperature, the phenomena, especially the tail region changes significantly.

very much, supporting the point that the bow shock is mainly determined by magnetosonic mach number M_f.

2. **Magnetotail:** as β decreases, which means the magnetic pressure is playing a more and more important role, we can observe that the tail structure is becoming stronger and stronger. In the last case shown in Figure 7.19(e), the tail is the strongest.

Through the observations above, one can conclude that the upstream β can significantly influence the tail structure. The tail structure will become stronger as the β decreases. When the magnetic force is taking control, the tail is the

strongest. The phenomena are so different that they can be easily identified in an XUV image. Thus, by identifying the features in a certain experimental result, one can infer the inflow properties. For example, when one does not observe any tail structure, that would probably mean that the physics is primarily driven by thermal pressure. On the other hand, if the tail structure is very strong, that means the physics is magnetically driven. We will discuss this in more detail and provide examples in section 7.6.

7.5 Comparison between the results of extended-MHD and MHD

In sections 7.4 and 7.3, we respectively discussed the shock-obstacle simulation with XMHD model and MHD model. As we noted, the results achieved are very different with these two models. The main difference between MHD and XMHD is summarized in Figure 7.20. The MHD result is shown in Figure 7.20(a) and the XMHD result shown in Figure 7.20(b). The key for the difference is the Hall term. As discussed in section 7.4.1, the Hall term suppresses the current in the low density region behind the obstacle, thus changing the magnetic field configurations. A question naturally arises that if we change the simulation parameters to render the Hall term ineffective, can we make the XMHD results approach the MHD results? On the other hand, if we also provide a resistivity in low-density regions that acts like the Hall resistivity, can we make the MHD results approach the XMHD results? In this section, we will carry out simulations to answer these two questions.

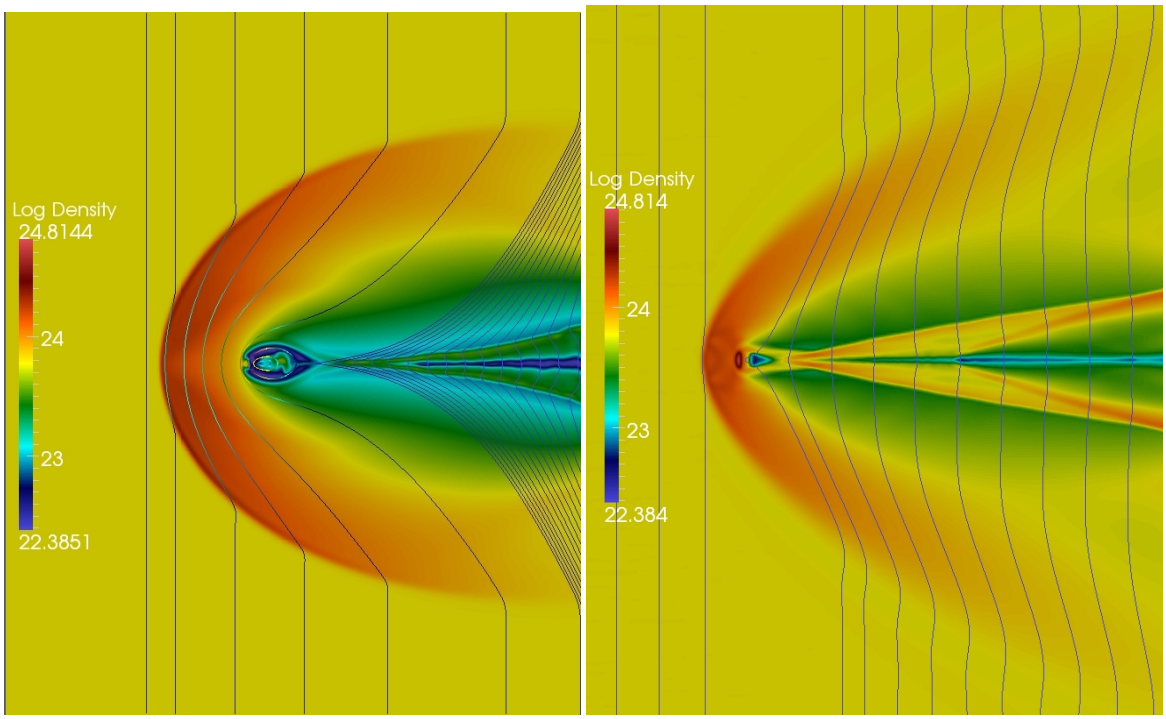

(a) Magnetic field lines with a background color plot $\log \rho$ for MHD

(b) Magnetic field lines with a background color plot $\log \rho$ for XMHD

Figure 7.20: Shock-obstacle simulation for MHD model and XMHD model, captured at $t = 140ns$

7.5.1 XMHD results to approach MHD results

For XMHD results to approach MHD, the Hall effect has to be rendered ineffective. The importance of Hall term can be quantified by its coefficient in Generalized Ohm's Law, which is proportional to λ_i/L. Thus, either by decreasing λ_i or increasing L, we can achieve this.

1. Decreasing λ_i: We can increase density to decrease λ_i, so as to make the Hall term less important. Here we provide an example with $dx/\lambda_i = 1.9$, i.e., the ion inertial length in the initial condition is under-resolved. The result is as shown in Figure 7.21. Besides increasing density, we also

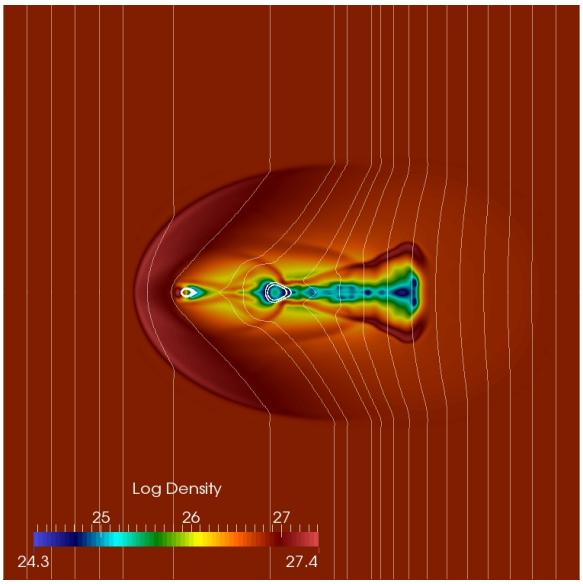

Figure 7.21: Magnetic field lines with a background color plot $\log \rho$ with XMHD; $dx/\lambda_i = 1.9$; Captured at 100ns.

increased magnetic field accordingly, so as to keep the Alfvén speed the same. For reference, ion inertial length is well resolved in Figure 7.20(b) with $dx/\lambda_i = 0.19$. Clearly from result 7.21, both reconnection and plasmoids occur. The field lines piled in front of the obstacle do not purely diffuse through, they get through by reconnection, just as in the MHD simulation with the same parameters. So when we are in a regime where ion inertial length is under resolved, the effects due to the Hall term are not obvious, and the XMHD results will approach MHD results. We notice that the parameters used in this simulation are achievable in the lab, so experimentalists can design experiment with these parameters to study the physics of reconnection and plasmoids in the lab.

2. Increase the scale length of the problem. We can change the scale of the obstacle to influence the scale length of the problem. If the diameter of the obstacle is much larger than λ_i, the Hall term will not matter at least in the

front portion of the region. Since in that region, the scale of the problem is related to the diameter of the obstacle. Let us do a simulation test to support this argument.

Now we increase the size of the obstacle to a cylinder with diameter $d = 6.17\lambda_i$. Note that $d \gg \lambda_i$, and the scale length of the whole problem is increased accordingly to much larger than the ion inertial length. Figure 7.22 shows the simulation results with both MHD and XMHD models. From these results, we can see that the front portion of the simulation region are very similar to each other, including the bow shock part, the way that the magnetic field lines get bent, and also the position where an X-point forms. This supports our argument that when we change the scale length of the problem to be much larger than λ_i, the Hall term will be rendered ineffective and the XMHD results will approach MHD results. However, the reconnection outflow part. One main difference in 7.22(a) and 7.22(c) is that in MHD results, there is a clear slow shock structure as indicated in the zoomed-in section in Figure 7.22(a). As discussed earlier in this thesis, the slow wave gets cut off in the Hall regime. Behind the obstacle, the length scale does not depend on the scale of the obstacle any more, and we enter the Hall regime. Thus we do not see the slow shock structure in the XMHD results. The MHD tail is much thinner than an XMHD tail and the X-shape opens up more in XMHD than in MHD. We know that the Hall term can facilitate reconnection [41]. The fact that the X-point opens up larger in XMHD suggests that reconnection is faster in this case according to Sweet-Parker's orginal theories [55, 43]. We will talk more about this property of the Hall term in section 7.7, where differences between XMHD and MHD results are more significant.

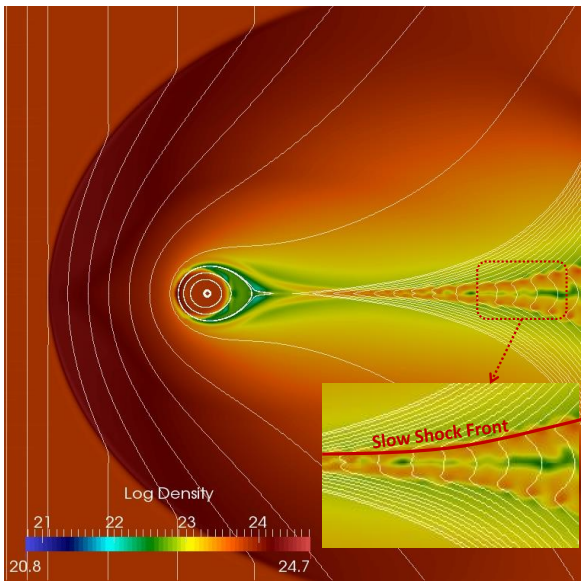

(a) Magnetic field lines with a background color plot $\log\rho$ with MHD model, the slow shock region is zoomed in, with slow shock front indicated by a red line

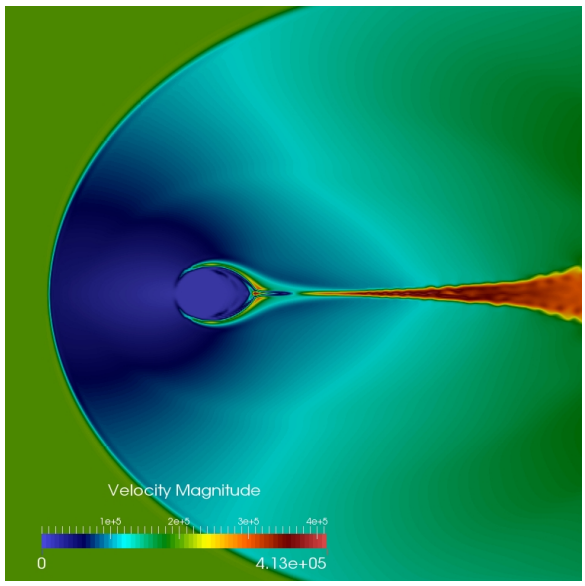

(b) Color plot on magnitude of velocity field $|\mathbf{v}|$ with MHD model

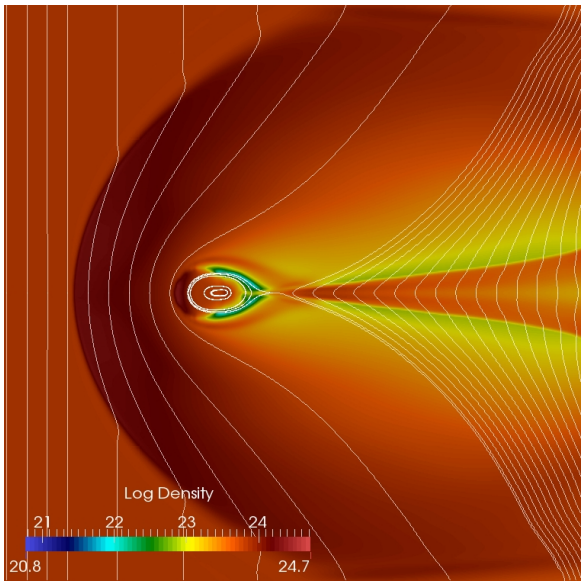

(c) Magnetic field lines with a background color plot $\log\rho$ with XMHD

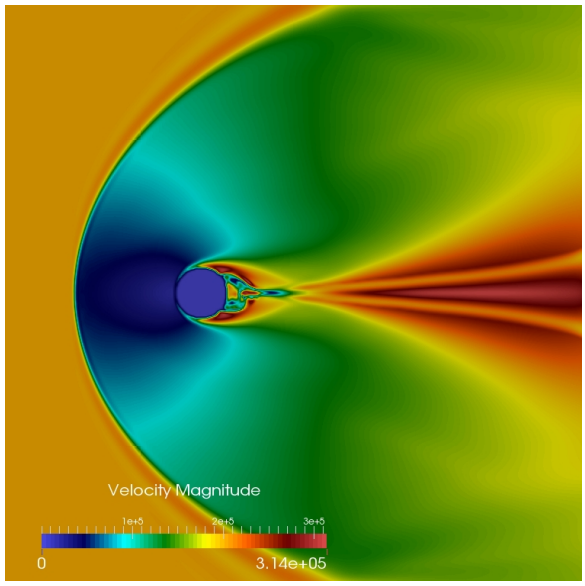

(d) Color plot on magnitude of velocity field $|\mathbf{v}|$ with XMHD model

Figure 7.22: Simulation results with larger obstacle with a diameter of $d = 6.17\lambda_i$, captured at $t = 184ns$. From the pictures, the front portion of the XMHD and MHD results are close to each other.

7.5.2 MHD results to approach XMHD results

Now let us answer the second question: if we artificially provide a resistivity in the low-density regions that acts like the Hall resistivity, will the MHD results approach the XMHD results? To test on this, we use a modified resistivity model for simulating the problem:

$$\eta = \eta_s + \eta_0 \frac{\rho_{floor}}{\rho}, \tag{7.4}$$

where η_s is the Spitzer resistivity, η_0 is the arbitrarily chosen vacuum resistivity coefficient, $\rho_{floor} = 10^{-9}$ in code unit defined in table 4.1. Here, we chose $\eta_0 = 2 \times 10^4$ in the code unit.

The results produced are in Figure 7.23, which show that the MHD results agree much better with the XMHD results. However, one does not know *a priori* the spatial form or value needed for the vacuum resistivity to achieve physical results. To conduct such a test with MHD model, one would first have to perform the more realistic XMHD simulation to which the MHD simulation could be adjusted to fit the results. This reveals the advantage of XMHD over MHD since one can use the realistic Spitzer resistivity model without any artificial modifications. This allows the self-consistent and physical transition from high density to low density regions. Moreover, one should not conclude that including a vacuum resistivity into the MHD equations is sufficient to recover all of the effects of the Hall term. Suppression of low-density currents is only one effect of the Hall term. The Hall modification of the electric field cannot be modeled by a vacuum resistivity and can generate anode-cathode asymmetries [21], enhanced magnetic reconnection [5], and can lead to instabilities not present in MHD [37] or instabilities modified by the Hall term [29, 30]. We will talk about one of these effects by the Hall term in later sections in this chapter, that is how

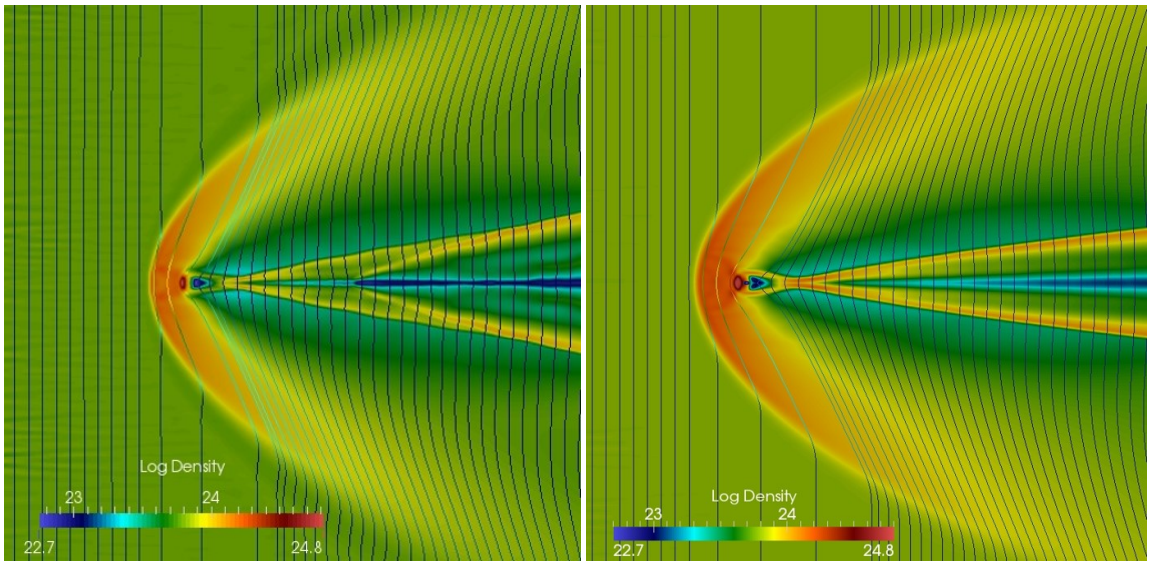

(a) Magnetic field lines with a background color plot $\log \rho$ with XMHD

(b) Magnetic field lines with a background color plot $\log \rho$ with MHD

Figure 7.23: Figure 7.23(b) shows the MHD simulation with the resistivity: $\eta = \eta_s + \eta_0 \frac{\rho_{floor}}{\rho}$, η_0 is chosen to be consistent with Hall resistivity. We can see that by changing the resistivity model, the MHD results become much more similar to the XMHD results.

the Hall effect facilitates reconnection.

7.6 Evaluation of Experimental Results

As explained in 7.1, we were motivated to study the flow-obstacle interaction to use as a diagnostic for the outflow in the two-wire magnetic reconnection experiment using XUV radiography. With this purpose, we put an obstacle in the outflow, and the XUV image for this is generated in Figure 7.24(a). The shock configuration formed by the interaction between outflow and the obstacle gives us a better insight into the properties of reconnection outflow.

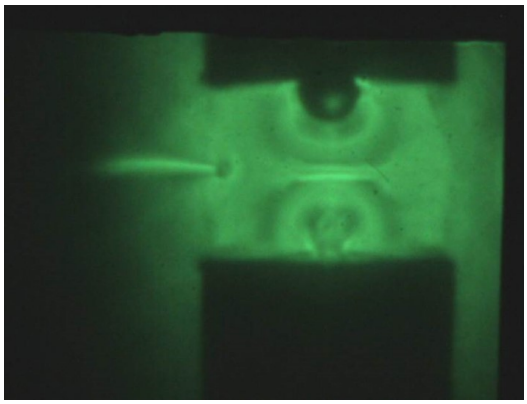

(a) XUV image of two-wire magnetic reconnection experiment with an obstacle in the outflow stream

(b) Enlargement of the interaction between the flow and obstacle

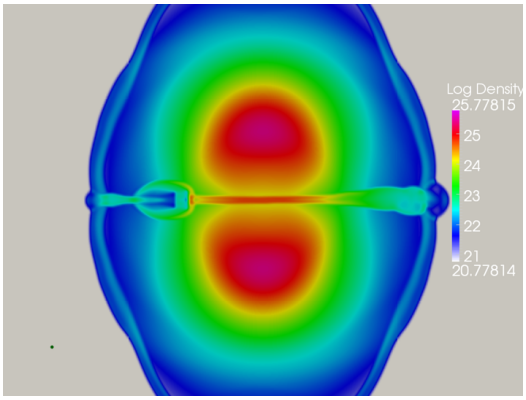

(c) Simulation of two-wire magnetic reconnection with an obstacle in the outflow stream, contour plot of $\log(\rho)$

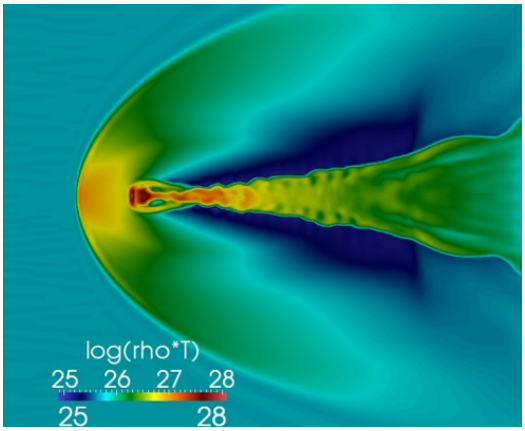

(d) Simulation of the interaction between flow and obstacle, contour plot of $\log(\rho^2 T)$

Figure 7.24: Experiments of two-wire reconnection with an obstacle in the outflow region, and the corresponding simulations.

The first obvious feature in XUV image is the bow shock. As we explained earlier, the bow shock can form whenever a disturbance propagates faster than the information transfer speed. In the hydrodynamic case, that would mean the disturbing source is travelling faster than the sound wave. In a magnetized fluid, the presence of the bow shock would suggest that the disturbing source is travelling faster than the fast magnetosonic speed. Now the question arises whether this is a magnetized or un-magnetized case. For answering this ques-

tion, we need to refer to the second feature.

The second obvious feature is a bright tail starting immediately from the obstacle. Since this is an XUV image showing the radiation profile, it suggests that the tail is a concentration of mass or temperature. In both the MHD and XMHD simulation, we found this bright tail structure. The formation in the tail structure in XMHD simulation as shown in Figure 7.23(a) is due to the $\mathbf{J} \times \mathbf{B}$ force. On the other hand, in the MHD simulation shown in Figure 7.20(a), the tail forms as the reconnection outflow, which is bounded by the slow shock. In both cases, the tails are magnetically driven. Now we examine whether the converse of this conclusion is still true, that is if we observe a bright tail, whether it has to be driven by magnetic force.

To answer this question, we do a pure hydrodynamic simulation, and the result is as shown in Figure 7.25. We set up this problem such that the sonic Mach number is equal to the fast magnetosonic Mach number. We clearly get a bow shock structure, but the high density/temperature tail is missing. Thus we conclude that for the appearance of the tail, magnetic field has to present.

Now, does the orientation of the magnetic field play a role here? Again, we notice that for achieving both the magnetic reconnection configuration, or the redirection of the flow towards the central line, the magnetic field has a component that is in plane and perpendicular to the flow direction, which is the direction **y**, or at least has a component on that direction. Is there any chance that we still get a tail structure with zero magnetic field projection on the **y** direction? We also carry out a simulation to test on this case. If **B** lies in the $x - z$ plane, then B_y is 0. We test on an extreme case where **B** is purely on the **z** direction. For the definitions of **x**, **y**, **z**, refer to Figure 7.1(b). As shown in

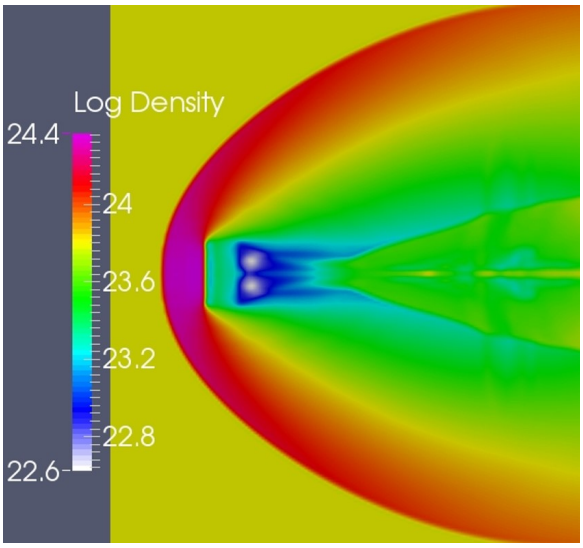

Figure 7.25: Hydrodynamic simulation, bow shock feature is clear, but the bright tail feature is missing; thus does not agree with the experiment.

figure 7.26, we did a simulation test with **B** of the same magnitude into the plane. We did not detect a clear bright tail feature. The result shows that the orientation of the driving magnetic field also matters to the appearance of the tail structure. Our simulation tests show that the tail structure only appears when magnetic field has a component of **B** perpendicular to the direction **u** in the plane perpendicular to the cylinder.

Apparently, the tail structure only occurs when β is small enough, i.e., the magnetic pressure is sufficiently important compared to the thermal pressure, with which we can guarantee the phenomena is a magnetically dominated event, instead of a quasi-hydrodynamical event.

With all that discussed above together with all the analysis in the previous sections, we can gain some insight into the flow in the two-wire magnetic reconnection experiment shown in Figures 7.24(a) and 7.24(b):

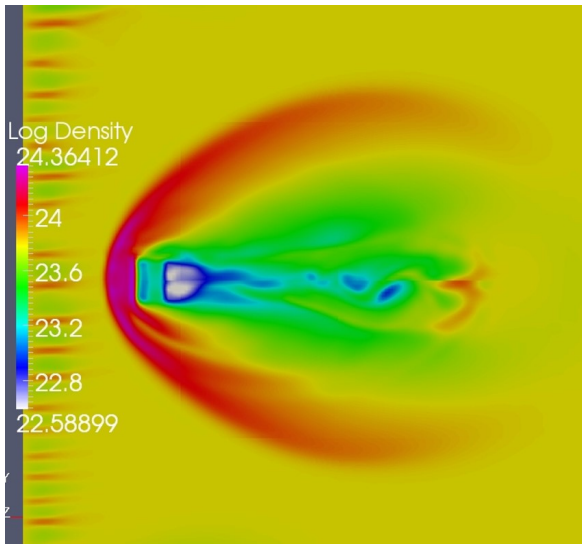

Figure 7.26: Simulation with magnetic field into the plane, bow shock feature is clear, but the bright tail feature is missing; thus does not agree with the experiment. The striations at the left boundary are due to an instability that we have not studied in detail.

1. The flow direction: the direction of the tail should be the direction of the inflow, with the assumption that there are no significant forces for changing the tail direction other than the inflow and the magnetic field lines associated with the inflow.
2. The appearance of the bow shock shows that the flow is super-fast-Magnetosonic, i.e., $M_f > 1$.
3. The appearance of the tail following the obstacle implies that there is a component of magnetic field perpendicular to the inflow and is in the simulation plane.
4. The tail being bright means that the magnetic pressure is dominating, and $\beta < 1$ in the inflow.

As a summary, the reconnection outflow shown in the XUV image 7.24(a) is

super-magnetosonic, **B** has a component that is perpendicular to the flow direction, and $\beta < 1$.

Let us evaluate another circumstance as shown in the XUV image 5.10 (b). In this experiment, no bright bow shock is observed, however, we still observe a slightly darker, diverging wing-shaped wake. This case can be matched to the simulation test done in Figure 7.18(a), where the inflow is sub-Alfvénic and sub-magnetosonic. So we can safely conclude that the outflow in this case is magnetized, but possesses a speed that is less than v_+ or v_A. In this case, the driving current follows a crowbarred pulse, i.e., the driving current does not decrease, thus the reverse skin effect does not happen. The outflow is driven out purely by the pressure gradient ∇, and cannot reach a speed as high as v_A. A message delivered in this case is that, the appearance of the tail structure does not necessarily come together with the appearance of a bow shock. When we only observe the tail structure but no bow shock, it suggests that the flow is magnetized but sub-magnetosonic.

7.7 Hall Term Facilitates Reconnection

Now we study the functionality of Hall term on a different parameter scale, i.e., the interplanetary scale. Actually, we utilize the solar wind parameters and the Mars parameters, and are simulating a problem with the solar wind interacting with Mars except for the fact that we are using a cylinder (due to the limitation of a 2D simulation). The inflow parameters can be found in section 8.2.1. We use this as an example here to show how the Hall term facilitates or enhances the reconnection rate. In the next chapter, we will explain more about this pa-

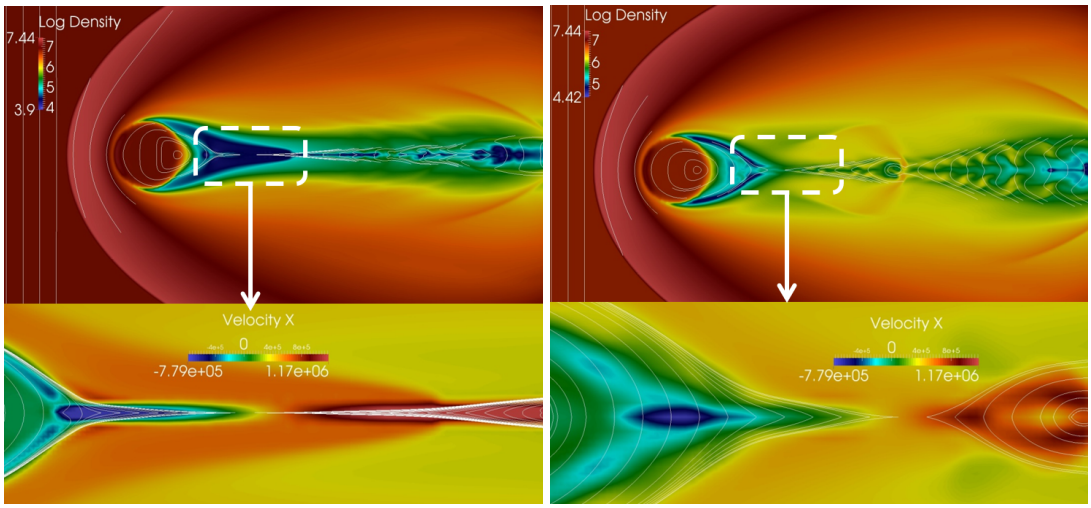

(a) MHD simulation of solar wind-Mars interaction; Density plot of log(ρ)

(b) XMHD simulation of solar wind-Mars interaction; Density plot of log(ρ)

Figure 7.27: The MHD simulation of Mars (a) reveals significant difference from the XMHD simulation (b), especially in the tail part. The main reason is due to the fact that Hall term can facilitate reconnection, making the reconnection rate faster; For that reason, we can observe the X-shape opens up more

rameter space, and we will do 3D simulation for a more realistic modeling of Mars and other rocky planets.

For the parameters we used to study Mars, we have $\frac{\lambda_i}{\mathrm{d}x} = 1$ in the inflow region, in this regime, XMHD should converge to MHD, as explained in the earlier sections. The non-MHD effect, including the Hall effect, should not be obvious in this regime. This hypothesis is supported by simulation results presented in Figure 7.27, XMHD result is in Figure 7.27(b), and MHD result in Figure 7.27(a). We found from the figures that the inflow region and the bow shock region of an XMHD result almost agree with the MHD simulation result. The tail parts also look quite similar, except for the reconnection region. In the reconnection region, the difference is significant. If we look at the whole process, we will find that the plasmoid appears much earlier in XMHD than MHD,

and the whole region is significantly more distorted by the plasmoids than in MHD case. Two issues to consider here are: first, the density drops off behind the obstacle making the Hall terms more significant, secondly, the Hall term can facilitate reconnection [41]. From the two simulations as shown in Figures 7.27(a) and 7.27(b), it is rather clear that the X shape in XMHD opens up more than in MHD. Based on Sweet-Parker's classical theory, this is clear evidence that the reconnection in XMHD is faster. This also explains why the plasmoids appear earlier and are larger in XMHD simulations. The clear differences between MHD and XMHD results in turn provide direct evidence that Hall term facilitates magnetic reconnection, without having to analytically compute the magnetic reconnection rate.

As a summary of the implications of the Hall term in the shock-obstacle simulation, the Hall term mainly reveals its significance in two ways: 1. Provided that the inflow is in the regime where Hall term is important as well as the scale length of the problem is comparable to λ_i, the Hall term suppresses the current in vacuum or low density regions, thus allows the field lines to diffuse through; while with an MHD model without vacuum resistivity, there is not enough diffusion to help the magnetic field lines piled up in the front to diffuse through, so they have to get through via reconnection. These two processes are considerably different, as shown in Figure 4.8(a) and Figure 4.8(b). 2. When the problem is in the regime where reconnection emerges behind the obstacle, since the Hall term can facilitate reconnection, the XMHD results also turn out significantly different from MHD results.

7.8 Biermann Battery Effect

Equation (2.36) can be reformatted into:

$$\mathbf{E} = \frac{m_e}{n_e e^2}\left(\partial_t \mathbf{J} + \nabla\cdot\left[\mathbf{J}\mathbf{u} + \mathbf{u}\mathbf{J} - \frac{1}{Zen}\mathbf{J}\mathbf{J}\right]\right) - \frac{m_e}{n_e e}\nabla P_e + \eta\mathbf{J} + \frac{1}{n_e e}\mathbf{J}\times\mathbf{B} - \mathbf{u}\times\mathbf{B} \quad (7.5)$$

Substitute 7.5 into (2.34), we have:

$$\frac{\partial \mathbf{B}}{\partial t} = -\nabla\times\left\{\frac{m_e}{n_e e^2}\left(\partial_t \mathbf{J} + \nabla\cdot\left[\mathbf{J}\mathbf{u} + \mathbf{u}\mathbf{J} - \frac{1}{Zen}\mathbf{J}\mathbf{J}\right]\right) - \frac{m_e}{n_e e}\nabla P_e + \eta\mathbf{J} + \frac{1}{n_e e}\mathbf{J}\times\mathbf{B} - \mathbf{u}\times\mathbf{B}\right\} \quad (7.6)$$

A battery effect is a thermoelectric effect that can generate an electric/magnetic field with a zero initial electric/magnetic field. Thus we only keep the terms in (7.6) that are nonzero when **B**, **E**, **J** are zeroed out. Then equation (7.6) becomes:

$$\begin{aligned}\frac{\partial \mathbf{B}}{\partial t} &= \nabla\times\left\{\frac{m_e}{n_e e}\nabla P_e\right\} \\ &= -\frac{m_e \nabla n_e \times \nabla P_e}{e n_e^2}\end{aligned} \quad (7.7)$$

We notice that the right hand side of Equation (7.7) does not depend on **B** or **E**, meaning it still exists even if the system starts without an electric/magnetic field. So if the spatial variances of electron density ∇n_e and ∇P_e satisfy $\nabla n_e \times \nabla P_e \neq 0$, magnetic field **B** can be generated. This effect is named the Biermann Battery Effect after Biermann [4].

We carry out a simulation test with the set up 7.1(a), but without applying magnetic field. The result is as shown in 7.8, which clearly shows that a magnetic field perpendicular to the plane exists. The obstacle disturbs the incoming flow, and causes the spatial variance of n_e and P_e. This results in a non-zero RHS of equation (7.7), thus a magnetic field is generated. The corresponding currents flow in the bow shock region towards the obstacle and the return currents flow from the obstacle down the tail. During this process, other forms of energy are converted into magnetic energy.

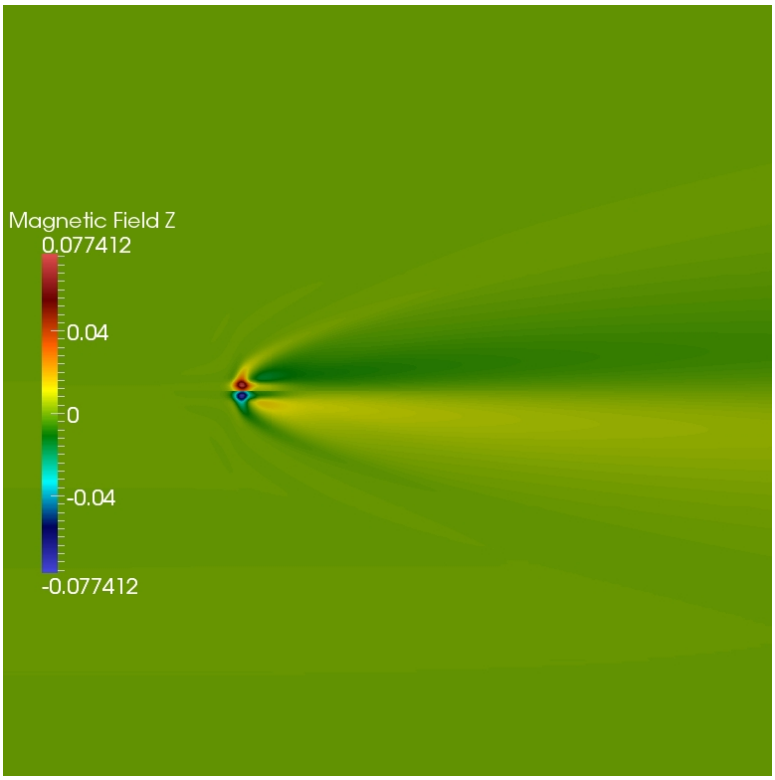

Figure 7.28: Color Plot of B_z. Inflow from the left boundary into an obstacle. The presence of the obstacle caused a spatial variance of electron density and a spatial variance of P_e, this results in a non-zero $\nabla n_e \times \nabla P_e$, which means, the RHS of (7.7) is nonzero, that induces a magnetic field. Since the spatial variances of n_e and P_e are both in plane, $\nabla n_e \times \nabla P_e$, if nonzero, has to be out of plane, which means that B_z is induced.

CHAPTER 8

SIMULATION ON INTERPLANETARY PHYSICS OF MARS

The same set up as described in the last chapter with the right parameters can be used to model interplanetary (IP) physics. Physics in IP space are of considerable interest, which include kinetic effects, the energy dissipation mechanism of IP shock waves, and nightside behavior such as magnetic reconnection.

We choose to study the interaction processes between the solar wind and Mars. Although a strong ancient intrinsic magnetic field existed long time ago [35]. Mars does not have an appreciable intrinsic magnetic field at present. For this reason, we can safely assume Mars as unmagnetized, and model it as a nonmagnetized object. Modeling Mars or other weakly or nonmagnetized planets helps to avoid the complexity raised by accurately modeling an intrinsic magnetic field.

We set up the simulation with DG-PERSEUS in 3D Cartesian coordinates. We set the parameters of inflow from left boundary with averaged values of parameters of solar winds at the distance of Mars. Mars is represented by an impenetrable sphere. We use the XMHD model to study this problem.

In previous chapters, we have demonstrated the feasibility to carry out an experiment to study the interaction between Alfvénic flow and an impenetrable obstacle. In this chapter, we scale the parameter regime of Mars down to the laboratory regime. Simulation results suggest that the simulated Martian phenomena can also be achieved with lab parameters. If we can set up an experiment based on these parameters, which is a slight modification of our shock-obstacle experiment, we can study the IP problem in the lab.

We need to point out here that, although we try to be as realistic as possible, there are certain limitations preventing the simulation from being more accurate. Firstly, our code is based on a fluid model, thus we are not able to study the wave-particle related dissipation mechanisms and kinetic effects in this problem. Secondly, we do not include radiation physics in our model, thus radiation is not modeled. Thirdly, Mars has local crustal magnetic sources which are too complicated to be considered here. Lastly, the solar wind varies over time, which is also beyond our scope for now.

8.1 Solar wind Interaction of Planets

The Sun has an appreciable amount of magnetic energy which is the driver of most solar and geomagnetic activities. The solar wind is released from corona of the Sun. It was long believed that solar wind is accelerated out by thermal energy. Until 1960s, it was clearly found that thermal acceleration alone cannot account for the high speed of solar wind. Magnetic fields are now believed to be an additional source of the acceleration mechanism of solar wind. [69]

Roughly 10^9 kg of mass per second is expelled from the sun at speeds in a range of roughly 300 km/s to over 800 km/s [59]. The temperature of the solar wind is in the range of $1.4 - 1.6 \times 10^6 K$.

The solar wind has a tremendous effect on all bodies in the solar system. Some planets, like Earth, Jupiter, Saturn and Uranus, have intrinsic magnetic fields. Others, like Mercury, Venus and Mars, possess much weaker magnetic fields. The reason for these differences has to do with the properties of the interiors of these planets, which is beyond the scope of this study. In this section,

we only discuss the Earth and the Mars, respectively as the representatives of intrinsic magnetic field planets and unmagnetized planets. Previous studies [40, 18, 33] show that the solar wind produces different environments when it interacts with these two planets, but they also share some common features [40], such as: 1. they both include a bow shock upstream of the obstacle that slows and deflects the solar wind; 2. they both have a region between the shock and the planet, where the solar-wind plasma and magnetic field are compressed. This region is called magnetosheath; 3. if the interplanetary magnetic field (IMF) is oriented at a substantial angle to the solar wind, then the field will appear to drape around the obstacle.

The study of the interaction between the solar wind and the Earth has been presented in numerous papers. Here we briefly review the behavior of the interaction. The magnetic pressure of the Earth's internal dipolar field is able to balance the dynamic pressure of the incoming solar wind. The area where this balance is reached is called magnetopause. On the night side, a magnetotail forms, which is composed of stretched-out dipole field lines as an extension to the magnetic polar regions of the planet. The tail contains two lobes, referred to as the northern and southern tail lobes. The two lobes are separated by a plasma sheet, where there is a neutral point with the magnetic field canceled out. The magnetotail is where reconnection occurs. Magnetic field lines periodically disconnect and reconnect, creating explosions to release the energy. The disconnected bits of the tail are called 'plasmoids', they get ejected into space at a speed around 900 km/s [67].

In this chapter, we will only talk about solar wind interaction of Mars based on our XMHD simulation.

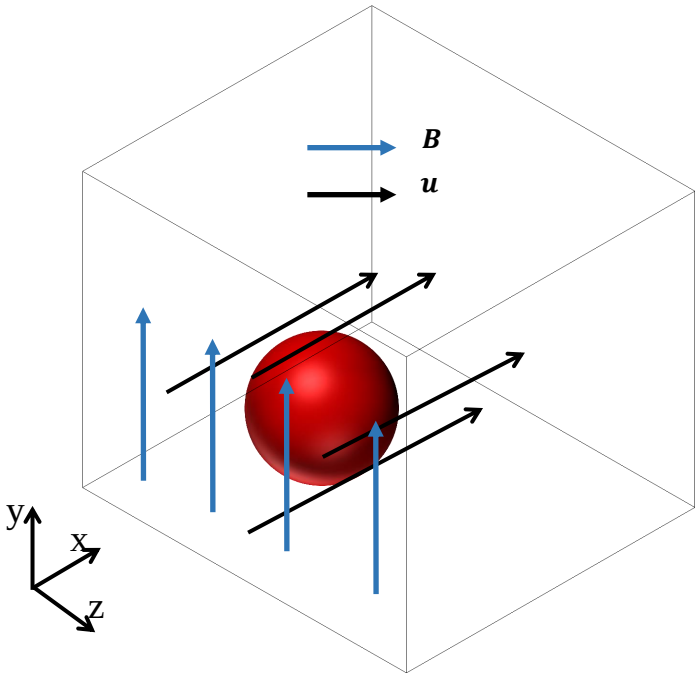

Figure 8.1: Set Up of the simulation for studying the solar wind interacting with Mars, the flows are magnetized with a magnetic field that is perpendicular to the flow direction; The speed is **u**, the driving magnetic field is **B**.

8.2 XMHD simulation of Mars

8.2.1 Problem Set Up

The problem is set up following the diagram 8.2.1. Average solar wind properties at the Mars position should approximately be: $n \approx 7\text{cm}^{-3}$, $u \approx 400\text{km/s}$, $T \approx 10$ eV, $B \approx 10\text{nT}$, $M_s \approx 10$, $M_A \approx 4$. The radius of Mars is approximately 3.39×10^6 m. So we set up the inflow boundary condition on the left boundary and the initial condition according to these parameters. The size of the region is $l_x = 5 \times 10^7$ m on the x direction, $l_y = 5 \times 10^7$ m on the y direction, and $l_z = 5 \times 10^7$ m on the z direction. Mars is simulated with a sphere with the center $0.35l_x$

from the left boundary, $0.5l_y$ from the lower boundary and $0.5l_z$ from the front boundary. 160 cells are used in each dimension. For accurate computation, we nondimensionalize all the numbers in the code following $\mathbf{U} = U_0\tilde{\mathbf{U}}$, where $\tilde{\mathbf{U}}$ is the set of dimensionless variables and U_0 is the set of dimensional normalization factors. For U_0, we use the numbers listed in table 8.1.

Table 8.1: Characteristic Scales used to Non-dimensionalize Parameters

Variable Name	Notation	U_0
Number Density	n_0	$10^7\mathrm{m}^{-3}$
Time	t_0	20s
Length	L_0	$10^7\mathrm{m}$
Velocity	v_0	$5 \times 10^5\mathrm{m/s}$
Magnetic field	B_0	$1.0243 \times 10^{-7}\mathrm{T}$
Electric field	E_0	$5.122 \times 10^{-2}\mathrm{V/m}$

8.2.2 Simulation Results

The simulation is carried out with 3D DG-PERSEUS code, we took clip through the axis of symmetry, which is shown in Figure 8.2.2.

We see some plasma piled up in front of the obstacle and the field lines are compressed and piled up in front of the obstacle. The incident solar wind dynamic pressure is balanced by the pressure of the plasmas which are piled up in front of the obstacle. The magnetic pressure generated by the piled up magnetic field also helps to balance the incoming dynamic pressure. This is different

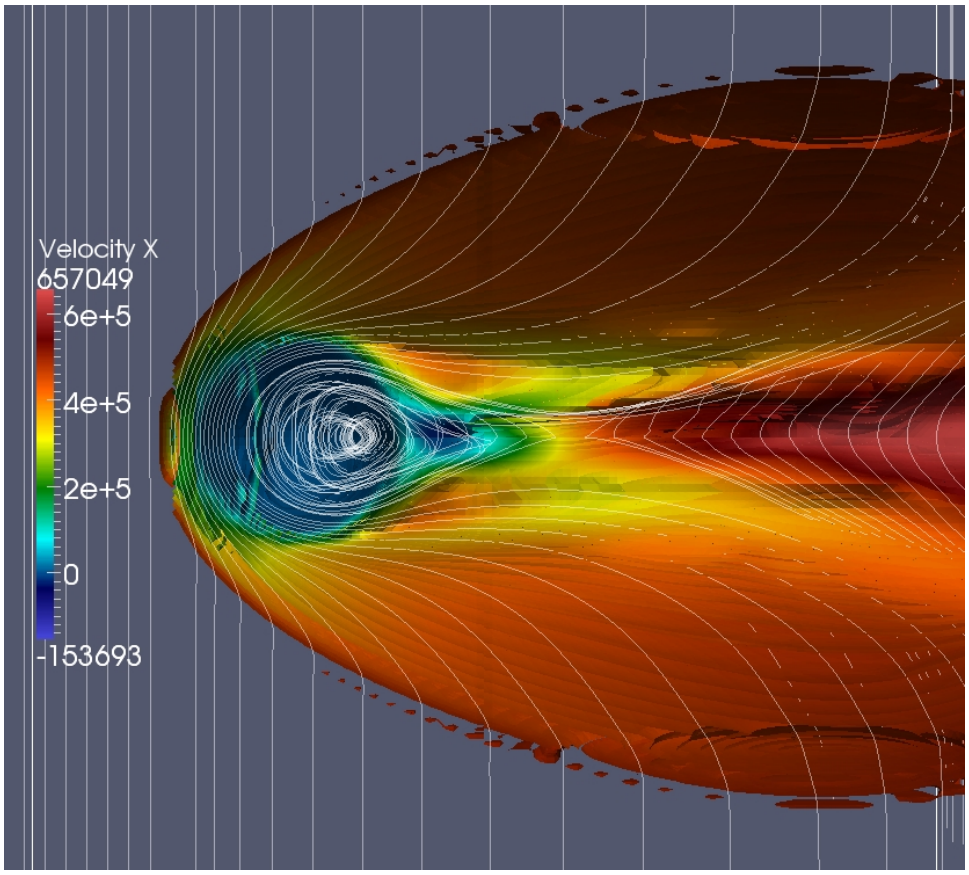

Figure 8.2: Simulation of Solar Wind Interacting with Mars. A slip through the axis of symmetry of the 3D XMHD simulation result: Magnetic field lines with background color plot of x component velocity v_x.

from Earth, where magnetic pressure from intrinsic magnetic field can balance the incoming pressure.

The mechanism for forming the Martian tail structures is also different from the magnetotail of Earth. The magnetotail of the Earth is composed of stretched-out dipole field lines of the planet, but Mars does not have dipole field lines. From Figure 8.2.2, we can see that Mars also has a two-lobed magnetotail, but it is composed of interplanetary or solar wind field lines that appear to have become hung up in the plasma close to the surface as they drape around the

planet. Despite the different forming mechanisms, our simulation shows that the magnetotails of these two planets share a common feature, which is reconnection. We already know that reconnection occurs in the magnetotail of the Earth. From the result shown in 8.2.2, we see an X-point between the two tail lobes, in the region to the left of the X-point, the velocity is negative, meaning the flow is towards the obstacle, whereas the flow to the right of the X-point directs away from the obstacle. These are all clear signatures of magnetic reconnection. This finding agrees with the observations presented in [57, 16]. Thus, in unmagnetized planets, reconnection can also occur with involving only the field lines from the solar wind.

8.3 Reproduction of Martian Phenomena with Lab Parameters

Using the same inflow as given in section 7.1(a), only replacing the cylindrical obstacle with a ball of radius 3.2 mm. We use Aluminum as the material with Spitzer resistivity model. The result is as shown in Figure 8.3.

The basic features agree with the Martian simulation, for example, we also obtain a bow shock structure, we also have an X-point behind the obstacle, and we also observe reconnection signatures. However, there are differences, which are not unexpected. When we scale down the parameters, some things have to change. For example, the resistivity is different. The laboratory plasmas are much more resistive than interplanetary plasmas. The Hall effect also changes, since it is dependent on density, magnetic field, etc.. Radiation loss also changes, but the radiative physics is left out in our model, so we do not consider that. Even with all these factors that can make the scaling down quite challenging,

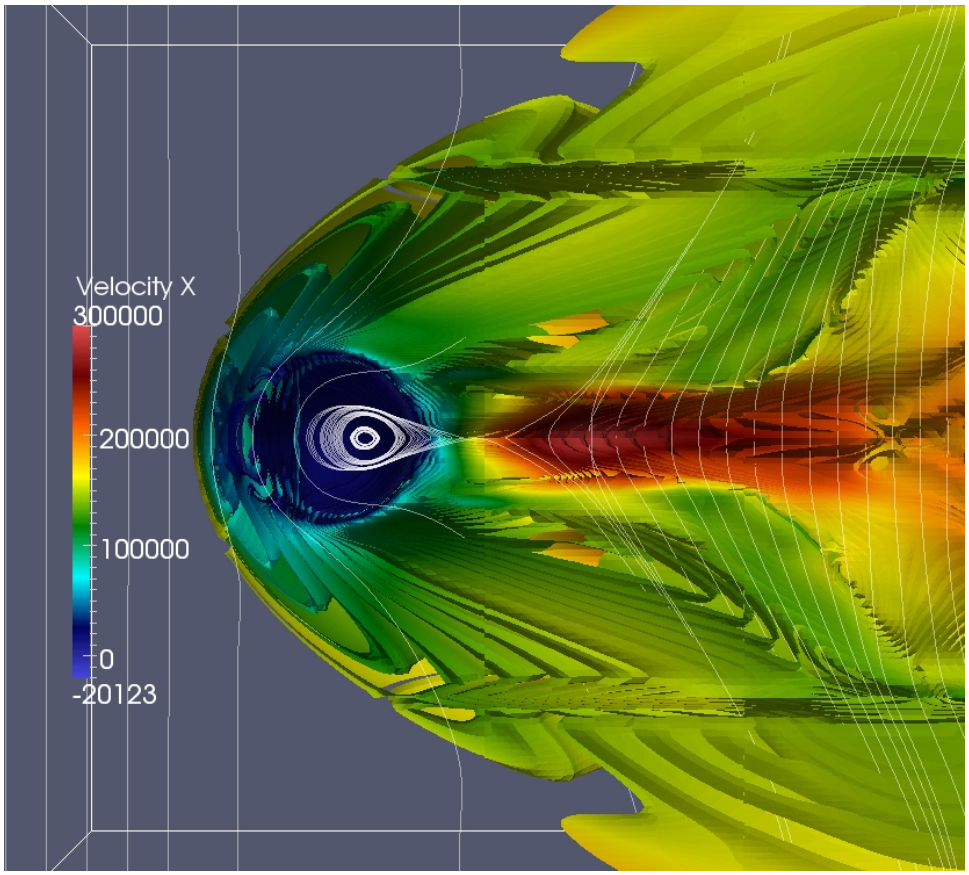

Figure 8.3: Simulation with Lab Parameters to Reproduce Martian Phenomena. A slip through the axis of symmetry of the 3D XMHD simulation result: Magnetic field lines with background color plot of x component velocity v_x.

we still obtain a result which agrees favorably with the Mars simulation. Note that the inflow we use for this simulation is in the same parameter regime with the outflow from the two-wire magnetic reconnection, meaning that these parameters are easily achieved in our Lab. This simulation provides guidance for the experimentalists who desire to study interplanetary physics in the lab.

CHAPTER 9

CONCLUSIONS

9.1 Summary

In this thesis, we constructed a positivity-preserving DG scheme that solves an XMHD model. As constructed, the scheme is able to handle challenging problems having a large dynamic density range (from near-vacuum to solid density), which covers the entire density range of interest in HED plasma problems. Because the XMHD model is physically consistent from high densities to vacuum, it can properly treat the low-density regions, and eliminate the need for the non-physical vacuum resistivity required in MHD models.

The DG scheme has a number of distinct advantages for HED type problems: it is accurate for problems with δ-function discontinuities; step-type contact and shock discontinuities; and very importantly, boundary layers and small-scale structure variations due to non-MHD effects at the ion and electron inertial scales.

We have proven that the PP-limiter preserves the stability of a system governed by an XMHD model or an MHD model. This is essential, as the sharp transitions from a dense state of matter to near vacuum greatly stress any numerical method to keep the density, and in particular, the pressure positive. Also there is an advantage PP-limiter over TVD limiter, that is, it does not degrade the order of accuracy at smooth extrema.

We have shown that the XMHD equations can be solved by the DG method in the context of a relaxation system using an implicit-explicit scheme. This is

a critical requirement since most HED problems evolve on times scales many orders of magnitude slower than the natural frequencies of the XMHD or two-fluid model. In order to solve HED problems using an XMHD model we must in practice step over the plasma frequency and electron cyclotron frequencies. We have demonstrated that the method presented in this paper succeeds well in this regard as we are able to accurately solve high-density problems with a time step that is many orders of magnitude larger than $1/\omega_{pe}$.

The extended-MHD code DG-PERSEUS, which is an implementation of this semi-implicit positivity-preserving DG scheme, has been applied to various problems. In this thesis, the primary focus has been the study of two physics problems. First problem is the magnetic reconnection problem, and second is the magnetized shock problem. These two problems are closely related to each other, as they both can occur as the result of each other.

We have studied a novel configuration for producing a two wire reconnection, which is driven by an inverse skin effect. The sudden reversal of the driving current induces a reversal current on the surface of the plasma column, thus producing a Lorentz force to expand the plasma column with the reversed current on the expanding front. When the expanding fronts from the two wires meet, a reversed current sheet forms, supporting an X-type magnetic field configuration. The plasmas and the magnetic fluxes in the inflow regions get out through this X-point, producing a super-Alfvénic outflow bounded by slow shocks.

The study of magnetized shocks, specifically the shock-obstacle problem, was motivated by the intent to diagnose the outflow characteristics from the two-wire reconnection experiments. We found that with different inflow prop-

erties, the interactions of the flow with the obstacle are also quite different. Among all the parameters of the flow, we found that the Mach numbers are the most influential factor on the structure of the interaction. We found that by recognizing the features that only appear in certain parameter regime, we can infer the inflow properties. The features include bow shock, wake flow, etc.. The bow shock is a fast magnetosonic shock, with a shape that is mainly determined by the fast magnetosonic Mach number M_f of the incoming flow. In the wake flow, a high energy density tail structure forms. The mechanism for forming this tail can be: 1. convergence due to the $\mathbf{J} \times \mathbf{B}$ force; 2. the outflow of a magnetic reconnection. Although not enough evidence can be found from the experimental results to determine which one is driving the tail in the experiment, we can confirm that the tail is a result of magnetic mechanism. Besides the tail structure, we also found that plasmoids can occur.

Two main inflow parameters are found to significantly impact the physical structure of this magnetized flow-obstacle interaction problem. The first one is the inflow mach number M_f. The increase of M_f will make the bow shock stronger and make the openning angle of the bow shock narrower. The second one is the ratio between thermal pressure and magnetic pressure β in the inflow. $\beta = \infty$ corresponds to a hydrodynamic case where there is no tail structure at all. The decrease of β will lead to a stronger tail structure. The change of the physical structures is easily identifiable, which can in turn serve as a diagnostic tool for the flow.

We found that the Hall term can play a very important role in this problem, which in some cases leads to very different results. If we limit the importance of Hall term, for example, increase the characteristic length or decrease the ion

inertial length, the XMHD results will converge to MHD results. We also found direct evidence that the Hall term facilitates reconnection.

The 3D DG-PERSEUS code is used to study the solar wind interaction with Mars, and found that magnetic reconnection occurs in the magnetotail, just as in the magnetotail of the earth. We also found a parameter regime, where similar phenomena can be realized in the laboratory, which may allow experimentalists to design an experiment to study interplanetary physics.

9.2 Future Work

For an HED plasma code, there are a number of effects that we have neglected that should be included. These are the collisional transport phenomena such as: ionization, thermal conduction, radiation transport, Nernst and Ettinghausen effects, etc.. Relativistic effects should also be included in XMHD model, for problems involving high-speed electrons or ions. As of the time of writing this thesis, DG-PERSEUS is only available in Cartesian coordinates, one can extend it to a cylindrical coordinate system or a spherical coordinate system, to better study the radial foil problems, cylindrical wire array problems, etc..

Secondly, in regard to the physics, we demonstrate in this thesis through simulations that interplanetary physics can be reproduced in the laboratory. Experiments can be carried out following the simulation parameters.

APPENDIX A

ENERGY CONSERVATIVE FORM WITH EXTENDED-MHD MODEL

Here, we derive a conservative form of energy in a system governed by extended-MHD model, and we take the approximation to the order of $\bigcirc(m_e/m_i)$.

$$\frac{\partial \mathbf{J}}{\partial t} = -\nabla \cdot (\mathbf{uJ} + \mathbf{Ju} - \frac{1}{Zne}\mathbf{JJ} - \frac{e}{m_e}\mathbf{I}P_e) + \frac{Zne^2}{m_e}[\mathbf{E} + \mathbf{u} \times \mathbf{B} - \frac{1}{Zne}\mathbf{J} \times \mathbf{B} - \eta \mathbf{J}] \quad \text{(A.1)}$$

$n = \rho/m_i$ is ion density

$$\mathbf{J} = Zne(\mathbf{u_i} - \mathbf{u_e}) \equiv Zne\mathbf{v} \quad \text{(A.2)}$$

$$\mathbf{u} = \frac{m_i}{m_i + Zm_e}\mathbf{u_i} + \frac{Zm_e}{m_i + Zm_e}\mathbf{u_e} \quad \text{(A.3)}$$

$$\begin{cases} \mathbf{u_i} = \mathbf{u} + \frac{Zm_e}{m_i+Zm_e}\mathbf{v} \approx \mathbf{u} + \frac{Zm_e}{m_i}\mathbf{v} \\ \mathbf{u_e} = \mathbf{u} - \frac{m_i}{m_i+Zm_e}\mathbf{v} \approx \mathbf{u} - (1 - \frac{Zm_e}{m_i})\mathbf{v} \end{cases} \quad \text{(A.4)}$$

$$\mu = \frac{Zm_em_in}{m_i + Zm_e};\ \rho = (Zm_e + m_i)n;\ \rho_e = Zm_en \quad \text{(A.5)}$$

Also we assume we have quasi-neutral condition, namely we have:$n_e = Zn_i = Zn$. Based on the above equations, we have the momentum equation for electrons and ions as follows:

$$\begin{cases} m_in_i\partial_t\mathbf{u_i} + m_in_i\mathbf{u_i} \cdot \nabla\mathbf{u_i} = -\nabla P_i + Zen_i(\mathbf{E} + \mathbf{u_i} \times \mathbf{B}) \\ m_en_e\partial_t\mathbf{u_e} + m_en_e\mathbf{u_e} \cdot \nabla\mathbf{u_e} = -\nabla P_e - en_e(\mathbf{E} + \mathbf{u_e} \times \mathbf{B}) \end{cases} \quad \text{(A.6)}$$

$\Rightarrow$

$$\begin{cases} m_in\partial_t\mathbf{u} + \frac{Zm_e}{m_i} \cdot m_in\partial_t\mathbf{v} + m_in\mathbf{u} \cdot \nabla\mathbf{u} + \frac{Zm_e}{m_i}m_in\mathbf{u} \cdot \nabla\mathbf{v} + \frac{Zm_e}{m_i}m_in\mathbf{v} \cdot \nabla\mathbf{u} \\ = -\nabla P_i + Zen(\mathbf{E} + \mathbf{u} \times \mathbf{B} + \frac{Zm_e}{m_i}\mathbf{v} \times \mathbf{B}) \\ Zm_en\partial_t\mathbf{u} - Zm_en\partial_t\mathbf{v} + Zm_en\mathbf{u} \cdot \nabla\mathbf{u} + Zm_en\mathbf{v} \cdot \nabla\mathbf{v} - Zm_en\mathbf{u} \cdot \nabla\mathbf{v} - Zm_en\mathbf{v} \cdot \nabla\mathbf{u} \\ = -\nabla P_e - Zen(\mathbf{E} + \mathbf{u} \times \mathbf{B} - \mathbf{v} \times \mathbf{B} + \frac{Zm_e}{m_i}\mathbf{v} \times \mathbf{B}) \end{cases} \quad \text{(A.7)}$$

add the two equations in equation (7), we have:

$$(m_i + Zm_e)n\partial_t \mathbf{u} + (m_i + Zm_e)n\mathbf{u}\cdot\nabla\mathbf{u} + Zm_e n\mathbf{v}\cdot\nabla\mathbf{v} = -\nabla(P_e + P_i) + Zen\mathbf{v}\times\mathbf{B} \quad \text{(A.8)}$$

$\Rightarrow$

$$\rho\partial_t \mathbf{u} + \rho\mathbf{u}\cdot\nabla\mathbf{u} = -\nabla P + Zen\mathbf{v}\times\mathbf{B} - \rho_e\mathbf{v}\cdot\nabla\mathbf{v} \quad \text{(A.9)}$$

By dotting equation (9) with **u**, we can obtain:

$$\frac{1}{2}\rho\partial_t u^2 + \rho\mathbf{u}\cdot[\mathbf{u}\cdot\nabla\mathbf{u}] = -\mathbf{u}\cdot\nabla P + Zen\mathbf{u}\cdot(\mathbf{v}\times\mathbf{B}) - \rho_e\mathbf{u}\cdot[\mathbf{v}\cdot\nabla\mathbf{v}] \quad \text{(A.10)}$$

$\Rightarrow$

$$\frac{1}{2}\rho\partial_t u^2 + \frac{1}{2}\rho\mathbf{u}\cdot\nabla u^2 = -\mathbf{u}\cdot\nabla P + Zen\mathbf{u}\cdot(\mathbf{v}\times\mathbf{B}) - \rho_e\mathbf{u}\cdot[\mathbf{v}\cdot\nabla\mathbf{v}] \quad \text{(A.11)}$$

$\Rightarrow$

$$\begin{aligned}\partial_t(\frac{1}{2}\rho u^2) + \nabla\cdot(\frac{1}{2}\rho u^2\mathbf{u}) - \frac{1}{2}u^2\partial_t\rho - \frac{1}{2}u^2\nabla\cdot(\rho\mathbf{u}) \\ = -\mathbf{u}\cdot\nabla P + Zen\mathbf{u}\cdot(\mathbf{v}\times\mathbf{B}) - \rho_e\mathbf{u}\cdot[\mathbf{v}\cdot\nabla\mathbf{v}]\end{aligned} \quad \text{(A.12)}$$

By multiplying the continuity equation by $u^2/2$, and add it to equation (12) we can obtain:

$$\partial_t(\frac{1}{2}\rho u^2) + \nabla\cdot(\frac{1}{2}\rho u^2\mathbf{u}) = -\mathbf{u}\cdot\nabla P + Zen\mathbf{u}\cdot(\mathbf{v}\times\mathbf{B}) - \rho_e\mathbf{u}\cdot[\mathbf{v}\cdot\nabla\mathbf{v}] \quad \text{(A.13)}$$

From equation (5), we can write $\mathcal{E}_k$ as:

$$\mathcal{E}_k = \frac{1}{2}m_e u_e^2 + \frac{1}{2}m_i u_i^2 = \frac{1}{2}\rho u^2 + \frac{1}{2}\mu v^2 \quad \text{(A.14)}$$

And we also have:

$$\rho_e = n_e m_e = Zm_e n \approx \mu \quad \text{(A.15)}$$

From equation (13), (14) and (15), we have:

$$\partial_t \mathcal{E}_k + \nabla \cdot (\frac{1}{2}\rho u^2 \mathbf{u}) = \partial_t (\frac{1}{2}\mu v^2) - \mathbf{u} \cdot \nabla P + Zen\mathbf{u} \cdot (\mathbf{v} \times \mathbf{B}) - \mu \mathbf{u} \cdot [\mathbf{v} \cdot \nabla \mathbf{v}] \tag{A.16}$$

We have the internal energy equation as:

$$\partial_t \mathcal{E}_i + \nabla \cdot (\mathcal{E}_i \mathbf{u} - \frac{\mathbf{J} P_e}{neZ(\gamma - 1)}) = \eta J^2 - P\nabla \cdot \mathbf{u} + P_e \nabla \cdot \mathbf{v} \tag{A.17}$$

And the EM energy equation is:

$$\partial_t \mathcal{E}_m + \nabla \cdot (\mathbf{E} \times \mathbf{B}) = -\mathbf{J} \cdot \mathbf{E} \tag{A.18}$$

Substitute $\mathbf{J}$ in ohm's law (1) with $\mathbf{J} = Zne\mathbf{v}$ from (5), we have:

$$Zen\partial_t \mathbf{v} + Ze\mathbf{v}\partial_t n = -\nabla \cdot (Zne\mathbf{u}\mathbf{v} + Zne\mathbf{v}\mathbf{u} - Zne\mathbf{v}\mathbf{v} - \frac{e}{m_e} P_e) + \frac{Zne^2}{m_e}[\mathbf{E} + \mathbf{u} \times \mathbf{B} - \mathbf{v} \times \mathbf{B} - \eta \mathbf{J}] \tag{A.19}$$

$\Rightarrow$

$$n\partial_t \mathbf{v} + \mathbf{v}\partial_t n = -\nabla \cdot (n\mathbf{u}\mathbf{v} + n\mathbf{v}\mathbf{u} - n\mathbf{v}\mathbf{v} - \frac{1}{Zm_e} P_e) + \frac{ne}{m_e}[\mathbf{E} + \mathbf{u} \times \mathbf{B} - \mathbf{v} \times \mathbf{B} - \eta \mathbf{J}] \tag{A.20}$$

Dot equation (20) with $\mathbf{v}$ we have:

$$\frac{1}{2} n\partial_t v^2 + v^2 \partial_t n = -\mathbf{v} \cdot [\nabla \cdot (n\mathbf{u}\mathbf{v})] - \mathbf{v} \cdot [\nabla \cdot (n\mathbf{v}\mathbf{u})] + \mathbf{v} \cdot [\nabla \cdot (n\mathbf{v}\mathbf{v})] + \frac{1}{Zm_e} \mathbf{v} \cdot [\nabla \cdot P_e] + \frac{ne}{m_e} \mathbf{v} \cdot [\mathbf{E} + \mathbf{u} \times \mathbf{B} - \eta \mathbf{J}] \tag{A.21}$$

Since $\mu = \frac{Zm_e m_i n}{m_i + Zm_e} \approx Zm_e n$, multiplying equation (21) with Zm_e, we have:

$$\frac{1}{2} \mu\partial_t v^2 + v^2 \partial_t \mu = -\mathbf{v} \cdot [\nabla \cdot (\mu\mathbf{u}\mathbf{v})] - \mathbf{v} \cdot [\nabla \cdot (\mu\mathbf{v}\mathbf{u})] + \mathbf{v} \cdot [\nabla \cdot (\mu\mathbf{v}\mathbf{v})] + \mathbf{v} \cdot [\nabla \cdot P_e] + Zne\mathbf{v} \cdot [\mathbf{E} + \mathbf{u} \times \mathbf{B} - \eta \mathbf{J}] \tag{A.22}$$

If we add the RHS of equation (16)(17)(18), we have:

$$\partial_t(\frac{1}{2}\mu v^2) - \mathbf{u}\cdot\nabla P + Zen\mathbf{u}\cdot(\mathbf{v}\times\mathbf{B}) - \mu\mathbf{u}\cdot[\mathbf{v}\cdot\nabla\mathbf{v}] + \eta J^2 - P\nabla\cdot\mathbf{u} + P_e\nabla\cdot\mathbf{v} - \mathbf{J}\cdot\mathbf{E}$$
$$= \partial_t(\frac{1}{2}\mu v^2) - \mathbf{J}\cdot(\mathbf{E}+\mathbf{u}\times\mathbf{B}) - \nabla\cdot(P\mathbf{u}) + \eta\mathbf{J}^2 - \mu\mathbf{u}\cdot[\mathbf{v}\cdot\nabla\mathbf{v}] + P_e\nabla\cdot\mathbf{v} \quad (A.23)$$

From equation (22), we have:

$$\partial_t(\frac{1}{2}\mu v^2) = -\frac{1}{2}v^2\partial_t\mu - \mathbf{v}\cdot[\nabla\cdot(\mu\mathbf{u}\mathbf{v})] - \mathbf{v}\cdot[\nabla\cdot(\mu\mathbf{v}\mathbf{u})] + \mathbf{v}\cdot[\nabla\cdot(\mu\mathbf{v}\mathbf{v})] + \mathbf{v}\cdot[\nabla\cdot P_e] + Zne\mathbf{v}\cdot[\mathbf{E}+\mathbf{u}\times\mathbf{B}-\eta\mathbf{J}] \quad (A.24)$$

substitute $\partial_t(\frac{1}{2}\mu v^2)$ in equation (23) by equation (24), we have the RHS of the addition of equation (16)(17)(18) as:

$$-\frac{1}{2}v^2\partial_t\mu - \mathbf{v}\cdot[\nabla\cdot(\mu\mathbf{u}\mathbf{v})] - \mathbf{v}\cdot[\nabla\cdot(\mu\mathbf{v}\mathbf{u})] + \mathbf{v}\cdot[\nabla\cdot(\mu\mathbf{v}\mathbf{v})] + \mathbf{v}\cdot[\nabla\cdot P_e] + \mathbf{J}\cdot[\mathbf{E}+\mathbf{u}\times\mathbf{B}-\eta\mathbf{J}]$$
$$-\mathbf{J}\cdot[\mathbf{E}+\mathbf{u}\times\mathbf{B}-\eta\mathbf{J}] - \nabla\cdot(P\mathbf{u}) - \mu\mathbf{u}\cdot[\mathbf{v}\cdot\nabla\mathbf{v}] + P_e\nabla\cdot\mathbf{v}$$
$$= -\frac{1}{2}v^2\partial_t\mu - \mathbf{v}\cdot[\nabla\cdot(\mu\mathbf{u}\mathbf{v})] - \mathbf{v}\cdot[\nabla\cdot(\mu\mathbf{v}\mathbf{u})] + \mathbf{v}\cdot[\nabla\cdot(\mu\mathbf{v}\mathbf{v})] + \nabla\cdot(P_e\mathbf{v}) - \nabla\cdot(P\mathbf{u})$$
$$-\mu\mathbf{u}\cdot[\mathbf{v}\cdot\nabla\mathbf{v}]$$
$$= \frac{v^2}{2}\nabla\cdot(\mu\mathbf{u}) + \frac{1}{2}\mu\mathbf{u}\cdot\nabla v^2 - \nabla\cdot[\mu\mathbf{u}v^2] - \nabla\cdot[\mu\mathbf{v}\mathbf{u}\cdot\mathbf{v}] + \nabla\cdot(P_e\mathbf{v}) - \nabla\cdot(P\mathbf{u})$$
$$+\mathbf{v}\cdot[\nabla\cdot(\mu\mathbf{v}\mathbf{v})]$$
$$= -\nabla\cdot(\frac{1}{2}\mu v^2\mathbf{u}) - \nabla\cdot(\mu\mathbf{u}\cdot\mathbf{v}\mathbf{v}) + \nabla\cdot(P_e\mathbf{v}) - \nabla\cdot(P\mathbf{u}) + \nabla\cdot(\frac{1}{2}\mu v^2\mathbf{v}) \quad (A.25)$$

So the addition of equations (16)(17)(18) will result in:

$$\frac{\partial}{\partial t}(\mathcal{E}_k+\mathcal{E}_i+\mathcal{E}_m) + \nabla\cdot[\mathcal{E}_k\mathbf{u}+\mathcal{E}_i\mathbf{u}+\mathbf{E}\times\mathbf{B}+P\mathbf{u}-\frac{\mathbf{v}P_e}{\gamma-1}-\frac{1}{2}\mu v^2\mathbf{v}+\mu\mathbf{u}\cdot\mathbf{v}\mathbf{v}] = 0 \quad (A.26)$$

From equation (26), we can conclude that the energy conservation law still holds for approximation to the first order of $(\frac{m_e}{m_i})$.

APPENDIX B

CALCULATION OF FREEZING SPEED

Write the (2.30) - (2.36) in terms of the vector's components, we get 14 equations:

$$
\begin{aligned}
&\partial_t \rho + \frac{\partial m_x}{\partial x} + \frac{\partial m_y}{\partial y} = 0 \\
&\frac{\partial m_x}{\partial t} + \frac{\partial (m_x v_x + P)}{\partial x} + \frac{\partial (m_y v_y)}{\partial y} = J_y B_z - J_z B_y \\
&\frac{\partial m_y}{\partial t} + \frac{\partial (m_y v_x)}{\partial x} + \frac{\partial (m_y v_y + P)}{\partial y} = J_z B_x - J_x B_z \\
&\frac{\partial m_z}{\partial t} + \frac{\partial (m_z v_x)}{\partial x} + \frac{\partial (m_z v_y + P)}{\partial y} = J_x B_y - J_y B_x \\
&\frac{\partial E_n}{\partial t} + \frac{\partial ((E_n + P) v_x)}{\partial x} + \frac{\partial ((E_n + P) v_y)}{\partial y} \\
&= v_x (J_y B_z - J_z B_y) + v_y (J_z B_x - J_x B_z) + v_z (J_x B_y - J_y B_x) + \eta (J_x^2 + J_y^2 + J_z^2) \\
&\frac{\partial E_x}{\partial t} - c^2 \frac{\partial B_z}{\partial y} = -\frac{J_x}{\epsilon_0} \\
&\frac{\partial E_y}{\partial t} + c^2 \frac{\partial B_z}{\partial x} = -\frac{J_y}{\epsilon_0} \\
&\frac{\partial E_z}{\partial t} - c^2 \frac{\partial B_y}{\partial x} + c^2 \frac{\partial B_x}{\partial y} = -\frac{J_z}{\epsilon_0} \\
&\frac{\partial B_x}{\partial t} + \frac{\partial E_z}{\partial y} = 0 \\
&\frac{\partial B_y}{\partial t} - \frac{\partial E_z}{\partial x} = 0 \\
&\frac{\partial B_z}{\partial t} + \frac{\partial E_y}{\partial x} - \frac{\partial E_x}{\partial y} = 0 \\
&\frac{\partial J_x}{\partial t} + \frac{\partial (v_x J_x + J_x v_x - \frac{1}{ne} J_x J_x)}{\partial x} + \frac{\partial (v_y J_x + J_y v_x - \frac{1}{ne} J_y J_x)}{\partial y} \\
&= \frac{ne^2}{m_e} (E_x + v_y B_z - \frac{1}{ne} J_y B_z - \eta J_x) \\
&\frac{\partial J_y}{\partial t} + \frac{\partial (v_x J_y + J_x v_y - \frac{1}{ne} J_x J_y)}{\partial x} + \frac{\partial (v_y J_y + J_y v_y - \frac{1}{ne} J_y J_y)}{\partial y} \\
&= \frac{ne^2}{m_e} (E_y + v_z B_x - \frac{1}{ne} J_z B_x - \eta J_y) \\
&\frac{\partial J_z}{\partial t} + \frac{\partial (v_x J_z + J_x v_z - \frac{1}{ne} J_x J_z)}{\partial x} + \frac{\partial (v_y J_z + J_y v_z - \frac{1}{ne} J_y J_z)}{\partial y} \\
&= \frac{ne^2}{m_e} (E_z + v_x B_y - \frac{1}{ne} J_x B_y - \eta J_z)
\end{aligned}
\tag{B.1}
$$

The fluxes for each variable are lined up as follows:

$$
\begin{aligned}
F_{\rho} &= m_x \\
F_{m_x} &= \frac{m_x^2}{\rho} + (\gamma - 1)(E_n - \frac{0.5(m_x^2 + m_y^2 + m_z^2)}{\rho}) \\
F_{m_y} &= \frac{m_y m_x}{\rho} \\
F_{m_z} &= \frac{m_z m_x}{\rho} \\
F_{E_n} &= (E_n + (\gamma - 1)(E_n - \frac{0.5(m_x^2 + m_y^2 + m_z^2)}{\rho}))\frac{m_x}{\rho} \\
F_{b_x} &= 0 \\
F_{b_y} &= -e_z \\
F_{b_z} &= e_y \\
F_{e_x} &= 0 \\
F_{e_y} &= cfva2 * b_z \\
F_{e_z} &= -cfva2 * b_y \\
F_{j_x} &= \frac{m_x j_x + j_x m_x - lil0 j_x j_x}{\rho} \\
F_{j_y} &= \frac{m_x j_y + j_x m_y - lil0 j_x j_y}{\rho} \\
F_{j_x} &= \frac{m_x j_z + j_x m_z - lil0 j_x j_z}{\rho}
\end{aligned}
\tag{B.2}
$$

part 1 of the table

Par	ρ	m_x	m_y	m_z	E_n
ρ	0	1	0	0	0
m_x	$-\frac{(m_x)^2}{\rho^2}$ + $\frac{0.5(m_x^2+m_y^2+m_z^2)(\gamma-1)}{\rho^2}$	$2\frac{m_x}{\rho} - \frac{m_x(\gamma-1)}{\rho}$	$-\frac{m_y(\gamma-1)}{\rho}$	$-\frac{m_z(\gamma-1)}{\rho}$	$\gamma - 1$
m_y	$-m_y\frac{m_x}{\rho^2}$	$\frac{m_y}{\rho}$	$\frac{m_x}{\rho}$	0	0
m_z	$-m_z\frac{m_x}{\rho^2}$	$\frac{m_z}{\rho}$	0	$\frac{m_x}{\rho}$	0
E_n	$-\frac{m_x}{\rho^2}(\gamma E_n - 0.5\frac{(m_x^2+m_y^2+m_z^2)(\gamma-1)}{\rho})$ + $\frac{m_x(\gamma-1)}{2\rho}\frac{m_x^2+m_y^2+m_z^2}{\rho^2}$	$\frac{1}{\rho}(\gamma E_n - 0.5\frac{(m_x^2+m_y^2+m_z^2)(\gamma-1)}{\rho})$ $-\frac{m_x^2(\gamma-1)}{\rho^2}$	$-\frac{m_y m_x(\gamma-1)}{\rho^2}$	$-\frac{m_z m_x(\gamma-1)}{\rho^2}$	$\gamma\frac{m_x}{\rho}$
bx	0	0	0	0	0
by	0	0	0	0	0
bz	0	0	0	0	0
ex	0	0	0	0	0
ey	0	0	0	0	0
ez	0	0	0	0	0
jx	$\frac{lil0j_x^2-m_x j_x-j_x m_x}{\rho^2}$	$\frac{2j_x}{\rho}$	0	0	0
jy	$\frac{lil0j_x j_y-m_x j_y-j_x m_x}{\rho^2}$	$\frac{j_y}{\rho}$	$\frac{j_x}{\rho}$	0	0
jz	$\frac{lil0j_x j_y-m_x j_z-j_x m_z}{\rho^2}$	$\frac{j_z}{\rho}$	0	$\frac{j_x}{\rho}$	0

Part 2 of the table, following from the last page

Par	b_x	b_y	b_z	e_x	e_y	e_z	j_x	j_y	j_z
ρ	0	0	0	0	0	0	0	0	0
m_x	0	0	0	0	0	0	0	0	0
m_y	0	0	0	0	0	0	0	0	0
m_z	0	0	0	0	0	0	0	0	0
E_n	0	0	0	0	0	0	0	0	0
b_x	0	0	0	0	0	0	0	0	0
b_y	0	0	0	0	0	-1	0	0	0
b_z	0	0	0	0	1	0	0	0	0
e_x	0	0	0	0	0	0	0	0	0
e_y	0	cfva2	0	0	0	0	0	0	0
e_z	-cfva2	0	0	0	0	0	0	0	0
j_x	0	0	0	0	0	0	$\frac{2m_x - lil0\, j_x}{\rho}$	0	0
j_y	0	0	0	0	0	0	$\frac{m_y - lil0\, j_y}{\rho}$	$\frac{m_x - lil0\, j_x}{\rho}$	0
j_z	0	0	0	0	0	0	$\frac{m_y - lil0\, j_z}{\rho}$	0	$\frac{m_x - lil0\, j_x}{\rho}$

The tables can be divided into the following three blocks:

1. first block, the fluid block:

Par	ρ	m_x	m_y	m_z	E_n
ρ	0	1	0	0	0
m_x	$-\frac{(m_x)^2}{\rho^2}+\frac{0.5(m_x^2+m_y^2+m_z^2)(\gamma-1)}{\rho^2}$	$2\frac{m_x}{\rho}-\frac{m_x(\gamma-1)}{\rho}$	$-\frac{m_y(\gamma-1)}{\rho}$	$-\frac{m_z(\gamma-1)}{\rho}$	$\gamma-1$
m_y	$-m_y\frac{m_x}{\rho^2}$	$\frac{m_y}{\rho}$	$\frac{m_x}{\rho}$	0	0
m_z	$-m_z\frac{m_x}{\rho^2}$	$\frac{m_z}{\rho}$	0	$\frac{m_x}{\rho}$	0
E_n	$-\frac{m_x}{\rho^2}(\gamma E_n - 0.5\frac{(m_x^2+m_y^2+m_z^2)(\gamma-1)}{\rho}) + \frac{m_x(\gamma-1)}{2\rho}\frac{m_x^2+m_y^2+m_z^2}{\rho^2}$	$\frac{1}{\rho}(\gamma E_n - 0.5\frac{(m_x^2+m_y^2+m_z^2)(\gamma-1)}{\rho}) - \frac{m_x^2(\gamma-1)}{\rho^2}$	$-\frac{m_y m_x(\gamma-1)}{\rho^2}$	$-\frac{m_z m_x(\gamma-1)}{\rho^2}$	$\gamma\frac{m_x}{\rho}$

The calculated eigenvalue for this matrix is:

$$
\begin{aligned}
\lambda_1 &= v_x \\
\lambda_2 &= v_y \\
\lambda_3 &= v_z \\
\lambda_4 &= |\frac{m_x}{\rho}| + \sqrt{\frac{\gamma(\gamma-1)(E_n - \frac{m_x^2+m_y^2+m_z^2}{2\rho})}{\rho}} \\
\lambda_5 &= |\frac{m_x}{\rho}| - \sqrt{\frac{\gamma(\gamma-1)(E_n - \frac{m_x^2+m_y^2+m_z^2}{2\rho})}{\rho}}
\end{aligned}
\tag{B.3}
$$

Say the above block matrix is A_1, then right eigen vectors X_i, ie, $A_1 X_i = \lambda_i X_i$ is:

$$\begin{aligned}
X_1 &= [-1, -v_x, 0, 0, E_k/\rho - v_x^2]' \\
X_2 &= [v_z, v_x v_z, 0, E_k/\rho - v_x^2, 0]' \\
X_3 &= [v_y, v_x v_y, E_k/\rho - v_x^2, 0, 0]' \\
X_4 &= [1, \lambda_4, v_y, v_z, \frac{E_n}{\rho}\gamma - (\gamma-1)\frac{E_k}{\rho} + v_x(\lambda_4 - v_x)]' \\
X_5 &= [1, \lambda_5, v_y, v_z, \frac{E_n}{\rho}\gamma - (\gamma-1)\frac{E_k}{\rho} + v_x(\lambda_5 - v_x)]'
\end{aligned} \tag{B.4}$$

The left eigen vectors Y_i, ie, $Y_i A_1 = \lambda_i Y_i$ are:

$$\begin{aligned}
Y_1 &= [v_x^2 + (\gamma-1)\frac{E_k}{\rho} - \gamma\frac{E_n}{\rho}, -v_x, 0, 0, 1] \\
Y_2 &= [0, -v_x v_y, v_x^2 - \gamma\frac{E_n}{\rho} + (\gamma-1)\frac{E_k}{\rho}, 0, v_y] \\
Y_3 &= [0, -v_x v_z, 0, v_x^2 - \gamma\frac{E_n}{\rho} + (\gamma-1)\frac{E_k}{\rho}, v_z] \\
\text{define: } P_4 &= \frac{1}{\lambda_4}(v_x v_y^2 + v_x v_z^2 - \gamma\frac{E_n}{\rho}v_x + 2(\gamma-1)v_x\frac{E_k}{\rho} + (v_x^2 - (\gamma-1)\frac{E_k}{\rho})(\gamma v_x - \lambda_4)/(\gamma-1)) \\
Y_4 &= [P_4, -(\gamma v_x - \lambda_4)/(\gamma-1), -v_y, -v_z, 1] \\
\text{define: } P_5 &= \frac{1}{\lambda_5}(v_x v_y^2 + v_x v_z^2 - \gamma\frac{E_n}{\rho}v_x + 2(\gamma-1)v_x\frac{E_k}{\rho} + (v_x^2 - (\gamma-1)\frac{E_k}{\rho})(\gamma v_x - \lambda_5)/(\gamma-1)) \\
Y_5 &= [P_5, -(\gamma v_x - \lambda_5)/(\gamma-1), -v_y, -v_z, 1]
\end{aligned} \tag{B.5}$$

So the left eigenvector matrix L_1 of A_1 is:

$v_x^2 + (\gamma-1)\frac{E_k}{\rho} - \gamma\frac{E_n}{\rho}$	$-v_x$	0	0	1
0	$-v_x v_y$	$v_x^2 - \gamma\frac{E_n}{\rho} + (\gamma-1)\frac{E_k}{\rho}$	0	v_y
0	$-v_x v_z$	0	$v_x^2 - \gamma\frac{E_n}{\rho} + (\gamma-1)\frac{E_k}{\rho}$	v_z
P_4	$-(\gamma v_x - \lambda_4)/(\gamma-1)$	$-v_y$	$-v_z$	1
P_5	$-(\gamma v_x - \lambda_5)/(\gamma-1)$	$-v_y$	$-v_z$	1

Q(rh,mx,my,mz,en) are first transformed to charasteristic variables g = L_1Q:

$$\begin{aligned} g_x &= L_1 Q_x \\ \Delta^+ g_0 &= L_1(Q_0^{i+1} - Q_0^i) \\ \Delta^- g_0 &= L_1(Q_0^i - Q_0^{i-1}) \end{aligned} \tag{B.6}$$

then we use:

$$Q_x = L_1^{-1} minmod(g_x, \Delta^+ g_0, \Delta^- g_0) \tag{B.7}$$

to transform the value back to get the limited form of Q_x.

PS: L_1^{-1} is such a mess that it won't be shown here, but it has been inserted in in the code.

2. second block, the magnetic block:

Par	b_x	b_y	b_z	e_x	e_y	e_z
b_x	0	0	0	0	0	0
b_y	0	0	0	0	0	-1
b_z	0	0	0	0	1	0
e_x	0	0	0	0	0	0
e_y	0	0	cfva2	0	0	0
e_z	0	-cfva2	0	0	0	0

The calculated eigenvalue for this matrix is:

$$\lambda_1 = 0,\ \lambda_1 = 0,\ \lambda_3 = clt,\ \lambda_4 = clt,\ \lambda_5 = -clt,\ \lambda_6 = -clt \tag{B.8}$$

Say the above block matrix is A_2, then right eigen vectors X_i, ie, $A_2 X_i = \lambda_i X_i$ is:

$$\begin{aligned} X_1 &= [1,0,0,0,0,0]' \\ X_2 &= [0,0,0,1,0,0]' \\ X_3 &= [0,1,0,0,0,-clt]' \\ X_4 &= [0,0,1,0,clt,0]' \\ X_5 &= [0,1,0,0,0,clt]' \\ X_6 &= [0,0,1,0,-clt,0]' \end{aligned} \tag{B.9}$$

The left eigen vectors Y_i, ie, $Y_i A_2 = \lambda_i Y_i$ are:

$$\begin{aligned} Y_1 &= [1,0,0,0,0,0] \\ Y_2 &= [0,0,0,1,0,0] \\ Y_3 &= [0,1,0,0,0,-\frac{1}{clt}] \\ Y_4 &= [0,0,1,0,\frac{1}{clt},0] \\ Y_5 &= [0,1,0,0,0,\frac{1}{clt}] \\ Y_6 &= [0,0,1,0,-\frac{1}{clt},0] \end{aligned} \tag{B.10}$$

So the left eigenvector matrix L_2 of A_2 is:

1	0	0	0	0	0
0	0	0	1	0	0
0	1	0	0	0	-1/clt
0	0	1	0	1/clt	0
0	1	0	0	0	1/clt
0	0	1	0	-1/clt	0

Q(bx,by,bz,ex,ey,ez) are first transformed to charasteristic variables g = L_2Q:

$$\begin{aligned} g_x &= L_2 Q_x \\ \Delta^+ g_0 &= L_2(Q_0^{i+1} - Q_0^i) \\ \Delta^- g_0 &= L_2(Q_0^i - Q_0^{i-1}) \end{aligned} \tag{B.11}$$

then we use:

$$Q_x = L_2^{-1} minmod(g_x, \Delta^+ g_0, \Delta^- g_0) \tag{B.12}$$

to transform the value back to get the limited form of Q_x.

We do the inversion of matrix L_2 to get L_2^{-1}:

1	0	0	0	0	0
0	0	0.5	0	0.5	0
0	0	0	0.5	0	0.5
0	1	0	0	0	0
0	0	0	0.5clt	0	-0.5clt
0	0	-0.5clt	0	0.5clt	0

3. third block, the GOL block:

Par	j_x	j_y	j_z
j_x	$\frac{2m_x - lil0 j_x}{\rho}$	0	0
j_y	$\frac{m_y - lil0 j_y}{\rho}$	$\frac{m_x - lil0 j_x}{\rho}$	0
j_z	$\frac{m_y - lil0 j_z}{\rho}$	0	$\frac{m_x - lil0 j_x}{\rho}$

The calculated eigenvalue for this matrix is:

$$\lambda_1 = \frac{m_x}{\rho} - \frac{lil0 j_x}{\rho} \lambda_2 \quad = \frac{m_x}{\rho} - \frac{lil0 j_x}{\rho} \lambda_3 = 2\frac{m_x}{\rho} - \frac{lil0 j_x}{\rho} \tag{B.13}$$

Say the above block matrix is A_3, then right eigen vectors X_i, ie, $A_3 X_i = \lambda_i X_i$ is:

$$\begin{aligned}
denote: v_x &= \frac{m_x}{\rho} \\
denote: v_y &= \frac{m_y}{\rho} \\
denote: v_z &= \frac{m_z}{\rho} \\
denote: l_1 &= \frac{lil0 j_x}{\rho} \\
denote: l_2 &= \frac{lil0 j_y}{\rho} \\
denote: l_3 &= \frac{lil0 j_z}{\rho} \\
X_1 &= [0, 0, 1]' \\
X_2 &= [0, 1, 0]' \\
X_3 &= [v_x, v_y - l_2, v_y - l_3]'
\end{aligned} \tag{B.14}$$

The left eigen vectors Y_i, ie, $Y_i A_3 = \lambda_i Y_i$ are:

$$\begin{aligned}
Y_1 &= [0, v_y - l_3, -v_y + l_2] \\
Y_2 &= [v_y - l_3, 0, -v_x] \\
Y_3 &= [1, 0, 0]
\end{aligned} \tag{B.15}$$

So the left eigenvector matrix L_3 of A_3 is:

0	$v_y - l_3$	$-v_y + l_2$
$v_y - l_3$	0	$-v_x$
1	0	0

Q(jx,jy,jz) are first transformed to charasteristic variables g = L_3Q:

$$\begin{aligned}
g_x &= L_3 Q_x \\
\Delta^+ g_0 &= L_3 (Q_0^{i+1} - Q_0^i) \\
\Delta^- g_0 &= L_3 (Q_0^i - Q_0^{i-1})
\end{aligned} \tag{B.16}$$

then we use:

$$Q_x = L_3^{-1} minmod(g_x, \Delta^+ g_0, \Delta^- g_0) \tag{B.17}$$

to transform the value back to get the limited form of Q_x.

We do the inversion of matrix L_3 to get L_3^{-1}:

0	0	1
$1/(v_y - l_3)$	$(-v_y + l_2)/(v_x(v_y - l_3))$	$(v_y - l_2)/v_x$
0	$-1/v_x$	$(v_y - l_3)/v_x$

BIBLIOGRAPHY

[1] Balsara, D. S. (2004). Second-order-accurate schemes for magnetohydrodynamics with divergence-free reconstruction. The Astrophysical Journal Supplement Series, 151(1), 149.

[2] Balsara, D. S. (2009). Divergence-free reconstruction of magnetic fields and WENO schemes for magnetohydrodynamics. Journal of Computational Physics, 228(14), 5040-5056.

[3] Balsara, D. S. (2012). Self-adjusting, positivity preserving high order schemes for hydrodynamics and magnetohydrodynamics. Journal of Computational Physics, 231(22), 7504-7517.

[4] Biermann, L., Naturforsch, Z., 5a, 65(1950)

[5] Birn, J., Drake, J. F., Shay, M. A., Rogers, B. N., Denton, R. E., Hesse, M., ... & Pritchett, P. L. (2001). Geospace Environmental Modeling (GEM) magnetic reconnection challenge. Journal of Geophysical Research: Space Physics (19782012), 106(A3), 3715-3719.

[6] Boyd, T.J.M., & Sanderson, J.J. (2003). The Physics of Plasmas.

[7] Brio, M., & Wu, C. C. (1988). An upwind differencing scheme for the equations of ideal magnetohydrodynamics. Journal of Computational Physics, 75(2), 400-422.

[8] Cheng, Y., Li, F., Qiu, J., & Xu, L. (2013). Positivity-preserving DG and central DG methods for ideal MHD equations. Journal of Computational Physics, 238, 255-280.

[9] Chacn, L., & Knoll, D. A. (2003). A 2D high-β Hall MHD implicit nonlinear solver. Journal of Computational Physics, 188(2), 573-592.

[10] Cockburn, B., Hou, S., & Shu, C. W. (1990). The Runge-Kutta local projection discontinuous Galerkin finite element method for conservation laws. IV. The multidimensional case. Mathematics of Computation, 54(190), 545-581.

[11] Cockburn, B., Li, F., & Shu, C. W. (2004). Locally divergence-free discontinuous Galerkin methods for the Maxwell equations. Journal of Computational Physics, 194(2), 588-610.

[12] Cockburn, B., & Shu, C. W. (1989). TVB Runge-Kutta local projection discontinuous Galerkin finite element method for conservation laws. II. General framework. Mathematics of Computation, 52(186), 411-435.

[13] Cockburn, B., Lin, S. Y., & Shu, C. W. (1989). TVB Runge-Kutta local projection discontinuous Galerkin finite element method for conservation laws III: one-dimensional systems. Journal of Computational Physics, 84(1), 90-113.

[14] Cockburn, B., Hou, S., & Shu, C. W. (1990). The Runge-Kutta local projection discontinuous Galerkin finite element method for conservation laws. IV. The multidimensional case. Mathematics of Computation, 54(190), 545-581.

[15] Cockburn, B., & Shu, C. W. (1998). The RungeKutta discontinuous Galerkin method for conservation laws V: multidimensional systems. Journal of Computational Physics, 141(2), 199-224.

[16] Eastwood, J. P., Brain, D. A., Halekas, J. S., Drake, J. F., Phan, T. D., ieroset, M., ... & Acua, M. (2008). Evidence for collisionless magnetic reconnection at Mars. Geophysical Research Letters, 35(2).

[17] Falle, S. A. E. G., Komissarov, S. S., & Joarder, P. (1998). A multidimensional upwind scheme for magnetohydrodynamics. Monthly Notices of the Royal Astronomical Society, 297(1), 265-277.

[18] Fedorov, A., Ferrier, C., Sauvaud, J. A., Barabash, S., Zhang, T. L., Mazelle, C., ... & Bochsler, P. (2008). Comparative analysis of Venus and Mars magnetotails. Planetary and Space Science, 56(6), 812-817.

[19] Giovanelli, 1946

[20] Godunov, S. K. (1959). A difference method for numerical calculation of discontinuous solutions of the equations of hydrodynamics. Matematicheskii Sbornik, 89(3), 271-306.

[21] Gourdain, P. A., & Seyler, C. E. (2013). Impact of the Hall Effect on High-Energy-Density Plasma Jets. Physical review letters, 110(1), 015002.

[22] Greenly, J., Seyler, C., & Zhao, X. (2014). Pulsed-Power Driven Magnetic Reconnection and the Inverse Skin Effect, submitted to Physics Review Letters.

[23] Haines, M.G. (1959). Proc. phys. Soc. 74, Part 5, 479

[24] Hakim, A., Loverich, J., & Shumlak, U. (2006). A high resolution wave propagation scheme for ideal Two-Fluid plasma equations. Journal of Computational Physics, 219(1), 418-442.

[25] Hakim, A. H. (2008). Extended MHD modeling with the ten-moment equations. Journal of Fusion Energy, 27(1-2), 36-43.

[26] Hamlin, N. (2010). The role of the Kelvin-Helmholtz instability in the evolution of magnetized relativistic sheared plasma flows (Doctoral dissertation, University of California, Los Angeles).

[27] Hoteit, H., Ackerer, P., Mos, R., Erhel, J., & Philippe, B. (2004). New twodimensional slope limiters for discontinuous Galerkin methods on arbitrary meshes. International journal for numerical methods in engineering, 61(14), 2566-2593.

[28] Huba, J. D. (2005, March). Numerical Methods: Ideal and Hall MHD. In Proceedings of ISSS (Vol. 7, pp. 26-31).

[29] Huba, J. D. (1994). Hall dynamics of the Kelvin-Helmholtz instability. Physical review letters, 72(13), 2033.

[30] Huba, J. D., & Winske, D. (1998). RayleighTaylor instability: Comparison of hybrid and nonideal magnetohydrodynamic simulations. Physics of Plasmas (1994-present), 5(6), 2305-2316.

[31] Johnson, E. A. (2013). Gaussian-Moment Relaxation Closures for Verifiable Numerical Simulation of Fast Magnetic Reconnection in Plasma (Doctoral dissertation, UNIVERSITY OF WISCONSIN).

[32] Jones, I. R., & Silawatshananai, C. (1980). Observation of the reversed current effect. Plasma Physics, 22(5), 501.

[33] Kallio, E. (1996). An empirical model of the solar wind flow around Mars. Journal of Geophysical Research: Space Physics (19782012), 101(A5), 11133-11147.

[34] LeVeque, R. J. (2002). Finite volume methods for hyperbolic problems (Vol. 31). Cambridge university press.

[35] Lichtenegger, H., Lammer, H., & Stumptner, W. (2002). Energetic neutral atoms at Mars 3. Flux and energy distributions of planetary energetic H atoms. Journal of Geophysical Research: Space Physics (19782012), 107(A10), SSH-6.

[36] Li, F., & Shu, C. W. (2005). Locally divergence-free discontinuous Galerkin methods for MHD equations. Journal of Scientific Computing, 22(1-3), 413-442.

[37] Liverts, E., & Mond, M. (2004). The Hall instability in accelerated plasma channels. Physics of Plasmas (1994-present), 11(1), 55-61.

[38] Loverich, J., & Shumlak, U. (2005). A discontinuous Galerkin method for the full two-fluid plasma model. Computer Physics Communications, 169(1), 251-255.

[39] Loverich, J., Hakim, A., & Shumlak, U. (2010). A discontinuous Galerkin method for ideal two-fluid plasma equations. arXiv preprint arXiv:1003.4542.

[40] Luhmann, J. G., Russell, C. T., Brace, L. H., & Vaisberg, O. L. (1992). The intrinsic magnetic field and solar-wind interaction of Mars. Mars, 1, 1090-1134.

[41] Malakit, K., Cassak, P. A., Shay, M. A., & Drake, J. F. (2009). The hall effect in magnetic reconnection: Hybrid versus Hallless hybrid simulations. Geophysical Research Letters, 36(7).

[42] Martin, M. (2010). Generalized Ohm'S Law At The Plasma-Vacuum Interface (Doctoral dissertation, Cornell University).

[43] Parker, E. N. (1957). Sweets mechanism for merging magnetic fields in conducting fluids. J. Geophys. Res., 62:509.

[44] Parker, E. N. (1963). The Solar-Flare Phenomenon and the Theory of Reconnection and Annihiliation of Magnetic Fields. Astrophysical Journal Supplement, 8:177.

[45] Petschek, H. E. (1964) Magnetic field annihilation. In W. N. Ness, editor, AAS/NASA Symposium on the Physics of Solar Flares, page 425. NASA, Washington, DC.

[46] Schnack, D. D. (2009). Lectures in Magnetohydrodynamics: With an Appendix on Extended MHD (Vol. 780). Springer.

[47] Seyler, C. E., & Martin, M. R. (2011). Relaxation model for extended magnetohydrodynamics: Comparison to magnetohydrodynamics for dense Z-pinches. Physics of Plasmas, 18, 012703.

[48] Shay, M. A., Drake, J. F., & Swisdak, M. (2007). Two-scale structure of the electron dissipation region during collisionless magnetic reconnection. Physical review letters, 99(15), 155002.

[49] Sovinec, C. R., Schnack, D. D., Pankin, A. Y., Brennan, D. P., Tian, H., Barnes, D. C., ... & Jardin, S. C. (2005, January). Nonlinear extended magnetohydrodynamics simulation using high-order finite elements. In Journal of Physics: Conference Series (Vol. 16, No. 1, p. 25). IOP Publishing.

[50] Srinivasan, B. (2006). A comparison between the discontinuous galerkin method and the high resolution wave propagation algorithm for the full two-fluid plasma model (Doctoral dissertation, University of Washington).

[51] Saitou, Y., Nakamura, Y., Kamimura, T., & Ishihara, O. (2012). Bow Shock Formation in a Complex Plasma. Physical review letters, 108(6), 065004.

[52] Srinivasan, B., Hakim, A., & Shumlak, U. (2011). Numerical methods for two-fluid dispersive fast MHD phenomena. Communications in Computational Physics, 10(1), 183.

[53] Shu, C. W., & Osher, S. (1988). Efficient implementation of essentially non-oscillatory shock-capturing schemes. Journal of Computational Physics, 77(2), 439-471.

[54] Shumlak, U., & Loverich, J. (2003). Approximate Riemann solver for the two-fluid plasma model. Journal of Computational Physics, 187(2), 620-638.

[55] Sweet, P. A. (1958). The neutral point theory of solar flares. In B. Lehnert, editor,Electromagnetic Phenomena in Cosmical Physics, page 123. Cambridge University, Press, New York.

[56] Trac, H., & Pen, U. L. (2003). A primer on eulerian computational fluid dynamics for astrophysics. Publications of the Astronomical Society of the Pacific, 115(805), 303-321.

[57] Uluen, D., & Linscott, I. (2008). Lowenergy electron current in the Martian tail due to reconnection of draped interplanetary magnetic field and crustal magnetic fields. Journal of Geophysical Research: Planets (19912012), 113(E6).

[58] Van Leer, B. (1979). Towards the ultimate conservative difference scheme. V. A second-order sequel to Godunov's method. Journal of computational Physics, 32(1), 101-136.

[59] Wilson III, L. B. (2010). The microphysics of collisionless shocks.

[60] Yang, Y., Roy, I., Shu, C.-W., & Fang, L.-Z. (2013). The angular distribution of Lyα resonant photons emerging from an optically thick medium. The Astrophysical Journal, 772(1), 3.

[61] Yang, Y., & Shu, C. W. (2013). Discontinuous Galerkin method for hyperbolic equations involving delta-singularities: negative-order norm error estimates and applications. Numerische Mathematik, 1-29.

[62] Yang, Y., Wei, D.M., & Shu, C.W. (2013). Discontinuous Galerkin method for Krause's consensus models and pressureless Euler equations. Journal of Computational Physics, Volume 252, p. 109-127.

[63] Zahedi, S., & Tornberg, A. K. (2010). Delta function approximations in level set methods by distance function extension. Journal of Computational Physics, 229(6), 2199-2219.

[64] Zhang, X., & Shu, C. W. (2010). On positivity-preserving high order discontinuous Galerkin schemes for compressible Euler equations on rectangular meshes. Journal of Computational Physics, 229(23), 8918-8934.

[65] Zhang, X., & Shu, C. W. (2010). A genuinely high order total variation diminishing scheme for one-dimensional scalar conservation laws. SIAM Journal on Numerical Analysis, 48(2), 772-795.

[66] Zhao, X., Yang, Y., & Seyler, C. E. (2014). A positivity-preserving semi-implicit discontinuous Galerkin scheme for solving extended magnetohydrodynamics equations. Journal of Computational Physics, 278, 400-415.

[67] `http://www.nasa.gov/mission-pages/ibex/news/spaceweather.html.VFlt1XiDBhE`

[68] http://farside.ph.utexas.edu/teaching/plasma/Plasmahtml/node65.html

[69] http://en.wikipedia.org/wiki/Solar-wind